Innovative micro-NMR/MRI functionality utilizing flexible electronics and control systems

Zur Erlangung des akademischen Grades eines

DOKTORS DER INGENIEURWISSENSCHAFTEN (Dr.-Ing.)

von der KIT-Fakultät für Maschinenbau des

Karlsruher Instituts für Technologie (KIT)

angenommene

Dissertation

von

M.Sc. Omar Nassar

Tag der mündlichen Prüfung: 27.07.2021

Hauptreferent: Prof. Dr. Jan G. Korvink

Korreferent: Prof. Dr. Michael Bock

Karlsruher Institut für Technologie

Institut für Mikrostrukturtechnik

Hermann.-v.-Helmholtz Platz 1

76344 Eggenstein-Leopoldshafen

Abstract

The central theme of this work is developing and integrating flexible electronics for micro Magnetic Resonance (MR) applications. Two crucial applications have been covered within this dissertation; one application in the field of Magnetic Resonance Imaging (MRI) and the other in the field of Nuclear Magnetic Resonance (NMR). The MRI application focus on solving the safety and reliability issues involved with MR-catheters. The NMR application introduces a novel approach for enhancing the NMR spectroscopy throughput.

The first part of the dissertation covers the various developed technologies to fabricate flexible electronics on the micro-scale. The covered MR applications required the fabrication of inductors, capacitors, and diodes on flexible substrates. Hence, the first covered technology within the frame of micro-fabrication is depositing of conductive seed-layers onto flexible substrates. Several techniques have been tested and compared. The developed technology enables multi-layer fabrication for the conductive structure on a flexible substrate ($\approx 50\,\mu m$ thickness) suitable for wrapping around the slender tube ($> 0.5\,mm$ diameter). The second covered method is inkjet printing of high-density low loss coefficient capacitors. Two custom polymer-based dielectric inks were synthesized, by the dispersion of TiO_2 and $BaTiO_3$ in benzocyclobutene (BCB) polymer. The inkjet-printed capacitors show a relatively high capacitance per unit area up to $69\,pF\,mm^{-2}$ while achieving quality factor (Q) up to 100. Moreover, a technique was developed for an inkjet-printed rectifying Schottky diode. The last covered technology is the electroplating of the conductive seed-layers. Electroplating is a well-explored technology and a very crucial process in the field of micro-fabrication. However, it is highly dependent on the operator's level of experience. In addition, precision control of the electroplating power is required, particularly when creating small structures, where pulse electroplating has proven to provide a high degree of control over the deposited structure. In this context, a highly versatile current source was developed based on a microcontroller unit to bring accuracy into the generation of optimal plating recipes. The current source was built based on a Modified Howland Current Source (MHCS) configuration using a high-power operational amplifier. As a result, the current source was validated and verified, and its high capability was demonstrated by conducting some unique applications, most important of which is enhancing the adhesion of the inkjet-printed seed-layer on flexible substrates.

The second part of the dissertation addresses interventional MRI using MR-Catheter. MR-Catheters potentially have a significant impact on the field of minimally invasive medical operations. Implanted elongated transmission conductors and detector coils act as an antenna, that couple to the MR radio frequency (RF) transmit field, thereby making the catheter visible during use in an MRI scanner. However, this coupling potentially heats the conductors, causing possible tissue damage, and has prevented this technology from finding widespread use. An alternative approach is to couple a resonator on the catheter tip inductively coupling to a wired surface coil outside of the body. However, The micro-resonator on the catheter's tip could heat during the excitation phase. Moreover, as the catheter axial orientation changes during motion, the visibility of the catheter tip changes and can be lost if the wireless resonator and external coil's magnetic fields are orthogonal. In this contribution, the tuning capacitance of the catheter's micro detector is controlled wirelessly via pulse sequence control sent to an RF tuning circuit integrated

with a detector coil. The integrated circuit generates direct current (DC) from the transmitted RF for controlling capacitance remotely, creating an intelligent embedded tunable detector on the catheter tip. During RF transmission, decoupling is done by adjusting the micro-detector operating frequency away from the Larmor frequency. Additionally, a novel detector design is introduced based on two perpendicularly oriented micro-saddle coils that maintain constant visibility of the catheter for the entire range of axial orientations with no dead angle. The system was experimentally verified in a 1 T MR scanner.

The third part of the dissertation addresses NMR spectroscopy throughput. Flow-based NMR is a promising technique for improving NMR throughput. However, a common challenge is the relatively large dead volume in the flow tube feeding the NMR detector. In this contribution, a novel approach is introduced for fully automated high throughput NMR spectroscopy with enhanced mass sensitivity. The developed approach is accomplished by taking advantage of microfluidic technologies combined with thin-film micro-NMR detectors. A customized NMR probe head is developed with a microfluidic system featuring: i) a micro-saddle detector for NMR spectroscopy and ii) a pair of flow sensors flanking the NMR detector and interfaced to a microcontroller unit. A microfluidic tube is used to transport a sample series through the probe head, comprising an unlimited number of different sample plugs separated by an immiscible fluid. The developed system tracks the samples' position and velocity in this dual-phase flow and synchronizes the NMR acquisition. The developed custom build probe head is plug-and-play ready with market-available NMR systems. The system was successfully utilized for automating flow-based NMR measurement in a 500 MHz NMR system. The developed micro-NMR detector enables high-resolution spectroscopy with NMR sensitivity of 2.18 nmol s$^{1/2}$ with the flow sensors in operation. The flow sensors featured high sensitivity to an absolute difference of 0.2 in relative permittivity, enabling differentiation between most common solvents. It was illustrated that a fully automated NMR spectroscopy of nine different 120 µL samples could be achieved within 3.6 min or effectively 15.3 s per sample.

Zusammenfassung

Das zentrale Thema dieser Arbeit ist die Entwicklung und Integration von flexibler Elektronik für Mikro-Magnetresonanz (MR)-Anwendungen. Zwei wichtige Anwendungen wurden in der Dissertation behandelt; eine Anwendung auf dem Gebiet der Magnetresonanztomographie (MRI) und die andere auf dem Gebiet der Kernspinresonanz (NMR). Die MRI-Anwendung konzentriert sich auf die Lösung der Sicherheits- und Zuverlässigkeitsaspekte von MR-Kathetern. Die NMR-Anwendung stellt einen neuartigen Ansatz zur Steigerung des Durchsatzes bei der NMR-Spektroskopie vor.

Der erste Teil der Dissertation behandelt die verschiedenen Technologien die zur Herstellung flexibler Elektronik auf der Mikroskala entwickelt wurden. Die behandelten MR-Anwendungen erfordern die Herstellung von Induktoren, Kondensatoren und Dioden auf flexiblen Substraten. Die erste Technologie, die im Rahmen der Mikrofabrikation behandelt wird, ist das Aufbringen einer leitfähigen Startschicht auf flexiblen Substraten. Es wurden verschiedene Techniken getestet und verglichen. Die entwickelte Technologie ermöglicht die Herstellung einer mehrschichtigen leitfähigen Struktur auf einem flexiblen Substrat ($50\,\mu m$ Dicke), die sich zum Umwickeln eines schlanken Rohres ($> 0.5\,mm$ Durchmesser) eignet. Die zweite Methode ist der Tintenstrahldruck von Kondensatoren mit hoher Dichte und niedrigem Verlustkoeffizienten. Zwei dielektrische Tinten auf Polymerbasis wurden synthetisiert, durch die Dispersion von TiO_2 und $BaTiO_3$ in Benzocyclobuten (BCB) Polymer. Die im Tintenstrahldruckverfahren hergestellten Kondensatoren zeigen eine relativ hohe Kapazität pro Flächeneinheit von bis zu $69\,pF\,mm^{-2}$ und erreichen dabei einen Qualitätsfaktor (Q) von etwa 100. Außerdem wurde eine Technik für eine tintenstrahlgedruckte gleichrichtende Schottky-Diode entwickelt. Die letzte behandelte Technologie ist die Galvanisierung der leitenden Startschichten. Die Galvanik ist eine gut erforschte Technologie und ein sehr wichtiger Prozess auf dem Gebiet der Mikrofabrikation. Sie ist jedoch in hohem Maße von der Erfahrung des Bedieners abhängig. Darüber hinaus ist eine präzise Steuerung der Galvanikleistung erforderlich, insbesondere bei der Herstellung kleiner Strukturen, wobei sich die Pulsgalvanik als ein Verfahren erwiesen hat, das ein hohes Maß an Kontrolle über die abgeschiedene Struktur bietet. In diesem Zusammenhang wurde eine hochflexible Stromquelle auf Basis einer Mikrocontroller-Einheit entwickelt, um Genauigkeit in die Erstellung optimaler Galvanikrezepte zu bringen. Die Stromquelle wurde auf Basis einer modifizierten Howland-Stromquelle (MHCS) unter Verwendung eines Hochleistungs-Operationsverstärkers (OPAMP) aufgebaut. Die Stromquelle wurde validiert und verifiziert, und ihre hohe Leistungsfähigkeit wurde durch die Durchführung einiger schwieriger Anwendungen demonstriert, von denen die wichtigste die Verbesserung der Haftung der im Tintenstrahldruckverfahren gedruckten Startschicht auf flexiblen Substraten ist.

Der zweite Teil der Dissertation befasst sich mit interventioneller MRT mittels MR-Katheter. MR-Katheter haben potenziell einen erheblichen Einfluss auf den Bereich der minimalinvasiven medizinischen Eingriffe. Implantierte längliche Übertragungsleiter und Detektorspulen wirken wie eine Antenne und koppeln sich an das MR-Hochfrequenz (HF)-Sendefeld an und machen so den Katheter während des Einsatzes in einem MRT-Scanner sichtbar. Durch diese Kopplung können sich die Leiter jedoch erhitzen, was zu einer gefährlichen Erwärmung des Gewebes führt und eine breite Anwendung dieser Technologie bisher verhindert hat. Ein alternativer Ansatz besteht darin, einen Resonator an der Katheterspitze induk-

tive mit einer Oberflächenspule außerhalb des Körpers zu koppeln. Allerdings könnte sich auch dieser Mikroresonator an der Katheterspitze während der Anregungsphase erwärmen. Außerdem ändert sich die Sichtbarkeit der Katheterspitze, wenn sich die axiale Ausrichtung des Katheters während der Bewegung ändert, und kann verloren gehen, wenn die Magnetfelder des drahtlosen Resonators und der externen Spule orthogonal sind. In diesem Beitrag wird die Abstimmkapazität des Mikrodetektors des Katheters drahtlos über eine Impulsfolgensteuerung gesteuert, die an einen HF-Abstimmkreis gesendet wird, der in eine Detektorspule integriert ist. Der integrierte Schaltkreis erzeugt Gleichstrom aus dem übertragenen HF Signal zur Steuerung der Kapazität aus der Ferne, wodurch ein intelligenter eingebetteter abstimmbarer Detektor an der Katheterspitze entsteht. Während der HF-Übertragung erfolgt die Entkopplung durch eine Feinabstimmung der Detektorbetriebsfrequenz weg von der Larmor-Frequenz. Zusätzlich wird ein neuartiges Detektordesign eingeführt, das auf zwei senkrecht ausgerichteten Mikro-Saddle-Spulen basiert, die eine konstante Sichtbarkeit des Katheters für den gesamten Bereich der axialen Ausrichtungen ohne toten Winkel gewährleisten. Das System wurde experimentell in einem 1 T MRT-Scanner verifiziert.

Der dritte Teil der Dissertation befasst sich mit dem Durchsatz von NMR-Spektroskopie. Flussbasierte NMR ist eine vielversprechende Technik zur Verbesserung des NMR-Durchsatzes. Eine häufige Herausforderung ist jedoch das relativ große Totvolumen im Schlauch, der den NMR-Detektor speist. In diesem Beitrag wird ein neuartiger Ansatz für vollautomatische NMR-Spektroskopie mit hohem Durchsatz und verbesserter Massensensitivität vorgestellt. Der entwickelte Ansatz wird durch die Nutzung von Mikrofluidik-Technologien in Kombination mit Dünnfilm-Mikro-NMR-Detektoren verwirklicht. Es wurde ein passender NMR-Sensor mit einem mikrofluidischen System entwickelt, das Folgendes umfasst: i) einen Mikro-Sattel-Detektor für die NMR-Spektroskopie und ii) ein Paar Durchflusssensoren, die den NMR-Detektor flankieren und an eine Mikrocontrollereinheit angeschlossen sind. Ein mikrofluidischer Schlauch wird verwendet, um eine Probenserie durch den Sondenkopf zu transportieren, die einzelnen Probenbereiche sind durch eine nicht mischbare Flüssigkeit getrennt, das System erlaubt im Prinzip eine unbegrenzte Anzahl an Proben. Das entwickelte System verfolgt die Position und Geschwindigkeit der Proben in diesem zweiphasigen Fluss und synchronisiert die NMR-Akquisition. Der entwickelte kundenspezifische Sondenkopf ist Plug-and-Play-fähig mit marktüblichen NMR-Systemen. Das System wurde erfolgreich zur Automatisierung von flussbasierten NMR-Messungen in einem 500 MHz NMR-System eingesetzt. Der entwickelte Mikro-NMR-Detektor ermöglicht hochauflösende Spektroskopie mit einer NMR-Empfindlichkeit von 2.18 nmol s$^{1/2}$ bei Betrieb der Durchflusssensoren. Die Durchflusssensoren wiesen eine hohe Empfindlichkeit bis zu einem absoluten Unterschied von 0.2 in der relativen Permittivität auf, was eine Differenzierung zwischen den meisten gängigen Lösungsmitteln ermöglichte. Es wurde gezeigt, dass eine vollautomatische NMR-Spektroskopie von neun verschiedenen 120 μL Proben innerhalb von 3.6 min oder effektiv 15.3 s pro Probe erreicht werden konnte.

Nomenclature

Abbreviations

Abbreviation	Meaning
2D	Two dimensional
3D	Three dimensional
AC	Alternating current
ADC	Analog-to-digital converter
BBB	BeagleBone Black
BCB	Benzocyclobutene
BST	Barium strontium titanate
CDC	Capacitance-to-digital converter
CMOS	Complementary metal–oxide–semiconductor
CMRR	Common mode rejection ratio
CT	Computed tomography
CVD	Chemical vapor deposition
DAC	Digital-to-analog converter
DC	Direct current
DI	Deionized
EDL	Electric double layer
EF	Fermi level
FE	Phase encoding
FFT	Fast Fourier transform
FID	Free induction decay
FoV	Field of view
FWHM	Full width at half-maximum
GBWP	Gain-bandwidth product
GUI	Graphical user interface
I^2C	Inter-integrated circuit
IC	Integrated circuit
IDC	Interdigitated capacitive sensor
iMRI	Interventional magnetic resonance imaging
IPA	Isopropyl alcohol (isopropanol)
LOD	Limit of detection
LTC	Low temperature cure
MCU	Microcontroller unit
MEMS	Microelectromechanical systems
MHCS	Modified Howland current source
MI	Magneto-inductive

Abbreviation	Meaning
MIM	Metal-insulator-metal
MR	Magnetic resonance
MRI	Magnetic resonance imaging
MRS	Magnetic resonance spectroscopy
MS	Metal-semiconductor
nLOD	normalised limit of detection
NMR	Nuclear magnetic resonance
NP	Nanoparticles
Opamp	Operational amplifier
PCB	Printed circuit board
PE	Phase encoding
PFG	Pulsed field gradient
pH	potential of hydrogen
PI	Polyimide
PLA	Polylactic acid
PMMA	Poly(methyl methacrylate)
ppb	Part per billion
ppm	Part per million
PTAA	Poly(triaryl amine) semiconductor
PTFE	Polytetrafluoroethylene (Teflon)
PVD	Physical vapor deposition
PVP	Polyvinylpyrrolidone
RF	Radio frequency
RFID	Radio-frequency identification
SAR	Specific absorption rate
SEM	Scanning electron microscopy
SMD	Surface mount devices
SNR	Signal-to-noise ratio
SPI	Serial peripheral interface
SRF	Self resonant frequency
SS	Slice selection
TE	Echo time
TR	Repetition time
UV	Ultraviolet
VCCC	Voltage controlled current circuit
WF	Work function
WLI	White light interferometry
XRD	X-ray powder diffraction

Symbols

Symbol	Definition	Unit
B_0	Static magnetic field	T
B_1	RF magnetic field	T
M_0	Net magnetization	$\mathrm{A\,m^{-1}}$
γ	Gyromagnetic ratio	$\mathrm{rad\,s^{-1}\,T^{-1}}$
$\vec{\mu}$	Magnetic moment	$\mathrm{A\,m^2}$
$\vec{S}$	Spin angular momentum	$\mathrm{kg\,m^2\,s^{-1}\,rad^{-1}}$
ω_0	Larmor frequency	$\mathrm{rad\,s^{-1}}$
T_1	Spin-lattice relaxation time	s
T_2	Spin-spin relaxation time	s
α_{fa}	Flip angle	$^\circ$
τ	Pulse duration	s
δ	Skin depth	m
f	Frequency	Hz
f_0	Resonance frequency	Hz
μ	Permeability	$\mathrm{H\,m^{-1}}$
ρ	resistivity	Ω
T	Temperature	K
ε_r	Relative permittivity	$\mathrm{F\,m^{-1}}$
η	Viscosity	$\mathrm{Pa\,s}$
$\dot{\gamma}$	Shear rate	$\mathrm{s^{-1}}$
ϕ_B	Schottky barrier	eV
ϕ_M	Metal's working function	eV

Constants

Symbol	Value	Unit	Definition
h	6.626×10^{-34}	$\mathrm{J\,s}$	Max Planck's constant
$\hbar$	$h/2\pi$	$\mathrm{J\,s}$	Reduced Max Planck's constant
K_B	1.381×10^{-23}	$\mathrm{J\,K^{-1}}$	Boltzmann constant
ε_0	8.854×10^{-12}	$\mathrm{F\,m^{-1}}$	Vacuum permittivity
μ_0	$4\pi \times 10^{-7}$	$\mathrm{H\,m^{-1}}$	Vacuum permeability
R	8.314462618	$\mathrm{J\,mol^{-1}\,K^{-1}}$	Molar gas constant
F	96500	C	Faraday constant

Contents

Contents

1 Introduction

1.1 Motivation

Since the magnetic resonance (MR) concept was first introduced, it led to the development of two versatile technologies: magnetic resonance imaging (MRI) and magnetic resonance spectroscopy (MRS). MRI is a non-invasive medical imaging technique used extensively in hospitals and clinics to investigate and diagnose tumors, internal bleeding, and infections. What distinguishes MRI as an imaging technique is that it does not involve any harmful ionizing radiation. On the other hand, MRS is an information-rich spectroscopic technique widely used in chemistry and biology to characterize materials by determining and quantifying molecular structure. In addition, MRS offers broad chemical coverage and is a non-destructive technique, allowing further upstream analytics.

In its very primitive structure, besides the interface electronics, the MRI or MRS hardware consists of three main components: 1) a large permanent magnet responsible for the polarizing static magnetic field (B_0), 2) a radio frequency (RF) transmitter coil responsible for the excitation of the alternating magnetic field (B_1), and 3) an RF receiver to acquire the MR signals, which is commonly done using the RF transmitter coil itself. Employing micro-MR probes is a well-established approach to enhance the signal-to-noise ratio (SNR) of the MR experiment if only a small amount of sample is available. Integrating microfluidic technologies and micro-embedded systems with micro-MR detectors has continued to evolve since the first NMR-detector reports. These integrations lead to a wide range of novel applications such as biological sample monitoring [1–3], chemical reaction tracking [4–8], sensitivity enhancement techniques [9–12], and electrochemical functionality [13].

An example of the contribution of micro-MR detectors in the field of MRI is the development of MR-catheter for minimally invasive medical operations. Locating a micro-MR detector on a catheter's tip acts as an antenna and couples to the magnetic resonance RF transmit field, thereby making the catheter visible during use in an MR scanner. This approach provides surgeons with an accurate geometrical orientation of the catheter's tip relative to the patient's body. Catheter-based intervention is among the primary methods used in the treatment diagnosis of heart diseases. Over the past two decades, cardio-vascular diseases have been reported as the leading cause of death globally, with more than seventeen million deaths in 2017 surpassing all other medical causes combine [14]. However, during the excitation stage, the coupling between the catheter detector and the RF magnetic field can heat the conductors, causing hazardous tissue heating, which has kept this technology from being widely used. Furthermore, as the catheter's axial direction alters during interventions, the visibility of the catheter tip changes in the MR image and can be lost if the magnetic fields of the wireless resonator and external coil are orthogonal.

An example of the contribution of micro-MR detectors in the field of NMR is the development of flow-based NMR spectroscopy. Flow-based NMR is a promising technique for transporting the samples through the NMR detector in a microfluidic tube without the need for hardware disassembling and assembling. However, a common challenge is the relatively large dead volume in the flow tube feeding the NMR detector that results in the fact that NMR is a low throughput method. Therefore, there is

a disconnect between applications that require large parameter spaces screening and the opportunity to take advantage of this information-dense method. Addressing the NMR throughput challenge could lead to a significant push to diverse fields, including drug discovery screening, clinical analysis, chemical process monitoring, bio-fluid metabolomics, and food analysis. Consider the field of drug discovery as an example; NMR can resolve the binding of drugs to pathogens and can be utilized for screening compound libraries to investigate the molecular interactions with target proteins [15, 16]. Pharmaceutical companies have molecular libraries containing millions of compounds, which is ever-increasing as new molecules are being synthesized utilizing combinatorial methods. For example, Pfizer, Inc. maintains 4 million compounds inside their molecular library that can be used for analyzing potential medicines, as reported in 2017 [17]. Hence, the development of high throughput NMR methods is a must to enhance the screening efficiency of these massive and ever-increasing molecular libraries.

1.2 Objective

To tackle the challenges facing the MR-catheters and NMR spectroscopy throughput, the present work aims to address three main hypotheses:

- **Interventional MRI using MR-catheters**

  Integrating micro-MR detector with micro-embedded systems to wirelessly decouple the micro-resonator on the catheter's tip to circumvent the heating hazard. The developed system needs to be controlled wirelessly to avoid using conductive wires inside the patient, as they are the main cause of dangerous heating. The developed embedded system should have an antenna to pick up the transmitted RF control signal operating at a frequency range away from the Larmor frequency and rectify it to control the NMR detector's variable capacitance of. The whole system should have a thickness below 80 μm with a high degree of flexibility to be rolled around the slender catheter tube (5 fr). Moreover, the detector has to be designed in a way to keep coupling with the surface coil through the whole axial orientations to avoid losing the catheter's visibility at any orientation.

- **Automated high throughput NMR spectroscopy**

  Integrating micro-NMR detector with microfluidic technologies to build a customized probe head capable of online synchronization of NMR acquisition for two-phase follow. The dead volume in the flow tube is eliminated by loading the tube with plugs of different samples separated by immiscible fluid. The customized probe head should possess a sensing system for real-time monitoring of the position and velocity of the fluid interface. The sensing system should be sensitive to different NMR samples and integrates a low-cost embedded controller to synchronize the NMR acquisition. In addition, the system should be compatible with market-available NMR systems.

- **Micro-fabrication of flexible electronics**

  To achieve the previously mentioned objectives, the fabrication of thin, flexible electronics needs to be addressed by focusing on: 1) enhancing the thin-film fabrication technology for depositing conductive layers onto flexible substrates, 2) developing thin-film flexible capacitors with high capacitance density to reduce their volume to be integrated on the catheter tip, and 3) developing an electroplating method for enhancing the adhesion of the conductive structure on the flexible substrates.

1.3 Thesis outline

This thesis consists of ten chapters structured in three main parts, accompanied by two introductory chapters and the conclusion. The thesis is organized as follow:

- **Introductory chapters**

  1. Chapter 1 provides a quick introduction with the motivation of the topic and the objectives.

  2. Chapter 2 presents an overview of the theoretical MR concepts referred to by the rest of the thesis. In the beginning, the fundamentals of MR with explaining the origin of the signal are explained. Then the NMR spectroscopy and MRI scanner hardware and concept of operation are briefly discussed.

- **Part I** covers the developed technologies for fabricating flexible electronics on the micro-scale.

  3. Chapter 3 presents the different developed processes for depositing conductive seed layers onto flexible substrates and provides a comparison between these processes. It introduces the developed micro-fabrication process for fabricating thin-film capacitors and diodes.

  4. Chapter 4 presents the development of a flexible, versatile current source for electroplating. It covers the different novel plating applications conducted using the developed plating system.

- **Part II** addresses the MRI application; interventional MRI using MR-Catheter.

  5. Chapter 5 is an overview of state-of-the-art MR-catheters focusing on the different developed techniques for solving the heating issue.

  6. Chapter 6 presents a thorough description of the design and development of the introduced micro embedded system for the interventional MRI application.

- **Part III** addresses the NMR application; automated high throughput NMR spectroscopy.

  7. Chapter 7 is an overview of state-of-the-art high throughput NMR spectroscopy. The chapter also presents a brief overview of the state-of-the-art micro-NMR detectors and flow sensors since they are employed for building the introduced high throughput NMR approach.

  8. Chapter 8 presents a thorough description of the design, characterization, and fabrication of the fully automated high throughput NMR system.

  9. Chapter 9 presents various NMR flow experiments demonstrating the the versatility of the developed technology for realizing automated high throughput NMR spectroscopy with high mass sensitivity.

- **Conclusion and outlook chapter**

  10. Chapter 10 concludes the entire thesis and gives an outlook for future work.

1.4   Main results

The research conducted during the PhD work has led to four main publications with contribution as the first author (three published and one in preparation) and three other publications with contribution as coauthor (two published and one in preparation).

<u>**Micro-fabrication of flexible electronics**</u>

1. **Load sensitive stable current source for complex precision pulsed electroplating**

   Published in: Review of Scientific Instruments [ON1]

   Authorship status: Lead author

   Content: This paper presents a highly flexible current source based on a microcontroller unit used for the electroplating process. The functionality and stability of the developed system under different plating parameters were described. The developed system was used for conducting two nontrivial plating applications.

   Contribution: Involved in conceiving the idea. Designed, developed, and characterized the electroplating power source. Carried out the application of electroplating of inkjet-printed tracks. Lead in writing the manuscript and preparation of figures.

2. **Polyaramid-Based Flexible Antibacterial Coatings Fabricated Using Laser-Induced Carbonization and Copper Electroplating**

   Published in: ACS Applied Materials & Interfaces [ON2]

   Authorship status: Coauthor

   Content: This paper introduced a fabrication method for developing electrical circuits on flexible polyaramid substrates using laser-induced carbonization and copper electroplating.

   Contribution: Performed and optimized the electroplating processes.

<u>**Interventional MRI using MR-catheters**</u>

3. **Wireless Double Micro-Resonator for Orientation Free Tracking of MR-Catheter During Interventional MRI.**

   Published in:IEEE Journal of Electromagnetics, RF and Microwaves in Medicine and Biology [ON3]

   Authorship status: Lead author

   Content: This work proposed a novel micro-resonator based on two perpendicularly oriented saddle coils that create a homogeneous magnetic field when wrapped around a catheter tube.

   Contribution: Convinced the idea. Designed, optimized, and fabricated the introduced micro-resonator. Performed the MRI experiments. Lead in writing the manuscript and preparation of figures.

4. **Topologically optimized magnetic lens for magnetic resonance applications.**

   Published in: Magnetic Resonance [ON4]

   Authorship status: Coauthor

   Content: This work employed the topology optimization technique to develop optimal layouts of a Lenz lens to improve the SNR of MR detection.

   Contribution: Conducted the initial inductive coupling experiments.

5. **Wireless tuning system towards safe interventional magnetic resonance imaging.**

   Manuscript status: In preparation

   Authorship status: Lead author

   Content: This work introduces a novel wireless tuning system to decouple MR-catheter in an iMRI operation during RF excitation to avoid the heating hazard.

   Contribution: Convinced the idea. Designed, fabricated, and characterized the wireless tuning system. Lead in writing the manuscript and preparation of figures.

Automated high throughput NMR spectroscopy

6. **Integrated impedance sensing of liquid sample plug flow enables automated high throughput NMR spectroscopy.**

   Published in: Nature - Microsystems & Nanoengineering [ON5]

   Authorship status: Lead author

   Content: The paper introduced a novel customized NMR probe head that is plug-and-play ready with market-available NMR systems for enhancing NMR spectroscopy throughput. The paper demonstrates the capability and the applications of the introduced technology.

   Contribution: Involved in conceiving the idea. Designed, fabricated, and optimized the experimental setup. Conducted the system characterization, performed the NMR experiments, and conducted data analysis. Lead in writing the manuscript and preparation of figures.

7. **Highly fluorinated peptide probes with enhanced in vivo stability for ^{19}F-MRI.**

   Manuscript status: In preparation

   Authorship status: Coauthor

   Content: This work aimed to develop peptide-based 19F labels suited for 19F MRI at micron to milli-scale. The Highly fluorinated peptides bearing up to 27 fluorine nuclei possess high biocompatibility and in vivo stability, achieving in situ labeling on BSA and glutathione.

   Contribution: Developed the micro-MR saddle detector used for the MRI experiments, and participated in conducting the MRI experiments.

2 Theoretical background

Nuclear Magnetic Resonance (NMR) has a very wide range of applications in chemistry, biology, and medicine. Isidor Isaac Rabi first introduced NMR in 1938 [18] where he was awarded the Nobel Prize in physics in 1944 for his techniques of using nuclear magnetic resonance to determine the nuclear spin and magnetic moment of atoms. Later in 1952, Felix Bloch [19] and Mills Purcell [20] shared the Nobel Prize in physics for expanding the NMR technique to include solids and liquids, leading to a new branch of science. The further research and development of NMR were highlighted with three additional Nobel Prizes; in 1991 in chemistry by Richard R. Ernst for the development of Fourier transform NMR spectroscopy, in 2002 in chemistry by Kurt Wüthrich for studying biological molecules using NMR, and in 2003 in physiology or medicine by Mansfield and Lauterbur for developing magnetic resonance imaging (MRI). Paul Christian Lauterbur first introduced MRI in 1973 [21].

In this chapter, the fundamental concepts of NMR and MRI, which are most relevant to this thesis, are introduced. The chapter is divided mainly into four sections. In Section 2.1, the fundamental concepts and terminologies of the NMR, such as nuclear spins, polarization, excitation, and relaxation, are introduced. Section 2.2 presents the basics of acquiring an NMR spectrum by explaining the concept of chemical shift and spins coupling. Section 2.3 discusses the primary technique for collecting an MR image and the field encoding. lastly, Section 2.4 introduces the MR system's main hardware components by highlighting the different elements between an NMR spectrometer and an MRI scanner. Within the last subsection, some of the essential parameters for evaluating the NMR spectrum signal-to-noise ratio are discussed. The information presented in this introductory chapter were mostly collected from the following three textbooks:

- **Spin Dynamics** by Malcolm Levitt [22]

- **NMR Spectroscopy** by Harald Günther [23]

- **MRI from picture to proton** by Donald W. McRobbie [24]

2.1 Magnetic resonance fundamentals

Nowadays, the concept of Nuclear Magnetic Resonance (NMR) is widely used in various applications. These applications could be categorized mainly into NMR spectroscopy and magnetic resonance imaging (MRI). NMR spectroscopy is also known as magnetic resonance spectroscopy (MRS), and it is an analytical technique to study molecules and compounds by determining and quantifying their molecular structure. Therefore, it is extensively used in medicine, chemistry, and biology. On the other hand, hence MRI is an imaging technique; its mainly used for diagnosing diseases such as tumors or internal bleeding.

2.1.1   Spin angular momentum

Spin is the keyword of NMR. Every atomic nucleus consists of elementary particles called protons and neutrons, which are composite fermions particles. Fermions are particles that have half-odd integer spin and are described by the Pauli exclusion principle. Accordingly, spinning is an intrinsic property of the nuclei of the atoms. The particles' spinning originates a spin angular momentum vector $(\vec{S})$, which can be described in:

$$|S| = \hbar\sqrt{I(I+1)}, \tag{2.1}$$

Where $\hbar$ is the Planck constant $(6.62607015 \times 10^{-34}\,\mathrm{J\,s})$ divided by 2π and I is defined as the nuclear spin quantum number.

I plays a significant role in determining the possibility of detecting a material using the NMR technique. NMR detects signals only for a non-zero nuclear spin. If a nucleus has an even number of protons and neutrons, then the nucleus has no spin $(I = 0)$, and it is NMR silent. ^{32}S, ^{16}O, and ^{12}C are examples of NMR silent nuclei. On the other hand, if the number of either the proton or neutron or both is odd, then it has a non-zero nuclear spin $(I \neq 0)$ and detectable by NMR. Nuclei such as ^{1}H and ^{13}C are examples of nuclei with non-zero spin.

As a consequence of the spin of protons and neutrons (which have a positive charge), a magnetic moment vector $(\vec{\mu})$ is originated. The magnetic moment $(\vec{\mu})$ is proportional to spin angular momentum $(\vec{S})$ by the gyromagnetic ratio γ, which is a unique intrinsic property of each nucleus,

$$\vec{\mu} = \gamma\,\vec{S}. \tag{2.2}$$

The magnetic moment $(\vec{\mu})$ and the spin angular momentum $(\vec{S})$ are vector quantities, and based on their directions, the sign of the gyromagnetic ratio (γ) is defined. Thus if the two vectors have parallel alignment, then γ has a positive sign, while the negative sign describes anti-parallel alignment, as shown in Fig. 2.1. ^{13}C is an example of a positive gyromagnetic ratio $(\gamma > 0)$, while ^{15}N has a negative gyromagnetic ratio $(\gamma < 0)$.
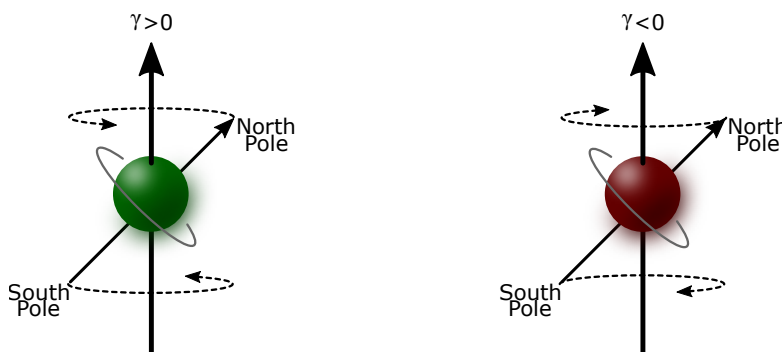

Figure 2.1: Determination of the gyromagnetic ratio's (γ) sign according to the alignment of the magnetic moment $(\vec{\mu})$ with respect to the magnetic moment $(\vec{S})$.

2.1.2   Spin polarization and Larmor precession

The spin quantum number describes the spin's possible orientation states, where $2I + 1$ can determine the number of the spin's possible orientations. The hydrogen atom (^{1}H) has one proton, which means that $I = \dfrac{1}{2}$. Therefore there are two possible orientations spin for the hydrogen proton. In the absence of an external energy source, such as a static magnetic field, both orientations have the same energy level. On the other hand, with the presence of a magnetic field, the two orientations have two quantized energy levels described by Zeeman splitting with magnetic the quantum number m ($m = \pm\dfrac{1}{2}$ for a proton), as shown in Fig.2.2a. The first possible orientation is the lower energy level, known as α spin state, and it's parallel to the magnetic field. The other orientation has higher energy, known as β spin state, and opposes the magnetic field. The total energy difference is (ΔE) proportional to the strength of the applied magnetic field ($\vec{B}_0$), as shown in Fig.2.2b based on:

$$\Delta E = -\vec{\mu} \cdot \vec{B}_0. \tag{2.3}$$

Conventionally the static magnetic field is in the z-direction ($B_Z = \left| \vec{B}_0 \right| = B_0$ and $B_X = B_Y = 0$) and the magnetic moment in the z-direction is $\mu_Z = \gamma m \hbar$. Hence, the total energy difference (ΔE) for proton is,

$$\Delta E = E_{m=-\frac{1}{2}} - E_{m=+\frac{1}{2}} = -(-\frac{1}{2})\hbar\gamma B_0 + (\frac{1}{2})\hbar\gamma B_0 = \hbar\gamma B_0. \tag{2.4}$$

With the absence of the external magnetic field ($B_0 = 0$) and the assumption that there is no spin to spin interaction, the magnetic moments have random orientations and degenerated energy levels. If, in contrast, a homogeneous static magnetic field $\vec{B}_0$ is applied, conventionally in z-direction, and due to the spin vectors' energetic preference for parallel alignment with respect to the external magnetic field, more spins prefer the parallel alignment than the anti-parallel states. Consequently, a bulk macroscopic magnetization $\vec{M}_0$ originates, due to nuclear magnetism, parallel to the external magnetic field and proportional to the quantity difference of the parallel and anti-parallel states, as shown in Fig 2.3. This process of generating the net magnetization ($\vec{M}_0$) of a sample is known as polarisation. The magnetic moment rotates
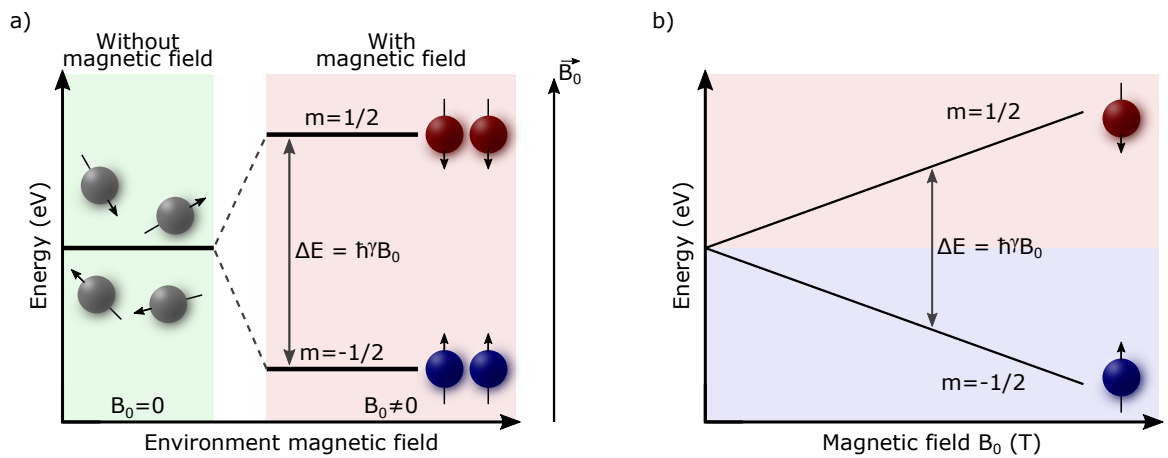

Figure 2.2: Zeeman splitting. **(a)** Zeeman splitting of ^{1}H nuclei with the application of an external magnetic field ($\vec{B}_0$). **(b)** The energy difference between the two quantized energy levels is proportional to the external magnetic field's strength (B_0).

a)

b)

α or +1/2
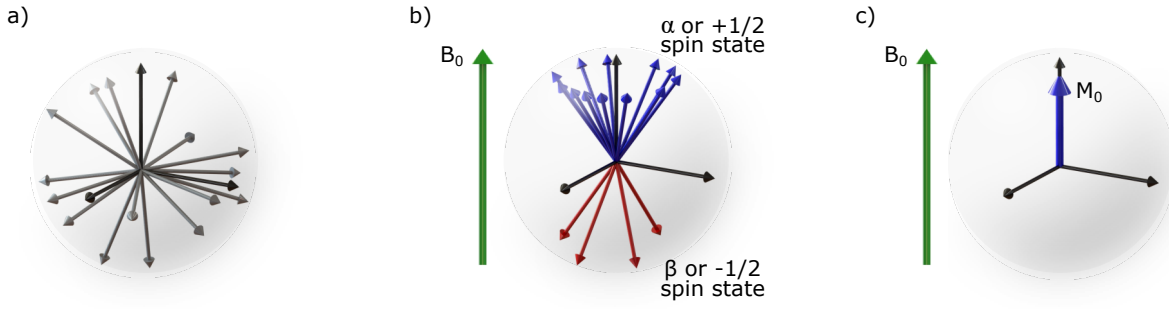spin state

B₀

β or -1/2
spin state

c)

B₀

M_0

Figure 2.3: Effect of applying an external magnetic field on spin orientations. **(a)** Random spin orientations with the absence of an external magnetic field. **(b)** Applying an external magnetic field ($\vec{B}_0$), align the spins parallel and anti-parallel to the applied field building the two energy levels α and β. **(c)** The majority of the spins align in parallel to the external magnetic field generating the net magnetization (M_0).

around the external magnetic field vector with a specific frequency called Larmor frequency (ω_0), and this rotation is known as precession, shown in Fig.2.4a. According to the Plank-Einstein relation, the proton's energy (E) is proportional to the frequency(ν) ($E = h\nu = h\dfrac{\omega}{2\pi} = \hbar\omega$), then Larmor frequency can be formulated using Equation 2.4,

$$\omega_0 = \frac{E}{\hbar} = \gamma B_0. \tag{2.5}$$

Equation 2.5 reveals the linear relation between the Larmor frequency and the applied static magnetic field (B_0), as shown in Fig. 2.4b. Hence, a homogeneous B_0 magnetic field is required to achieve a proper spectral distribution without losing the sensitivity and selectivity of the NMR. Additionally, the radio frequency (RF) circuits in the NMR should be correctly designed to operate at the Larmor frequency.

The spin's probability distribution of occupying one of the two available energy states is described by Boltzmann distribution (e^{-E/K_BT}). Hence, the ratio between the populations of the occupied high and low Zeeman states is,

$$\frac{N_{high}}{N_{lower}} = \frac{N_{-1/2}}{N_{+1/2}} = \frac{e^{\frac{-E_{-1/2}}{K_BT}}}{e^{\frac{-E_{+1/2}}{K_BT}}} = e^{\frac{-\Delta E}{K_BT}}, \tag{2.6}$$

Where K_B is the Boltzmann constant ($1.38 \times 10^{-23}\,\mathrm{J\,K^{-1}}$) and T is the temperature in K. Substituting in Equation 2.6 by Equation 2.4 with considering an approximation,

$$\frac{N_{high}}{N_{lower}} \approx 1 - \frac{\hbar\gamma B_0}{K_BT}. \tag{2.7}$$

The net magnetization can be be expressed in terms of total spin (N_0) using the population difference (ΔN),

$$\vec{M}_0 = \Delta N\gamma\vec{S} = \frac{B_0\vec{N_0}\gamma^2\hbar^2}{4K_BT}. \tag{2.8}$$
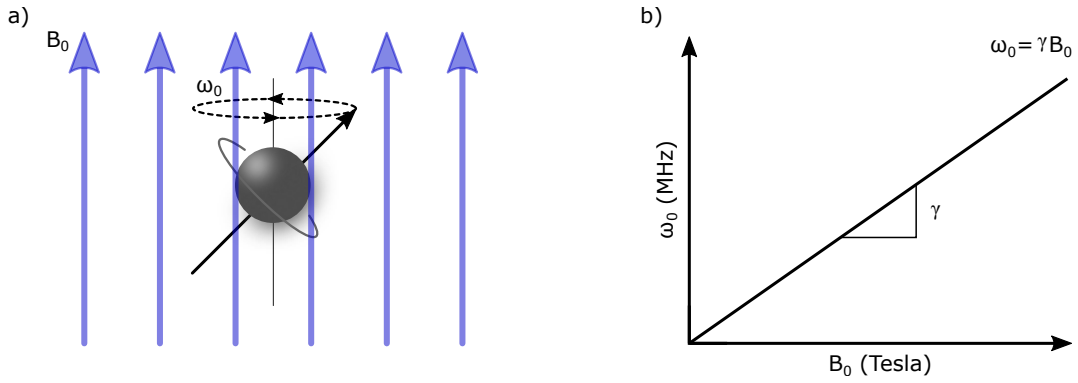
Figure 2.4: Spin precession and Larmor frequency. **(a)** The spin polarization axis's precession around the static magnetic field vector ($\vec{B}_0$) with the Larmor frequency (ω_0). **(b)** The linearity between the Larmor frequency and the applied static magnetic field.

2.1.3   Excitation and relaxation

To conduct an NMR measurement, first, the target sample is polarized by applying the external magnetic field (B_0) to establish the longitudinal net magnetization vector M_0 parallel to B_0 (conventionally in the z-direction). An excitation process is then done by applying a time-varying magnetic field pulse (B_1), subsequently evaluating the response of the nuclear magnetic moments (spins).

To realize the resonance condition, the time-varying excitation magnetic field (B_1) should operate at Larmor frequency (ω_0) using an RF inductor. The B_1 field should be superimposed perpendicular to the external B_0 field to forces the net magnetization vector to flip toward the transversal XY plane and produce a flip angle (α_{fa}) with respect to the Z-axis, as shown in Fig.2.5,

$$\alpha_{fa} = \gamma B_1 \tau. \tag{2.9}$$

Equation 2.9 reveals the direct proportionality of the flip angle to the B_1 field strength and the pulse duration (τ). Soft pulses, such as weak fields and long pulse durations, are mainly used to select narrow bandwidth frequencies. On the other hand, hard pulses, with a strong field and short pulse duration, excite a wide bandwidth. Therefore, the B_1 field's pulse duration is precisely controlled to achieve a flip angle of 90°.

Before applying the RF excitation pulse, the net magnetization vector entirely points in the direction of the polarizing static B_0 field, in this case, $M_Z = M_0$, and $M_X = M_Y = 0$. The excitation processes result in a tilted magnetization vector with three components M_X, M_Y, and M_Z. During the excitation process, the magnetization vector $\vec{M}$ rotates in the space around the Z-axis within the XY-plane, forming a spherical pattern due to the torque T ($\vec{T} = \dfrac{d\vec{s}}{dt}$) produced by the B_1 field, as shown in Fig. 2.5. Accordingly, the longitudinal magnetization component decreases, and the transversal component increases till the flip angle reaches 90°, at which $M_Z = 0$, $M_X = M_0 \cos(\omega_0 t)$, and $M_Y = M_0 \sin(\omega_0 t)$). Felix Bloch described the nuclear induction phenomenon as a mathematical analysis using Bloch equations:

$$\vec{M}(t) = \begin{bmatrix} M_X(t) \\ M_Y(t) \\ M_Z(t) \end{bmatrix} = \begin{bmatrix} M_0 \cos(\omega_0 t) \sin\alpha\, e^{-t/T_2} \\ M_0 \sin(\omega_0 t) \sin\alpha\, e^{-t/T_2} \\ M_0 \cos\alpha + (1 - e^{-t/T_1})(M_0 - M_0 \cos\alpha) \end{bmatrix}. \tag{2.10}$$
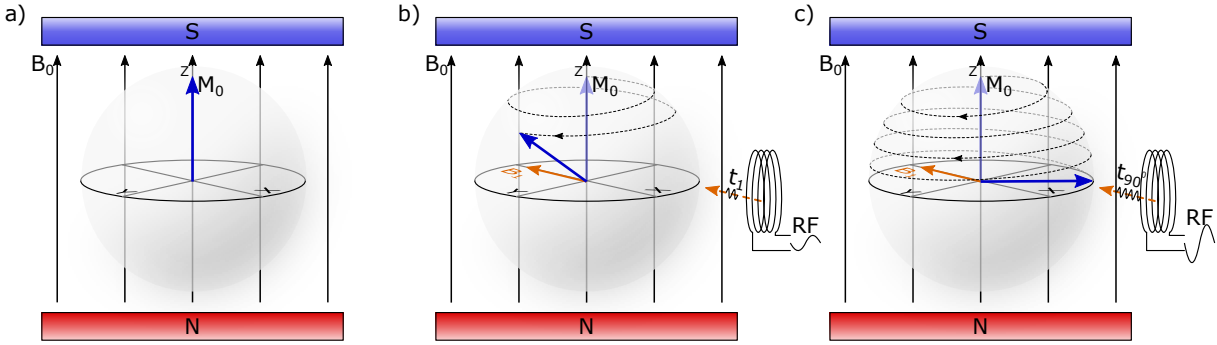
Figure 2.5: Impact of a time-varying excitation magnetic field (B_1) on the magnetization vector (M_0) of a polarized sample. **(a)** With the absence of the excitation field (B_1), The magnetization vector (M_0) points in the direction of the polarizing static (B_0) field ($M_Z = M_0$ and $M_X = M_Y = 0$). **(b)** Applying a soft pulse with a duration t_1 results in the magnetization vector's inclination with a flip angle of α_{fa1} ($\alpha_{fa1} < 90°$). **(c)** A 90° excitation RF pulse is applied, resulting in a total tilt of the magnetization vector to the XY plane ($M_Z = 0$, $M_X = M_0 \cos(\omega_0 t)$, and $M_Y = M_0 \sin(\omega_0 t)$).

Where T_1 and T_2 are relaxation time constants describing the net magnetization vector's motion within the relaxation stage to reestablish thermal equilibrium. The relaxation process occurs by terminating the RF excitation pulse resulting in an alternating electric field that could be detected using an RF coil; this signal is known as the NMR signal.

During the relaxation stage, the transverse magnetization M_T ($M_T = M_X + jM_Y$) decays exponentially ($M_T \propto e^{-t/T_2}$) following the T_2 relaxation time constant (spin to spin relaxation), which describes the dephasing of spins. This decay is called free induction decay (*FID*), resulting from the fluctuations of the frequency due to the inter-nuclear actions, such as the chemical interactions between the spins because of anisotropies. After starting the relaxation process by time T_2, the transversal net magnetization decays to 37% of its maximum value M_0.

Simultaneously, the longitudinal net magnetization M_Z increases exponentially ($M_Z \propto (1 - e^{-t/T_1})$) to restore its full longitudinal magnetization. T_1 relaxation is described as spin to lattice relaxation. The
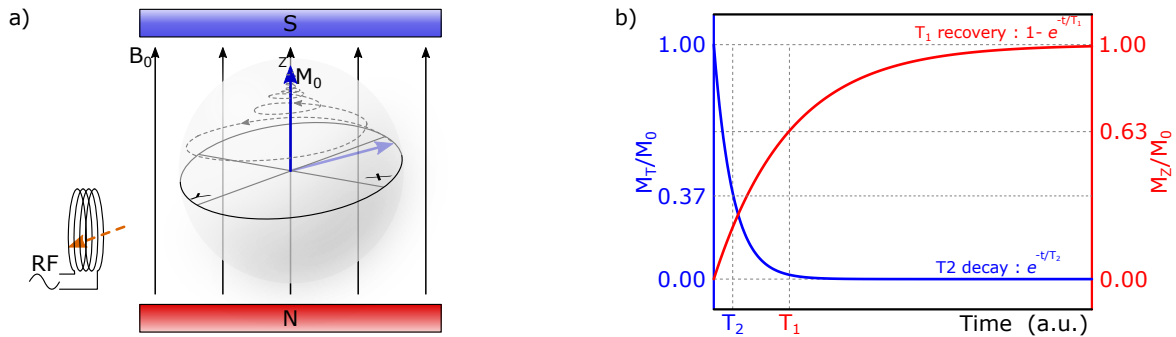

Figure 2.6: Magnetization vector's behavior during the relaxation stage after being excited with a 90 degree flip angle. **(a)** Re-alignment of the magnetization vector ($\vec{M_0}$) with the polarizing field ($\vec{B_0}$). The trajectory of M_0 follows an envelope shape function due to the ratio between the time constants T_1 and T_2. **(b)** Longitudinal recovery of M_Z and transverse decay of M_{XY} over time.

system emits the excess energy out to the environment as photons to reach equilibrium and achieve the preferred minimum energy situation. After starting the relaxation process by time T_1, the longitudinal net magnetization restores 63% of its maximum value M_0.

Typically, the transversal magnetization (M_T) vanishes before the longitudinal magnetization (M_Z) is fully restored as T_2 is shorter than T_1. Thus, a spiral pattern describes the magnetization vector's rotation during the relaxation stage, as shown in Fig. 2.6.

2.1.4 Free Induction Decay (FID)

As explained in the previous subsection, the total transversal magnetization (M_T) is a complex sum of the magnetizations in both coordinates, X and Y,

$$M_T = M_X + jM_Y = M_0 \cos{(\omega_0 t)} e^{-t/T_2} + jM_0 \sin{(\omega_0 t)} e^{-t/T_2} = M_0 e^{j\omega_0 t} e^{-t/T_2}. \qquad (2.11)$$

M_T decays exponentially by the decay constant T_2, so during relaxation, the magnetization vector rotates around the Z-axis, and simultaneously its amplitude shrinks, as shown in Fig. 2.7a. The real and imaginary parts of M_T decay are shown separately in Fig. 2.7b. The real and imaginary signals are sinusoidal with exponentially decaying amplitudes, and they have different phases. A Fourier transform is applied to represent the signals in the frequency domain instead of the time domain, as shown in Fig. 2.7c. The Fourier transform (FT) is a mathematical transformation by integrating the product of a sinusoidal signal and the MR time-domain signal,

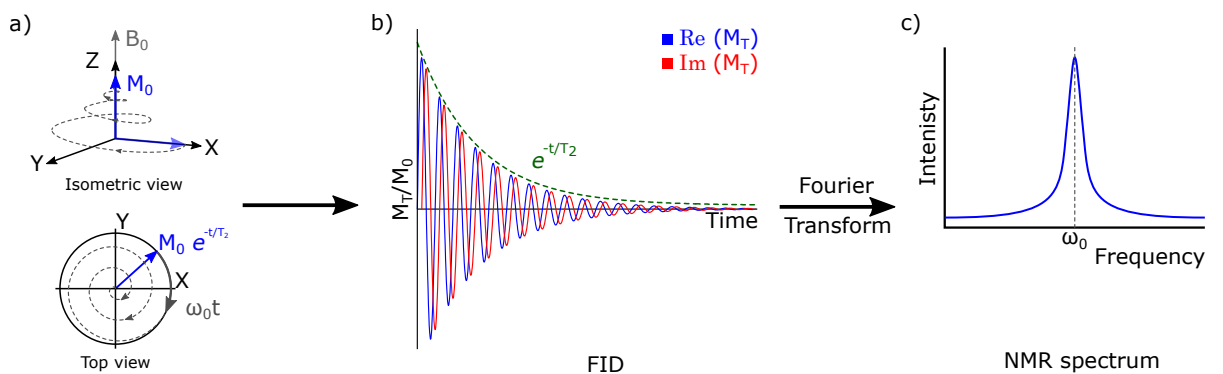$$M(\omega) = \int_{\infty}^{-\infty} M(t) \, e^{-j\omega t} \, dt. \qquad (2.12)$$

Figure 2.7: Generation of the NMR signal during the relaxation stage. **(a)** During relaxation, $\vec{M}_0$ rotates around $\vec{B}_0$ while precessing with the Larmor frequency to re-align with $\vec{B}_0$. **(b)** The precessing magnetic moment generated a magnetic field, which can be picked up using an RF coil. The generated signal in the time domain is an exponentially decaying sinusoidal with Larmor frequency. **(c)** Fourier transform is applied to transfer the signal from the time domain to the frequency domain to acquire the NMR spectrum.

By applying Fourier transform for the transversal magnetization vector (M_T):

$$M(\omega) = \int_0^\infty M_0 e^{j\omega_0 t} e^{-t/T_2} e^{-j\omega t} \, dt = \int_0^\infty M_0 e^{[j(\omega-\omega_0)-1/T_2]t} \, dt$$

$$= M_0 \frac{e[-j(\omega-\omega_0)-1/T_2]t}{-j(\omega-\omega_0)-1/T_2} \Big|_0^\infty$$

$$= \frac{M_0}{j(\omega-\omega_0)+1/T_2} \times \frac{-j(\omega-\omega_0)+1/T_2}{-j(\omega-\omega_0)+1/T_2}$$

$$\frac{M(\omega)}{M_0} = \frac{1/T_2}{(\omega-\omega_0)^2+1/T_2^2} - j\frac{(\omega-\omega_0)}{(\omega-\omega_0)^2+1/T_2^2}. \tag{2.13}$$

The line-shapes of the real and imaginary parts in Equation 2.13 are called absorption and dispersion mode Lorentzian line-shapes. At the Larmor frequency ($\omega = \omega_0$), the real part reaches it's maximum amplitude of T_2, while the imaginary part is eliminated, as shown in Fig.2.8a. To calculate the full width at half maximum ($FWHM$) of the absorption, the real part is equated to $T_2/2$:

$$Re\left(\frac{M(\omega)}{M_0}\right) = \frac{1/T_2}{(\omega_{1/2}-\omega_0)^2+1/T_2^2} = \frac{T_2}{2}$$

$$\therefore (\omega_{1/2}-\omega_0)^2 = \frac{1}{T_2^2} \quad \rightarrow \quad \omega_{1/2} = \omega_0 + \frac{1}{T_2} \; or \; \omega_0 - \frac{1}{T_2}$$

$$\therefore FWHM = \Delta\omega = \omega_0 + \frac{1}{T_2} - \left(\omega_0 - \frac{1}{T_2}\right)$$

$$= \frac{2}{T_2} \, \text{rad} \, \text{s}^{-1}. \tag{2.14}$$

Accordingly, the absorption's maximum amplitude and FWHM are directly dependent on the relaxation time constant T_2. Practically, due to the arbitrary initial phase shift (φ) between the real and imaginary parts of the M_T signal in the time domain, the frequency domain's line-shapes may neither be absorption nor dispersion, as shown in Fig.2.8. Consequently, after acquiring the NMR spectrum, a phase correction for the real part is required to phase the spectrum in absorption mode. This process is called phasing the NMR spectrum.

An RF coil with electrical resistance (R_l) and inductance (L) is placed close to the target sample to obtain the NMR signal. According to Faraday's law, based on the change in the net magnetization vector with time, an electromotive force (ε) is induced in the RF coil,

$$\varepsilon(t) = -\frac{d\phi_B}{dt} = -\frac{d(\vec{B} \cdot \vec{A})}{dt} = -L\frac{dI_l}{dt}. \tag{2.15}$$

Where ϕ_B is the magnetic flux, equal to the dot product of the magnetic flux density $\vec{B}$ and the perpendicular vector area $\vec{A}$. I_l is the induced current in the RF coil as a result of the change in the transversal magnetization $\vec{M}_T$ based on the external applied excitation magnetic field $\vec{B}_1$. Consequently, the induced electromotive force (ε) is the NMR signal with direct proportionality to $\vec{M}_T$. The evolution of this signal is described by the free induction decay (FID), as shown in Fig. 2.7.

2.2   Nuclear Magnetic Resonance (NMR) spectroscopy

Chemists massively utilize NMR spectroscopy to analyze compounds and determine their structure and molecular identity. NMR spectroscopy is based on two essential phenomena, chemical shift and J-
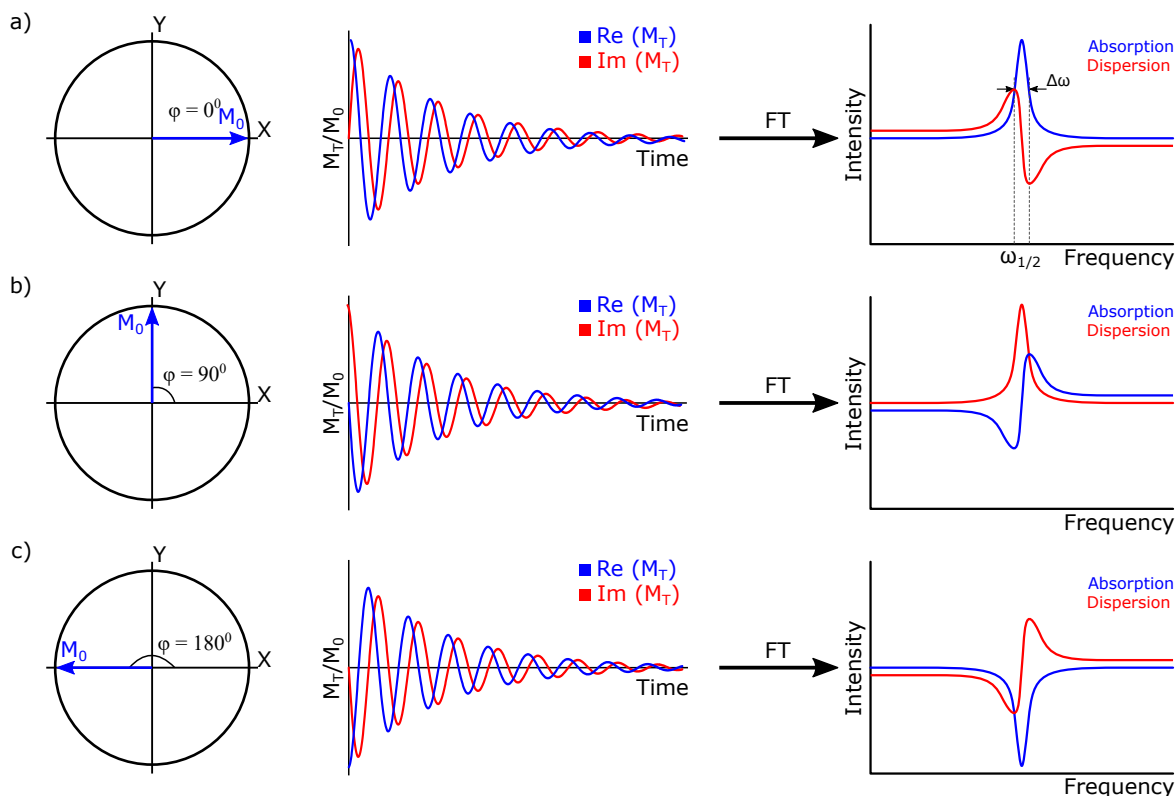
Figure 2.8: Effect of the arbitrary initial phase shift on the line-shape in the frequency domain. **(a)** The magnetization vector (M_0) has no initial phase shift ($\varphi = 0°$); hence the absorption line doesn't need phase correction in the frequency domain. **(b)** and **(c)** M_0 has an initial phase shift (φ) of 90° and 180°, resulting in an out of phase absorption peak in the frequency domain that requires phase correction.

coupling, to have the ability to differentiate the molecules. The fundamental steps of the NMR spectroscopy could be summarized in few steps, as shown in Fig. 2.9:

1. The target sample is located in a homogeneous static magnetic field $\vec{B}_0$ for polarization. The energy levels are distributed to a high level (β) and a low-level (α) spin states.

2. An external RF magnetic field $\vec{B}_1$ is applied under the resonance frequency for the excitation process. The protons perform a spin-flip after absorbing the required amount of energy to move from α to β spin states.

3. The RF B_1 field is switched off for the relaxation process. The protons release their extra energy to restore their preferred low energy spin state (α) resulting in a chemical shift (δ).

2.2.1 Chemical shift

Chemical shift is a fundamental phenomenon of the NMR. The atoms' bonds result in a slight change in the energy gap between α and β spin states. Consequently, a slight shift in the range of a few Hz could be observed on the precession frequency. However, NMR mainly focuses on the nucleus, where the
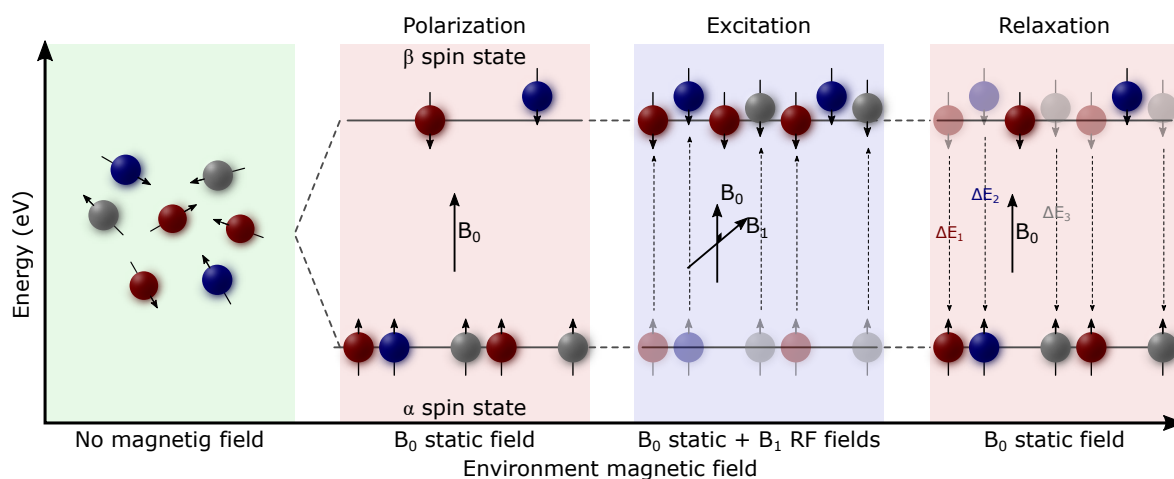
Figure 2.9: Basic procedures of NMR spectroscopy. Place the target sample in a static magnetic field (B_0) for polarization, then apply an alternating RF magnetic field (B_1) at Larmor frequency for excitation and finally switch off the B_1 field for relaxation and picking up the nuclear magnetic field.

atom's bonds and the electrons distribution affect the output signal. As described previously, the protons' dynamics are based on the absorbed energy after being exposed to the external magnetic field. The electron distribution around the nucleus plays a significant role as it could shield the external magnetic field from reaching the nucleus, as shown in Fig. 2.10. In the case of high electron density (strong shield), the external static field has a lower effect on the nucleus, and the NMR spectrum appears at a lower frequency (upfield) and vice versa. The primary source changing the electrons distribution in an atom is the bonds with its neighboring atoms.

Figure 2.11 shows the typical NMR spectra of methyl chloride (CH_3Cl) and methyl fluoride (CH_3F) as an example of the electron shield's effect on the NMR spectrum. For methyl chloride, the carbon atom has a polar bond with the chlorine atom, which contains 17 electrons around its nucleus. On the other hand, for methyl fluoride, the carbon atom has a polar bond with the fluorine atom, which contains only 9 electrons. Due to the higher electron density in the chlorine atom, the electron shield in methyl chloride
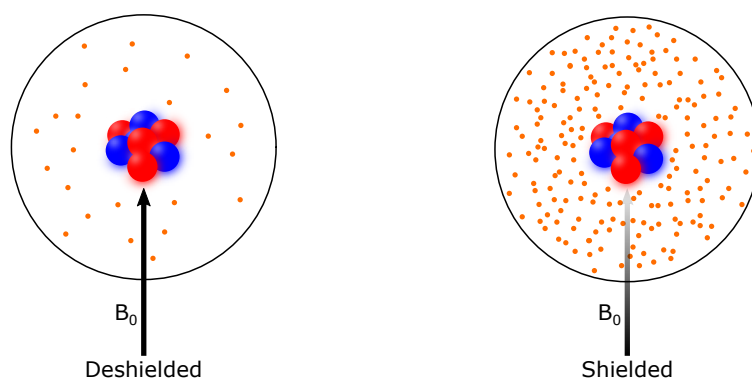

Figure 2.10: The electrons shield the nucleus from the external magnetic field. The nucleus on the left experience a stronger magnetic field compared to the nucleus on the right due to the lower electron density.
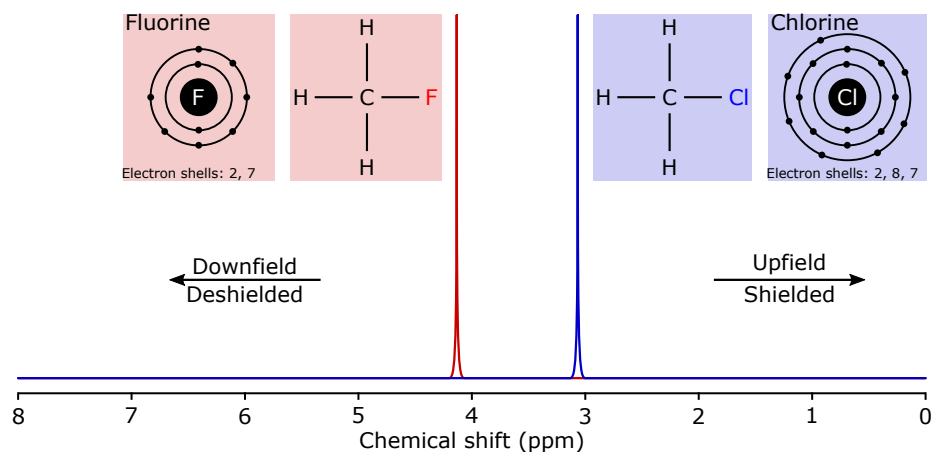
Figure 2.11: NMR spectra of methyl chloride (blue) and methyl fluoride (red). The different chemical shifts (δ) are due to the different electron densities around the chlorine and fluorine nuclei, which shield the external magnetic field differently.

is higher than that in methyl fluoride. Therefore, the methyl fluoride's chemical shift (towards downfield) is higher than that for methyl chloride (towards upfield).

$$\delta(\text{ppm}) = \frac{\Delta\nu(\text{Hz})}{\nu_0(\text{MHz})} \times 10^6 = \frac{(\nu(\text{Hz}) - \nu_r ef(\text{Hz}))}{\nu_0(\text{MHz})} \times 10^6, \tag{2.16}$$

where ν is the measured frequency, and $\nu_r ef$ is a known frequency for a used reference sample for calibrating the output signals such as 3-(trimethylsilyl)- propionic-2,2,3,3-d4 acid (TSP). The chemical shift is calculated relative to the NMR operating frequency to maintain the same chemical shift for each compound independent of the NMR operating frequency, leading to an independent field measure.

2.2.2 Spin-Spin coupling (*J*-coupling)

The NMR spectra consists of singlets peaks with chemical shifts in between corresponding to the different protons. On the other hand, within a particular molecule, the spin-spin coupling affects the resulting spectrum. There are mainly two different spin-spin coupling mechanisms: the direct dipole-dipole coupling and the indirect dipole–dipole coupling. The rapid tumbling of the molecule suppresses the direct dipole-dipole coupling.

The indirect dipole-dipole coupling, also known as *J*-coupling, is the coupling of the nuclear spins through the assistance of the electrons resulting in the observed multiplet structures. The magnetic field generated by a spinning proton magnetizes the electrons, affecting other neighboring protons; therefore, it's known as indirect coupling. Figure 2.12 shows different conditions for the *J*-coupling. For example, in a molecule containing one ^{1}H and one ^{13}C, ^{1}H can adopt one of the two possible alignments (aligned with or opposed to B_0). Consequently, the NMR spectrum of ^{13}C in *CH* group is split into two peaks of equal intensity due to the proton's effect. In case ^{13}C is coupled to two ^{1}H in a CH_2 group, then the peak is split twice, one for each bond. Each of two hydrogen protons has two possible alignments with the B_0 field resulting in four possible alignments combinations. The combinations result in three magnetic
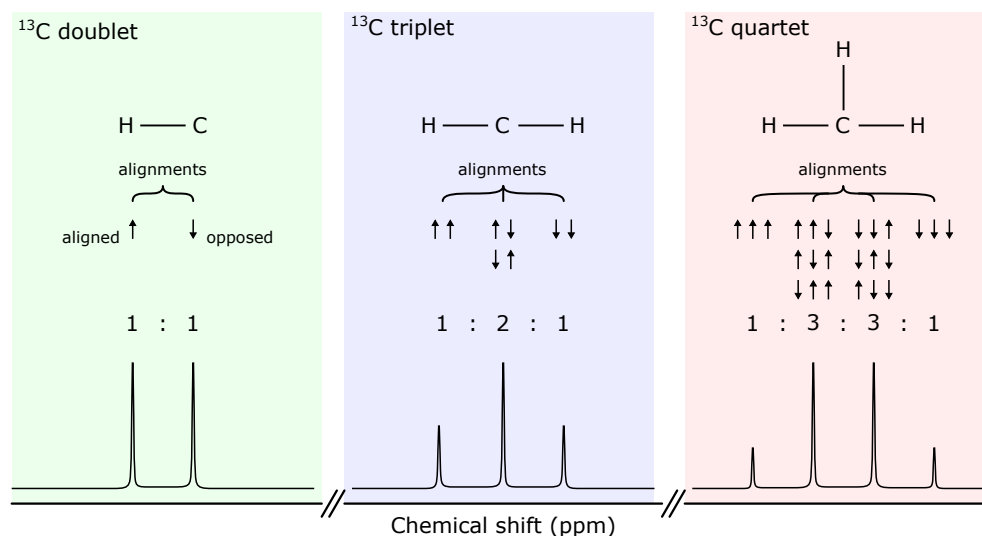
Figure 2.12: Resulted multiplet structure due to the indirect dipole-dipole coupling (*J*-coupling). A ^{13}C doublet, triplet, quartet resulted from coupling to one, two, or three ^{1}H protons, respectively.

effects. Due to the ratio between the alignments combinations, the peaks' intensities have a ratio of $1:2:1$. In case ^{13}C is coupled to three ^{1}H in a CH_3 group, the peak is split into a quartet pattern with an intensity ratio of $1:3:3:1$. The frequency separation between the peaks resulted from the J-coupling is specified in Hz. For example, the *J*-coupling frequency separation between the ^{1}H and ^{13}C spins in the ethanol's CH_3 group is 124.9 Hz.

2.3 Magnetic Resonance Imaging (MRI)

Magnetic Resonance Imaging (MRI) is another unique application based on the MR principle. MRI is a medical imaging technique that is used to create images of the internal organs without interventions. MRI is widely used to diagnose tumors, internal bleeding, developmental anomalies, and other internal disorders. Another medical technique for internal imaging organs is computerized tomography (CT) which is based on sending X-rays through the body and analyzing the receptor waves, then the physical location is reconstructed numerically. CT suffers from involving harmful radiation and, in most cases, it demands contrast agents.

In contrast to CT, MRI doesn't include radiation exposure. The location in 3D space is reconstructed by using magnetic fields to manipulate the atoms' magnetic properties based on particular frequency and phase. The pure MR output signal shows the net magnetization and doesn't provide information about the spatial distribution. Hence, the keyword for MRI is the spatial encoding by using gradient coils to encode the MR FID signal, as shown in Fig. 2.13.

2.3.1 MRI spatial encoding

The three linear gradient magnetic field coils shown in Fig. 2.13b are used for encoding the magnetic field through the three primary spatial directions by performing slice selection (SS), frequency encoding
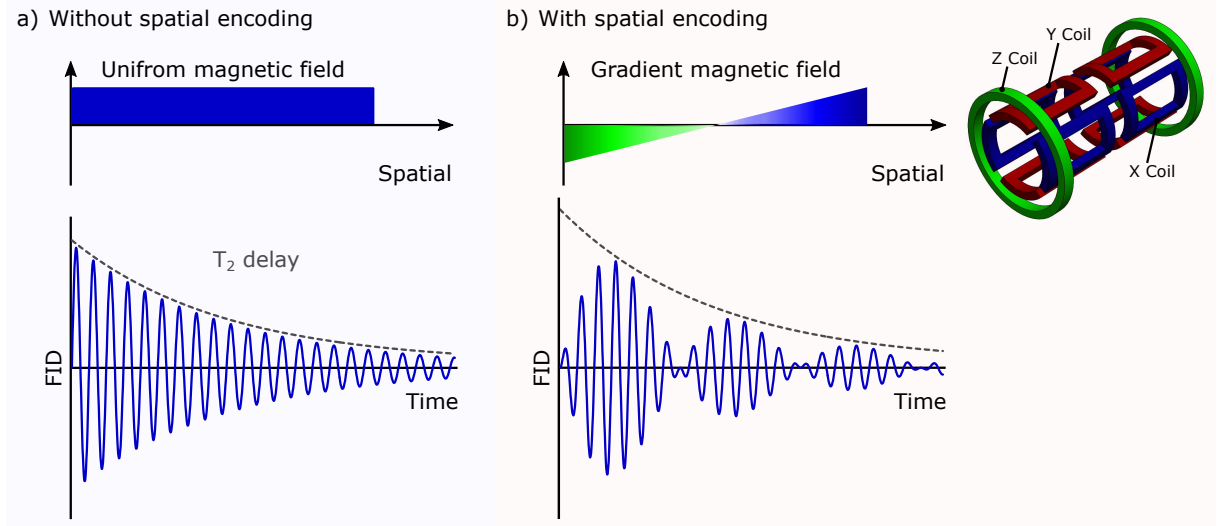
Figure 2.13: The MR free induction decay (FID) signals (a) without and (b) with spatial encoding. Encoding the FID is done by employing gradient coils [top right] for creating gradient magnetic fields in three spatial directions; X, Y, and Z.

(FE), and phase encoding (PE). The part that needs to be imaged is in 3D shape, so in the beginning, the target part should be divided into slices, then processing each slice in 2D. Slice selection is based on the fact that only the exciting spins could generate nuclear magnetic signals. Slicing is done by applying linear-gradient (G_Z) in the z-direction with a proper excitation profile to achieve the desired slicing, as shown in Fig. 2.14. Simultaneously, an RF excitation pulse is applied with an appropriate profile, corresponding to a rectangular waveform in the frequency domain and a Sinc waveform in the time domain, with excitation bandwidth Δf_{exc}. The slice thickness (ΔZ) is proportional to excitation bandwidth and slope of the linear-gradient, and it represents the depth of the voxel:

$$B_Z(z) = B_0 + G_Z Z, \tag{2.17}$$

$$\Delta Z = \frac{\Delta f_{exc}}{\gamma G_Z}. \tag{2.18}$$

The slice thickness is determined by the gradient field's steepness in the z-direction and the RF pulse bandwidth, as shown in Fig. 2.15. The slice thickness can be reduced by increasing the G_Z gradient steepness or narrowing the Rf pulse's bandwidth.

Subsequently, another spatial dimension is encoded using phase coding (PE) to differentiate the pixel within the desired slice. A linear-gradient G_P is applied in the Y-direction for a short time between the excitation and acquisition stages. As a result of this gradient, each pixel's phase within the slice changes with respect to its position on the Y-axis. The field of view (FOV_P), which represents the size of the area that the phase encoding covers, is proportional to the phase gradient and the number of points N with respect to the total duration T_P,

$$FOV_P = \frac{N}{\gamma G_P T_P} = \frac{1}{\gamma G_P \tau}, \tag{2.19}$$

Where τ is the pulse duration corresponding to the total duration divided by the number of points.
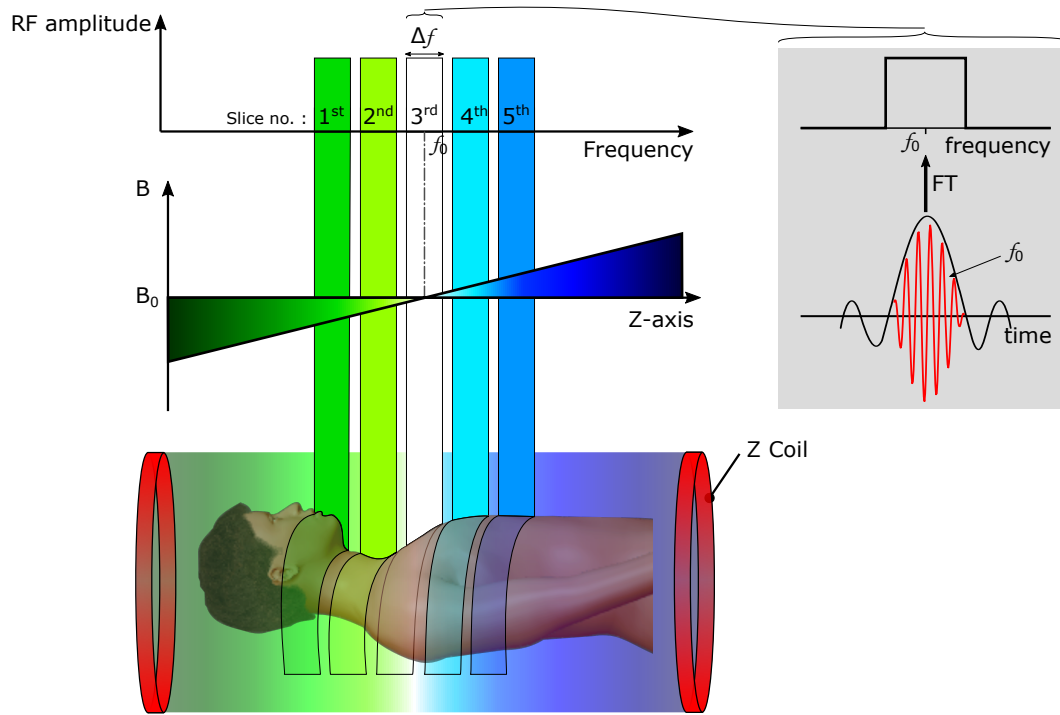
Figure 2.14: Slice selection (SS) is done by applying linear-gradient field (G_Z) in the z-direction and RF excitation pulse with a profile corresponding to a rectangular waveform in the frequency domain represented by a Sinc waveform in the time domain.

Lastly, during the readout stage, the third spatial dimension is considered for frequency encoding (FE) by applying a linear gradient G_f in the X-direction. Similarly, its FOV_f is proportional to the frequency gradient and digitized bandwidth Δf, which is the receiver bandwidth Δf_{acq} divided by total numbers of points M.

$$FOV_f = \frac{\Delta f_{acq}}{\gamma G_f M} = \frac{\Delta f}{\gamma G_f}. \tag{2.20}$$

Consequently, in the end, spatial information for each voxel within the target part is available to construct
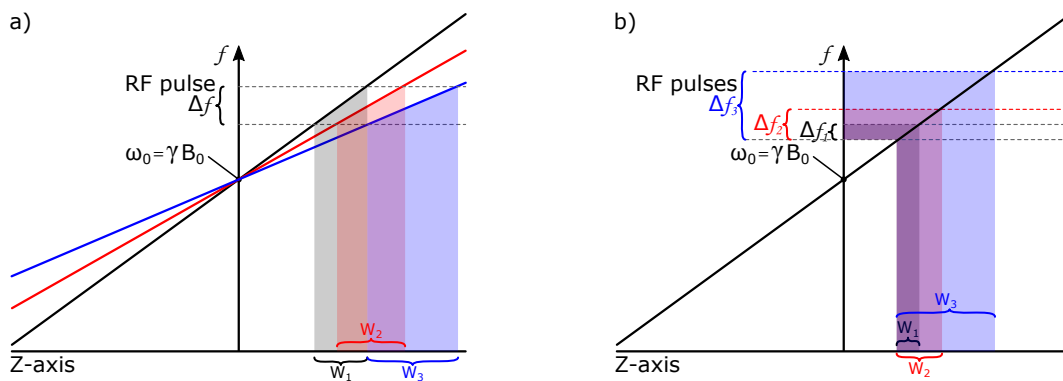

Figure 2.15: Effect of changing the gradient's strength in the z-direction and the RF pulse bandwidth on the slice thickness. **(a)** The strength of the gradient field in the z-direction is inversely proportional to the slice thickness. On the other hand, **(b)** The RF pulse bandwidth is directly proportional to the slice thickness.

the image. The combination of the RF excitation pulses with the three different gradient magnetic fields to generate the MR image is known as the MR imaging sequence. Each imaging sequence has a different order of applying the slice selection (SS), the phase encoding (PE), and the frequency encoding (FE) with respect to the RF excitation signal. There are various MR imaging sequences to acquire voxels' information of a target part. Two of the standard MRI sequences are the spin-echo and the gradient-echo sequences. The timing diagram of both MRI sequences is shown in Fig. 2.16.

In a typical spin-echo sequence, a 90° excitation RF pulse is applied simultaneously with the slice selecting gradient in the z-direction. Consequently, the desired slice is selected, and its spins are excited. After that, a defined phase encoding pulse is applied in Y-direction. Another 180° excitation RF pulse is then applied along with the z-direction gradient to enhance the magnetic moments after dephasing to increase the net magnetization before recording the MR signals. Applying the 180° RF pulse is the main drawback of this imaging sequence because of the high RF power demand. Finally, the frequency encoding pulse is applied while the MR echo signal is recorded. These steps are repeated N times based on phase encoding steps. The time required to acquire one echo signal is called the echo time (TE) and is defined by the time between the centers of the excitation pulse and the echo signal. The time between two consecutive excitation pulses for the various phase encoding steps is known as repetition time (TR).

The gradient-echo MRI sequence is almost similar to the spin-echo sequence without the 180° excitation RF pulse. At first, a 90° excitation pulse is applied along with the slice selection gradient as in the spin-echo imaging sequence. Simultaneously, with applying the phase encoding pulse, a negative frequency encoding pulse is applied to compensate for the expected magnetic moment's dephasing during the readout gradient. This negative frequency encoding technique is used to refocus the magnetic moment instead of using the 180° excitation RF pulse.
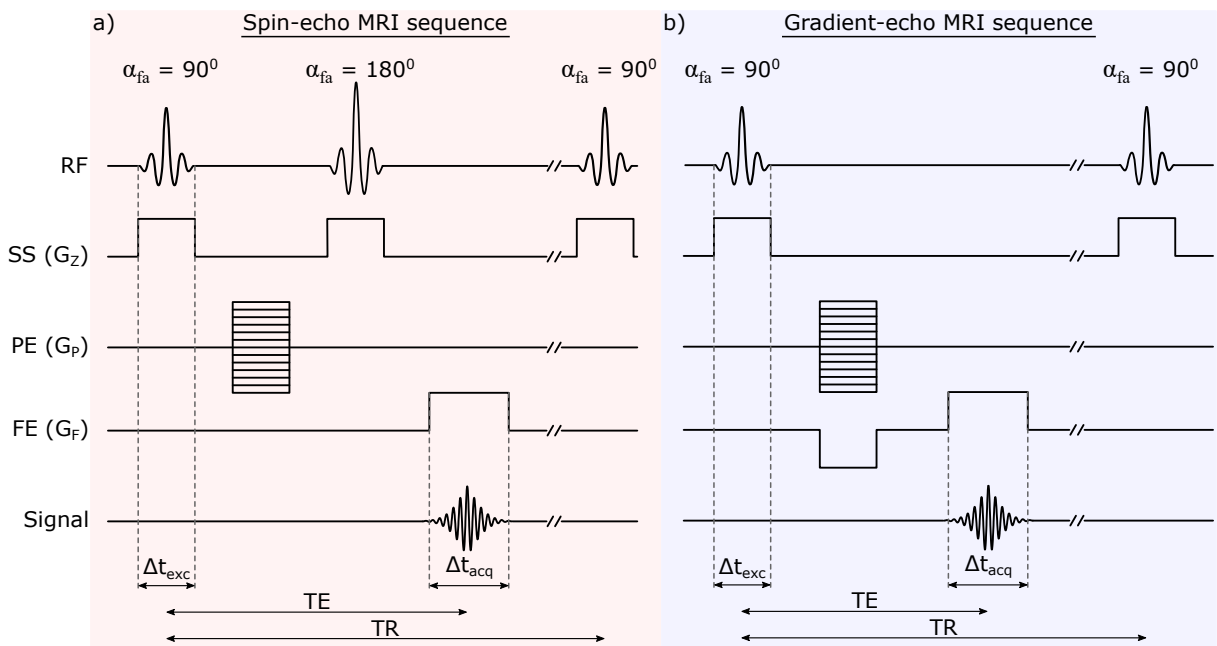

Figure 2.16: The MRI sequence timing diagrams of a standard spin-echo imaging sequence and standard gradient-echo imaging sequence.

2.3.2   K-space matrix and image computation

For obtaining a computational image, all the acquired encoded MR signals are recorded in a matrix known as the k-space matrix with size $(M \times N)$. The k-space matrix represents an array of spatial frequencies. The MR signal (or FID) is sampled and filled into the k-space matrix during the data acquisition. There are various filling schemes, and one of the standard schemes is the sequential acquisition or Cartesian filling, where the k-space points are determined as follows:

1. In the case of the frequency encoding (in the X-direction),

$$k_f = m\Delta k_f = m\frac{1}{FOV_f}, \tag{2.21}$$

where $m \in 1, 2, ..., M$. Substituting by Equation 2.20 in Equation 2.21 and $\Delta f = 1/\Delta t$ where Δt is
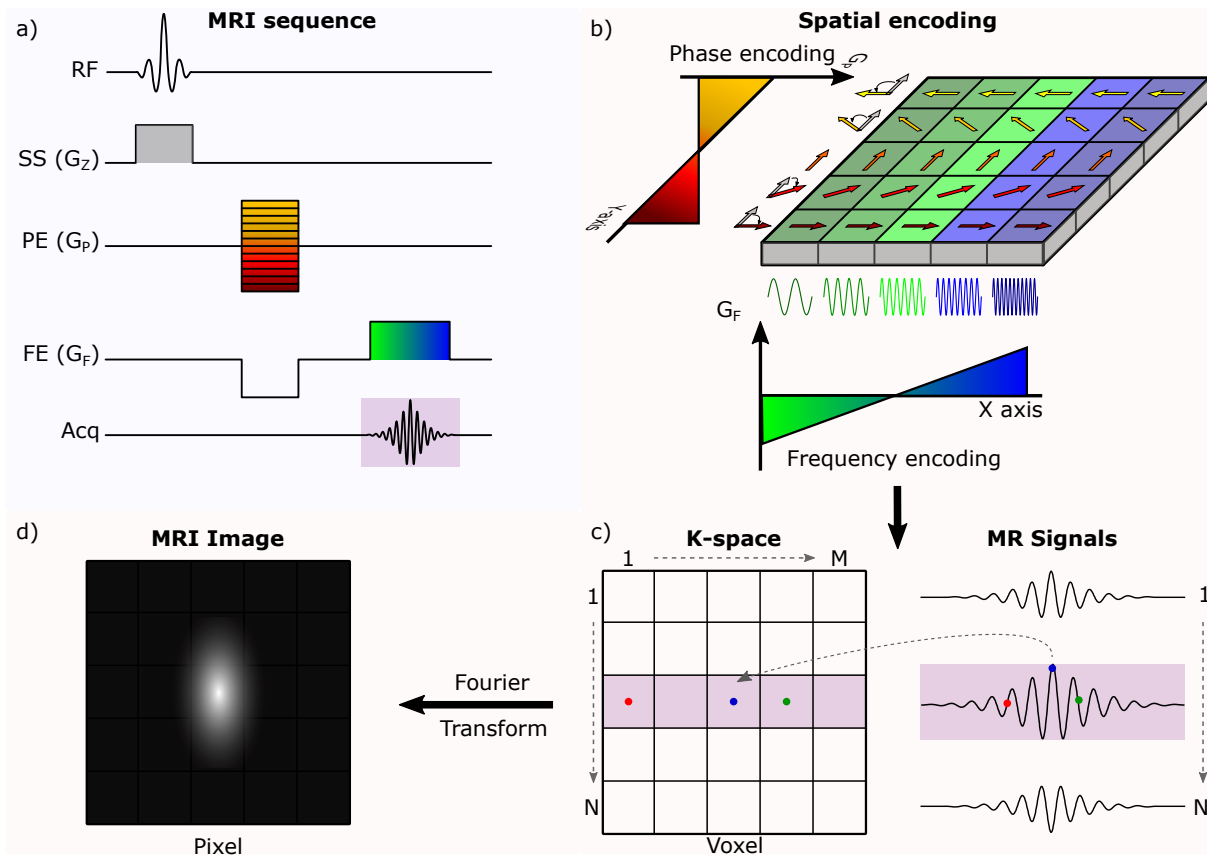

Figure 2.17: Obtaining an MRI image by applying the three axes gradient fields. **(a)** A typical MRI spin-echo pulse sequence for encoding the magnetic field. **(b)** First, slice selection (SS) is achieved by applying a gradient field in the z-direction and an RF pulse, then phase encoding (PE) and frequency encoding (FE) are applied to encode the selected slice. PE is achieved by applying gradient field in the Y-direction, leading to phase change of the magnetic moments with respect to their Y-axis position. FE is achieved by applying a gradient field in the X-direction, magnetic moments are subjected to a different frequency with respect to their X-axis position. **(c)** The sampled MR echo signals are used to fill the k-space matrix . **(d)** Finally, the MRI image is acquired by applying 2D Fourier transform to the k-space matrix.

the period of the sampling pulse,

$$\therefore k_f = m\gamma G_f \Delta t. \tag{2.22}$$

2. Similarly, in the case of the phase encoding (in the y-direction) and by using Equation 2.19,

$$k_P = n\Delta k_P = n\gamma \Delta G_P \tau. \tag{2.23}$$

After filling the k-space matrix, a 2D discrete Fourier transform is performed to the matrix to convert the spatial frequencies (k_f, k_P) to the positions (X,Y) representing spin density distribution to compute the final image, as shown in Fig. 2.17

2.4 Magnetic resonance hardware

The NMR spectrometer and the MRI scanner have the same hardware units except for the gradient coils, present only in the MRI scanner. Nevertheless, some NMR experiments might require gradient fields,i.g., voxel-based or Self-Diffusion (SD) NMR spectroscopy. Figure 2.18 show the main building unit of MRI scanners which consists of;

1. Magnet for providing the static B_0 magnetic field for magnetization.

2. Shimming coils to generate the shim magnetic field, which is superimposed to the static magnetic field to compensate for its minor spatial inhomogeneities.

3. Radio frequency (RF) coil for generating the electromagnetic B_1 field for excitation and detecting the nuclear magnetic signal.

4. Three gradient coils for spatial encoding.

2.4.1 Static magnet and shim field

The magnet is responsible for producing the static B_0 field for polarizing the sample by aligning the magnetic moments of the sample's spinning nuclei. For human MRI applications, hospitals usually have standard MRI scanners with 1.5 or 3 T. The approved limit for the human MRI scanner is 7 T. Researchers are trying to push the human MRI limits for higher fields where a 10.5 T magnet was used for human imaging [25]. For an NMR spectroscopy, superconducting magnets are commercially available that can provide highly homogeneous magnetic fields of up to 25.9 T [26].

The static magnetic field needs to be highly homogeneous within 1 ppb (part-per-billion) for high-resolution NMR spectroscopy and to prevent geometrical distortions in the MR imaging. Consequently, shim coils are used to generate spherical harmonic magnetic fields, which are superimposed to the main magnet B_0 static field for inhomogeneity compensation. The inhomogeneities result from internal ferro-magnetic materials, sample permeability, probe material, and imperfection of the main magnet.
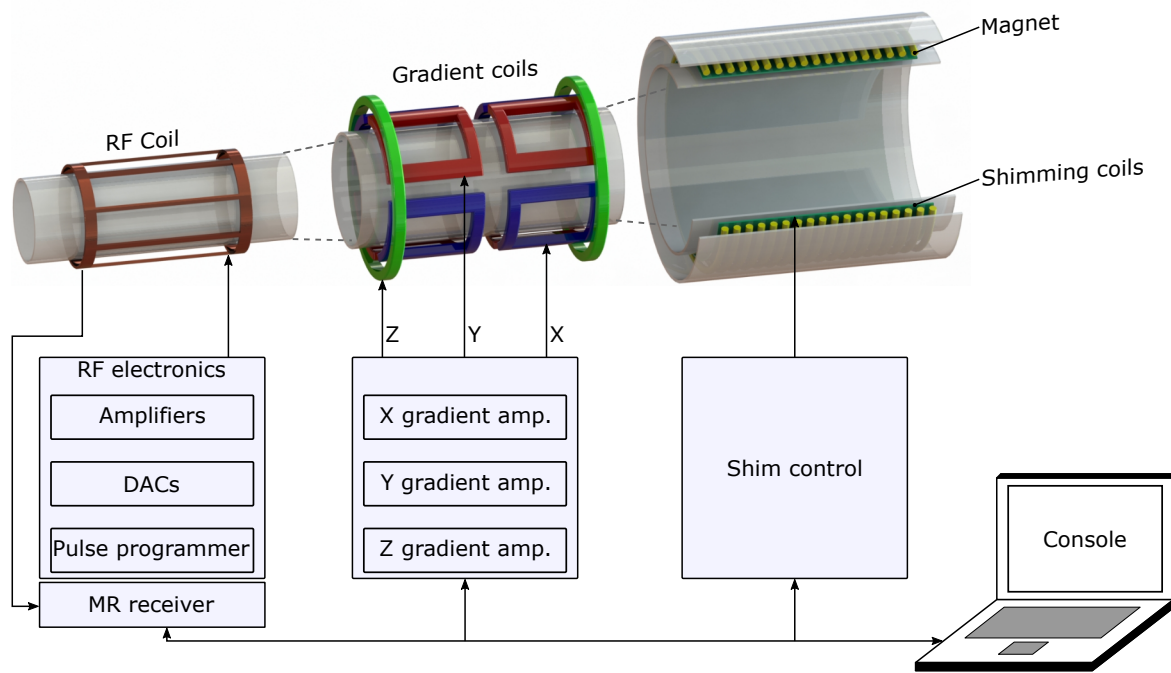
Figure 2.18: Overview of the main hardware components of a typical magnetic resonance imaging (MRI) scanner.

2.4.2   Gradient coils

The gradient coils are used for performing spatial encoding. There are three gradient coils aligned in the three space directions X, Y, and Z. For each gradient coil, linear gradients are produced based on two variable spatial encoding parameters; i) The first parameter corresponds to the gradient strength at the position Tm^{-1}, ii) The second parameter is the gradient slope which represents the field's change with respect to time ms. The gradient coils are connected to electronics circuits consisting of current amplifiers, gradient pulse programmers, and digital to analog converters (DAC). The user controls the pulses' width, amplitude, and shape using the gradient pulse programmer through a computer user interface. The signals are then converted to analog data using DAC. Finally, the current amplifier amplifies the pulse signals to drive the gradient coils.

2.4.3   Radio frequency coils

The MR (FID) signal is generated by changing the orientation of the net magnetization vector by a certain flip angle. This excitation procedure is performed using an alternating RF field generated by an RF coil. In general, Two RF coils are required; i) the first coil is used for excitation by producing the RF magnetic field (B_1). The generated magnetic field can be manipulated to establish a particular flip angel,e.g., 180° flip angles in the spin-echo imaging sequence, ii) The second the RF coil is employed to acquires the MR signal (FID) during the relaxation process. Two separate RF coils could be used as transmitter and receiver, or one RF coil could be used as a transceiver based on the reciprocity principle.

The RF coils are attached to an electronic circuit consisting of a pulse programmer, an RF signal source,

and power amplifier. The RF coil should be tuned at the corresponding Larmor frequency to excite the spins or acquire the MR signal either as transmitter or receiver. As a transmitter, the pulse duration (τ) can be adjusted through the pulse programmer via a fast switch called a pulse gate. The adjusted pulse duration corresponds to a certain flip angle of the net magnetization vector based on the application. As a receiver, the coil should be placed near the sample, where the released energy from the sample during the relaxation induces an electromotive force in the RF coil.

For an RF coil to be utilized for MR measurement it requires an adjusting interface circuit called matching and tuning circuit. The matching procedure is performed to adjust the RF coils' internal impedance to match the connecting cable's impedance to avoid losses resulting from power reflections. The tuning procedure is essential to tune the resonance frequency of the RF coil to the Larmor frequency to excite the spins during the excitation process and pick up the MR signal during the relaxation process. The standard matching and tuning circuit consists of a variable tuning capacitor (trimmer) attached in parallel with the RF coil. In contrast, a variable matching capacitor is shunted in series with the coil, as shown in Fig. 2.19a. The equivalent electrical circuit of an RF coil consists of inductance L_{Coil}, intrinsic resistance R_{Coil}, and parasitic internal capacitance C_{Coil}.

The static magnetic field B_0 has a much stronger field than the generated RF magnetic field B_1 by a factor of 10^6. Hence, the RF coil should resonate at Larmor frequency to minimize the required energy to excite the spins and produce the flip angle. For an RF coil to excite the spins, the generated energy should cover the Zeeman states' energy difference.

The upper limit of the resonance frequency of an RF coil is defined by its internal components. For any RF coils, the resonance frequency (ω_r) is proportional to the coil's inductance and capacitance ($\omega_r = 1/\sqrt{L_{Coil} C_{Coil}}$). Hence, for utilizing an RF coil in MR measurements, it should be designed to have a self resonance frequency (SRF) higher than the Larmor frequency. Consequently, the coil's resonance frequency can be shifted down toward the Larmor frequency by increasing either the inductance or equivalent capacitance. For MR applications, the equivalent capacitance is increased by adding the tuning capacitor (C_T) in parallel to the coil. The resonator's equivalent capacitance is the summation of the coil's internal capacitance and the tuning capacitance ($C_{Total} = C_{Coil} + C_T$). Therefore, the resonance frequency of the MR resonator could be adjusted by increasing the tuning capacitor to lower the frequency till it is tuned to the Larmor frequency as follow:

$$\omega_r = \omega_0 = \frac{1}{\sqrt{L_{Coil}(C_{Coil} + C_T)}}. \tag{2.24}$$

Due to the non-ideality of the RF coil, it has an internal resistance modeled in series with its inductance resulting in a complex impedance of the coil (Z_{Coil}), shown in Equation 2.25. The coil's impedance is the summation of the coil resistance R_{Coil} and the equivalent reactance (X_{Coil}) of the inductance and capacitance. For connecting two circuits, such as the RF coil and the power amplifier, their impedance should be matched to efficiently transfer signals and avoid power reflections. The internal amplifier impedance and the resistance of the connecting coaxial cables are $50\,\Omega$, so the coil impedance should also be matched to $50\,\Omega$ at the resonance frequency ($Z_{coil} = 50\,\Omega$ and $X_{Coil} = 0$). Adding a matching capacitor (C_M) in series with the Coils gives control over the coil impedance's reactance. Hence, C_T is used to tune the coil to the Larmor frequency and set the real part of the coil's impedance to $50\,\Omega$, while
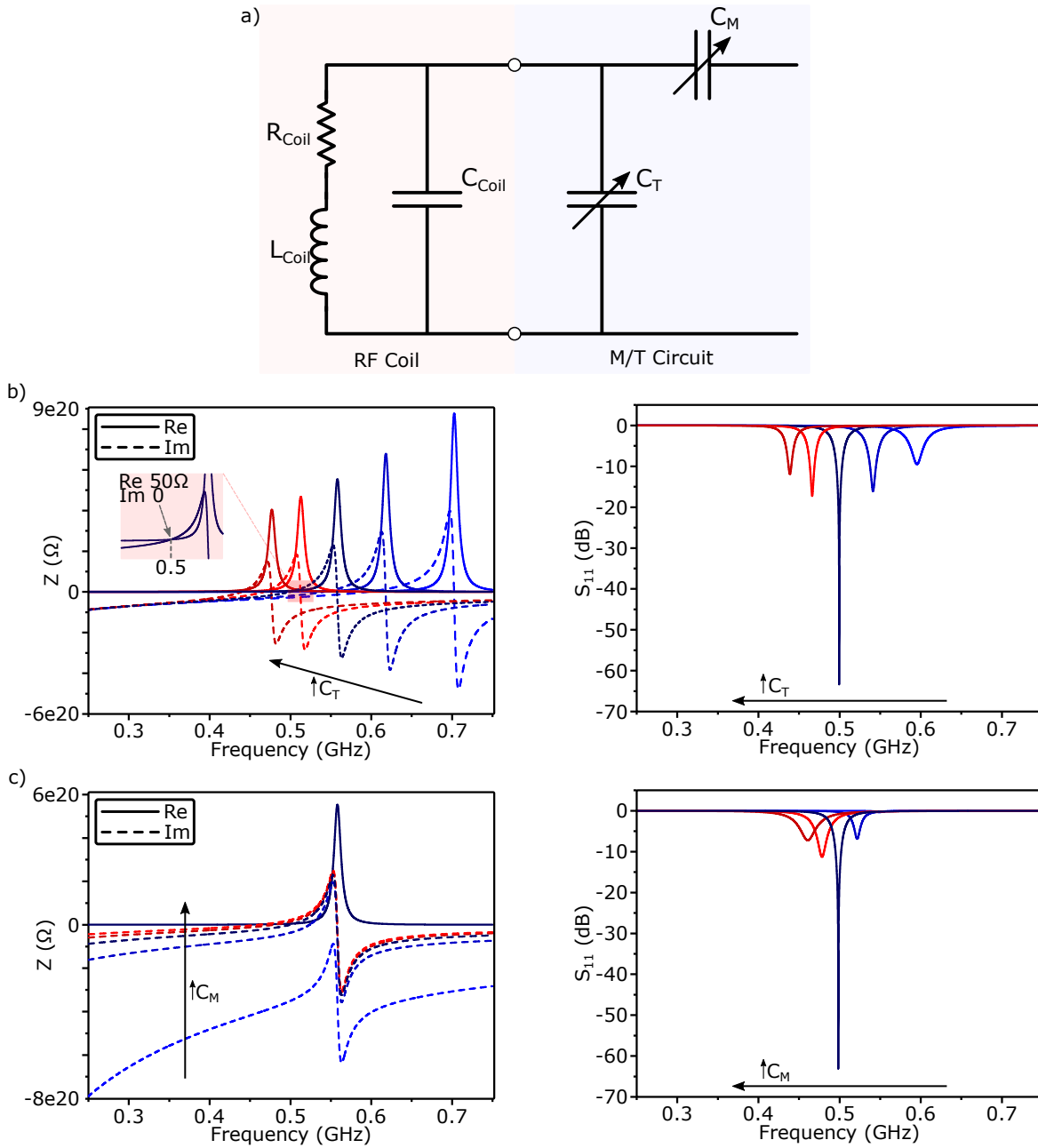
Figure 2.19: Typical matching and tuning network circuit and simulated behavior. **(a)** Schematic of the equivalent circuit of a non-ideal coil attached to matching and tuning capacitors. **(b)** and **(c)** Simulation results using Advanced Design System (ADS) software for the equivalent circuit in (a). The modeled coil ($L_{Coil} = 30\,\text{nH}$, $R_{Coil} = 2\,\Omega$) was tuned to a resonance frequency of $500\,\text{MHz}$ using $C_T = 2.71\,\text{pF}$ and matched to $50\,\Omega$ using $C_M = 0.68\,\text{pF}$. (b) the results of sweeping C_T with keeping C_M constant. (c) The results of sweeping C_M with keeping C_T constant.

C_M is used to eliminate the residual imaginary part, using Equation 2.26.

$$Z_{coil} = \frac{\dfrac{1}{j\omega C_{Coil}}(R_{coil} + j\omega L_{Coil})}{\dfrac{1}{j\omega C_{Coil}} + (R_{coil} + j\omega L_{Coil})}, \tag{2.25}$$

$$\Re[\frac{Z_{Coil}\frac{1}{j\omega C_T}}{Z_{Coil}+\frac{1}{j\omega C_T}}]=50\ ,\quad \Im[\frac{Z_{Coil}\frac{1}{j\omega C_T}}{Z_{Coil}+\frac{1}{j\omega C_T}}+\frac{1}{j\omega C_M}]=0. \tag{2.26}$$

A numerical simulation was done using Advanced Design System (ADS) software for the matching and tuning circuit shown in Fig. 2.26a. The modeled inductor has an inductance of $L_{Coil} = 30\,\text{nH}$ and an intrinsic resistance of $R_{Coil} = 2\,\Omega$. It was tuned to a resonance frequency of $\omega_0 = 500\,\text{MHz}$ using $C_T = 2.71\,\text{pF}$ and matched to $50\,\Omega$ using $C_M = 0.68\,\text{pF}$. The tuning capacitor (C_T) was then swept from 1.71 pF to 3.71 pF with a step of 0.5 pF with keeping the matching capacitor at a constant value of 0.68 pF. The effect of changing C_T on the circuit impedance and reflection coefficient (S_{11}) is presented in Fig. 2.19b. C_M was then swept from 0.08 pF to 1.28 pF with a step of 0.3 pF with keeping C_T at a constant value of 2.71 pF. The effect of changing C_M on the circuit impedance and reflection coefficient (S_{11}) is presented in Fig. 2.19c. Changing C_T affects both the real and imaginary parts of the circuit's impedance, while C_M only affects the impedance's imaginary part. Therefore, C_T is adjusted first to tune the circuit, and C_M is then used to eliminate the imaginary term.

The matching and tuning circuit configuration shown in Fig.2.19a is known as the unbalanced matching scheme. The balanced matching scheme can be achieved using two matching capacitors instead of one capacitor, one at each terminal of the RF coil, as shown in Fig. 2.20a. The balanced scheme reduces the coil to ground losses as long as the voltage amplitude is the same at the two terminals of the circuit with inverted phase. In NMR spectroscopy, the RF coil is placed onto the probe-head inside the magnet where it is difficult to reach. So the matching and tuning capacitors ($C_{T,Ph}$ and $2 \times C_{M,Ph}$) could be used to pre-adjust the RF coil before connecting it to the NMR probe. Additionally, two more variable capacitors ($C_{T,Pb}$ and $C_{M,Pb}$) are built-in the probe and can be mechanically controlled from outside the magnet using rods for fine-tuning, as shown in Fig.2.20a.

The probe's trimmers ($C_{T,Pb}$ and C_{Mpb}) are connected in series with the RF resonator. Hence, both trimmers will provide the matching capacitor's functionality, which does not offer full control of the RF coil. Therefore, a shunt capacitor (C_P) is added to set $C_{T,Pb}$ in parallel with the RF resonator to give it the tuning functionality. Based on the lumped-model presented in Fig. 2.20a, the equivalent impedance (Z_{Total}) was driven with and without (C_P). In Equations 2.27 and 2.28, the terms highlighted in blue set the tuning frequency, and the terms highlighted in red affect only the imaginary part of the impedance resulting in a matching behavior. Equations 2.27 and 2.28 reveal the role of C_P in providing $C_{T,Pb}$ the tuning functionality.

$$Z_{Total}\text{ "W/O }C_P\text{"} = \frac{Z_{coil}\cdot 1/j\omega C_{T,Ph}}{Z_{coil}+1/j\omega C_{T,Ph}} + \frac{1}{j\omega}(\frac{2}{C_{M,Ph}}+\frac{1}{C_{M,Pb}}+\frac{1}{C_{T,Pb}})\ , \tag{2.27}$$

$$Z_{Total}\text{ "With }C_P\text{"} = [(\frac{Z_{coil}\cdot 1/j\omega C_{T,Ph}}{Z_{coil}+1/j\omega C_{T,Ph}})+(\frac{1}{j\omega}(\frac{2}{C_{M,Ph}}+\frac{1}{C_{T,Pb}}))]\parallel C_P + \frac{1}{j\omega C_M}. \tag{2.28}$$

A numerical simulation was done using ADS software for the balanced matching and tuning circuit shown in Fig. 2.20a. The modeled inductor has an inductance of $L_{Coil} = 50\,\text{nH}$, an intrinsic resistance of $R_{Coil} = 2\,\Omega$, and the internal capacitance is neglected $C_{Coil} = 0$. The coil is tuned to a resonance
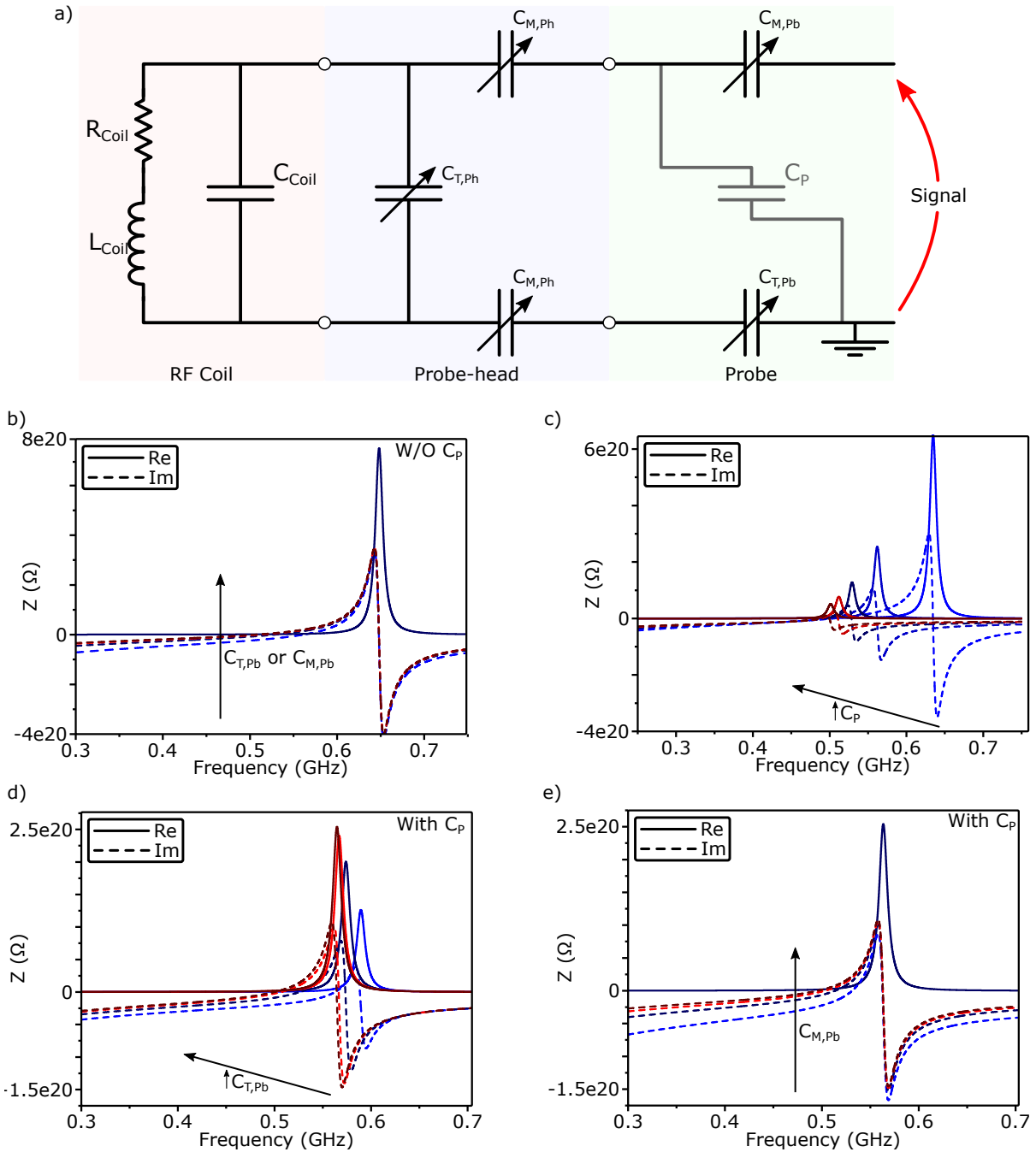
Figure 2.20: Schematic circuit and simulated behavior of the balanced matching and tuning network attached to a coil on a typical NMR probe. **(a)** Schematic of the equivalent circuit of an RF coil on an NMR probe. The non-ideal coil is connected to a balanced matching and tuning circuit on the probe-head ($C_{T,Ph}$ and $2 \times C_{M,Ph}$) for pre-tuning and the probe's trimmers ($C_{T,Pb}$ and $C_{M,Pb}$) for fine-tuning. **(b)-(e)** Simulation results using Advanced Design System (ADS) software for the equivalent circuit in (a). The modeled coil ($L_{Coil} = 30$ nH, $R_{Coil} = 2\,\Omega$) was tuned to a resonance frequency of 500 MHz and matched to 50 Ω using $C_{T,ph} = 2$ pF, $C_{M,Ph} = 10$ pF, and $C_{T,Pb} = C_{M,Pb} = 3.5$ pF. The simulation results show the change in the circuit equivalent impedance by sweeping: (b) $C_{T,Pb}$ and $C_{M,Pb}$ with C_P as an open circuit, (c) C_P while keeping the rest of the capacitors constant, (d) sweeping $C_{T,Pb}$ with $C_P = 1$ pF, and (e) $C_{M,Pb}$ with $C_P = 1$ pF.

frequency of 500 MHz with selecting the capacitance values of $C_{T,Ph} = 2\,\text{pF}$, $C_{M,Pb} = 10\,\text{pF}$, and $C_{T,Pb} = C_{M,Pb} = 3.5\,\text{pF}$. First, each of $C_{T,Pb}$ and $C_{M,Pb}$ were swept separately from 1 pF to 4 pF with a step 1 pF, with holding the other capacitor at a constant value of 3.5 pF and without C_P. The result is presented in Fig. 2.20b, which demonstrates that both $C_{T,Pb}$ and $C_{M,Pb}$ have a matching effect by changing only the imaginary part of the impedance. Next, C_P is added, and its value was swept from 0.1 pF to 4 pF with a step 1 pF. The effect of sweeping C_P on the impedance is plotted in Fig. 2.20c. With $C_P = 1\,\text{pF}$, each of $C_{T,Ph}$ and $C_{M,Ph}$ were swept again (from 1 pF to 4 pF with a step 1 pF), with holding the other capacitor at a constant value of 3.5 pF. The effect of sweeping $C_{T,Pb}$ with the presence of C_P on the impedance is shown in Fig. 2.20d. C_P sets $C_{T,Pb}$ in parallel with the RF resonator, affecting both the real and imaginary parts of the impedance giving it the tuning functionality. On the other hand, since $C_{M,Pb}$ stays in series with the RF resonator, it keeps its matching effect as shown in Fig 2.20e.

2.4.4   MR characterization

The quality of the acquired MR signal and the hardware components' functionality can be evaluated by devaluing the Signal-to-Noise (SNR) Ratio of the resulted MR data. The SNR is a common concept in signal processing. According to conventional signal theory, SNR is defined as the square root of the ratio between the signal intensity and the noise intensity. However, in the NMR community, SNR is the fraction between the signal amplitude of the NMR spectrum and the root-mean-square of the noise as described by Hoult and Richards [27]. A reformulated closed-form version of the SNR was introduced by Peck et al. [28] as follow:

$$SNR = \frac{\text{peak signal}}{\text{RMS Noise}} = \frac{k_0(B_1/i)V_{sample}N\gamma\hbar^2 I(I+1)\dfrac{\omega_0^2}{3\sqrt{2}k_B T}}{\sqrt{4k_B T R_{noise}\Delta f}}, \tag{2.29}$$

where k_0 is a scaling factor related to the homogeneity of the alternating B_1 field, i is the current flowing through the RF coil, R_{noise} is the AC electrical resistance of the coil comprising the proximity and skin effects, V_{sample} is the active sample volume, N is the spin density, and Δf is the spectral bandwidth.
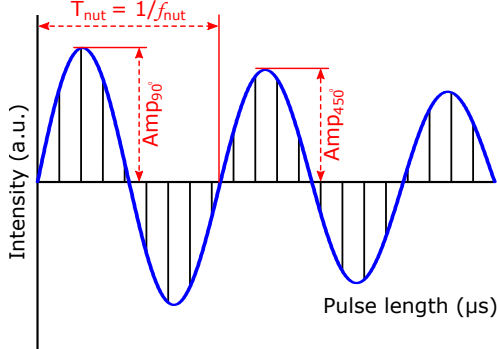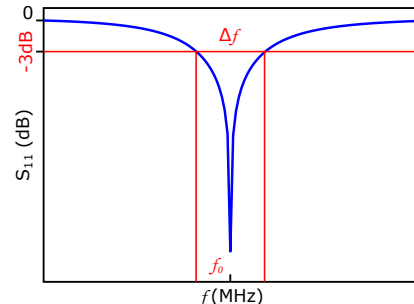
Equation 2.29 indicates that besides the temperature and the B_0 field intensity, the RF coil is the fundamental unit affecting the SNR since it has to pick up the weak MR signal. Hence, the design and optimization of the RF coil should be done with great attention to reduce the noise it generates, especially while receiving the MR signal. The SNR denominator represents the MR coil's noise which is mainly thermal noise developed in the coil and sample. This noise is commonly known as Johnson noise [29] and is described by Nyquist formula:

$$V_{noise} = \sqrt{4k_B T R_{noise}\Delta f}. \tag{2.30}$$

The main parameters to characterize the MR coil performance are the $B1$ homogeneity, probe efficiency (η_P), and Quality factor (Q_P) to enhance its performance and thus the SNR. The mathematical and practical methods for evaluating these parameters are summarized in Table 2.1.

The filling factor (α_F) is another critical parameter that differentiates one MR coil topology from another. The filling factor is the ratio between the sample volume observed by the B_1 field to the whole B_1 field

Table 2.1: Methods for evaluating the MR coil's characterization parameters

	Theoretical	Practical
Probe efficiency (η_P)	The NMR probe's efficiency can be calculated by dividing B_1 field strength over the square root of applied power (P_{Coil}), which is also equivalent to the sensitivity (B_1/i) divide by the square root of coil resistance (R_{Coil}) [30], $$\eta_P = \frac{B_1}{\sqrt{P_{Coil}}} = \frac{B_1}{i\sqrt{R_{Coil}}}. \qquad (2.31)$$ For any given coil geometry, the magnetic field can be calculated following Biot-Savart law at any point with position vector r, $$B(r) = \frac{\mu_0}{4\pi}\int_C \frac{Idl \times r}{|r|^3}, \qquad (2.32)$$ where I is the current and μ_0 is the permeability. The higher the efficiency, the less the required power to achieve a 90° flip angle.	The probe efficiency can be experimentally determined according to the frequency (f_{nut}) of the nutation spectrum[a] $$f_{nut} = \frac{1}{2}\gamma B_1 \sin\theta. \qquad (2.33)$$ This equation is used to determine B_1, and then η_P can be calculated. θ is the angle between the B_0 and B_1 field, ideally $\theta = 90°$.
B_1 homogeneity	B_1 homogeneity can be evaluated by calculating the B_1 field using the Biot-Savartt law at every point within the active sample volume and estimating the difference between the maximum and lower values. A homogeneous B_1 field results in equal excitation of the sample spins and enhances the MR signal.	The B_1 homogeneity can be determined from the decay rate of the nutation spectrum. A slow decay of the nutation curve reflects a high degree of B_1 homogeneity. The closer the ratio $Amp_{90°}/Amp_{450°}$ to unity, the higher the homogeneity.
Quality factor (Q_P)	The Quality factor Q_P describes the energy losses. Higher resistance leads to energy dissipation through the coil. Q_P is the ratio between the coil's reactance and resistance. $$Q_P = \frac{\omega_0 L_{Coil}}{R_{Coil}}. \qquad (2.34)$$	Q_P can be experimentally determined by measuring the reflection coefficient (S_{11}), knowing the bandwidth at -3 dB ($f_{-3\,dB}$) of the resonance frequency (f_0), $$Q_P = \frac{2f_0}{\Delta f_{-3\,dB}}. \qquad (2.35)$$

---

[a] The nutation spectrum is the magnetization progression with raising the excitation pulse length (τ) at a constant supplied power (P_{Coil}).

volume. α_F is evaluated by the weighted moment,

$$\alpha_F = \frac{\int B_1^2 \rho(r)dV}{\int B_1^2 dV},\tag{2.36}$$

where the parameter $\rho(r)$ is unity in the locations where the sample is affected by the B_1 field and zero elsewhere. For example, a solenoid coil with the internal volume filled with the sample has a filling factor of $\alpha_F = 1/2$; other typologies usually have a filling factor much lower than that. Selecting a proper filling factor is a matter of optimization as increasing the filling factor increases the NMR signal. On the other hand, the sample should also be kept far from the coil's material where the B_0 field is distorted due to the susceptibility mismatch, which leads to low spectral resolution. The NMR spectral line-shape is considered a benchmark of B_0 distortion, with signals showing a sharp narrow Lorentzian reflecting B_0 field with high homogeneity. Increasing the B_0 field strength or reducing the temperature boosts the spin polarization, enhancing the signal amplitude and SNR. The minimum detectable quantity of a sample for a given system is defined as the limited detection (LOD), which is inversely proportional to the SNR. The normalized limit of detection (nLOD) is defined for an SNR of 3 and is given by [30],

$$nLOD_\omega = \frac{3n_s\sqrt{\Delta t}}{SMR_\omega},\tag{2.37}$$

Where Δt is the single scan acquisition time, n_s is the number of spins presented in the sample, and SNR_ω is the calculated SNR in the frequency domain.

Part I.

Micro-Fabrication of Flexible Electronics

3 Flexible electronics fabrication

Flexible electronics have drawn significant attention since they first appeared in the 1960s because of their magnificent potential in several emerging applications [31]. The global market size of flexible electronics was valued at $23.64 billion in 2019 and is expected to rise rapidly to reach a value of $42.48 billion by 2027 [32]. Flexible electronics have found their way in many devices such as electronic components [33], displays [34], solar cells [35], and radio frequency identification devices (RFID) [36]. Flexible electronics provide a significant push for developing wide range of technologies as wearable electronics [37], health monitoring devices [38], and intelligent textile [39] as they are more efficient than conventional electronics.

The first part of the thesis (Chapters 3 and 4) discusses the different fabrication technologies developed for building flexible electronic devices that are used in the second part (MRI application) and the third part (NMR application) of the thesis. A flexible electronic device is generally built out of a thin passive flexible substrate with active electronic components on one or both sides of a substrate, enabling rolls, bends, folds, and stretches without hindering its performance.

The micro MR-detector consists mainly of inductors and capacitors. The different inductors' typologies can be achieved by structuring a conductive layer on a dielectric substrate. On the other hand, capacitors require structuring a dielectric layer on top of the conductive layer to realize parallel plate capacitors. Besides these two passive electronic components, fabricating diodes was needed for the MRI application. Hence, this chapter is divided into three sections. Section 3.1 discusses the different technologies for depositing a conductive seed-layer on a flexible substrate with focusing on the inkjet-printing technique. Section 3.2 introduces a novel insulator ink compatible with the inkjet-printing technique to realize a high dielectric high quality factor flexible capacitor. Section 3.3 explains a fabrication process for building flexible diodes using inkjet-printing.

3.1 Conductor seed-layer patterning

Substrate selection is an important step in the fabrication of flexible electronic devices [40]. The substrate's mechanical properties should meet the application specifications regarding flexibility, and it should be rigid enough to sustain mechanical stresses during the fabrication process. The electrical properties are essential to restrain leakage currents in electrical devices. The thermal properties play an essential role during the device operation for controlling the generated heat dissipation. Moreover, the substrate's characteristics, such as heat resistance, chemical resistance, and surface smoothness, determine the substrate's compliance with different manufacturing processes.

Several material categories have been used as a base substrate for flexible electronic devices; the most common ones are papers, textiles, and polymers. *Paper* substrates are very common in the field of flexible electronics [41]. They are mainly made out of compressed cellulose fibers into thin sheets. The cellulose mesh network and type of filler material define the paper's properties, structure, and thickness [42]. Paper-based substrates have a set of unique properties such as mechanical strength, flexibility,

and customizability. However, paper-based substrates suffer from poor thermal performance due to the large pore size and the presence of moisture in the paper [43]. Thus, paper substrates are not compatible with fabrication processes that include high curing temperature, i.e., limiting the deposition processes that can be used on paper. *Textile* substrates [39] have been recently considered for use in flexible electronic devices, with most applications related to wearable electronics [44]. Due to textiles' flexibility and stretch-ability, most of the coating processes used with them are rapid prototyping techniques, such as screen printing, dip coating, inkjet-printing, or hand stitching. *Polymer* substrates are one of the most attractive choices of materials for flexible electronics [45]. Polymer-based substrates can be divided into: 1) semi-crystalline polymers such as polyetheretherketone (PEEK), polyethylene tereph-thalate (PET), and polyethylene naphthalene (PEN); and 2) amorphous polymers such as polycarbonate (PC), polyethersulphone (PES), and polyimide (PI). Due to the different structural organization levels and different chemical compositions, these polymer substrates feature a wide range of mechanical, chemical, and thermal properties. PIs are of the most promising polymer substrates for flexible electronic devices due to their excellent mechanical, physical, thermal, and dielectric properties [46].

Through this thesis, Kapton polymer foil has been used as the base substrate to manufacture MRI and NMR flexible electronic devices. Kapton has several advantages which makes it a perfect candidate for our applications, such as [47]: 1) thermal stability over a wide range of temperatures (from $-269\,°C$ to $400\,°C$) makes it compatible with most of the micro-fabrication technologies; 2) perfect electrical insulation with good dielectric quality; 3) chemical stability, compatible with most solvents and solutions involved in the micro-fabrication process as well as in the NMR/MRI experiments; and 4) availability as ultra-thin sheets with thickness down to a few micrometers. Moreover, the Kapton polymer was chosen for the NMR/MRI applications due to its magnetic susceptibility, which is close to that of water [48].

Conductive electrodes are the primary building block of the flexible electronic devices. Depositing conductive electrodes with a specific structure, morphology, and pattern is an essential step in the electronic systems' fabrication process. In conventional micro-fabrication, conductive materials are deposited by employing physical vapor deposition (PVD) or chemical vapor deposition (CVD), which is commonly used in the semiconductor industry. Patterning the deposited conductive layer is conventional done with the mean of the photolithography process. On the one hand, this process results in uniform conductive tracks of a high degree of material purity with precise resolution and thickness. On the other hand, this micro-fabrication process involves using expensive instrumentation, which requires a clean-room environment adding to the process cost, complexity, and duration. Therefore, inkjet-printing, an alternative rapid prototyping approach, has been considered for depositing conductive tracks with the desired pattern. Inkjet-printing is done using a bench-top laboratory printer without the need for further special instrumentation, making it a relatively cheap and fast deposition method.

This section briefly describes the different fabrication processes tested for depositing conductive structures onto flexible Kapton film to produce NMR/MRI compatible sensors. Two categories of fabrication processes have been considered: 1) photolithography processes 3.1.1 that can be categorized to "mask and deposit methods" or "mask and etch method"; and ii) rapid prototyping process 3.1.2 where inkjet-printing is used (mask-free technique). By the end of the section, all processes have been compared with highlighting the processes used further for fabricating the NMR/MRI sensors.

3.1.1 Photolithography

Photolithography is the key fabrication technology in the semiconductor industry and mass production of silicon-based devices. Photolithography allows fabricating devices with resolutions down to several nanometers and is the leading operator behind the miniaturization trend known as Moore's law. Photolithography is an established micro-fabrication method that uses mostly UV-light for micro-structuring, hence also known as UV-lithography [49]. In its simplest form, a layer of photosensitive chemical is deposited on a base substrate, and a photon beam is used to transfer a pattern written on a photo-mask to the photosensitive layer [50]. A specific series of chemical treatments are then applied either for depositing another material in the exposure pattern onto the base substrate or etching the photo-mask pattern into the based substrate. Four different variants of the photolithography process have been tested to deposit structured conductive tracks on the Kapton foil: 1) lift-off process; 2) molding process ; 3) liquid photosensitive polyimide; and 4) wet etching process. The four tested approaches of photolithography are discussed below.

Lift-off micro-technology

Figure 3.1 summarizes the fabrication flow for the lift-off photolithography process. A 25 µm Kapton foil was utilized as the base substrate for the photolithography process. With a thickness of 25 µm, the base film is flexible enough to be rolled around the slender capillaries ($< 2\,$mm), satisfying the NMR/MRI applications, and simultaneously it can be mechanically handled through the fabrication process. To facilitate the Kapton foil handling during the lithography fabrication process, it was cut into the shape of a 100 mm wafer using an infrared laser cutter (VLS3.50, Universal Laser System). Then, it is laminated to a silicon wafer using a 2 µm ma-N 1420 negative photoresist layer (micro resist technology GmbH) to promote adhesion, spin-coated at 3000 rpm. The wafer with the laminated Kapton film was soft-backed at 80 °C for 1 min. Tiny air bubbles were observed between the silicon wafer and Kapton foil. However, the binding between the foil and substrate was enough to proceed with the subsequent processing steps. After rinsing the top side of the Kapton foil with acetone and DI water, a 2 µm layer of the negative photoresist ma-N 1420 was spin-coated on top of the foil. The wafer was then soft-baked on a hotplate at 100 °C for 2 min. After cooling down naturally, the coated negative photoresist was then structured by UV exposure at a dose of $680\,$mJ cm^{-2}. The photoresist was developed for 2 min using ma-D 533 s developer. The wafer was then cleaned with DI water and soft-backed at 80 °C for 1 min. 20 nm chromium and 60 nm gold layers were deposited on the wafer using the physical vapor deposition process (PVD, Univex 450) at deposition rates of $5\,$Å s^{-1} and $8\,$Å s^{-1}, respectively. The chromium layer is used to promote the adhesion between the foil and the gold layer. The patterned area on top of the sacrificial photoresist was then lifted off with acetone inside an ultrasonic bath for 5 min, followed by rinsing in IPA and DI water. Then the patterned region on top of the sacrificial photoresist was lifted off with acetone in an ultrasonic bath, then rinsed with DI water.

The deposited seed-layer (chromium and gold) using PVD results in a thin conductor layer with a thickness below 100 nm, which is not sufficient for RF applications. RF applications require a minimum thickness of the conductor; otherwise, the electric power suffers from high resistance. The required conductor thickness is calculated according to the operating frequency,i.e., the ^{1}H frequency at 11.7 T NMR
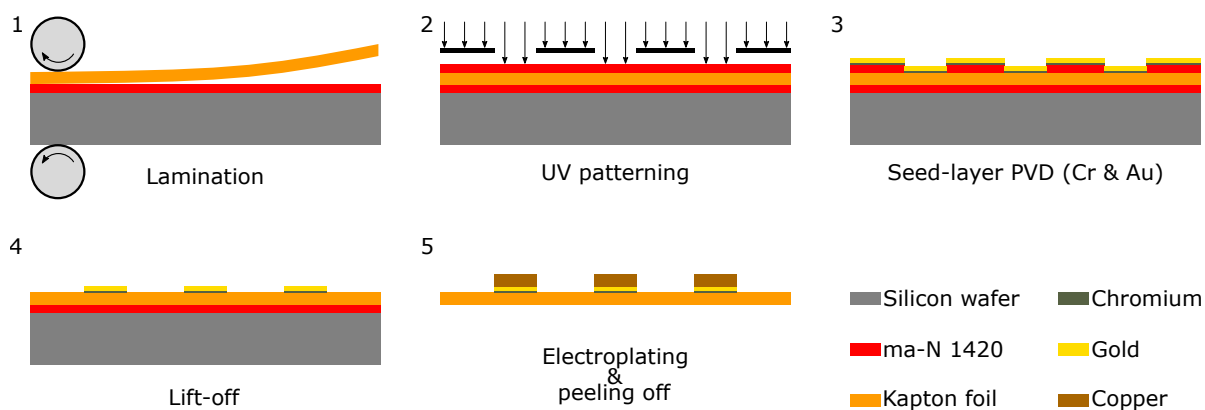
Figure 3.1: Schematic illustration of the lift-off micro-fabrication process. (**1**) Lamination of Kapton foil on a silicon wafer. (**2**) Patterning of a negative photoresist (ma-N 1420) layer using UV lithography. (**3**) Photoresist development and seed-layer deposition (Cr and Au). (**4**) Lifting off the sacrificial photoresist layer. (**5**) Peeling off the Kapton film from the silicon wafer and rinsing with acetone.

spectrometer is 500 MHz, thus, the copper tracks must be at least 6 μm thick. Hence, an electroplating process is employed to reach the required conductor height. However, electroplating results in peeling off most of the conductor layer from the Kapton foil. The solution for the electroplating problem is reported in Chapter 4. After electroplating, The film was finally peeled off from the silicon wafer and rinsed from both sides with acetone and DI water.

The lift-off is considered to be a relatively simple process as no etching is included. No aggressive chemical or plasma treatment is required that could affect the polyimide foil. However, the lift-off process suffers from some drawbacks. During the lift-off step, some unwanted parts of the deposited metal remain on the wafer as the resist below them was not removed. Moreover, some of the removed metal redeposited in random locations on the wafer and cannot be etched away easily.

The patterned structures on the wafer must all be connected for the electroplating process, as no common seed-layer connects the structures (i.e., during electroplating, the power source is connected to one point on the wafer where all structures need to be connected). Electroplating results in increasing the width of the tracks due to the absence of a mold.

Molding micro-technology

Figure 3.2 summarizes the fabrication flow for the molding photolithography process. A 25 μm Kapton foil was utilized as the base substrate for the photolithography process. The same lamination step is repeated as in the lift-off process to facilitate sample handling. The wafer was then soft-backed at 80 °C for 1 min. 20 nm chromium and 60 nm gold layers were deposited on the wafer using PVD. A 25 μm layer of the negative photoresist SU-8 3025 (micro resist technology GmbH) was spin-coated at 4000 rpm for 30 s on top of the gold layer to act as the electroplating mold. The wafer was then soft-baked on a hot plate at 95 °C for 13 min. After cooling down naturally, the coated negative photoresist was then structured by UV exposure at a dose of 400 mJ cm^{-2}. Then post-exposure bake was done at 95 °C for 4 min. The photoresist was developed for 30 min using a PGMEA developer. The wafer was then rinsed by immersion in isopropyl alcohol (IPA) for 30 min and then left to dry for 2 h at room temperatures. Electroplating
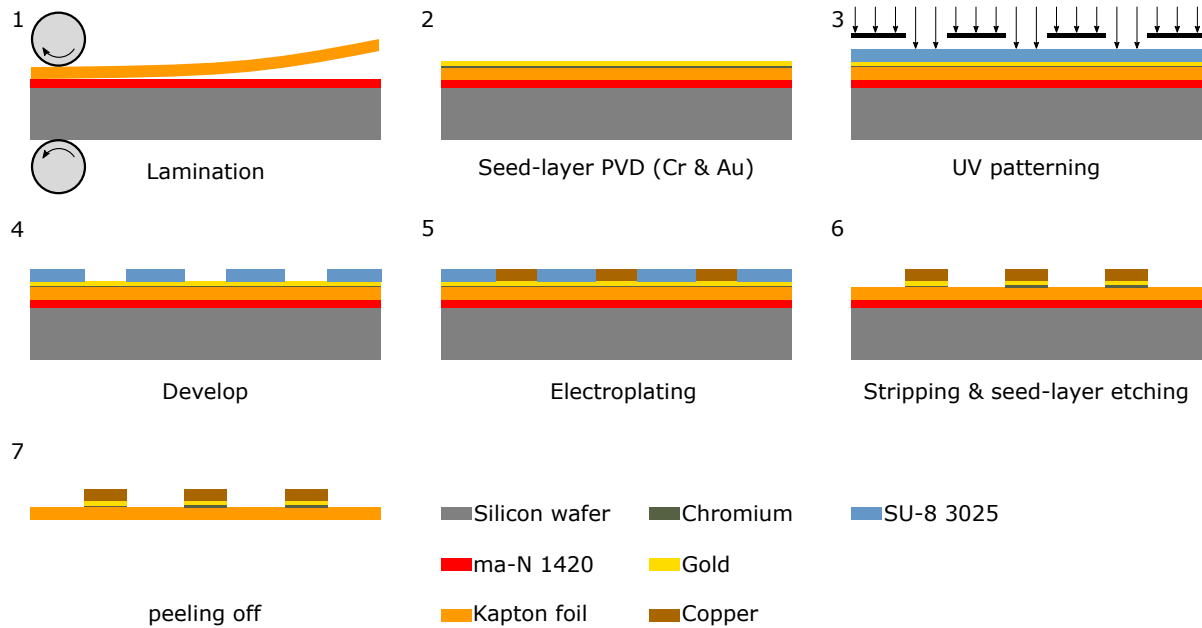
Figure 3.2: Schematic illustration of the molding micro-fabrication process. **(1)** Lamination of Kapton foil on a silicon wafer. **(2)** Seed-layer deposition (Cr and Au). **(3)** Patterning of a negative photoresist (SU-8 3025) layer using UV lithography. **(4)** Developing the negative photoresist to create molds for electroplating. **(5)** Electroplating process. **(6)** Stripping the negative photoresist and etching the seed-layer. **(7)** Peeling off the Kapton film from the silicon wafer and rinsing with acetone.

process was then conducted to reach the required conductor thickness. After electroplating, the SU-8 photoresist was stripped using R3T plasma etching. Then Au and Cr etching was done to remove the unused seed-layer, and the film was finally peeled off from the silicon wafer and rinsed from both sides with acetone and DI water.

The main advantage of the molding process is the presence of molds for the electroplating process. Hence, electroplating results in uniform tracks other than the lift-off process, where plating also occurs on the tracks' edges and sides. However, on the one hand, a stable photoresist is required to establish the mold to survive the electroplating bath. On the other hand, stripping this photoresist after electroplating usually requires aggressive plasma treatment, resulting in burning the polyimide foil.

Photosensitive polyimide

Other than the result of the studied process, a photosensitive liquid polyimide (LTC9310, FUJIFILM electronic materials) was used instead of foil polyimide. LTC9300 is a series of negative photoresist polyimide, where LTC stands for "Low Temperature Cure", it can be cured (from liquid to foil) by heating at $200\,°C$ other than standard PIs, which are cured with temperatures $> 350\,°C$.

Figure 3.3 summarizes the fabrication flow using liquid photosensitive polyimide. On the top of a silicon wafer, a 60 nm gold layer was deposited using PVD at deposition a rate of $8\,Å\,s^{-1}$. The gold layer was deposited in a way to keep the wafer border free from gold to promote adhesion between the silicon wafer and the polyimide that will be spin-coated in the next step. No chromium was added between the gold and the silicon wafer to facilitate the final step of peeling off the polyimide film with the gold layer.
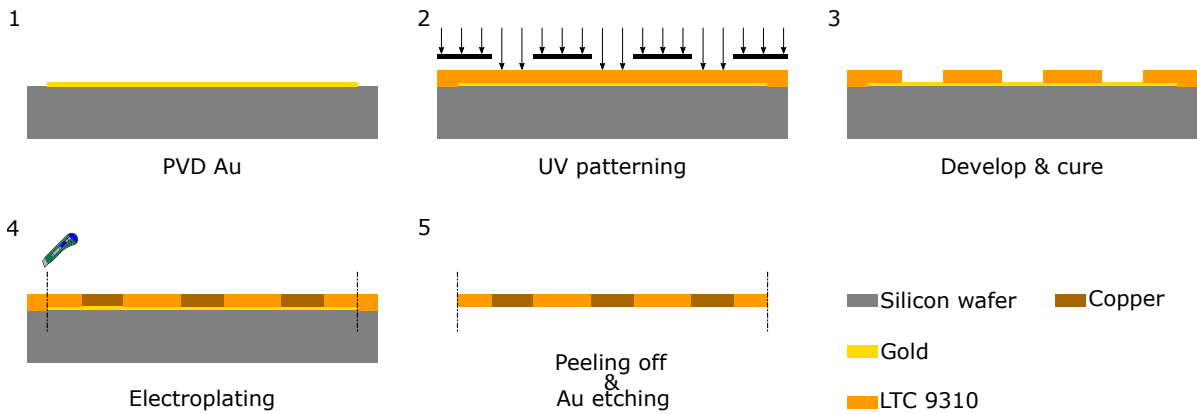
Figure 3.3: Schematic illustration of the liquid polyimide micro-fabrication process. **(1)** Seed-layer deposition (Au) with keeping the wafer border free to promote photosensitive polyimide adhesion. **(2)** Patterning of a negative photosensitive polyimide (LTC 9310) layer using UV lithography. **(3)** Developing the polyimide photoresist and cure in a vacuum oven. **(4)** Electroplating process and peeling off the cured polyimide film from the silicon wafer by cutting the border. **(5)** Etching the gold seed-layer from the polyimide film's backside.

On the top of the gold layer, a $30\,\mu m$ layer of LTC9310 was spin-coated at $1200\,rpm$ for $30\,s$. After soft-baking at $100\,°C$ for 4 min, LTC9310 was structured by UV exposure at a dose of $550\,mJ\,cm^{-2}$. The wafer was then continuously sprayed by QZ3512 (FUJIFILM electronic materials) for development and sprayed by QZ3501 for rinsing. The wafer was then transferred to a vacuum oven set to $250\,°C$ for 2 h, to cure the liquid polyimide into a flexible film with a thickness of around $20\,\mu m$. Electroplating process was then conducted to reach the required conductor thickness. Finally, the polyimide was peeled off by cutting the film around the wafer border. The polyimide film comes out with the gold layer from the backside, which can be easily etched away.

Using photosensitive liquid polyimide provides control over the polyimide film's thickness, which can be in a few μm range. Moreover, the structures can be embedded within the polyimide film, as in the process described here. In Chapter 6, this process was used to realize multilayer structures where vias were created within the polyimide film.

One of the difficulties facing this process is to predict the exact thickness of the final polyimide film since after curing, the thickness of the deposit polyimide reduces. This fabrication process's overall yield is not high as curing/electroplating can remove part of the polyimide from the silicon wafer.

Wet etching micro-technology

Figure 3.4 summarizes the fabrication flow for the wet-etching photolithography process. A $25\,\mu m$ Kapton film covered from a single side with a $9\,\mu m$ copper layer (AkaFlex KCL 2-9/25 HT, Krempel GmbH) was utilized as the base substrate for the photolithography process. The same lamination step is repeated as in the lift-off process except for the adhesive layer between the foil and the silicon wafer where a $3.3\,\mu m$ AZ4533 photoresist layer (Micro-Chemicals GmbH) was used, spin-coated at $4000\,rpm$. The wafer was then soft-backed at $95\,°C$ for 1 min. No air bubbles were observed between the Kapton foil and the silicon wafer, unlike the ma-N 1420 photoresist. To promote photoresist adhesion on the cop-
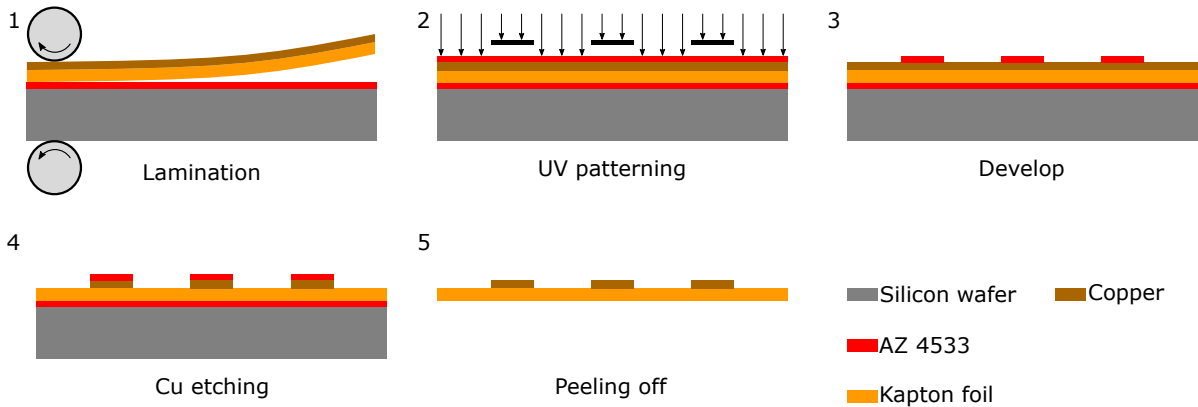
Figure 3.4: Schematic illustration of the wet etching micro-fabrication process. **(1)** Lamination of Kapton foil (covered with a copper layer) on a silicon wafer. **(2)** Patterning of a positive photoresist (AZ 4533) layer using UV lithography. **(3)** Developing the positive photoresist. **(4)** Copper layer wet etching. **(5)** Peeling off the Kapton film from the silicon wafer and rinsing with acetone and DI water.

per layer, the film was cleaned by etching the top layer of the copper surface by dipping the wafer into a sodium persulfate solution ($Na_2S_2O_8$, $240\,g\,L^{-1}$) for 15 s. After the etching process, the wafer was rinsed with DI water and dried with a pressurized nitrogen stream. Directly after the rinsing process, a $3.3\,\mu m$ layer of the positive photoresist AZ4533 was spin-coated on top of the copper layer to prevent oxidation. The wafer was then soft-baked on a hotplate at $95\,°C$ for 1 min. After cooling down naturally, the coated positive photoresist was then structured by UV exposure at a dose of $235\,mJ\,cm^{-2}$. The photoresist was developed for 3 min using a KOH-based AZ400K developer, prepared at 1:4 dilution. The wafer was then cleaned with DI water and soft-backed at $115\,°C$ for 2.5 min. The wafer was then immersed in the sodium persulfate solution for etching the exposed copper layer. The film was finally peeled off from the silicon wafer and rinsed from both sides with acetone and DI water.

This fabrication process's overall yield is very high (nearly 100%), owing to the standard processes used. Over etching reduces the track width, thus, the sample should be carefully observed during etching.

3.1.2   Inkjet-printing

Employing an additive manufacturing process in flexible electronics fabrication, such as inkjet-printing of conductive polymers on an unstructured fixable substrate, plays an essential role in research as well as in industry [51]. The global market size of printed electronics was valued at $7.8 billion in 2020 and is expected to have a bright future with an annual growth rate of 21.5% to reach a value of $20.7 billion by 2025 [52]. The global demand for low-cost, energy-efficient, thin, and flexible customize electronics is the main driving power for the printed electronics market's growth. Many versatile electronic components have been realized by printing, ranging from simple components such as resistors, capacitors, and indicators [53] to more complex devices such as diodes, transistors [54,55], displays [56], batteries [57], and microelectromechanical systems (MEMS) [58]. The inkjet-printing method is compatible with roll to roll process [59,60], which is used to achieve relatively high production rates.

Inkjet-printing of conductive polymer on polyimide substrates (few microns thickness) enables low-cost, highly flexible, lightweight, and yet complex electronic components. Via inkjet-printing, the conductive material can be precisely positioned using computer-aided tools without the need for a mask or subsequent etching processes, reducing the processing time and consumed materials [61–65], making the method both economically and ecologically attractive. The conductive material can be inkjet-printed as nanoparticles (NP) [66, 67] or metallo-organic decomposition (MOD) [68] inks. Silver nanoparticle inks are commonly used with the inkjet-printing method, enabling conductive tracks down to $\approx 30\,\mu m$ in width. A $25\,\mu m$ wide silver tracks have been successfully inkjet-printed onto an unstructured polyimide substrate [67].

Following printing, the conductive ink requires to be sintered to get rid of the solvent content, which typically demands high temperatures ($> 150\,°C$) for a duration of more than $30\,min$, limiting the materials that may be used as a substrate. Alternative low-temperature sintering techniques have also been considered [65] but have not yet become mainstream. Since the inks contains a relatively large percentage of solvent that evaporates, inkjet-printed and sintered conductors have thicknesses in the range of hundreds of nanometers. Hence, electroplating is an essential step for RF applications.

Throughout the whole thesis, Fujifilm Dimatix DMC-2800 printer was used for printing, loaded with a $10\,pL$ print head-cartridge (DMC-11610, Fujifilm Dimatix) filled with silver nanoparticle ink. The used ink was 30–35 wt.% suspension of silver nanoparticles (Sigma-Aldrich®) with diameters$\leq 50\,nm$ dispersed in triethylene glycol monomethyl ether. The silver ink is rated with a surface tension of 35-$40\,mN\,m^{-1}$ and a viscosity of 10-18 mPa s at room temperature.

The print head-cartridge posses 16 printing nozzles with an integrated heater. The control pulse supplied for all nozzles has the same waveform, but voltage levels can be controlled for each nozzle individually. The ink should have a viscosity of 10-12 mPa s and surface tension of 28-33 $mN\,m^{-1}$ at jetting temperature to achieve optimum printing performance. For high viscosity inks, the ink printability can be tuned by adjusting viscosity using the integrated heaters, which can heat the ink at the nozzle outlet up to $70\,°C$.
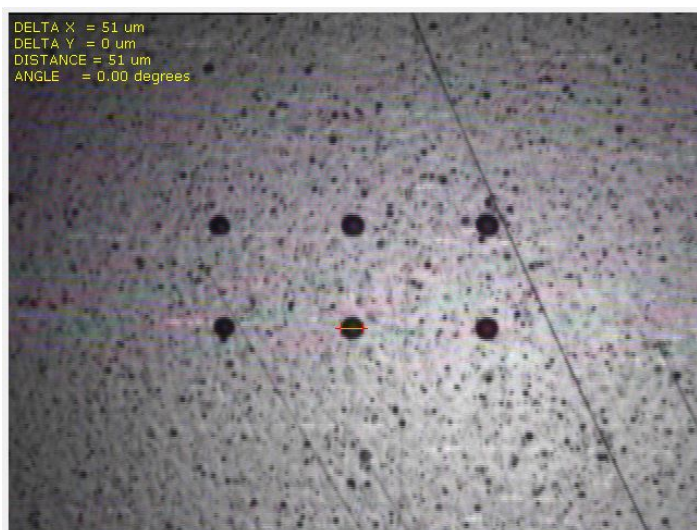

Figure 3.5: Printed droplets of silver ink. The droplet diameter was measured to be $51\,\mu m$, therefore, the dot spacing was set to $25\,\mu m$.
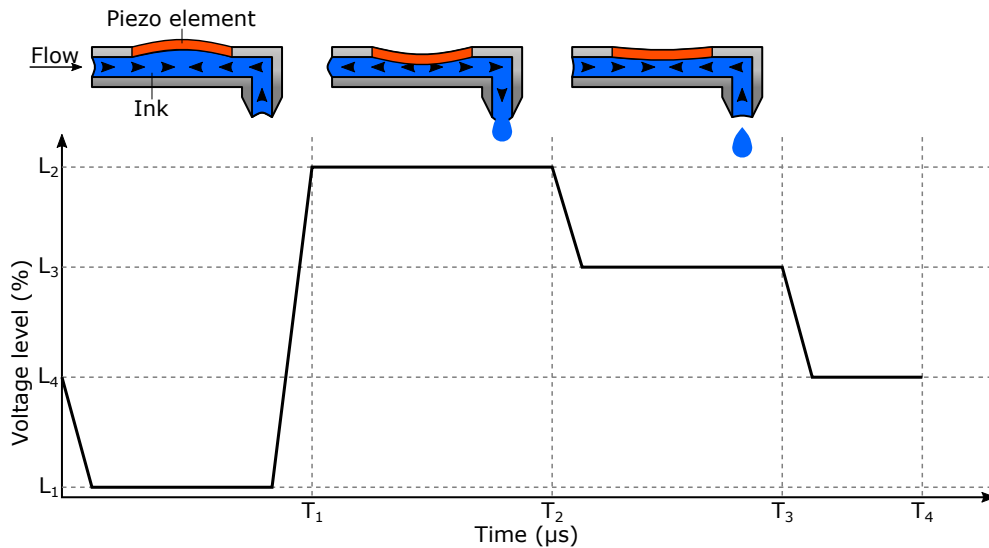
Figure 3.6: Inkjet-printing typical jetting waveform. The jetting waveform divided mainly into four consecutive phases: **(1)** Bending of the PZT element outward to draw ink; **(2)** Bending the PZT element inward to eject the ink; **(3)** Reducing the PZT element bending to release the droplet; **(4)** Resetting to the initial position to prepare for pulling the ink for the next droplet.

The dot spacing is set based on the droplet size, where every two successive droplets should half overlap to result in a uniform printed lines. Otherwise, if the dot spacing was small will result in the accumulation of the ink, and in case the dot spacing is wide will result in a wavy line. Figure 3.5 shows separately printed droplets of the silver ink. The average droplet diameter was measured to be 50 µm, therefore, the dot spacing was set to 25 µm, resulting in printable minimum line width of ≈ 60 µm. The droplet size can be controlled by optimizing the jetting waveform supplied to the printing nozzles. The printing nozzle
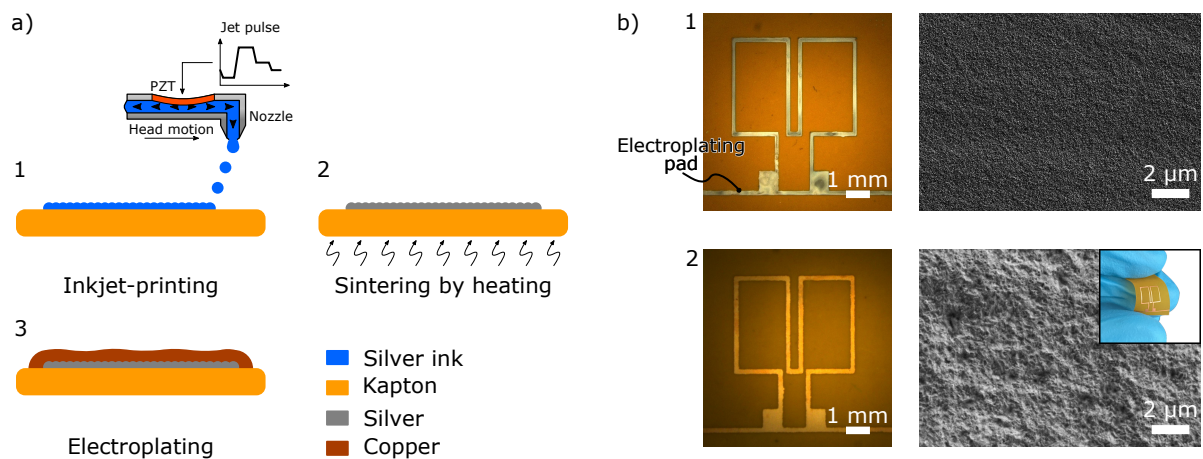
Figure 3.7: Inkjet-printing fabrication process flow and result. **(a)** Schematic illustration of the inkjet-printing process: (1) Silver ink printing; (2) Sintering the silver ink by heating; (3) Electroplating by a layer of copper to increase the printed track thickness. **(b)** Saddle coil fabricated using inkjet-printing. The coil is shown after (1) Printing and (2) Electroplating. The SEM images of the printed silver and electroplated copper are demonstrated.

contains a piezoelectric element (PZT) whose deflection is controlled by the jetting waveform, which in turn controls the droplet formation. Figure 3.6 demonstrates the typical jetting waveform supplied to a printing nozzle with illustrating a PZT element in operation. The jetting waveform is divided mainly into four consecutive segments (draw, eject, release, reset). The used time and voltage parameters for silver ink printing were $T_1 = 3.264\,\mu s$, $T_2 = 3.84\,\mu s$, $T_3 = 3.392\,\mu s$, $T_4 = 0.832\,\mu s$, $L_1 = 0\%$, $L_2 = 100\%$, $L3 = 60\%$, and $L_4 = 27\%$.

Figure 3.7a summarizes the inkjet-printing process, demonstrating a printed saddle coil in Fig. 3.7b. During printing, the substrate plate and the printing head were maintained at room temperature. Before printing, the Kapton film was rinsed with acetone and DI water. After printing, the film with the printed tracks was transferred to a hot plate for drying at 80 °C for 15 min, followed by sintering in an oven at 150 °C for 1 h. Subsequently, electroplating was carried out.

3.1.3 Micro-fabrication processes comparison

According to the extensive study of the previously mentioned different fabrication process:

- The lift-off process was not further utilized due to metals redeposition and removal of some parts of the structure during the lift-off step.

- The molding process was also not considered further due to the polyimide film's burning during the photoresist stripping step.

- The photosensitive polyimide process and the inkjet-printing process were selected for fabricating the MRI micro-systems, as explained in Chapter 6. The photosensitive polyimide process was chosen as it gives the possibility to achieve multilayer flexible electronic devices. The inkjet-printing method was selected since complex devices could be achieved with saving time, material, and effort.

- The wet etching process was selected for fabricating flow sensors and NMR micro-systems, as explained in Chapter 9. The wet etching process was chosen as the required devices have simple single-layered patterns, also it's compatible with mass production on the wafer scale.

Table 3.1 summarizes the main advantages and disadvantages of each of the studied micro-fabrication processes. The comparison focuses on the observed adhesion strength between the deposited seed-layer and the polyimide film before electroplating, as it was one of the main selecting criteria for the fabrication process.

Table 3.1: Micro-fabrication processes comparison

Fabrication Method	Adhesion	Advantage	Disadvantage
Lift-off process	Weak	Relatively simple process as no etching is included; no aggressive chemical or plasma treatment.	Unwanted parts of the seed-layer remain on the wafer, and some of the removed metal re-deposited on the wafer. The electroplating process results in increasing the tracks' width.
Molding process	Moderate	Electroplating process results in uniform tracks due to the presence of molds.	Stripping the electroplating compatible photoresist using plasma etching results in the burning of the polyimide substrate.
Liquid polyimide	Moderate	Control the polyimide film thickness. Embed the structures within the polyimide film. Create features within the base polyimide substrate such as vias.	The exact thickness of the final polyimide film after curing is variable ($\pm 3\,\mu$m). This fabrication process's overall yield is low.
Wet etching process	Strong	Overall yield is very high (nearly 100%). Require particular polyimide substrate, pre-covered with the conductive layer.	Require special etching facilities. Over etching reduce the tracks' width.
Inkjet-printing	Weak	Rapid prototyping, low-cost, energy-efficient, multi-layer, complex structures, and simple process	Not compatible with mass production. The resolution of deposited tracks' width is less than that for the photolithography processes.

3.2   Metal-insulator-metal (MIM) flexible capacitor

3.2.1   Introduction

Capacitors are one of the most essential and extensively used electronic passive components in modern electronics, with an estimated global market size of \$18.8 Billion in 2020 and expected to reach \$23.5 Billion by 2027 [69]. Thin-film flexible capacitors are a fundamental unit in various applications such as wearable devices, bendable devices, rollable displays, and interventional medicine [70–73].

Thin-film capacitors could be realized using inkjet-printing as printing has been used for depositing

conductive as well as semi-conductive and insulating films [74, 75]. However, printing the insulating layer of metal-insulator-metal (MIM) capacitors still cannot satisfy the need for high quality and high density capacitors due to the absence of printable materials with high relative permittivity (ε_r). Increasing the density of the printed capacitors is essential to reduce chip sizes and costs.

The typical capacitance formula of a parallel plate capacitor can be expressed as,

$$C = \frac{\varepsilon_0 \varepsilon_r A}{d}, \tag{3.1}$$

ε_0 is the vacuum permittivity, ε_r is the insulating layer permittivity (dielectric constant), A is the overlapped surface area between the two metal plates, and d is the gap between the two metal plates (insulator thickness). Achieving high capacitance density by decreasing the insulator thickness leads to increased current leakage and low RF loss tangent [76–78]. The apparent solution for realizing high capacitance density with high performance is by integrating a high permittivity insulating layer [79–81]. Hence, developing a printable high permittivity ink is a must.

Polymer-based inks were commonly used for inkjet-printing the insulating layer such as PI [82], poly(4-vinylphenol) (PVP) [83], poly(methyl methacrylate) (PMMA) [84], and SU-8 [85]. Nonetheless, all of which offer very low dielectric constants in the range of 2 to 4.3. Increasing a polymer's dielectric constant is commonly done by adding ceramic fillers with high permittivity to the polymer [86]. This technique is widely used in different applications but recently started getting attention in the inkjet-printing field. Lim et al. printed a $BaTiO_3$-resin with an ε_r of 70 at 1 MHz [87]. However, an infiltration printing technique was followed, resulted in a thick insulator layer of 20 μm. Kang et al. dispersed $BaTiO_3$ in PVP, but because of the low ceramic content used (20 wt.%), PVP ε_r was just doubled from 3.6 to 7.4 [83]. Vesico et al. used HfO_2 based ink, showing an ε_r of 12.6 at 1 MHz [88]. Mikolajek et al. dispersed barium strontium titanate (BST) in PMMA enhancing ε_r to 55 at 1 kHz [89].

In the following section, two ceramic/polymer composite inks were prepared for inkjet-printing high permittivity and high quality MIM insulating layer. The inks preparation and capacitor printing are described, and the MIM printed capacitors' characteristics are measured and discussed.

3.2.2 Material and method

Benzocyclobutene (BCB) polymers (CYCLOTENE 3022-35, Dow Chemical) is used as the inks' base polymer for its significant advantages as perfect adhesion to substrates, high planarization, thermal and chemical stability, and being pinhole-free [90]. More importantly, BCB has a low dissipation factor of 0.0008 [91] compared to that of SU-8 (0.015) and polyimide (0.025). BCB is commonly used in high-frequency multi-chip modules [90] and chips packaging.

TiO_2 and $BaTiO_3$ were chosen as examples of Class I and Class II ceramic dielectric fillers, respectively, for their high chemical stability and dielectric constants. Class II ceramics have relatively high dielectrics (1,000 to >20,000) compare to Class I ceramics (5 to a few hundred), but Class I ceramics have a lower dissipation factor (<<0.01) than Class II (0.01 to 0.03) [92]. Commercially available $BaTiO_3$ (50 nm cubic powder, Sigma-Aldrich) and TiO_2 (Anatase, 25 nm powder, Sigma-Aldrich) NPs were used to prepare the dielectric inks. The smallest available NPs were used to get smooth surfaces.

Each of the ceramic NPs (TiO$_2$ and BaTiO$_3$) were dispersed into the BCB polymer with two different concentrations (20wt.% and 40wt.%). Each ink was stirred at room temperature using a thermal shaker (Thermo shaker LLG-uniTHERMIX 1 pro) for 3 h at 1500 rpm. The viscosities of the inks were adjusted to 11 mPa s using Mesitylene (98%, Sigma-Aldrich) solvent to meet the inkjet-printing required viscosity (10-12 mPa s). The viscosities were evaluated at room temperature using a rheometer (Thermo Scientific HAAKE RheoStress 300) with a cone plate probe of 30 mm diameter. Figure 3.8 presents the measured viscosities of the prepared inks before adding the solvent. The viscosities (η) were measured as a function of shear rate ($\dot{\gamma}$). TiO$_2$ composites show higher viscosities than that of BaTiO$_3$, especially at high concentrations. Figure 3.8 shows photographs of the prepared inks after adding Mesitylene solvent to adjusts the viscosity. The inks were filtered before filling the inkjet printer's head-cartridge using a 0.45 μm pore size syringe filter. It was observed that the TiO$_2$ powder diffuse better than the BaTiO$_3$ powder in the BCB polymer, where less amount of TiO$_2$ remained in the filters than BaTiO$_3$.

Printing was done directly onto a 25 μm Kapton film. Piezoelectric cartridges of a 10 pL droplet volume and a total capacity of 1.5 mL were used. The BCB inkjet-printed droplet diameter was measured to be ≈ 105 μm (see Appendix A for a photo of printed droplets and lines of BCB), therefore, the dot spacing was set to 50 μm, and the same jetting waveform for the silver ink was used. Figure 3.9a summarizes the fabrication process flow and illustrates the dimensions of the printed MIM capacitor. Firstly, the bottom layer was printed using Ag ink with . Then the sample was dried on a hot plate at 90 °C for 15 min before printing the insulator to prevent layers dissolution. Before printing any of the dielectric inks, they were shaken for 30 min using a vibration shaker (Vortex-5 Shaker) to avoid sedimentation. The dielectric ink was then printed on the bottom layer and soft-backed using a hot plate at 90 °C for 15 min. The top conductive layer was then printed onto the top of the insulating layer and dried on a hot plate at 90 °C for 15 min. Three printed layers were required for the top layer to achieve a hole-free sheet. Finally, the device was hard-backed inside a vacuum oven at 200 °C for 1 h to remove any solvent content.
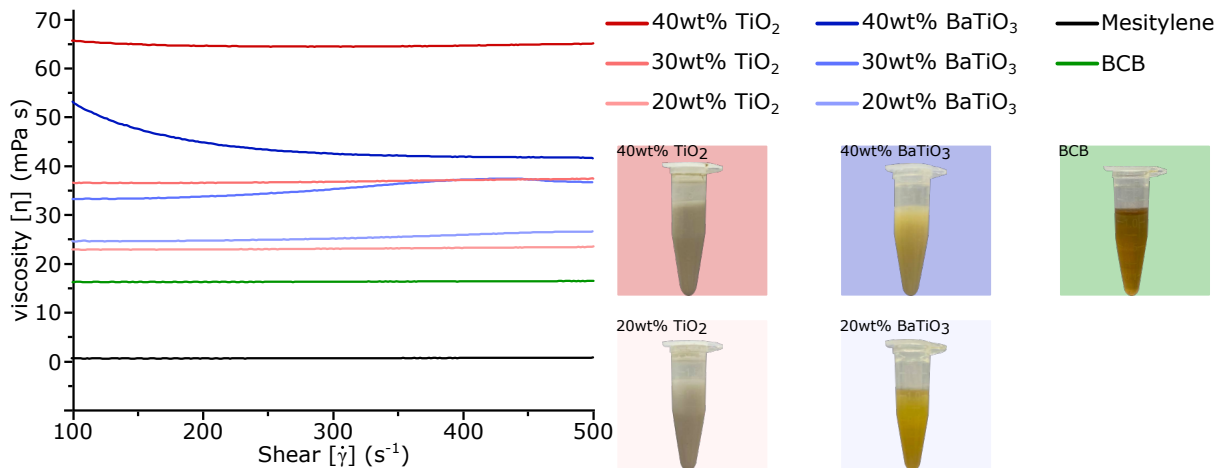
Figure 3.8: Measured viscosities of the prepared dielectric inks. The graph [left] presents the measured viscosities of the prepared inks before adding the solvent, as well as the viscosities of pure BCB (16.5 mPa s) and Mesitylene solvent (0.7 mPa s). The photographs [right] are of the prepared inks after adding Mesitylene solvent to adjusts the viscosity. TiO$_2$ powder was observed to diffuse better than BaTiO$_3$ powder in the BCB polymer.
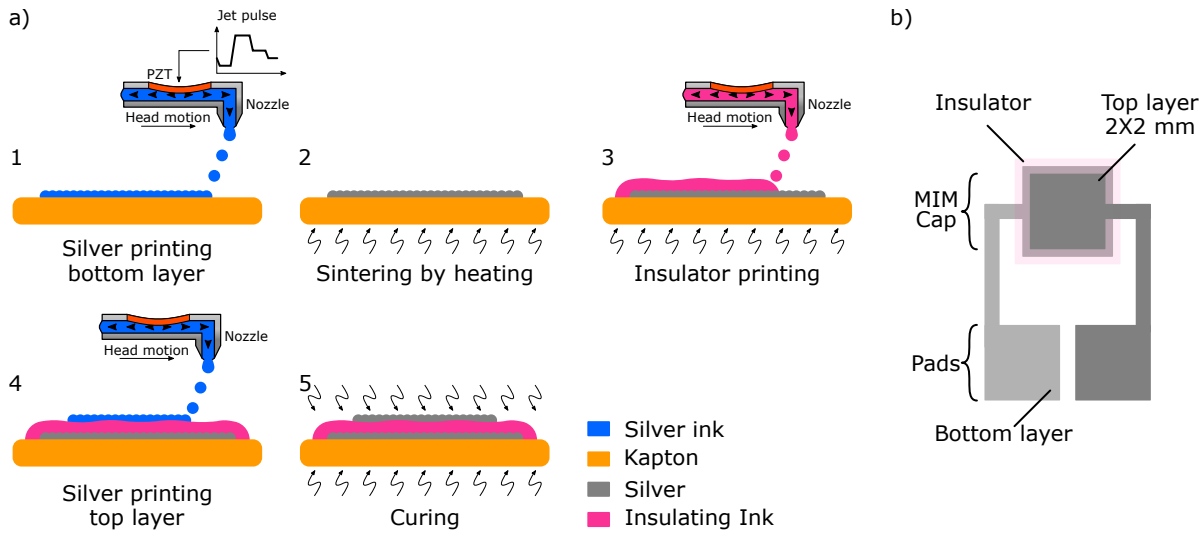
Figure 3.9: Inkjet-printing process of a metal-insulator-metal (MIM) capacitor. **(a)** Schematic illustration of the inkjet-printing process: (1) Bottom layer printing using silver ink; (2) Sintering of the silver ink by heating; (3) Insulating layer printing and sintering by heating; (4) Top layer printing using silver ink; (5) Curing of the device in a vacuum oven. **(b)** 2D schematic of the printed MIM capacitor. The printed parallel plate capacitor has an area of $4\,mm^2$.

The thickness, smoothness, and micro-structures of the printed layers were investigated using a chromatic white light interferometer (Bruker ContourGT-K 3D Optical Microscope) and a scanning electron microscope (Carl Zeiss AG—SUPRA 60VP SEM). The insulating layers' dielectric properties and the RF performance of the MIM capacitors were characterized using a network analyzer (E5071C, Keysight) connected to a probe station (MPS150, FormFactor Thiendorf, Germany) employing a Z-probe (Z0-20-K3N-GS-50, FormFactor Thiendorf, Germany). Measurements were done in ambient laboratory conditions.

3.2.3   Results and discussion

The roughness of the deposited insulating layer plays an essential role in defining the performance of the printed MIM capacitors; as the roughness of the deposited layer increases, the quality and the reproducibility of the capacitor decrease. Figure 3.10 presents SEM images and WLI measurements (2D and 3D) of the printed bottom silver and pure BCB insulating layers. The printed silver layer had a thickness and roughness of 470 nm and 73 nm, respectively. Printing one layer of the dielectric ink was not sufficient to prevent pinholes in the insulating film resulting in capacitors with a short circuit. Hence, at least three printed layers were required to avoid pinholes in the insulating film, resulting in a pure BCB layer with a thickness of 1.56 μm. The printed BCB layer was observed to be smooth with measured roughness of 69 nm. Dispersing ceramic fillers in the BCB polymer increases the deposited layer roughness, which reduces the quality factor of the printed capacitor. The minimum achievable thickness of the insulating layer is proportional to the percentage of the ceramic fillers' contents. The printed insulating layers using TiO_2 composite inks have rough surfaces (900-1250 nm) and a minimum film thickness in the range of 1.9-2.9 μm. On the other hand, the achieved insulating layers using $BaTiO_3$ composite inks
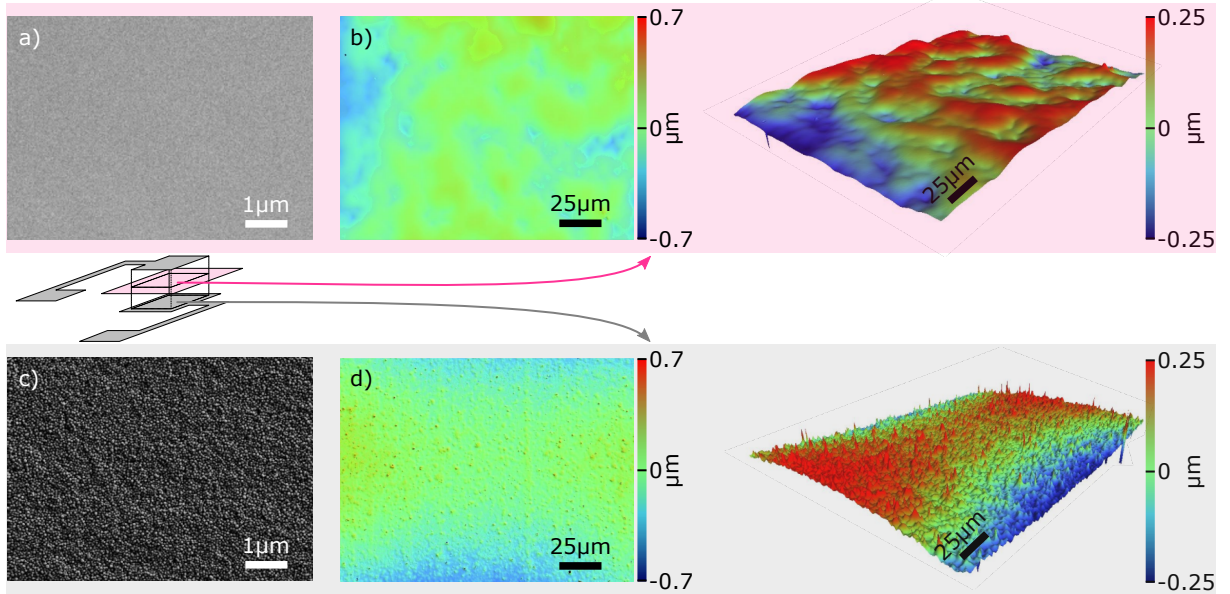
Figure 3.10: Surface morphology of inkjet-printed pure BCB insulating film and conductive silver layer. **(a)** and **(c)** Scanning electron microscope (SEM) images of the printed BCB and bottom silver BCB layers, respectively, with a magnification of ×20K. **(b)** and **(d)** White light interferometry (WLI) measurements with a focusing area of $131\,\mu m \times 174\,\mu m$. The roughnesses of the printed BCB and silver layer were 69 nm and 73 nm, respectively.

have roughness in the range of 800-1000 nm and a thick film with thicknesses in the range of 4.5-5 µm. Table 3.2 summarizes the roughness, minimum thickness, and loss tangent (tan δ = 1/Q-factor); see Appendix A for the SEM image and WLI measurement of the insulating film resulted from printing each of the composite inks.

The effect of printing multi-layers of the insulating BCB ink on the capacitance, self-resonance frequency (SRF), and quality factor of the capacitors was studied. The measured impedance ($Z = R_C + jX_C$) was used to calculate the capacitance ($C = 1/2\pi f X_C$) and the quality factor ($Q = -X_C/R_C$) of the capacitors over a frequency range of 100 kHz to 2.2 GHz. Figures 3.11 and 3.12 show the measured capacitance and quality factor of MIM capacitors with different numbers of printed insulating layers. Besides inkjet-printing, two capacitors were prepared by drop-casting (DC) of BCB inks, one with modified viscosity of 11 mPa s and the other with the viscosity provided by the supplier of 16 mPa s. Increasing the number of printed insulating layers results in: i) reducing the capacitance as it is inversely proportional to the distance between the capacitor's two conductive plates, as explained in Equation 3.1; 2) increasing of the capacitor's SRF as it is inversely proportional to the capacitance ($f = 1/\sqrt{LC}$); and iii) enhancing the capacitor's quality factor, as increasing the gap between the parallel plates avoid any current leakages or pinholes. The effect of adding the ceramic fillers (BaTiO$_3$ and TiO$_2$) with different concentrations on the relative permittivity and quality factor was investigated. The relative permittivity was calculated by substituting Equation 3.1 with the measured capacitance, measured insulating film thickness using WLI, and the capacitor dimensions. The dimensions of the capacitors' bottom and upper conductive layers are 2.2×2.2 mm and 2×2 mm, respectively, resulting in a capacitor area of 4 mm^2.
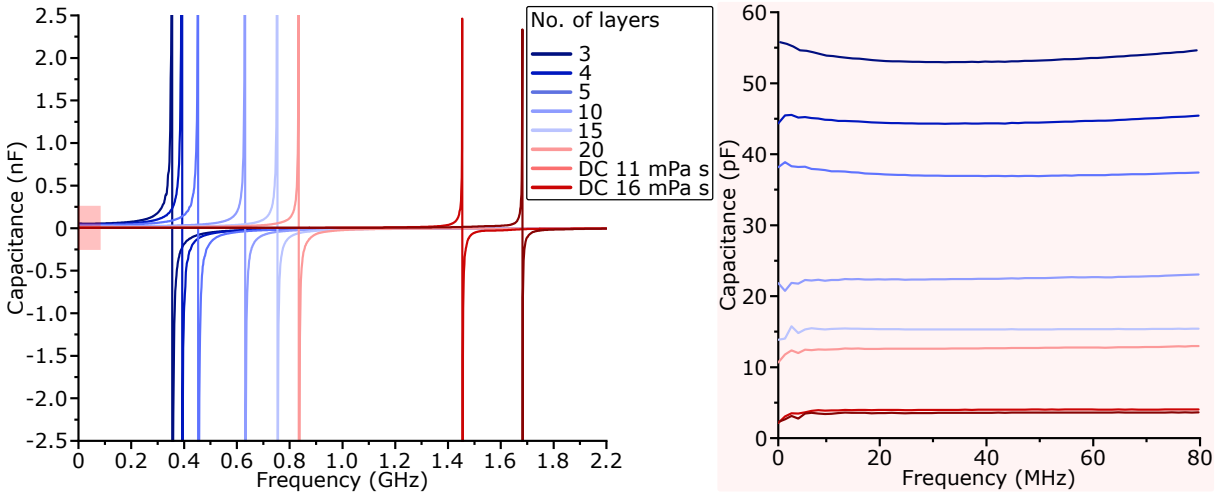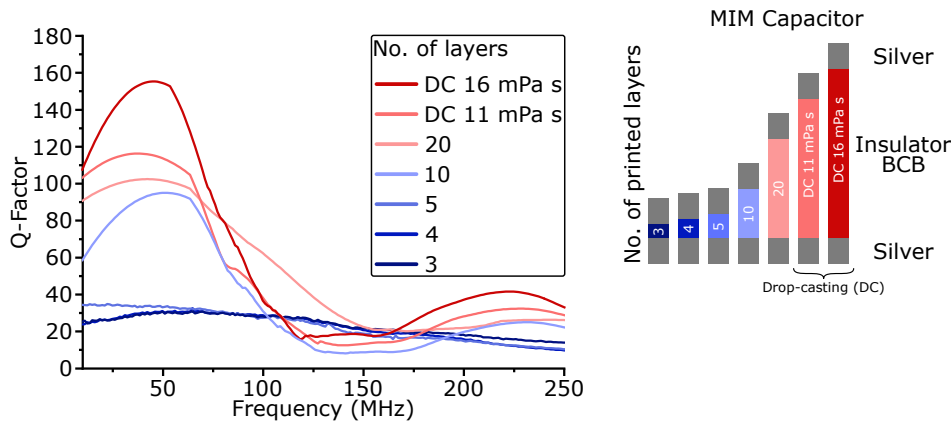
Figure 3.11: Effect of multi-layers printing and drop-casting (DC) of the insulating layer on the capacitance of a 4 mm^2 MIM capacitor. The capacitor's SRF increases as the gap between the two parallel plated increases since SRF is inversely proportional to the capacitance ($f = 1/\sqrt{LC}$). the Focused view [Left] show the capacitance at relatively low frequencies (100 kHz-80 MHz).

In the case of composite inks with 40wt.% concentration of BaTiO$_3$ and TiO$_2$, the relative permittivity of the BCB was enhanced from 2.3 to 37 and 20, respectively. The addition of the ceramic fillers leads to a decrease in the capacitor's quality factor since they increase the surface roughness; moreover, ceramic powders have higher dissipation factors than that of the BCB polymer. Dispersing of BaTiO$_3$ powder in the BCB polymers leads to less quality than adding TiO$_2$; however, BaTiO$_2$ leads to better enhancement in the relative permittivity. These results agree with the fact that TiO$_3$ belongs to Class I of the ceramic dielectrics, and BaTiO$_2$ belongs to class II [92]. Table 3.2 summarizes the measured parameters of the developed composite inks and composite inks from literature for comparison.

Figure 3.12: Effect of multi-layers printing and drop-casting (DC) of the insulating layer on the q-factor of a 4 mm^2 MIM capacitor. The quality factor increases at low frequencies as the gap between the capacitor's parallel plates increases. However, at wide gaps, the quality factor drops dramatically as the frequency increases.

Table 3.2: The measured parameters of the dielectric layers printed using developed composite inks - comparison with state of the art.

	Ink	Roughness (nm)	Thickness (μm)	Dielectric (ε_r) @1 MHz	tan δ (1/Q) @1 MHz	Cap. density[a] (pF mm^{-2})
This worK	BCB (3layers)	69	1.56	2.3	0.034	13.04
	BCB (20layers)	72	8.1	2.3	0.01	2.51
	20wt% TiO_2	972	1.9	7	0.04	32.6
	40wt% TiO_2	1217	2.8	20	0.037	63.2
	20wt% $BaTiO_3$	832	4.6	10	0.045	19.2
	40wt% $BaTiO_3$	994	4.9	37	0.052	66.8
Literature	$BaTiO_3$/resin [87]	-	20	70	0.011	30.9
	$BaTiO_3$/PVP [83]	-	1.06	7.4[b]	-	61.7
	HfO_2 [88]	-	0.4	12.6	0.0125	278.7
	BST/PMMA [89]	-	-	40[c]	0.06 [c]	-

[c] Calculated using insulating layer's thickness and dielectric coefficient

[b] The Measuring frequency isn't mentioned

[c] @ 0.1 MHz

3.3 Metal-semiconductor (MS) flexible diode

3.3.1 Introduction

Organic electronics in general and organic diodes, in particular, have attracted significant consideration for next-generation electronics due to their uncountable advantages as flexibility, scalability, light-weight, and applicability in numerous fields [93]. Organic diodes have been intensively investigated over the past decades, driven by commercial demands and improvement potential. Organic electronic components show their promising potential to be fabricated using rapid and cost-effective techniques that push toward an era of disposable electronics [94, 95].

Diodes are the primary building block in near field communication and wireless power transmission applications; they are employed as rectifying switches where high switching speeds between forward and reverse bias are required [96]. Schottky diodes are considered one of the simplest electronic components in the semiconductor industry; it consists of two parallel electrodes of different metals separated by a single layer of a p-type or n-type semiconductor, as shown in Fig. 3.13a. One of the metal/semiconductor (MS) interfaces presents low resistance current conduction, creating an ohmic contact. In contrast, the other MS interface is responsible for rectification by allowing charge injection in one bias direction and prevents it in the other direction creating a Schottky barrier (ϕ_B). In the case of a p-type semiconductor, the rectifying properties originate by bringing it in contact with a metal having a working function (WF) lower than the semiconductor's Fermi level (EF). The MS junction forces the two energy levels (metal's WF and semiconductor's EF) to align, leading to band bending and creating the Schottky barrier, as shown in Fig. 3.13c and d. The MS barrier height in Schottky diodes is lower than that of junction
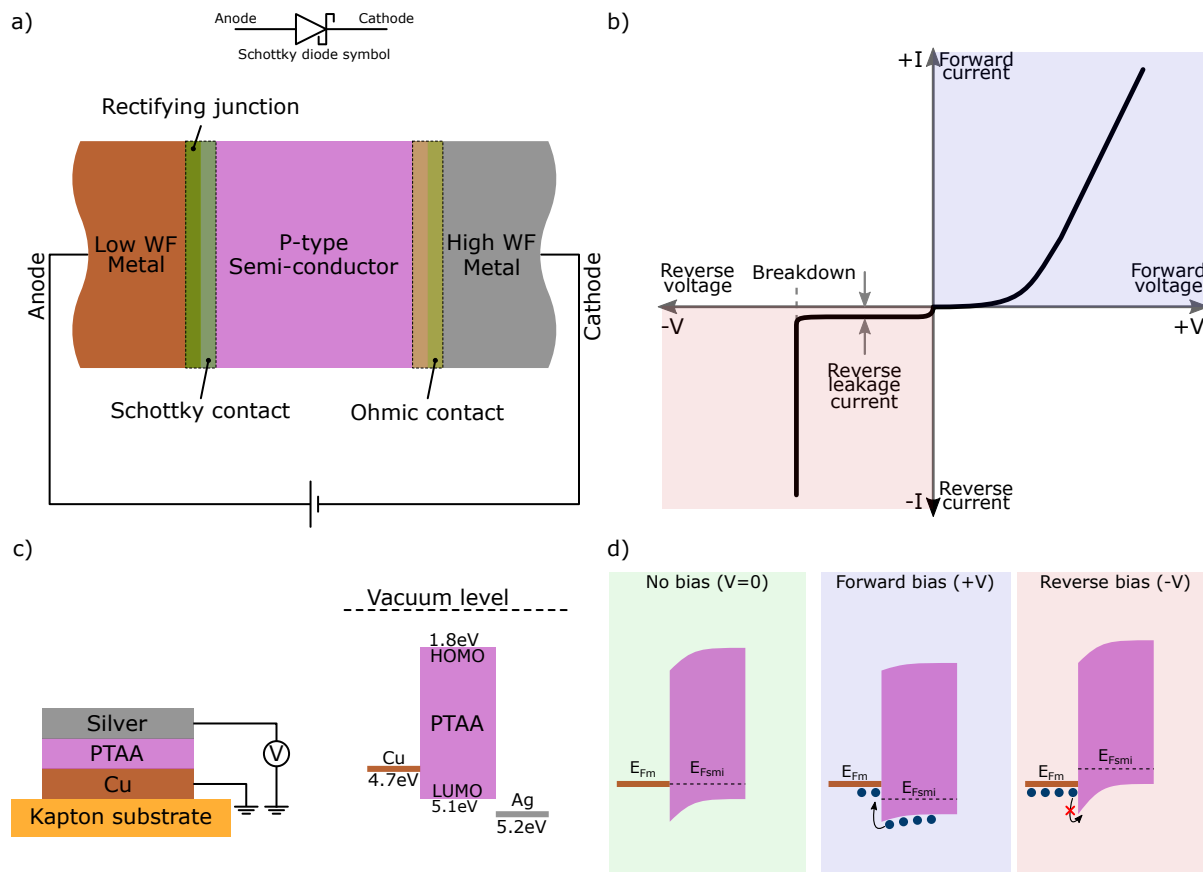
Figure 3.13: Schematic illustration of the working principle of the metal-semiconductor diode (Schottky diode). **(a)** Construction and symbol of the Schottky diode. The MS diode is constructed from a low WF metal, high WF metal, and p-type or n-type semiconductor. Based on the type of the semiconductor, one of the junctions creates ohmic contact (allow charge flow in both directions), and the other junction creates Schottky contact (has the rectification behavior. **(b)** VI-Characteristics of the Schottky diode. **(c)** [Right] coss-section view of the printed MS diode's structure. [Left] Energy band diagram showing the relative WF for copper (Cu), PTAA (p-type semiconductor), and silver (Ag) [Left]. **(d)** Energy band diagram of a Cu-PTAA-Ag diode under no, forward, and reverse biases. The arrows illustrate the holes' movement.

barriers in p–n junction diodes, resulting in a lower voltage droplet in the forward bias while allowing a higher forward current density. Moreover, the absence of a charge carrier depletion region in Schottky diodes eliminates the required reverse recovery time for switching the diode state from forward bias to reverse bias, leading to a higher switching frequency.

Schottky diodes based on vertical structures are the most compatible diode design with inkjet-printing [97]; vertical structures tend to reduce the lateral resolution requirement. Printed silver electrodes are always expected to create ohmic contact with a typical p-type organic semiconductor as silver features high WF ($\phi_M \approx -5.2\,\text{eV}$). However, printing a metal electrode with low WF to generate the Schottky barrier with organic semiconductors is still challenging. A low WF metal such as copper or aluminum is required for the Schottky diode's cathode electrode. Aluminum suffers from a high degree of oxidation, which leads to a forward voltage offset. On the other hand, copper does not suffer from the same degree of

oxidation as aluminum. Still, the available copper-based inks need aggressive post-treatments, making them incompatible with polymeric substrates and organic semiconductors [98, 99].

The following section demonstrates the fabrication of an inkjet-printed Schottky diode on an unstructured flexible polyimide substrate.

3.3.2 Method and results

The Schottky diode was printed directly onto an unstructured $25\,\mu m$ Kapton film. Silver NPs ink was used for printing the conductive electrodes. The low WF copper electrode was achieved by electroplating the printed silver electrode. The roughness of the plated copper layer can be controlled by employing pulse electroplating, as going to be discussed in Chapter 4.

Poly(triaryl amin) semiconductor (PTAA, Sigma-Aldrich®) was chosen as a p-type organic semiconducting with hole mobilities of 10^{-3} up to 10^{-2} cm^2 V^{-1} s^{-1}, resulting in high carrier mobility. PTAA was chosen for its excellent ambient air stability, not restricted to be used in an inert atmosphere like most other semiconductors. The PTAA's highest occupied molecular orbital (HOMO) and lowest unoccupied molecular orbital (LUMO) levels lie at $-5.0 \sim -5.1$ eV and $-1.8 \sim -2.0$ eV, respectively. Hence, PTAA is expected to create ohmic contact with printed silver ($\phi_M \approx -5.2$ eV) and Schottky contact with copper ($\phi_M \approx -4.7$ eV). A homogeneous solution of the PTAA was prepared by dispersing 2.0wt% of the polymer in toluene at room temperature. As the percentage of the PTAA to the solvent increases the operating frequency increases, due to the higher carrier mobility concentration. However, increasing the PTAA concentration leads to a cracked deposited layer. Hence, 2wt.% was found to achieve a hole-free layer (check Appendix A for spin-coated PTAA layers with 2.0wt.% and 5.0wt.% concentrations).
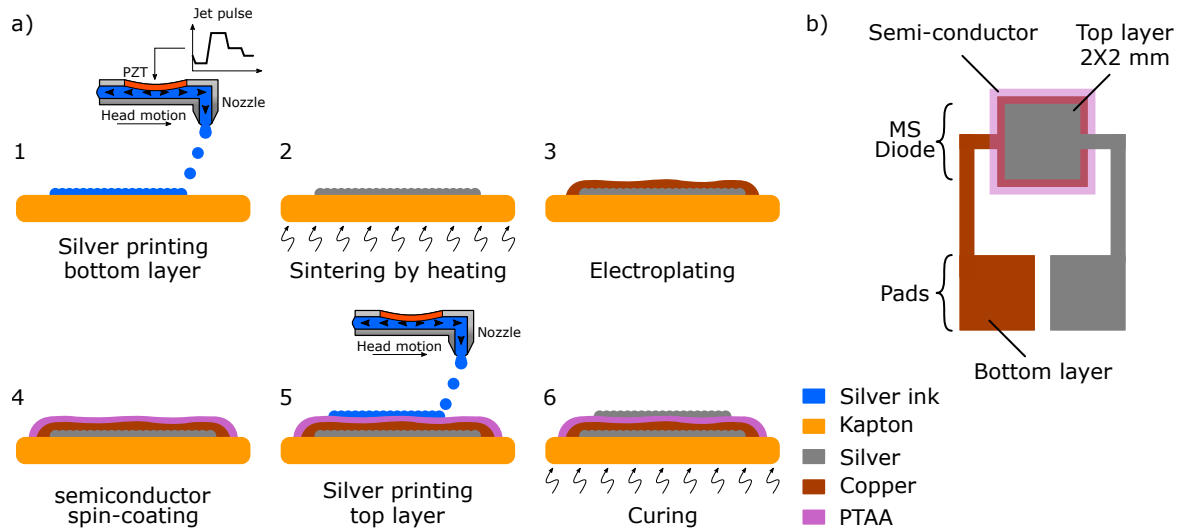
Figure 3.14: Inkjet-printing process of a metal-semiconductor (MS) diode. **(a)** Schematic illustration of the inkjet-printing process: (1) Bottom layer printing using silver ink; (2) Sintering of the silver ink by heating; (3) Electroplating of the bottom layer with copper; (4) Semiconductor layer spin-coating and sintering by heating; (5) Top layer printing using silver ink; (6) Curing of the device in a vacuum oven. **(b)** 2D schematic of the printed MS diode. The printed diode has an area of $4\,mm^2$.

Figure 3.14 summarizes the Schottky diode fabrication process flow. At first, the bottom layer was inkjet-printed directly on the Kapton film using silver ink. Then the sample was sintered using an oven at 150 °C for 1 h. The bottom silver layer was then electroplated with a 3 µm copper layer. Uni-polar pulse plating was implemented using a home-built power source (Section 4.3) to enhance the surface roughness. The plating waveforms are explained in detail in Chapter 4. On top of the copper electrode, a single layer of PTAA was spin-coated at 1000 rpm for 1 min and dried on a hot plate at 100 °C for 5 min. The top silver electrode was printed on the PTAA layer and dried on a hot plate at 90 °C for 15 min. For the top silver layer, at least three printed layers were required to achieve a hole-free sheet. Finally, the whole device was hard-backed in an vacuum oven 200 °C for 1 h to remove any solvent content. Vacuum ovens are generally recommended for hard-backing to prevent oxidation and help with gases extraction. Figure 3.15a shows a microscopic photo of the fabricated MS diode. The SEM images and WLI measurements of the spin-coated PTAA semiconductor layers and the bottom copper layer are shown in Fig. 3.15b and c. The spin-coated PTAA layer had a thickness and roughness of 410 nm and 52 nm, respectively.
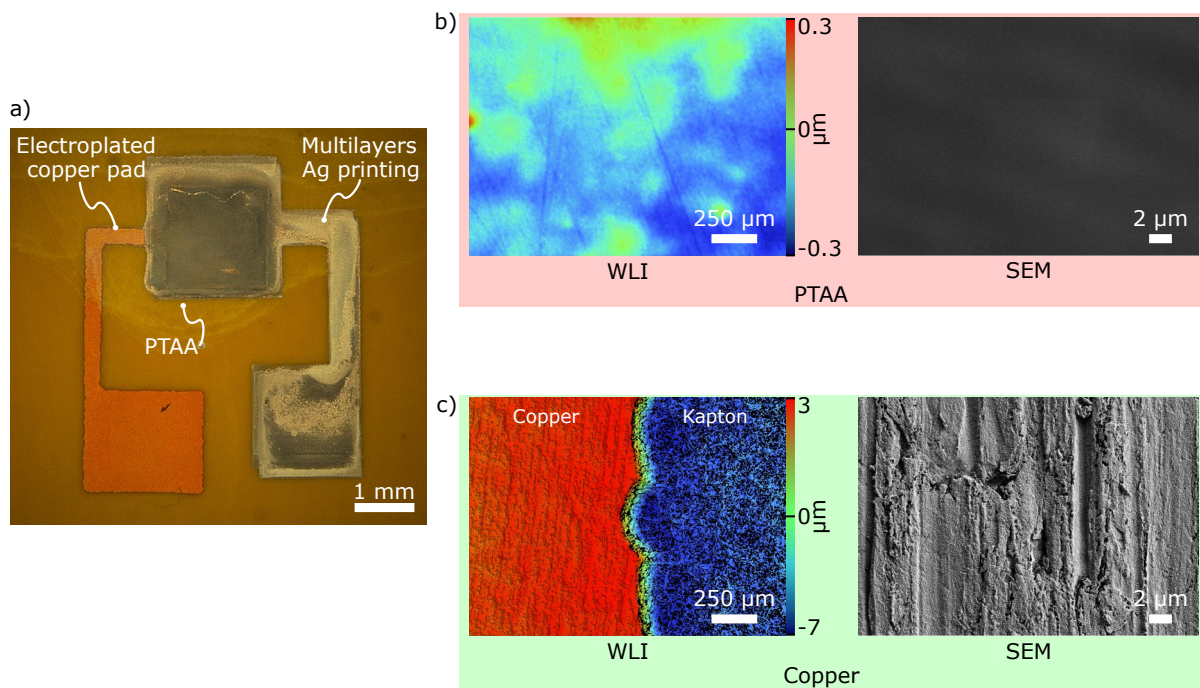
Figure 3.15: Fabricated MS diode using inkjet-printing. **(a)** Microscopic image of the fabricated MS diode. **(b)** SEM image and WLI measurement of the PTAA layer. The thickness and roughness of the PTAA layer were 410 nm and 52 nm. **(c)** SEM image and WLI measurement of the bottom copper layer. The thickness and roughness of the copper layer were 10 µm and 72 nm.

4 Electroplating[1]

Electroplating is a common technology in the area of micro-fabrication. Deposited seed-layers typically have thicknesses within the range of tens to hundreds of nanometers. Consequently, it results in high resistivity for applications that demand high electrical conductivity in DC to RF ranges. The high resistance generates Joule heat losses and affects the transferred electrical signal by introducing thermal noises. The high resistance of slender conducting tracks arises from the distribution of an AC signal throughout the conductor, where the current density is highest at the conductor's surface and drops exponentially with depth; this phenomenon is referred to as the skin effect. The current flows through the conductor's skin, which lies between the conductor's outside surface and a level known as the skin depth. The requisite minimum skin depth (δ) of the conductive tracks can be calculated using: $\delta = \sqrt{\rho/\pi f \mu}$, where f is the electrical signal's frequency, and μ and ρ are the permeability and resistivity of the conductive layer's material.

Electroplating has consistently shown its ability to coat different substrates with various materials efficiently. Pure metals, metal composites, alloys, conductive polymers, semiconductors, and oxides can be deposited via electroplating [100]. Due to the diverse applications of electroplating and its impact on the field of material science, it has been under investigation for the last centuries. Electroplating has been involved in multiple areas starting from the conventional ones as erosion, corrosion, and wear resistance [101], up to highly advanced applications such as micro and nano fabrication [61], integrated circuits [102], and thick-walled electroformed products (above millimeter) [100]. Electroplating is widely used in industry as well as in research due to its multiple benefits. Besides being low cost, rapid, and able to coat different substrates as well as controlled alloy composition, it results in pure free from pores structures with the range of mm down to nm [103, 104]. Manipulating the parameters involved in the electroplating process can control the deposited film features. Operating parameters such as applied current density, electrolyte bath temperature and composition, pH value, and additives provide control over the deposited film crystallite size, texture, and embedded film stresses [100].

This chapter focuses on controlling the deposited film features by controlling the waveform of the applied current density. Through the chapter, we also show the significant advantages of controlling the deposited film's micro-structures on the adhesion of inkjet-printed tracks onto an unstructured flexible substrate.

Generating current pulses for pulsed electroplating, especially with complex waveforms, typically requires complicated and expensive equipment compared to the conventional DC tools [105–107]. Hence, applications with more complex pulsed electroplating still face some difficulties and are seldom found in practice. In this chapter, we present an electroplating power source with high functional capability 4.3. The developed current source can be used for standard DC as well as complex pulsed electroplating. It can also be employed for galvanostatic and potentiostatic electroplating processes. The current source has been used for different complex applications, as demonstrated in the applications Sections 4.4 and 4.5.

---

[1]This chapter's text and figures were reproduced and adapted from the author's published work [ON1] with permission of the American Institute of Physics (AIP) Publishing (CC BY 4.0, 2019)

The fundamentals of the electroplating process presented in this chapter are mainly derived from the following two textbooks:

- **Modern Electroplating** by Mordechay Schlesinger and Milan Paunovic [100]

- **Electroplating: basic principles, processes and practice** by Nasser Kanani [108]

4.1 Electroplating working principle

By dipping a metal in an aqueous solution containing ions of that metal, ions exchange happens between the metal and solution. Some ions move from the crystal lattice structure of the metal electrode to the solution, and in return, some ions move from the solution to the metal's crystal lattice structure. Since the two ways of exchange happen at different rates, this leads to a potential difference. This potential interface difference for metal can be calculated according to the Nernst equation:

$$E = E^0 + \frac{RT}{zF} \ln a(M^{z+}), \tag{4.1}$$

E^0 is the relative standard electrode potential of the metal, R is the gas constant, T is the absolute temperature, z is the number of electrons in the reaction, F is Faraday constant, and $a(M^{z+})$ is the activity of the ion.

The relative standard electrode potential of metal can be measured by immersing the metal in a solution of its ions and connecting a reference electrode creating an electrochemical cell. Standard hydrogen electrode (SHE) is commonly used as the reference electrode since it has zero potential. The relative standard potential for electrodes of different materials is reported in the literature [109].
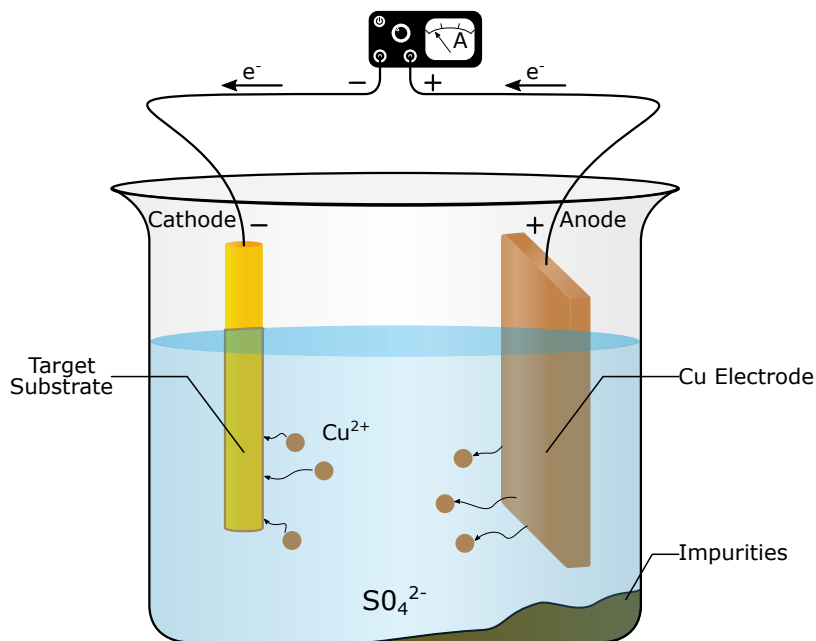
Figure 4.1: Schematic diagram of copper electroplating setup.

Electroplating a target conductive substrate with a particular ion can be achieved by immersing the substrate in a solution containing the ions of the desired metal and the plating metal electrode. A power source is used to force the ions to deposit from the plating electrode to the target substrate. The target substrate is connected to the cathode, and the plating electrode is connected to the anode, as shown in Fig. 4.1. Electrodeposition can be done in two manners, galvanostatic or potentiostatic. In the potentiostatic, the applied voltage is set to a constant level, leading to a current changing with time. In contrast, in the galvanostatic, the electric current is the controlled parameter leading to a continuous rate of deposition [106]. One of the common simple electroplating processes is copper electroplating, where at the anode copper is dissolved in copper sulfate ($CuSO_4$) electrolyte and at the cathode copper is deposited according to chemical formula [110]:

$$\text{At anode } Cu_{(dissolved)} \longrightarrow Cu^{2+} + 2\,e^-$$
$$\text{At cathode } Cu^{2+} + 2\,e^- \longrightarrow Cu_{(deposited)}$$
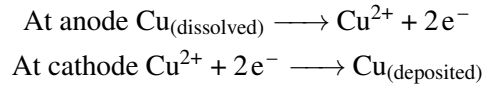
According to Faraday's law, the amount of electrochemical reactions within an electrochemical cell is proportional to the quantity of electric charge Q through the substance. For the accumulated weight w at the electrode in electrolysis, Faraday's law states the relationship:

$$w = Z \cdot Q, \quad \text{with} \quad Z = \frac{M}{z_i F} \quad \text{,and} \quad Q = \int i\,dt. \tag{4.2}$$

Z is the constant of proportionality and is known as the electrochemical equivalent, M is the molar mass of the substance, z_i is the valency of the ion, and F is the Faraday constant. The deposition rate can be within a wide range of $0.1\text{-}10\,\mu m/\min$. The deposit mass and thickness are calculated through Faraday's equations:

$$mass = \frac{\alpha I t M}{nF}, \tag{4.3}$$

α is the deposition efficiency, I the applied current, t the electroplating time, M Molar mass, n the charge state, and F Faraday's constant.

$$Thickness = \frac{M_a t}{Fn\rho}\varepsilon_f i, \tag{4.4}$$

i is the applied current density, M_a atomic weight, ρ metal density, n number of electron transfer in electroplating reaction, ε_f Faraday efficiency.

Three forms of current distributions impact metal deposition during the electroplating process: primary, secondary, and tertiary. The primary current distribution is influenced by the electroplating system's geometric aspects, especially the plated structures. Higher current densities are built at edges, resulting in more deposited metal around these areas leading to the well-known phenomena (dog boning). The secondary current distribution is the electron transfer associated with metal dissolving from the anode or depositing on the cathode. The tertiary current distribution is the ion's transportation within the electrolyte between the electrodes [106].

The deposition of metal can be modeled as a capacitor parallel to resistance, as shown in Fig. 4.2a. The capacitor represents the layer between the electroplated electrode (cathode) and the electrolyte, known as the electric double layer (EDL). The resistance represents the electrochemical reaction. When the power source is connected to the electrodes, the capacitive current I_C is used for charging the EDL. After the EDL is charged, the faradic current I_F deposits the metal. The deposition doesn't occur until the EDL is
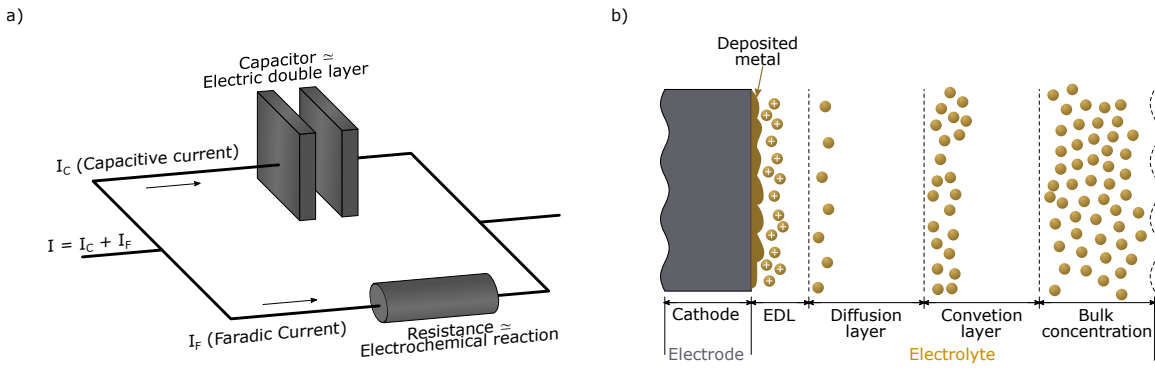
Figure 4.2: Equivalent electrical circuit and ion transportation of the electroplating process. **(a)** Schematic diagram of the electrode's equivalent electrical circuit [106, 111]. **(b)** Schematic diagram illustrating the different layers formed by the mass transportation of the ions from the anode toward the cathode within the electrolyte [112, 113].

charged. Turning off the power leads to the discharge of the EDL. The time is taken by I_F to reach 99% of the applied current (I_P) is the charging time (T_C). While the time taken by I_F to reach 1% of I_P is the discharging time (T_d) [114]. As a rule of thumb, the charging of the EDL is seven times faster than the discharging and can be roughly calculated by [115]

$$T_c = \frac{17}{I_P}, T_d = \frac{120}{I_P}.$$ (4.5)

4.2   Pulsed electroplating

Pulsed electroplating has drawn significant attention in research as well as in industrial fabrications. One of the first significant applications of pulsed electroplating was depositing gold toward switching crossover electronic circuits performed by Western Electric in the 1970s [116]. A reduction in the electroplating time by a factor of 2 was achieved when implementing pulsed electroplating compared to the conventional direct current electroplating. The timing parameter of pulsed electroplating of this application (on/off time is 0.1/0.9 s) is still used till today for soft gold deposition. Pulsed electroplating has been considered in other fields as well, e.g., in the field of optics, highly anti-reflective surfaces were achieved via the implementation of bipolar pulsed electroplating [117].

Modifying the current distribution with the electroplating bath results in controlling the deposited film's internal structure as well as its physical and mechanical properties. The current distributions within the electroplating bath can be modified either by adding chemical additives or employing pulsed electroplating [100]. However, it's preferable to limit the usage of the chemical additives for a more reliable electroplating process [118]. On the other hand, pulsed electroplating always shows its ability to control the deposited film properties without involving chemical additives. Furthermore, implementing reverse pulsed electroplating can replace the additives and eliminate the drawbacks resulting from using them [100].

Via pulsed electroplating, several features of the deposited material can be controlled, such as: the atomic
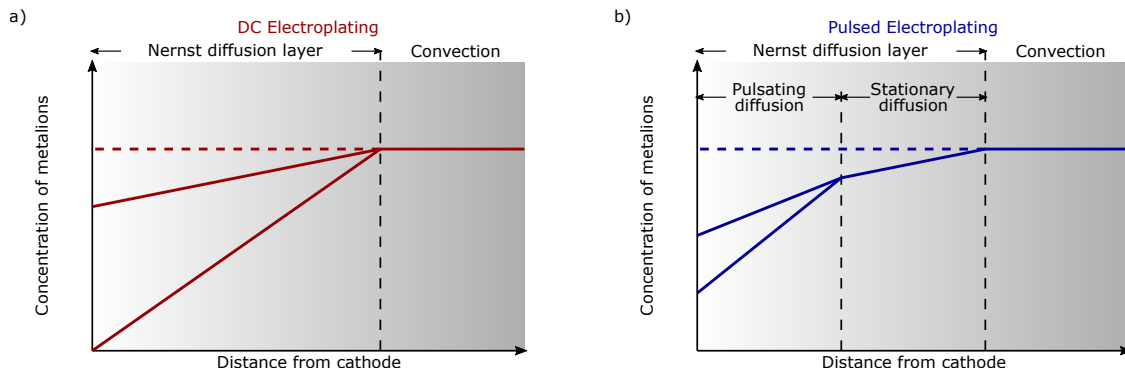
Figure 4.3: Diffusion layer within the electrolyte in case of direct and pulsed electroplating [106, 121]. **(a)** A single diffusion layer is formed in the case of direct electroplating. **(b)** The diffusion layer is divided into two layers by the pulsed electroplating, which results in a more uniform mass transportation and thus a more uniform metal deposition.

micro-scale structure [118], the grain size [ON1], the mechanical and physical properties of the deposited film [119], the surface roughness [ON1], and the hydrogen content [120].

Pulsed electroplating can be used to modify the diffusion layer, as shown in Fig. 4.3. In direct electroplating, a single diffusion layer is created. In contrast, pulsed electroplating leads to two diffusion layers, increasing uniformity in mass transportation, leading to a more uniform metal deposition and a better filling of holes and vias. The concentration of ions is constant with respect to the distance from the electrodes beyond the diffusion regions (bulk concentration) [106].

A passive negatively charged layer is built around the cathode during the DC electroplating. The formed layer hinders the ions from transferring uniformly toward the cathode. pulsed electroplating leads to a uniform transfer of the ions by discharging this built layer during the switch-off time. Moreover, applying the opposite polarity (reversed pulsed electroplating) reduces the discharging time [100, 105].

As discussed in the previous Section 4.1, the current density is not uniformly distributed within the electroplating bath, which leads to higher consumption of the ions in the spaces with high current density than that with lower current density resulting in a non-uniform deposition. Pulsating the applied current during the electroplating process allows the ions to transfer from high concentration to low concentration spaces leads to a uniform distribution of the ions within the bath hence a uniform deposited film.

4.2.1 Waveforms for pulsed electroplating

In pulsed electroplating, the applied current density is always alternating between different set-points, as shown in Fig. 4.4b and c. Other than the direct current electroplating, where the applied current density is set to a fixed value through the whole process as shown in Fig. 4.4a. The material's deposition rate and thickness in pulsed electroplating are equivalent to a DC electroplating operating at the average current density of the pulsed electroplating.

The pulsed electroplating processes are generally split into two categorize:
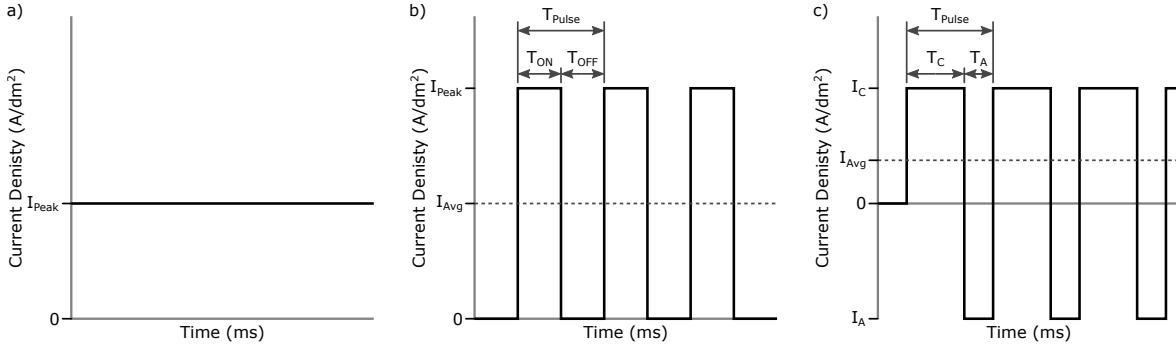
Figure 4.4: Main categories of the applied current densities Waveforms for electroplating. **(a)** Direct current pulsed electroplating. **(b)** Ordinary uni-polar pulsed electroplating. **(c)** Bipolar pulsed electroplating.

1. Uni-polar pulsed electroplating, also referred to as ordinary pulsed electroplating. In this category, all pulses have the same polarity and the applied current frequently oscillates between a positive state (I_{Peak}) and the off state, producing a sequence of pulses with similar duration and amplitude as shown in Fig. 4.4b. The duration of applied current is denoted as the on-time (T_{ON}), and the duration of the off-state is denoted as the off-time (T_{OFF}). The duty cycle of the pulse (γ) is the proportion of the on-time to the total pulse time (T_{Pulse}),

$$\gamma = \frac{T_{On}}{T_{On} + T_{Off}}. \tag{4.6}$$

The average current (I_{Avg}) is the actual applied value that is used for calculating the material depositions' rate and thickness. It can be calculated based on the peak current and the pulse duty cycle,

$$I_{Avg} = I_{Peak}\gamma. \tag{4.7}$$

2. Bipolar pulsed electroplating; also referred to as reverse pulsed electroplating. In this category, the applied current oscillates between values with different polarities. The applied waveform has a total time of T_{Pulse}. The cathodic part of the applied pulse with the positive polarity current is referred to as I_C operating for time T_C and the anodic part of the pulse has a negative polarity current referred to as I_A operating for time T_A, as shown in Fig. 4.4c. For bipolar pulsed electroplating, the duty cycle and the average current (I'_{Avg}) of the pulse can be calculated by:

$$\gamma' = \frac{T_A}{T_A + T_C}, \tag{4.8}$$

$$I_{Avg}' = \frac{I_A T_A - I_C T_C}{T_A + T_C}. \tag{4.9}$$

Besides the ordinary pulses, more complex waveforms have been investigated in the past [105, 107, 122], some of which are presented in Fig. 4.5 and Fig. 4.6. These waveforms provide higher control over the deposited materials. For uni-polar pulsed electroplating, the other candidates were:

1. Superimposed pulses, where the pulses are built on top of a constant value.

2. Duplex pulse, where the pulse is composed of sub-pulses with different current densities.

3. Pulsed pulse, where each pulse is composed of a group of sub-pulses.

4. Pulsed on the pulse, where each pulse has a series of sub-pulses built over a constant value.

For bipolar pulsed electroplating, the other introduced waveforms were:

1. Reverse pulse with off period, where the bipolar pulses are separated with off time.

2. Reverse duplex pulse, where the pulse is composed of bipolar sub-pulses with various current densities.

3. Reverse pulsed pulse, where each polar pulse is composed of a group of sub-pulses.

4. Reverse pulsed on pulse, where each polar pulse is formed of sub-pulses built over a constant value.
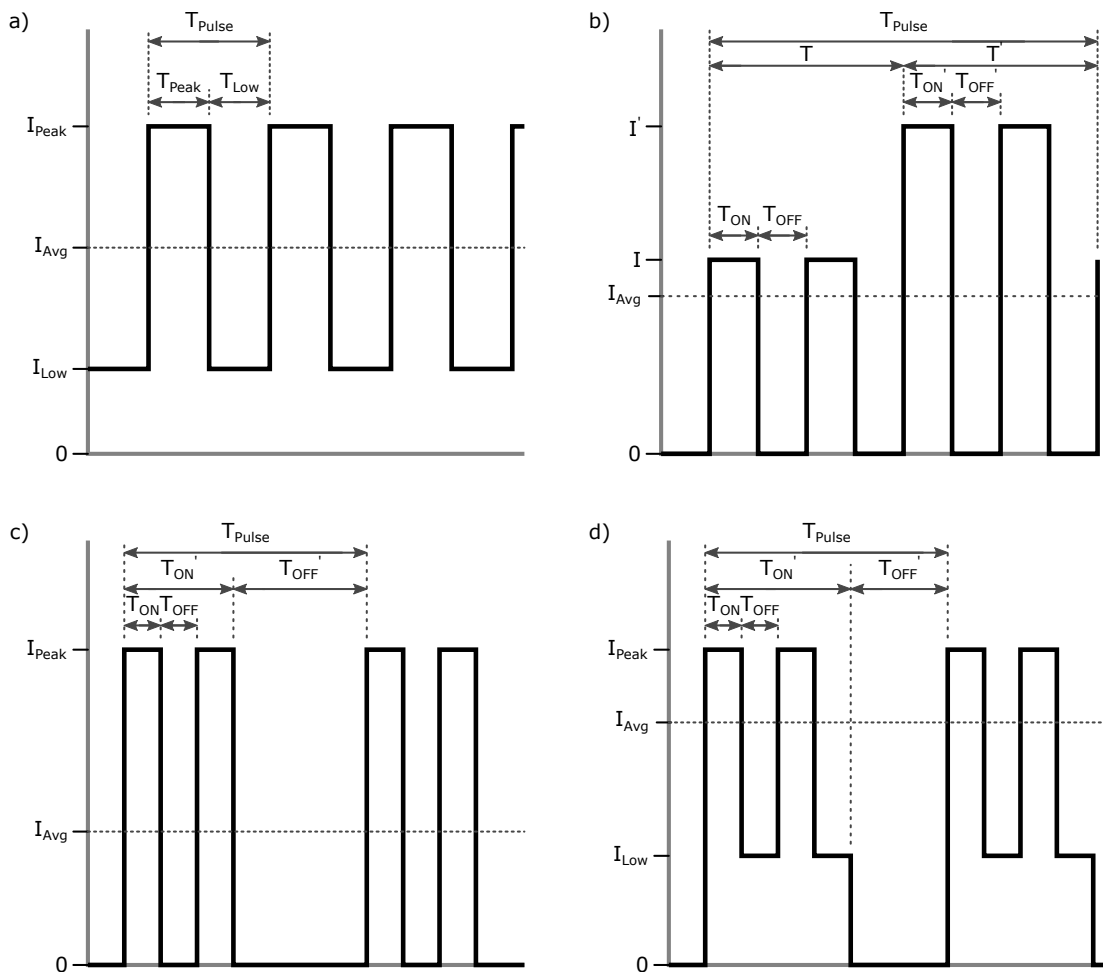
Figure 4.5: Different complex waveforms introduced for uni-polar pulsed electroplating. The candidates for uni-polar pulsed electroplating are **(a)** Superimposed pulse, **(b)** Duplex pulse, **(c)** Pulsed pulse, and **(d)** Pulsed on pulse. For all curves, the Y-axis is the current density (J), and the x-axis is the time (T).
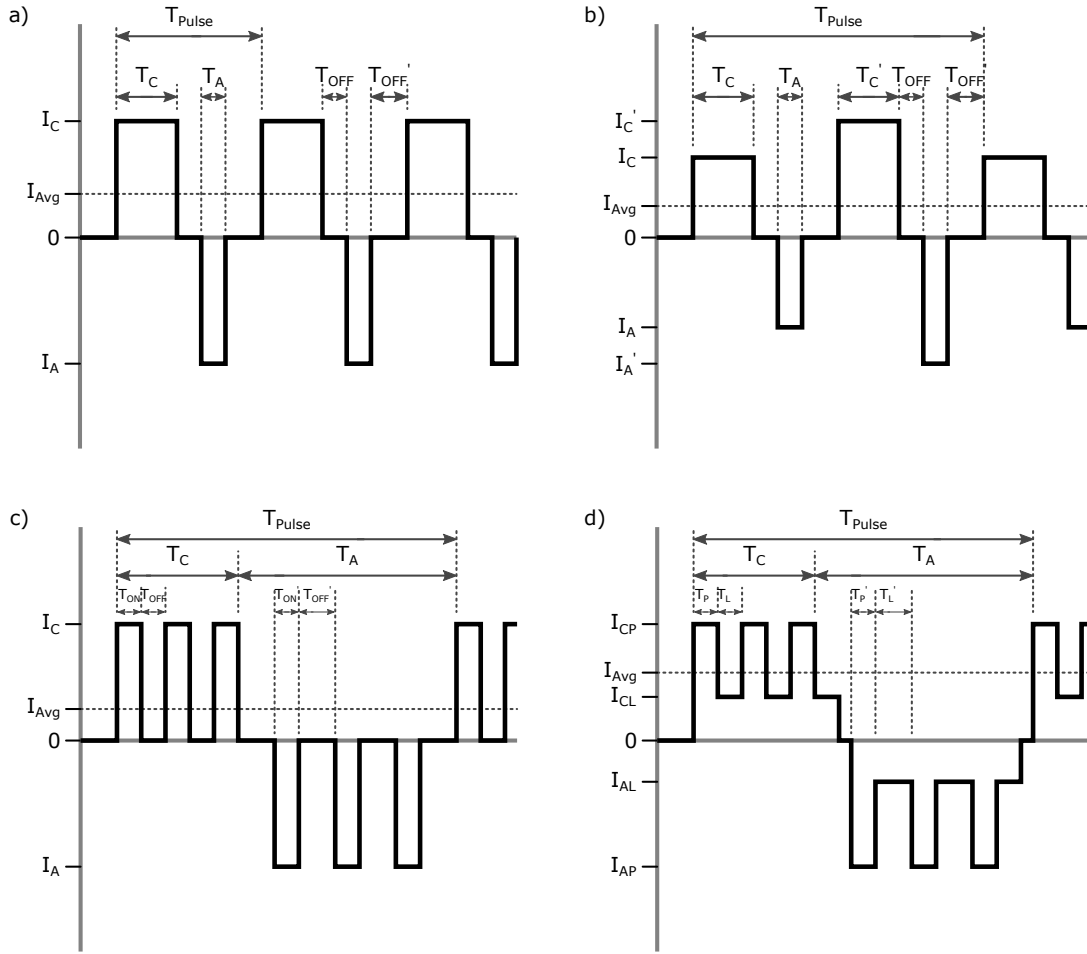
Figure 4.6: Different complex waveforms introduced for bipolar pulsed electroplating. The candidates for bipolar pulsed electroplating are (**a**) Reverse pulse with off-time, (**b**) Reverse duplex pulse, (**c**) Reverse pulsed pulse, and (**d**) Reverse pulsed on pulse. For all curves, the Y-axis is the current density (J), and the x-axis is the time (T).

For pulsed electroplating, typically, the pulse duration are in the range of milliseconds with a duty cycle $> 5\%$ to be enough for the EDL to charge and the deposition happens. For any of the mentioned complex waveforms in Fig. 4.5 and Fig. 4.6, the average current density can be determined by dividing the integration of the applied current through a single full pulse over the total pulse time,

$$I_{Avg} = \frac{1}{T_{Pulse}} \int_0^{T_{Pulse}} I(t)dt. \tag{4.10}$$

4.3 Electroplating tool: current source

Generating the complex waveforms mentioned in the previous section for the electroplating process is challenging. Numerous instruments and devices have been patented that are used for generating the required waveforms for pulsed electroplating and pulse anodization. The technologies range from manually switching the applied current for periods of a few minutes to a programmable power source using a microprocessor [123]. Silicon-based pulse rectifiers have been extensively considered. Nevertheless,

they suffer from relatively slow falling and rising times and cannot provide high pulse rates; they have grown into disuse. The review by Raj et al. [122] covers the various previously developed devices for pulse anodizing having similar specifications to those needed for pulsed electroplating.

In this section, a low-cost electroplating power source with high functional capability is introduced. The system can be used to perform complex galvanostatic and potentiostatic electroplating processes. The developed system was used to solve the difficulties of electroplating inkjet-printed conductive tracks on unstructured flexible substrates, as explained in Section 4.4. The system has also been used for performing other miscellaneous applications, as demonstrated in the applications Section 4.5.

4.3.1   Current source design

The developed power source precisely controls the waveform and the amplitude of the current pumped through the electroplating bath. The circuit possesses a feedback system for online monitor and recording the output current for documentation and diagnostic purposes. The circuit is controlled wirelessly over the internet connection via a developed graphical user interface (GUI).

A BeagleBone Black Wireless®(BBB) is used as a microcontroller unit (MCU) of the system. This microcontroller board posses a built-in wireless module that allows online access to the circuit over an internet connection. The remote access to the circuit gives the benefit of remotely setting the electroplating process parameter. Moreover, the vital benefit is observing the output voltage, which is used for monitoring the change in the impedance of the connected load. The BeagleBone is a Linux-based microcontroller. It includes an SD card as a storage memory, which provides enough space to record every electroplating process with different values. A real-time clock (RTC) integrated circuit (IC)(BQ32000, Texas Instruments®) is included in the circuit and connected to the MCU to keep track of the executed processes in real-time.

The current source was built mainly based on three modules and a microcontroller: (I) an isolated power supply for supplying the circuit with the necessary powers; (II) a feedback module to sense the output signal and send it to the microcontroller; and (III) a voltage-controlled current circuit (VCCC) to convert a voltage signal provided by the microcontroller to a controlled output current.

Module (I). A DC power supply is used to provide the circuit with a DC power of 12 V and 2 A. The input power provided by the supply is branched into four routes:

1. The first route is connected to an isolated 12 W input single and dual output DC-DC converters (NCS12D1205C, Murata Power Solutions) to supply the circuit with bipolar high power of ± 5 V and ± 1.2 A.

2. The second route is connected to a step-down voltage regulator (LM2596, Texas Instruments) to supply the circuit with 5 V that is employed for low power purposes as powering up the various ICs.

3. The third route is connected to low noise, low drift precision voltage reference to supply the circuit with 2.5 V, which is mainly used as a reference voltage. Any change in this reference

voltage dramatically affects the output signal; therefore, a high precision IC is used.

4. The last rout is connected directly to a filter and used to supply the circuit with 12 V used to power up a cooling fan.

Module (II). A feedback signal from the output port is shunted to a 16-bit analog to digital converter (*ADC*) (ADS1112, Texas Instruments®), which sends the converted signal to the microcontroller through the inter-integrated circuit (*I²C*) protocol. For protecting the microcontroller board, an *I²C* isolator chip (ADuM1250, Analog Devices) is located between the ADC and the microcontroller, as shown in Fig. 4.7.

Module (III). The microcontroller sets the control voltage ($V_{Control}$) through the serial peripheral interface (*SPI*) by a 16-bit digital to analog converter (*DAC*) (DAC8831, Texas Instruments®). The used DAC can generate a bipolar output signal in the range of $\pm V_{REF}$ when working with an external buffer. The reference voltage (V_{REF}) was set to 2.5 V. Since a bipolar *DAC* is used, the most significant bit (*MSB*) of the 16 bits acts as a sign bit, while the signal is defined by the rest of the acquired digital word. Hence, the resolution can be calculated as follow:

$$Resolution = \frac{V_{ref}}{2^{n-1}}. \tag{4.11}$$

For protecting the microcontroller board, an isolated dc-to-dc converter chip (ADuM6401, Analog Devices) is located between the DAC and the microcontroller, as shown in Fig. 4.7. The control signal ($V_{Control}$) is then provided to a VCCC, which is the most critical element of the whole circuit as it defines its performance. Numerous approaches and designs of the voltage-controlled current source have been introduced before and utilized in different applications [124–130]. The primary defining characteristic of a VCCC is the nominal value and stability of the output impedance while changing the connected load impedance or the output frequency. A current source derived from the modified Howland current source
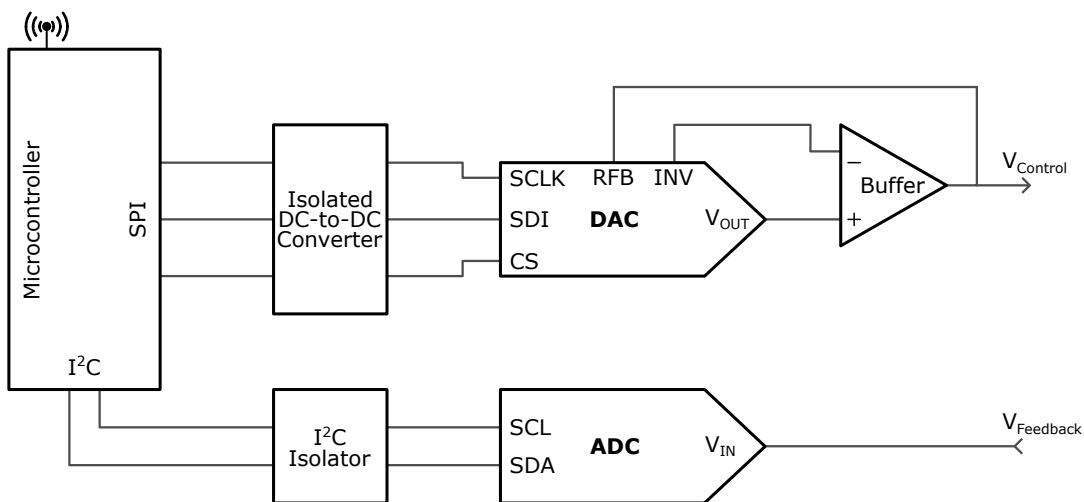
Figure 4.7: Schematic diagram illustrating the interface circuits connected to the microcontroller. The interface electronics are used for generating the input control signal ($V_{Control}$) to the VCCC and measuring the feedback signal ($V_{Feedback}$).

(MHCS) was developed, characterized, and subsequently used in our electroplating experiments. The (MHCS) was a perfect candidate as a VCCC for the electroplating application due to its simple configuration, stability and reliability in the performance under different surrounding conditions, and voltage compliance.

4.3.2 Voltage control current circuit (VCCC)

The modified Howland current source (MHCS) is used for controlling the amplitude and waveform of the output current as a function of the input control voltage. The MHCS is famous for the high stability of the output current over a broad frequency band. The MHCS configuration can sink or source bipolar current with a high output impedance, preventing the connected load from affecting the circuit's performance. Moreover, It can operate with floating or grounded loads [131]. The MHCS is appropriate for applications that require stability in the controlled current with different waveforms over a wide range of frequencies. Due to its reliable performance, The MHCS has been widely considered in numerous critical applications in different fields, e.g., detecting breast cancer using the electrical impedance tomography (EIT) [132] and in functional neural stimulation (FNS) [133, 134].

The basic Howland current pump (HCS) was first introduced by Prof. Bradford Howland of MIT for controlling current via voltage in 1962 [135]. However, in the initial proposed design, the output voltage did not swing close to the rail voltage supplied to the circuit leading to complications regarding the voltage compliance [136]. Hence, the basic configuration was inefficient with the loads that draw high voltages leading to waste in power. Consequently, the modified version was introduced where the non-inverting port of the OPAMP was connected to the output port via a passive resistor excluding the loading effects or the common-mode voltages.

A schematic figure of the MHCS is shown in Fig. 4.8. The MHCS consists mainly of a set of pas-
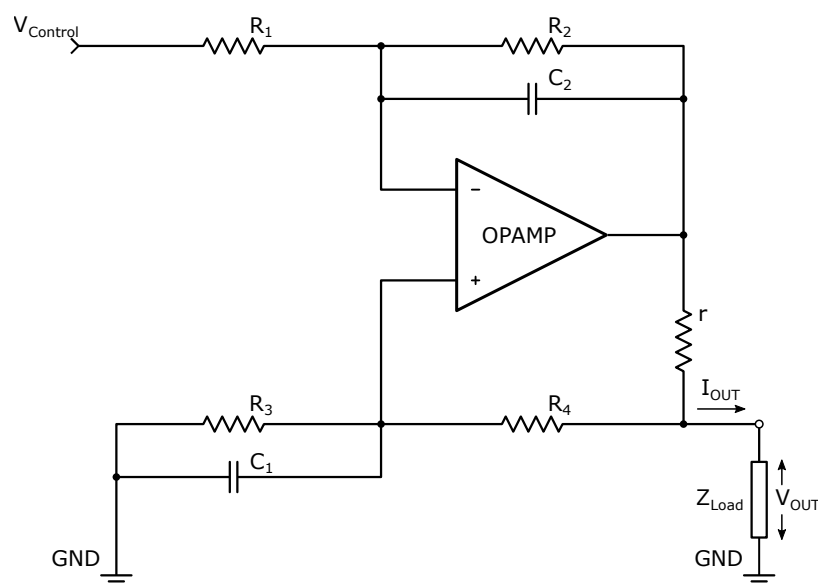
Figure 4.8: A schematic figure of the modified Howland current source (MHCS).

sive electronic components (resistors and capacitors) and one active electronics component (operational amplifier (OPAMP)). Through this subsection, the MHCS is modeled, then the circuit's different components (resistors, capacitors, and OPAMP) are discussed.

MHCS circuit modeling:

The transfer function between the input control signal ($V_{Control}$) and the output current (I_{OUT}) of a MHCS can be driven using a simple circuit analysis assuming an ideal OPAMP as shown in Equation 4.12 (see Appendix B for derivation). The transfer function of the MHCS reveals a simple linear relation between the input control voltage ($V_{Control}$) and output current (I_{OUT}).

$$I_{\text{OUT}} = -V_{Control}\frac{R_2}{R_1 r} + V_{OUT}\frac{R_1(R_4 + r) - R_2 R_3}{R_1 r (R_3 + R_4)}.$$ (4.12)

For a high precision current source, the circuit's output impedance must be much higher than the load through which the current is pumped, so that the load impedance doesn't affect the value of the output current. The output impedance (Z_{OUT}) of the MHCS can be derived by V_{OUT}/I_{OUT} while connecting the control signal ($V_{Control}$) to the ground as stated in Equation 4.13. In general, Z_{OUT} should be in the range of a few MΩ for single-digit currents and voltages.

$$Z_{OUT} = \frac{V_{OUT}}{I_{OUT}} = \frac{R_1 r (R_3 + R_4)}{R_1(R_4 + r) - R_2 R_3}.$$ (4.13)

Because of the OPAMP's non-ideal performance, it has a finite common mode rejection ratio (CMRR), which contributes to the output signal with a part known as common-mode noise. The CMRR of a differential amplifier is the ratio between the differential gain (A_d) and the common-mode gain (A_{CM}).

$$V_{out} = V_d A_d + V_{CM} A_{CM}, \quad CMRR = \frac{A_d}{A_{CM}}.$$ (4.14)

The close loop CMRR as function in the resistors can be derived by assuming a non-ideal OPAMP with finite gain (A). The output is calculated in the presence of inputs on the positive and negative terminal of the amplifier [137].

$$CMRR = 1 + 2A\left(\frac{R_1}{R_1 + R_2} + \frac{R_4}{r}\right).$$ (4.15)

As the opamp is the key component of the MHCS, the circuit's performance can be strongly affected as the opamp's temperature increases. Hence, for the application where high power is required for a long time, it's essential to provide an excellent cooling system. The power dissipation (PD) through the OPAMP can be estimated by the following,

$$PD = P_{Supply} - P_{Load} = V_S I - I^2 R_{Load}.$$ (4.16)

Equation 4.16 shows that the dissipated power in the OPAMP is the remaining of the supplied power (P_{Supply}) after deducting the power consumed by the load (P_{Load}). For resistive load, the power consumption is directly proportional to the square of the output voltage. Hence, the maximum power dissipation (PD_{max}) occurs at half of the maximum supplied voltage ($I = V_{Smax}/2R_{Load}$) [138], assuming that the output voltage can swing to the voltage's extreme. Hence, the maximum dissipated power in the OPAMP can be expressed by,

$$PD_{max} = \frac{V_{Smax}^2}{4R_{Load}}.$$ (4.17)

The power dissipation in the OPAMP can be used for estimating the junction temperature T_J by:

$$T_J = PD \; \theta_{JA} + T_A, \tag{4.18}$$

where θ_{JA} is the junction to ambient thermal resistance and T_A is the ambient temperature. θ_{JA} (°C/W) is function in the heat-sink's area attached to the OPAMP; this relation is usually provided in the OPAMP's technical data-sheet. Hence, the heat-sink's required area can be estimated to keep the OPAMP temperature below the safety limits.

Components selection:

The Howland current source's performance deviates from the theoretical predictions due to ideality assumptions. Hence, each of the passive and active components of the MHCS must be chosen carefully to achieve the high performance of stable and precise output current with broad bandwidth. The main affecting factors on the circuit's performance are the degree of non-ideality of the OPAMP and the tolerance in the values of the resistors. Several comprehensive studies were done to study the performance of the MHCS under different conditions, for example:

- Bertemes et al. studied the stability of the MHCS, due to the resistors' values mismatching, for a frequency range up to 10 MHz [131]. It was shown that for the MHCS to operate at high frequency, the open-loop gain needs to be raised. However, as the open-loop gain of the OPAMP increases, the circuit becomes more sensitive to the resistance tolerance. Hence the resistance needs to be perfectly matched for the MHCS to operate stably at high frequencies [131].

- Hammond et al. performed noise analysis for the MHCS by changing the resistance configurations and tolerance [139]. The resistors' ratios need to be matched carefully as this will affect the output impedance of the circuit [139].

- The practical problems involved with the different configurations of the Howland current sources were discussed by Texas instrument [136].

I. Resistors selection. The resistors' values should be selected in a way for the circuit to be symmetrical to improve the stability. By achieving $R_1 = R_3$ and $R_2 = R_4 + r$, so that R_1/R_2 match $R_3/(R_4 + r)$, achieves the goal. So that the total output current of MHCS (I_{OUT}) in Equation 4.12 will depend only on the control signal ($V_{Control}$) and is not affected by the output voltage (V_{OUT}), then it can be expressed as:

$$I_{OUT} = -V_{Control} \frac{R_2}{R_1 r}. \tag{4.19}$$

Equation 4.19 reveals the simple linear relation between the input control signal and output current, where r sets the gain and R_1/R_2 scales it. The resistor r is selected to have low resistance in the range of few to hundred ohms. The remainder of the circuit's resistors are in the range of kilo-ohms to mega-ohms. Consequently, $R_2 \gg r$ so the output current direction can be assumed to flow through r towards the load based on the current divider rule. Thus, a high power resistor is employed for r. A small value of r reduces Z_{OUT} in Equation 4.13, but at the same time, it improves the CMRR in Equation 4.15.

Resistance tolerance plays an essential role in the MHCS behavior. Any small miss-match between $R_2 R_3$ and $R_1(R_4 + r)$ will permit the connected load to influence the output current. On the other hand, Z_{OUT} and CMRR are both inversely proportional to the resistance tolerance [137, 140]. The resistors' miss-match results in poor CMRR no matter how good the OPAMP is. Consequently, as the used resistances in the MHCS have wide ranges of tolerance, the circuit's performance is strongly reduced. It's preferable to increase the close loop CMRR to overcome the common-mode input signal.

Trimming the resistances is essential to increase the CMRR and overcome the output current dependency on the load impedance leading to improved performance of the MHCS. Several approaches have been introduced to accurately set the resistance values, summarized in the technical report provided by Texas Instruments [136]. Trimming can be achieved by using trimmer resistors or using highly accurate resistors with low error percentages, which are relatively expensive. A potentiometer could be connected in series with R3 to balance the gain. Consequently, the output current can be controlled efficiently with a resolution in the µA range, with output voltages up to few volts.

II. OPAMP selection.   In general, any OPAMP can be utilized for building a MHCS. However, it's recommended to choose the OPAMP based on the application. In the case of applications where a wide range of output voltages are required, *OPAMPs with relatively high supply voltages (e.g., $\pm 15V$) should* be used. Additionally, It's recommended to use rail to rail OPAMP where the output voltage (dynamic range) can swing between the supply voltages' extremes. In the case of low output voltage applications, low voltage CMOS amplifiers can be utilized. For achieving a fast switching current pumps, current feedback amplifiers can be used. However, current feedback OPAMP usually operates at low impedance and has insufficient CMRR, even below 60 dB. Hence, excellent trimming of the resistors is required to balance the poor CMRR.

III. Capacitors selection.   Two essential capacitors need to be added to the MHCS. The added capacitors don't affect the amplitude of the output signal; however, they are necessary to suppress the noise that can influence the circuit's output.

1. The safety and stability of the MHCS under open output conditions can be ensured by using a capacitor of a few pF (C_1) to shunt the OPAMP's positive input to the ground. The added capacitor maintains the positive feedback to be always less than the negative feedback.

2. The higher frequency noise can be suppressed by adding a feedback capacitor C_2 in parallel with the negative feedback resistance R_2. The added negative feedback capacitor provides a single dominant pole in the negative feedback loop, which results in narrowing the bandwidth and prevents sustained oscillations. The negative feedback capacitor and resistor with the OPAMP creates an active low pass filter with a cut-off frequency (f_{CutOff}) calculated by,

$$f_{\text{CutOff}} = \frac{1}{2\pi C_2 R_2}. \tag{4.20}$$

   The negative feedback capacitor's value should be high in the range of a few nF to narrow the bandwidth and thereby enhances the output stability. On the other hand, a high capacitance will slow down the output. For the applications that require a borad bandwidth, the feedback capacitor's value can be reduced down to few pF.

The virtual capacitance of the MHCS (C_{OUT}) can be assessed using Equation 4.21 to estimate the circuit's dynamic behavior (see Appendix B for derivation).

$$C_{OUT} = \frac{I_O}{dV_O/dt} = \frac{R_3(R_1+R_2)^2}{2\pi r R_1^2(R_3+R_4)GBWP}. \tag{4.21}$$

Reducing the virtual capacitance of the circuit results in increasing the output speed. The virtual capacitance can be reduced either by increasing r or selecting an OPAMP with high gain-bandwidth product (GBWP).

4.3.3 Electroplating setup

Table 4.1 reports the actual components of the MHCS used for the construction of the electroplating current source shown in Fig. 4.9. Considering the output current will be flowing through *r*, a thick film power resistor with a rating power of 25 W is used for *r*. The maximum current that the circuit can provide is below 370 mA. Accordingly, the resistor's maximum dissipated power is estimated to be ≈ 1.4 W, which is way below the resistor's rating power. Thus, the resistor's temperature is ensured not to increase during the operation, keeping *r* at a stable value. For the rest of the resistors, low power resistors with excellent tolerances of $\pm 1\%$ were used; hence no trimming was required. The current source in isolation can operate up to a frequency of more than 1 MHz based on Equation 4.20, upon the used value for the negative feedback capacitor C_2 and resistor R_2.

A high-speed power OPAMP is used with dual supply voltages of $\pm 3.5 - \pm 7.5$V and can drive output current up to 1.2 A. The amplifier possesses a thermal shutdown safety option. Additionally, it provides a notification signal through a status pin (E/S) in case of thermal shutdown. The thermal shutdown option is essential for the electroplating application as processes can run continuously for hours. A sufficient cooling system should be provided to ensure the performance's stability and avoid the OPAMP's shutdown condition, mainly when operating a long electroplating process with relatively high current densities.

A cooling fan is used, as shown in Fig. 4.9. Additionally, a cooling pad with holes created in the *PCB* under the amplifier following the data-sheet recommendation. Under the operating parameters of $V_S =$

Table 4.1: The components used in constructing the modified Howland current source.

Component	Value	Comment
OPAMP	OPA561	Power operational amplifier, Texas Instruments
r	$10\pm5\%\Omega$	PWR163 series power resistor, Bourns
$R_1 = R_3$	$6800\pm1\%\Omega$	SMD E24 series resistor, Multicomp
R_2	$10\pm1\%$k$\Omega + 10\pm5\%\Omega$	
R_4	$10\pm1\%$kΩ	SMD E24 series resistor, Multicomp
C_1	$3\pm5\%$pF	MLCC - SMD 50V 0603 , Murata
C_2	$15\pm5\%$pF	MLCC - SMD 50V 0603 , Murata
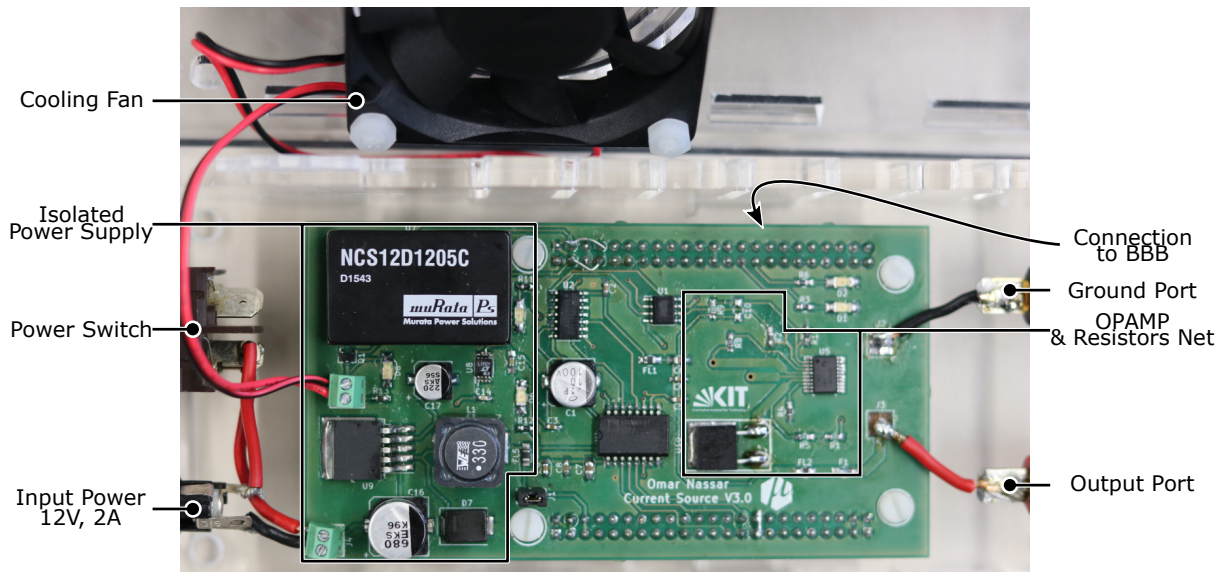
Figure 4.9: Photograph of the developed electroplating power supply. The power source features an isolated power supply, bipolar *DAC* for generating the control voltage signal, cooling fan, and the voltage-controlled current source (VCCC) based on the modified Howland current source (MHCS). The circuit is attached on the top of the BeagleBone black wireless (BBB) board.

$\pm 5\,\mathrm{V}$ and $r = 10\,\Omega$, the opamp's maximum dissipation power (PD_{max}) is estimated to be below 1 W, using Equation 4.17. Consequently, the amplifier junction temperature in case of maximum power dissipation is below $70\,^\circ\mathrm{C}$ at room temperature, which is sufficiently below the maximum junction temperature of the OPAMP of $150\,^\circ\mathrm{C}$.
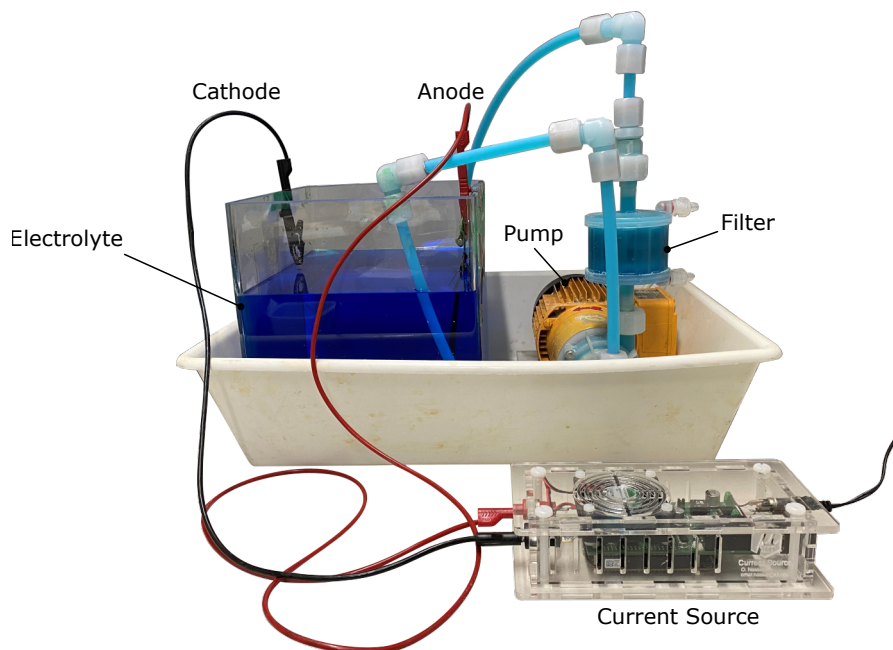
Figure 4.10: Photograph of the whole electroplating setup. The setup features copper electrolyte, electric pump for steering and filtering, the developed power source, and connecting wires.

A photograph of the full electroplating setup is shown in Fig. 4.10. A self-built copper electrolyte bath (Cuprostar® LP-1, Enthone-OMI GmbH) is used with a composition of 2 M concentration Cu_2SO_4, 0.7 mM H_2SO_4, and 0.009 mM HCL. The bath was continuously stirred and filtered using an electric pump. Schematic of each of the current source modules, as well as the whole circuit's schematic and the electrolyte composition, are available as supplementary material found in Appendix. B.

4.3.4 Graphical user interface (GUI)

A graphical user interface (GUI) is created based on a python script, as shown in Fig. 4.11. The GUI is pre-loaded on the MCU (Beaglebone) and can be accessed using a personal computer. The script is pre-programmed with all the previously mentioned electroplating waveforms in Subsection 4.2.1. The GUI allows the user to define the surface area required to be plated and the process total time. Then the user can choose from a drop-down list the required type of the waveform, which activates a query with the parameters that need to be filled by the user. The user fills the required electroplating current densities ($A\,dm^{-2}$), and the script calculates the required current (mA) based on the specified area and current densities. The developed device gives the advantages of autonomously running a series of different electroplating waveforms, allowing depositing several layers with different micro-structures, as discussed later in Section 4.4. The total electroplating time, the remaining time, the currently running waveform, and the measured output are displayed on the GUI with a real-time update.The python codes for controlling the current source and the BBB shell configuration file can be found in Appendix B.
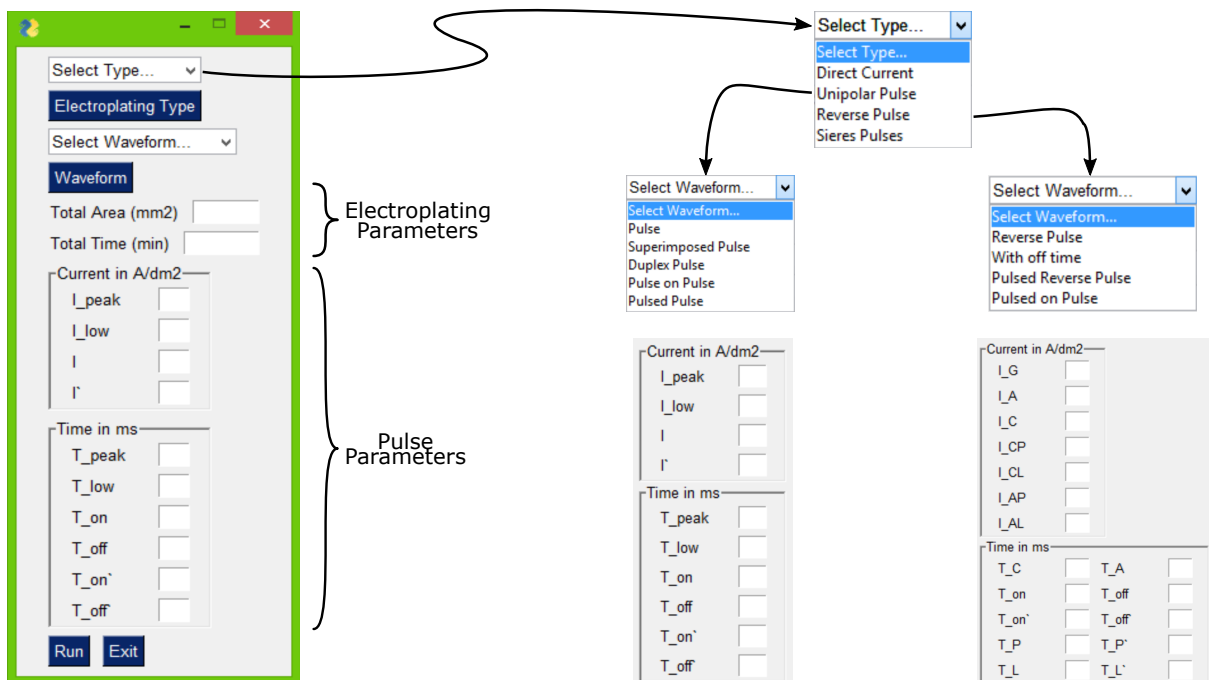
Figure 4.11: Graphical user interface (GUI) for controlling the electroplating current source.

4.3.5   Current source characterization

This subsection presents the experimental results of characterizing the circuit's output currents and voltages under different load resistances. Additionally, the time response of the developed current source was evaluated during switching between different current levels. Furthermore, the circuit was utilized to generate the different electroplating waveforms discussed previously in Section 4.2.1. The waveforms were generated with relatively high current densities while being connected to an electroplating setup.

For studying the effect of the load resistance on the circuit's output current, the current source was attached to a resistor kit, and an oscilloscope was connected in parallel with the load resistance to calculate the output current I_{OUT}. Figure 4.12 presents the experimental result of investigating the impact of the connected load resistance on the circuit's output current. The relationship between the programmed current (I_{IN}; the value inserted to the controller) and the actual measured output current when varying the connected load resistance is demonstrated in Fig. 4.12a. The reference line (black line) in the graph represents the current ideal performance, where the deviation from the reference line is the error value. The error increases proportionally with the circuit's output current value I_{OUT}. The measured error values are in the range of 0%–2% until the maximum driving voltage is reached, where the output current reaches a saturation state, after which it does not increase. Figure 4.12b presents the measured maximum output current I_{OUT} at each load resistance value. Increasing the load resistance limits the maximum current that the circuit can deliver. Electroplating setups typically have an electric resistance of only a few ohms. Hence, from the experimental characterization, the full range of output currents can be employed for the electroplating process.

Practically all current sources have a saturation value of the output voltage ($V_{Saturation}$). Below $V_{Saturation}$, the circuit's output current is constant, and above $V_{Saturation}$, the circuit's output current follows a decay-
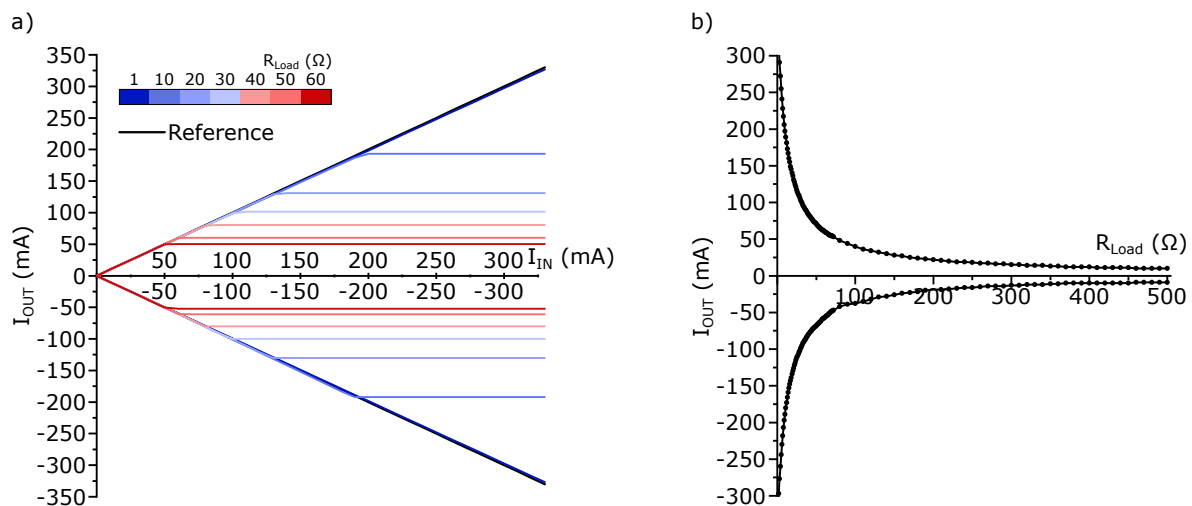
Figure 4.12: Experimental data showing the impact of the connected load resistance (R_{Load}) on limiting the circuit's output current (I_{OUT}). **(a)** The programmed output current (I_{IN}) versus its measured actual output current (I_{OUT}) value at different load resistances. **(b)** The maximum output current that can be pumped at different load resistances.

ing curve, as shown in Fig. 4.13b. This behavior is typical for most of the current sources where at low load resistance, the output current is constant and stable. In contrast, as the connected load increases, the output current starts dropping and deviates from the desired behavior. For the developed MHCS circuit, $V_{staturation}$ was measured to be ± 4.3 V, which is an excellent performance for an MHCS with an OPAMP supplied with voltages of ± 5 V. This good performance mainly results from carefully designing and choosing the electronics components to satisfy the points mentioned in the component selection Subsection 4.3.2.

During the pulsed electroplating process, the applied current continuously oscillates between different values; therefore, the settling time, overshoot, and final error of the output current are of interest. Figure 4.13a illustrates the alterations in these three parameters with respect to the difference between the output current levels while changing the connected load resistance. Three families of curves are shown, representing the different output current levels. Within each group of curves, the connected load resistance is swept. When the output current alternates between relatively close current levels, the circuit takes around 30 μs to settle to its final value. The settling time decreases as the gap between the output current levels increases. On the one hand, increasing the connected load resistance increases the circuit's settling time as well. On the other hand, a higher load resistance dampens the overshoot value. The overshoot value increases at higher output currents. For the pulsed electroplating process, the pulse width is in the range of ms, and hence, a settling time in the range of μs is acceptable.

The developed current source capability for electroplating was tested by generating the waveforms discussed in Subsection 4.2.1, Fig.4.5, and Fig. 4.6. The current source cathode was connected to a copper electrode, and the anode was connected to a metalized silicon substrate of rectangular shape, with dimensions of $4\,\text{cm} \times 1.5\,\text{cm}$. The silicon substrate was covered with 20 nm chromium and 60 nm gold layers. The chromium layer is used to promote the adhesion between the silicon and the gold layer. The chromium and gold layers were deposited using the physical vapor deposition process (PVD) (Univex
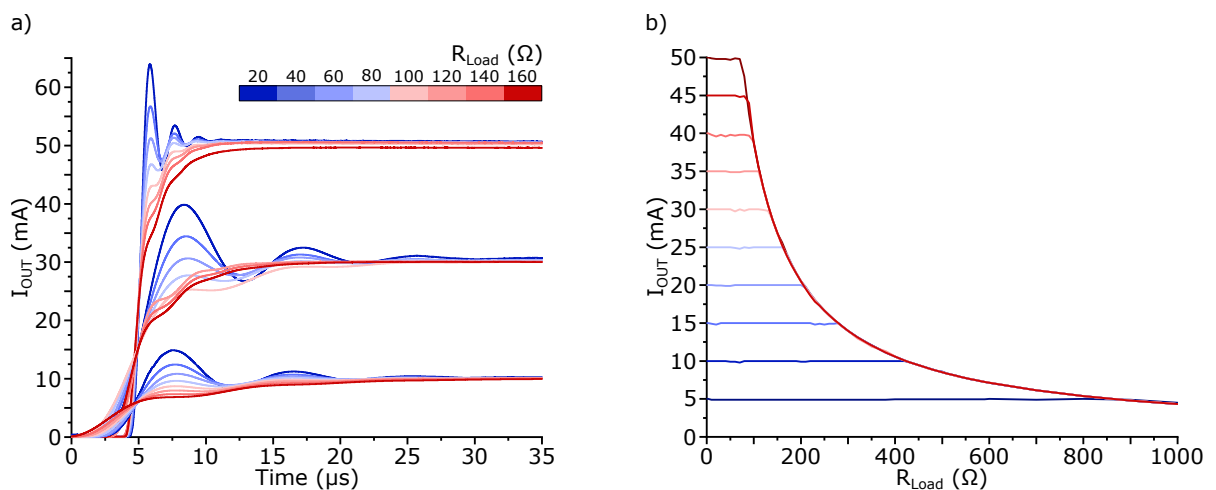
Figure 4.13: Dynamic behavior and saturation states of the developed current source. **(a)** The experimentally measured settling time of the circuit's output current I_{OUT} at different current levels and load resistances. **(b)** The experimentally acquired saturation curves, illustrating the output current drop at different load resistance.
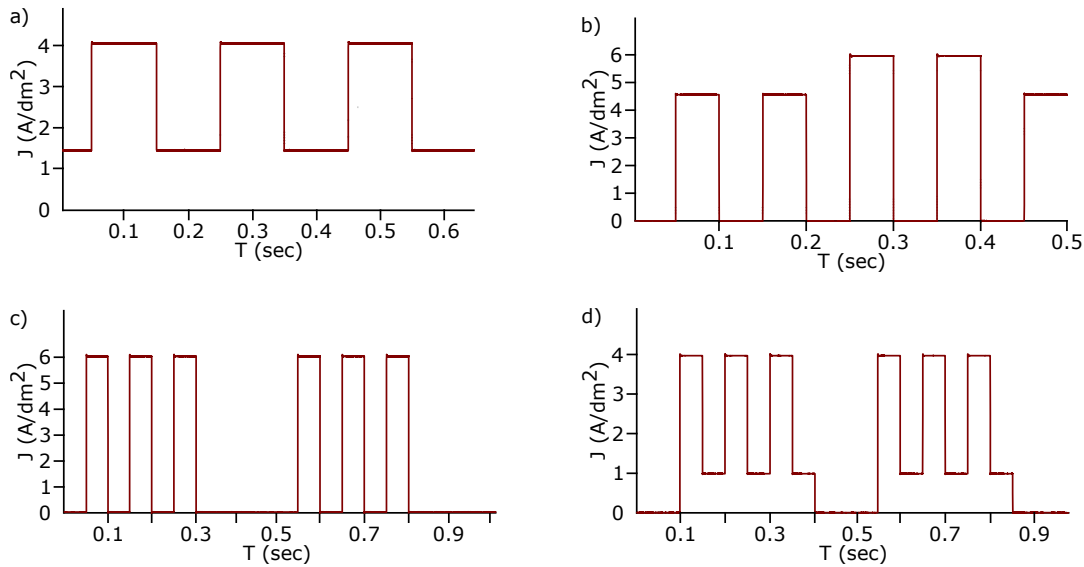
Figure 4.14: Different complex uni-polar waveforms generated by the current source when connected to an electroplating path. The generated uni-polar waveforms are: **(a)** Superimposed pulse; **(b)** Duplex pulse; **(c)** Pulsed pulse; and **(d)** Pulsed on pulse.

450) at deposition rates of $5\,\text{Å}\,\text{s}^{-1}$ and $8\,\text{Å}\,\text{s}^{-1}$, respectively. The copper electrode and metalized silicon substrate were immersed in a self-made sulfuric acid-based electrolyte bath (Cuprostar® LP-1, Enthone-OMI GmbH). The electrolyte was constantly stirred and filtered by an electric pump setup, as discussed previously in Fig. 4.10.

Figures 4.14 and 4.15 show samples of the waveforms that were successfully generated by the current source when connected to the electroplating bath. During the electroplating process, the pulse width should be enough for the EDL to be charged; otherwise, electrode-position will not happen. The negative
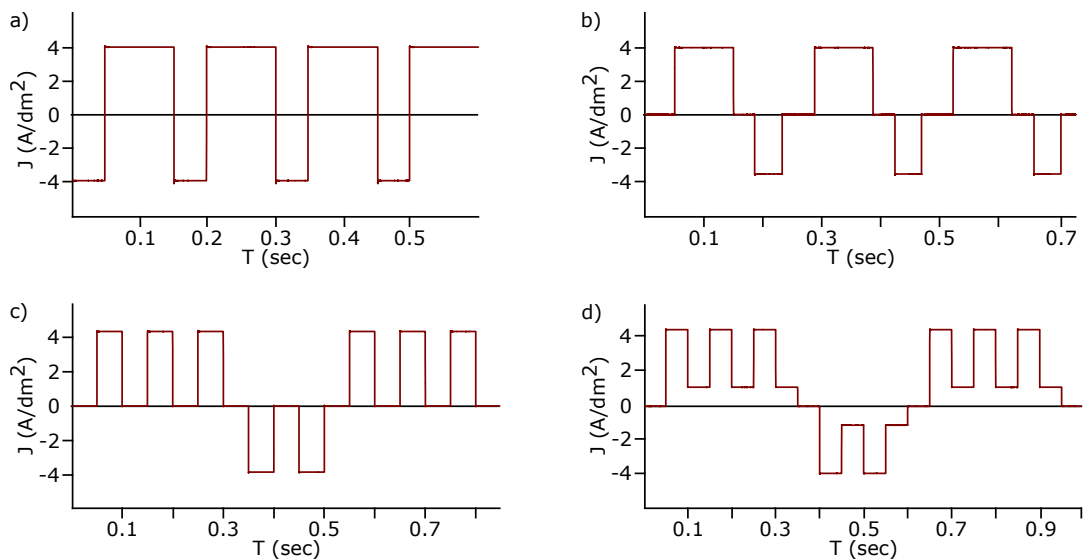
Figure 4.15: Different complex bipolar waveforms generated by the current source when connected to an electroplating path. The generated bipolar waveforms are: **(a)** Reverse pulse; **(b)** Reverse pulse with off-time; **(c)** Reverse pulsed pulse; and **(d)** Reverse pulsed on pulse.

pulse width should also be enough for the interface to discharge, as discussed previously in Section 4.1. Hence, The pulse widths were chosen in the range of ms to fit with the electroplating application. The ripples and oscillations on the measured waveforms are barely observed because of the time scale. The purpose of these experiments was to demonstrate the capability of the developed device under extreme conditions. Therefore, the generated waveforms had relatively high current densities of $6\,A\,dm^{-2}$. Moreover, each of the presented waveforms was kept running for more than 2 h. The circuit operated in a stable and robust manner in generating all indicated electroplating waveforms. It was also successful in generating the same waveforms with different time intervals and current densities.

4.4   Electroplating of inkjet-printed flexible electronics

Inkjet-printing a conductive seed-layer onto an unstructured polymer substrate is an essential process step in the field of flexible electronics [51,65], as discussed in the previous Chapter 3.1.2. The thickness of the printed layer is usually in the range of a few hundred nanometers which is very small for RF applications. Increasing the printed conductive layer's thickness can be realized either by printing multilayers [141] or by electroplating, which is more effective. Moreover, electroplating allows increasing the thickness of the conductive layer to several micrometers [61, 142, 143]. However, the adhesion of printed metallic films on the flexible substrate is particularly challenging, especially after electroplating. During electroplating the printed tracks, a charged layer is created around the electroplated tracks [105]. This charged layer results in high current concentrations nodes along the tracks' corners and edges, resulting in plating stress that leads to peeling off of the structures, as shown in Fig. 4.17. Using pulsed electroplating for manipulating this charged layer is a remedy and one of the main reasons for employing differentiated electroplating voltage waveforms.

In the following subsections, the developed current source is utilized to solve the adhesion problem accompanying the electroplating of printed conductive tracks on flexible substrates.

4.4.1   Materials and methods

Different electroplating waveforms were tested to study their impact on the adhesion of inkjet-printed tracks on a flexible substrate, as well as on the metallic micro-structure of the deposited layer. Silver rectangular tracks with $10\,mm \times 13\,mm$ dimensions were inkjet-printed on a $125\,\mu m$ Kapton sheet, as shown in Fig. 4.16. The ink used for inkjet-printing was 30–35 wt.% suspension of silver nanoparticles (Sigma-Aldrich®) with diameters≤ 50 nm dispersed in triethylene glycol monomethyl ether. The silver ink is rated with a surface tension of $35\text{-}40\,mN\,m^{-1}$ and a viscosity of 10-18 mPa s at room temperature. A Fujifilm Dimatix DMC-2800 printer was used for printing. A 10 pL print head-cartridge (DMC-11610, Fujifilm Dimatix) was filled with the ink and loaded to the printer.

During printing, the substrate plate and the printing head were maintained at a temperature of 25 °C. The printing dot spacing was set to 25 μm, and the printing frequency was set to 5 kHz using one of the 16 nozzles for printing, which resulted in uniformly printed tracks. Before printing, the Kapton foil was rinsed with acetone, isopropyl alcohol (IPA), and deionized water (DI water). After printing, the
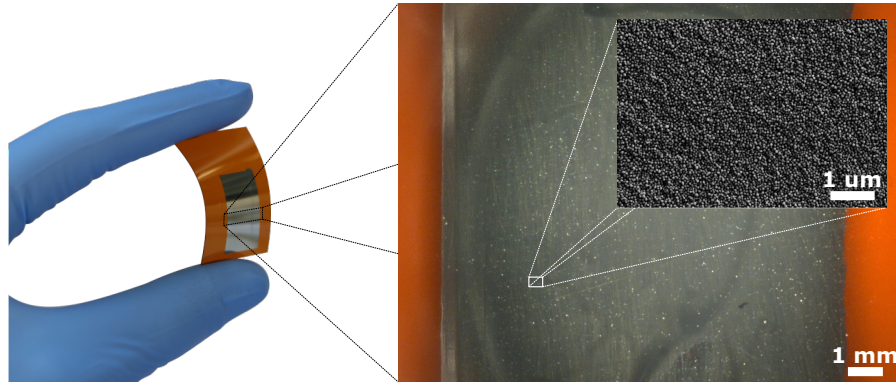
Figure 4.16: Inkjet-printed silver ink on a 125 μm Kapton film. The printed track is presented for three levels of detail. The inner focused view is a scanning electron micro-graph (SEM).

Kapton foil with the printed tracks was transferred to a hot plate for drying at 80 °C for 15 min, followed by sintering in an oven at 150 °C for 1 h. Subsequently, electroplating was carried out in the previously discussed setup in Subsection 4.3.3 and Fig. 4.10. Electroplating was performed without adding special additives or heating the bath, as the interest was to control the electroplating outcome by controlling the waveform only. After electroplating, the sample was rinsed using DI water, followed by drying using an air gun and placing the sample in a vacuum for 20 min to restrain oxidation.

4.4.2   Results

First, samples were electroplated by applying DC waveforms with relatively low, medium, and high current densities. The applied current densities were $0.5\,\mathrm{A\,dm^{-2}}$ for 90 min, $1.5\,\mathrm{A\,dm^{-2}}$ for 30 min and $3\,\mathrm{A\,dm^{-2}}$ for 15 min, leading to deposited copper layers of thickness of $\approx 10\,\mu\mathrm{m}$. For all samples electroplated using DC waveform, the tracks peeled off from the Kapton substrate, as shown in Fig. 4.17. It was observed that as the applied current density increases, the structures start to roll up due to the internal plating stress.

Then, samples were electroplated by applying pulsed electroplating. Uni-polar and bipolar with off-time waveforms were selected. The uni-polar waveform is defined with three parameters; I_{Peak}, T_{ON}, and
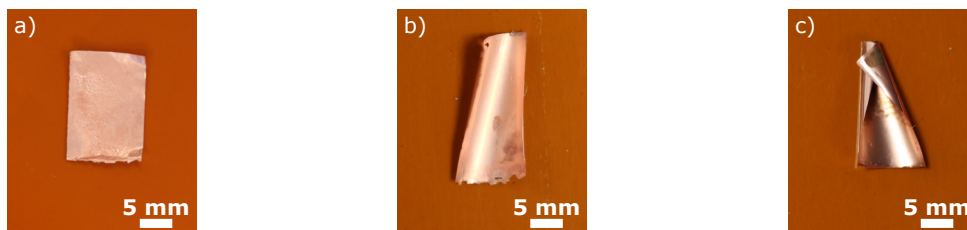
Figure 4.17: DC electroplating of inkjet-printed silver tracks on a 125 μm Kapton substrate using different current densities. The current densities applied are **(a)** low, **(b)** medium, and **(c)** high current. The plating stresses cause the curling of the electroplated films, which increases with the applied current densities as seen in (b) and (c).
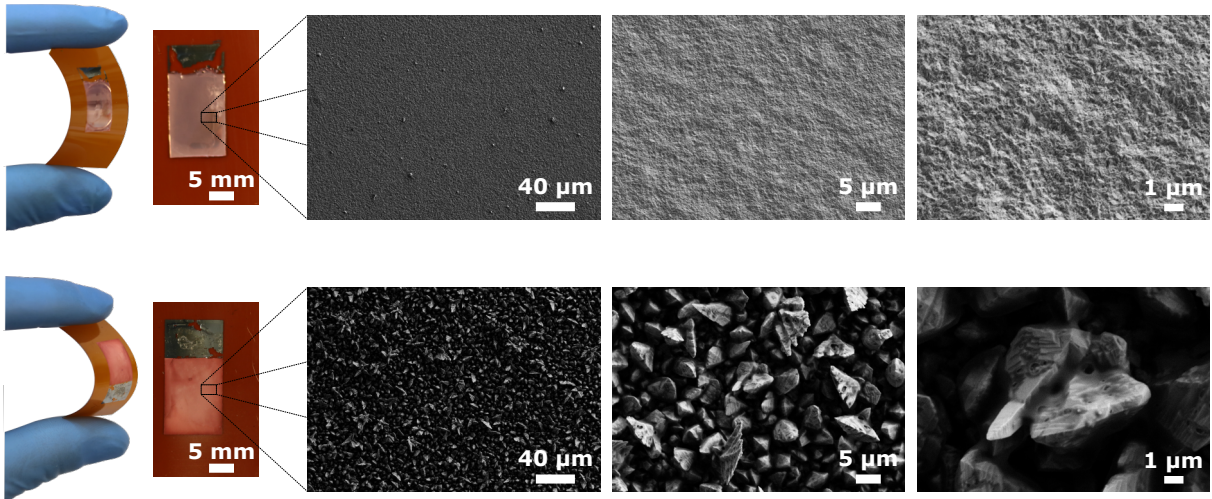
Figure 4.18: Pulsed electroplating of inkjet-printed silver tracks on a 125 μm Kapton substrate. The waveform used are **(a)** uni-polar and **(b)** bipolar pulsed electroplating. For each electroplated film, SEM images are presented.

T_{OFF}, as shown in Fig. 4.4b. The selected parameters of the uni-polar pulsed electroplating were $I_{Peak} =$ 0.6 A dm^{-2}, T_{ON} = 250 ms, T_{OFF} = 50 ms. The bipolar with off-time waveform is defined with six parameters; I_C, T_C, I_A, T_A, and the off-times between the pulses (T_{OFF} and T'_{OFF}), as shown in Fig. 4.6a. The selected parameters of the bipolar pulse were I_C = 0.8 A dm^{-2}, T_C = 300 ms, I_A = 1.5 A dm^{-2}, T_A = 50 ms, T_{OFF} = 10 ms, T'_{OFF} = 20 ms. Both types of waveforms have an average current density of 0.5 A dm^{-2} calculated using Equation 4.10, resulting in the same deposition rate. The pulsed electroplating processes were run for 90 min, achieving deposited copper layers of thickness $\approx$ 10 μm.

The film deposited by the bipolar waveform shows a perfect adhesion to the Kapton substrate. On the other hand, the film deposited by the uni-polar waveform show adhesion better than the DC waveform but not as good as the bipolar plating. The effect of the two waveforms on the metallic micro-structure of the deposited copper layer was investigated with respect to the surface topography, roughness, and grain size, employing three characterization techniques:

1. Scanning electron microscopy (SEM) (Carl Zeiss AG—SUPRA 60VP SEM) images are shown
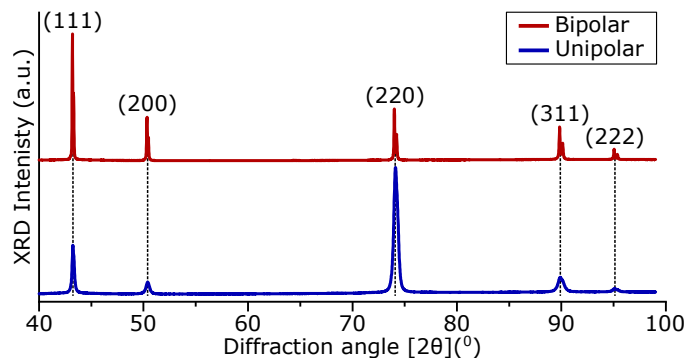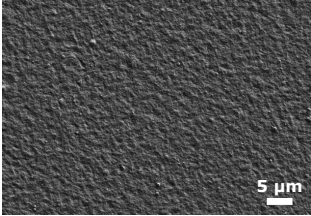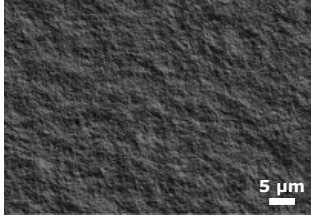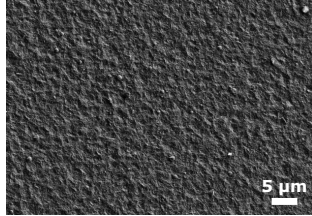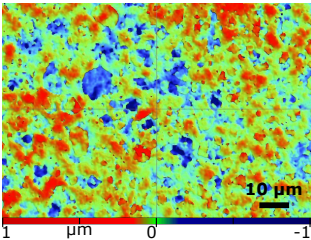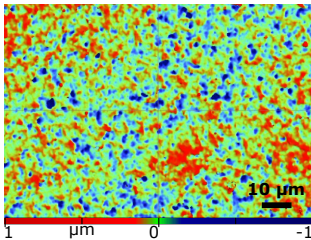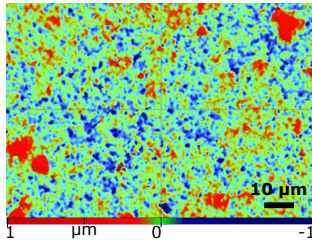
Figure 4.19: X-ray diffractograms of electroplated copper sheets with uni-polar and bipolar waveforms.

in Fig. 4.18. On the macro scale, the copper film deposited by the bipolar pulse was observed to be darker than that in the case of uni-polar plating. This was confirmed by the SEM images that show a relatively bigger deposited copper particles in the case of bipolar plating compared to that in uni-polar plating.

2. White light interferometry (WLI) (Bruker ContourGT-K 3D Optical Microscope) for measuring the surface roughness. A focusing area of $75\,\mu m \times 95\,\mu m$ was chosen for measurement, to avoid the Kapton film bending from affecting the roughness calculation. The uni-polar and bipolar electroplated copper sheets showed roughness values of 51 nm and 1840 nm, respectively.

3. X-ray diffraction (XRD) was conducted on a Bruker D8 Advance diffractometer in $\theta - \theta$ geometry using Cu-K$\alpha_{1,2}$ radiation. XRD measurement was done in the range between 40 °C and 99 °C, with the results presented in Fig. 4.19. The measured reflections in x-ray diffractograms consisted of peaks observed at 43.2°, 50.4°, 74.1°, 89.9°, and 95.1° that correspond to a planes (111), (200), (220), (311), and (222), respectively. Positions of these planes correspond to the Fm$\bar{3}$m space-group. Crystallite sizes were calculated following the Scherrer formula based on a method described by Warren [144]: $\tau = K\lambda/(\beta\,cos\theta)$, where τ is the ordered crystallite's mean size, K is the shape factor, λ is the X-ray wavelength ($\lambda = 1.54\,Å$), β is the selected reflection's full width at half-maximum (FWHM), and θ is Bragg's angle. The crystallite sizes for the uni-polar and bipolar plated samples were 30 nm and 307 nm, respectively.

Table 4.2: The effect of changing the uni-polar pulsed electroplating parameters on the metallic microstructure of plated inkjet-printed silver tracks on Kapton foil.

Parameter	$(I_{Avg} = 0.5\,A\,dm^{-2})^a$	$(I_{Avg} = 1.5\,A\,dm^{-2})^b$	$(I_{Avg} = 3\,A\,dm^{-2})^c$
SEM			
WLI			
Ra	78 nm	51 nm	29 nm
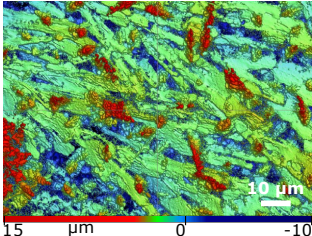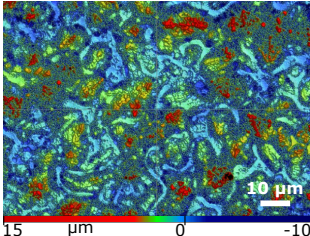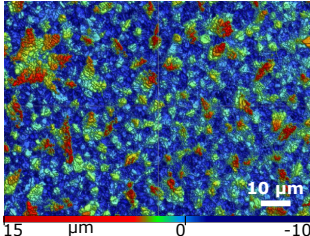
[a] $I_{Peak} = 0.6\,A\,dm^{-2}$, $T_{Total} = 90\,min$.
[b] $I_{Peak} = 1.8\,A\,dm^{-2}$, $T_{Total} = 30\,min$.
[c] $I_{Peak} = 3.6\,A\,dm^{-2}$, $T_{Total} = 15\,min$.
[a, b, c] $T_{ON} = 250\,ms$, $T_{OFF} = 50\,ms$.

Table 4.3: The effect of changing the bipolar pulsed electroplating parameters on the metallic micro-structure of plated inkjet-printed silver tracks on Kapton foil.

Parameter	$(I_{Avg} = 0.5\,A\,dm^{-2})^a$	$(I_{Avg} = 1.5\,A\,dm^{-2})^b$	$(I_{Avg} = 3\,A\,dm^{-2})^c$
SEM			
WLI			
Ra	1.8 μm	1.9 μm	2.2 μm

[a] $I_C = 0.8\,A\,dm^{-2}$, $I_A = 1.5\,A\,dm^{-2}$, $T_{Total} = 90\,min$.

[b] $I_C = 2.2\,A\,dm^{-2}$, $I_A = 3.3\,A\,dm^{-2}$, $T_{Total} = 30\,min$.

[c] $I_C = 4\,A\,dm^{-2}$, $I_A = 4.2\,A\,dm^{-2}$, $T_{Total} = 15\,min$.

[a, b, c] $T_C = 300\,ms$, $T_A = 50\,ms$, $T_{Off} = 10\,ms$, $T'_{Off} = 20\,ms$.

The impact of varying the pulsed electroplating parameters on the metallic micro-structure was investigated. For both uni-polar and bipolar electroplating, samples were plated with relatively low, medium, and high average current densities. The applied average current densities were $0.5\,A\,dm^{-2}$ for 90 min, $1.5\,A\,dm^{-2}$ for 30 min and $3\,A\,dm^{-2}$ for 15 min, leading to deposited copper layers of thicknesses of $\approx 10\,\mu m$. The used current densities ratings are equivalent to that used for the DC electroplating shown in Fig. 4.17.

Tables 4.2 and 4.3 summarize the plating printed silver layer results using uni-polar and bipolar wave-forms with different current densities (mentioned in the footnote of the tables). In uni-polar pulsed electroplating, the SEM images show a very similar micro-structure with increasing the applied current density. Additionally, the WLI measurements show that the surface roughness decreases as the applied current density increases. In the bipolar pulsed electroplating. The SEM shows different micro-structures with increasing the applied current density, where high current density leads to conglomerates formation. Moreover, the surface roughness was observed to be increasing proportionally with the applied current density. In conclusion, bipolar electroplating was observed to promote the printed conductive layer's adhesion to the flexible substrate compared to the uni-polar plating. However, the uni-polar electroplating results in a better surface finish with roughness below 80 nm other than the bipolar plating, which results in roughness in the μm scale.

The developed power source provides the flexibility to run a sequence of electroplating processes where
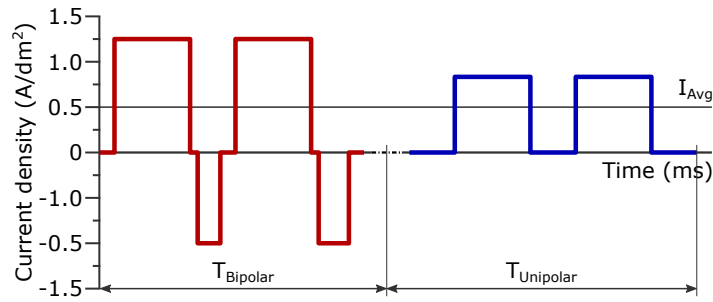
Figure 4.20: Double-layer electroplating waveform.

each process has different waveforms. With this sequence of the plating process, a film can be deposited with several layers where each has individually determined micro-structures. A series of bipolar and uni-polar pulsed electroplating was performed for an inkjet-printed silver track on a Kapton film, as indicated in Fig.4.20. This plating sequence combines the advantage of the bipolar plating on promoting the adhesion to the substrate and the advantage of the uni-polar waveform toward a better surface finish. The parameter of the conducted electroplating process is as follow: (1) the bipolar waveform: I_C = 1.25 A dm^{-2}, T_C = 250 ms, I_A = 1 A dm^{-2}, T_A = 100 ms, T_{OFF} = 25 ms, T'_{OFF} = 50 ms, and total process time ($T_{Bipolar}$) = 15 min; and (2) the uni-polar waveform: I_{Peak} = 0.8 A dm^{-2}, T_{ON} = 250 ms, T_{OFF} = 150 ms, and the total process time ($T_{Uni-polar}$) = 75 min.

Both pulses had an applied average current density of 0.5 A dm^{-2} and the total plating time was 90 min, resulting in a copper film with a total thickness of $\approx$ 10 μm. Figure 4.21 shows the SEM images of the printed silver layer as well as both of the deposited layers. SEM reveals both layers' micro-structures, where the first layer resulted from the bipolar waveform featured a relatively rough surface but resulted in good adhesion of the printed track to the Kapton substrate. In contrast, the upper layer resulted from the uni-polar waveform featured a smoother surface. The roughness of the final surface was measured using WLI to be 328 nm.
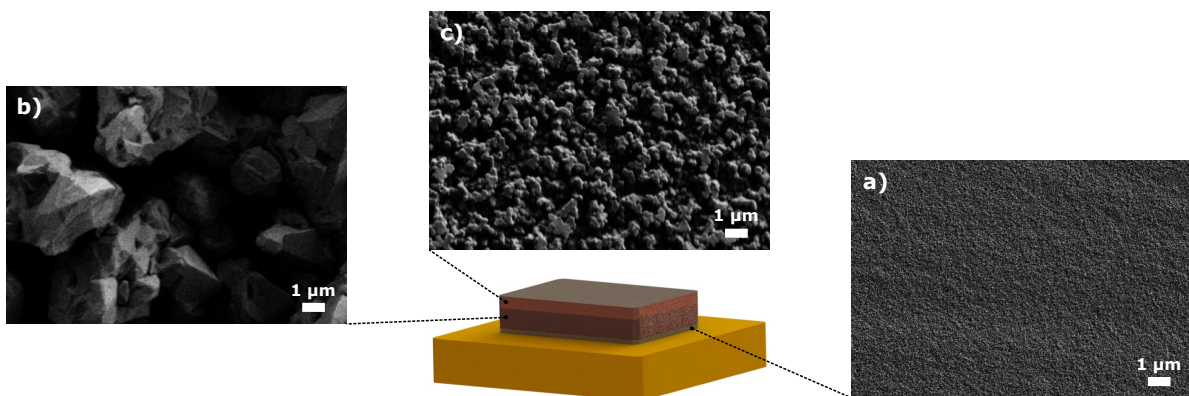
Figure 4.21: Double-layer electroplating of a printed silver track on a 125 μm Kapton film. The SEM micrographs are for: **(a)** Printed silver layer; **(b)** Bipolar electroplated layer, which promotes the adhesion of the conductive layer on the flexible substrate but results in a rough surface; and **(c)** Uni-polar electroplated layer with a relatively smooth surface for better surface finish.

4.5 Various applications for the developed current source

The developed electroplating current source was distributed in our research group and has been used for different applications. To show its applicability, three examples are selected and demonstrated in this section. The experiments shown here were not entirely conducted by myself: laser carbonization of Nomex in Subsection 4.5.1 was done by *Emil R. Mamleyev*, 3D printing of carbon micro-lattice architectures in Subsection 4.5.2 was done by *Monsur Islam*, and the setup presented in Subsection 4.5.3 was designed and built by *Markus V. Meissner*.

4.5.1 Electroplating of a laser carbonized polyaramid-based film.[2]

Electroplating substrates with a high electrical resistivity as carbon is challenging compared to electroplating materials with a high conductivity as gold or silver. The challenge arises from the electroplating process nature, where the electrical current should be pumped through the material that needs to be plated. Thus for electroplating material with high electrical resistivity, a powerful current source is required to pump the current through the resistive substrate. Within this subsection, the developed current source was successfully utilized for electroplating carbon tracks on polyaramid-based flexible substrate. The deposited copper layer was then used to generate customized flexible antibacterial coatings.

A 130 ± 13 µm thick Poly(1,3-phenylene isophthalamide) is used as the base substrate, it's commercially known as Nomex®Type 410 insulation paper (DuPont™; supplied by RS Components). Figure 4.22 summarizes the fabrication process. The Nomex film was first rinsed with isopropanol and dried for 10 min at room temperature. The film was then glued on a glass wafer with an acrylic adhesive sheet (3M-467MP) to prevent the film from bending during fabrication. Laser-induced carbonisation was performed using a CO_2-laser (ULS Versa Laser 3.50, wavelength: 10.6 µm, lens 2.0', beam diameter 120 µm at focus).
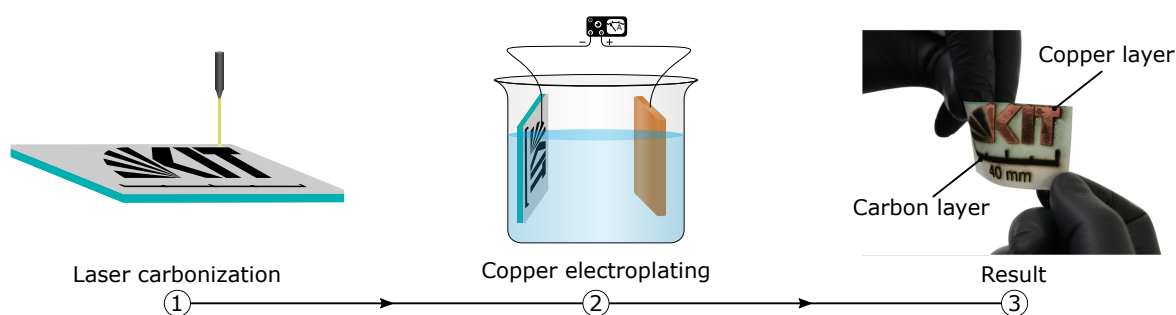
Figure 4.22: Schematic illustration of the fabrication flow of electroplating carbonized Nomex. **(1)** Laser irradiation of a Nomex sheet fixed on a glass substrate using LC2 and LC3 recipes. **(2)** Copper electroplating of the resulted carbonized tracks on the Nomex sheet. **(3)** Resulted flexible copper tracks on the Nomex sheet.

---

[2]This subsection's text and figures were partially adapted from the author's published work [ON2] with permission of American Chemical Society. Laser Carbonization of Nomex was done by *Emil R. Mamleyev*.

Performing carbonization with a single irradiation process results in carbon tracks with very high electrical resistivity. Thus, two different carbonization recipes with multiple irradiations were adopted for the manufacturing of the carbon layers. The first carbonization recipe was conducted with a double irradiation procedure, and the resulted samples are denoted as LC_2. During the first irradiation scan, parameters were adjusted to a scanning speed of 3 W, 13 cm s^{-1}, a distance between pulses in a line at $\sim$65 µm, an interline distance of $\sim$100 µm, and a focal distance of 2.5 mm. During a second irradiation scan, the scanning speed was raised to 32 cm s^{-1}, and the distance between pulses was lowered to $\sim$25 µm. The second carbonization recipe was performed with a triple irradiation procedure, and the resulted samples are denoted as LC_3. During the first irradiation scan, parameters were adjusted to a scanning speed of 3 W, 13 cm s^{-1}, a distance between pulses in a line at $\sim$25 µm, an interline distance of $\sim$25 µm, and a focal distance of 2.5 mm. Subsequently, the same procedures as LC_2 were repeated except for the pulse distance, which was kept at 25 µm for all scans. Subsequently, after carbonization, the LC_2 and LC_3 samples were electroplated using the developed electroplating setup discussed in the electroplating setup Subsection 4.3.3. A DC electroplating was applied with a current density of 1 A dm^{-2} for 5 min. After electroplating, the samples were rinsed with DI water and dried on a hot plate at 95 °C for 5 min to prevent copper oxidation by evaporating the residual moisture. Both samples LC_2 and LC_3 were successfully plated with copper. The samples maintained their electrical resistance and remained fixed to the Nomex substrate without damage even after bending. Figure 4.23 demonstrates the surface morphology of the carbon layer as well as the plated copper layer. The deposited copper particles have crystal-like shapes with lengths over 3.2 µm and 3 µm and widths over 1.13 µm and 1.15 µm for LC_2, and LC_3, respectively. In the LC_3 sample, most of the deposited crystals were established on a central active site and consistently interconnected with neighboring crystals, providing better electrical stability than LC_2. The thickness of the deposited copper layer was determined to be slightly above 3.5 µm.
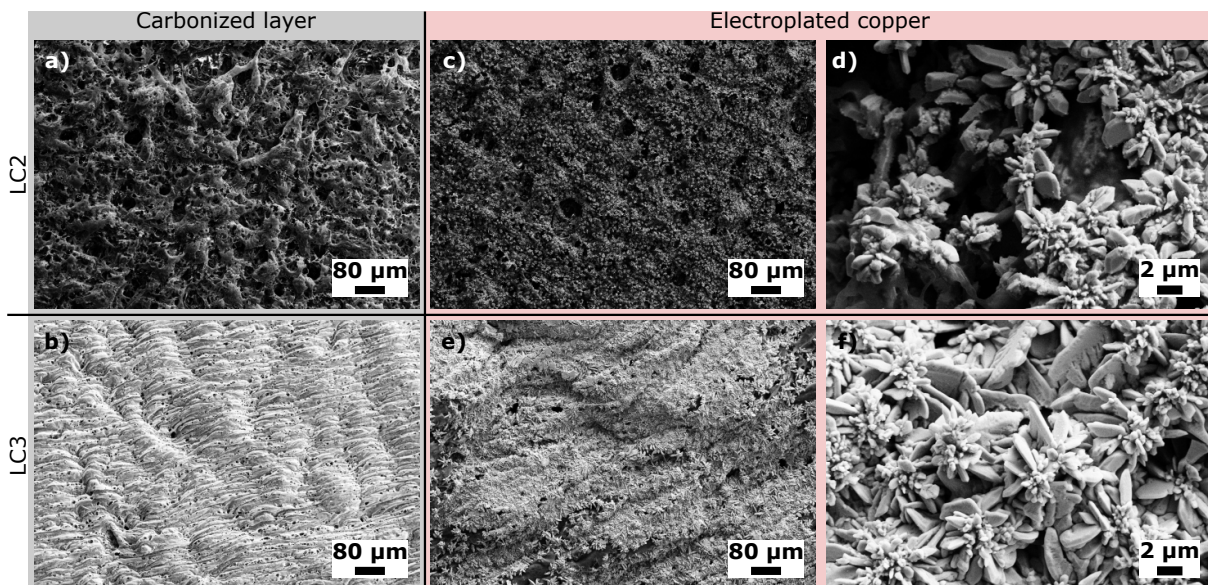
Figure 4.23: Surface morphology after carbonization and electroplating of Nomex. SEM images of the carbon layer generated by double LC_2 **(a)** and triple LC_3 **(b)** irradiation procedure. SEM images of the copper layer after electroplating of the LC_2 **(c, d)** and LC_3 **(e, f)** samples.

4.5.2   Electroplating of 3D printed carbon micro-lattice architectures[3]

This subsection introduces another application of the developed electroplating current source for plating 3D carbon structures. The 3D carbon architectures were fabricated by printing 3D structures out of an epoxy resin using stereo-lithography and then carbonized in a nitrogen environment [145]. SLA-3500 laser stereo-lithography system (3D Systems, USA) was used for printing the epoxy resin WaterShed XC11122 (DSM Desotech BV, Netherlands) to realize the 3D architectures. The stereo-lithography system works layer-by-layer, enabling the polymerization of the resin and produce 3D solid complex components. After printing the 3D prototype using stereo-lithography, it was rinsed by immersion in acetone for 2 min and post-cured in a UV oven for around 20 min to improve mechanical properties. The pyrolysis process for obtaining carbon scaffolds was conducted in a horizontal tube furnace (Carbolite Giro, Germany). The prototype obtained from the stereolithography process was heat-treated at 900 °C. The steps of the heat-treatment process were [146–149]: 1) heating from room temperature to 900 °C under a heating rate of 2.5 °C/min; 2) dwell for 1 h at 900 °C; and 3) cooling the sample down to room temperature by turning off the heater of the furnace. The whole heat-treatment process was conducted in an inert atmosphere achieved by a constant nitrogen flow with a flow rate of 0.8 L/min.

Before electroplating, the 3D carbon micro-lattice architectures were rinsed by immersion in DI water. Electroplating was performed using the developed electroplating setup. A DC electroplating was employed with a current density of 1.5 A dm^{-2} for 2 min. After plating, the sample was rinsed using DI water, followed by drying using an air gun and placing the sample in a vacuum for 30 min to restrain oxidation.
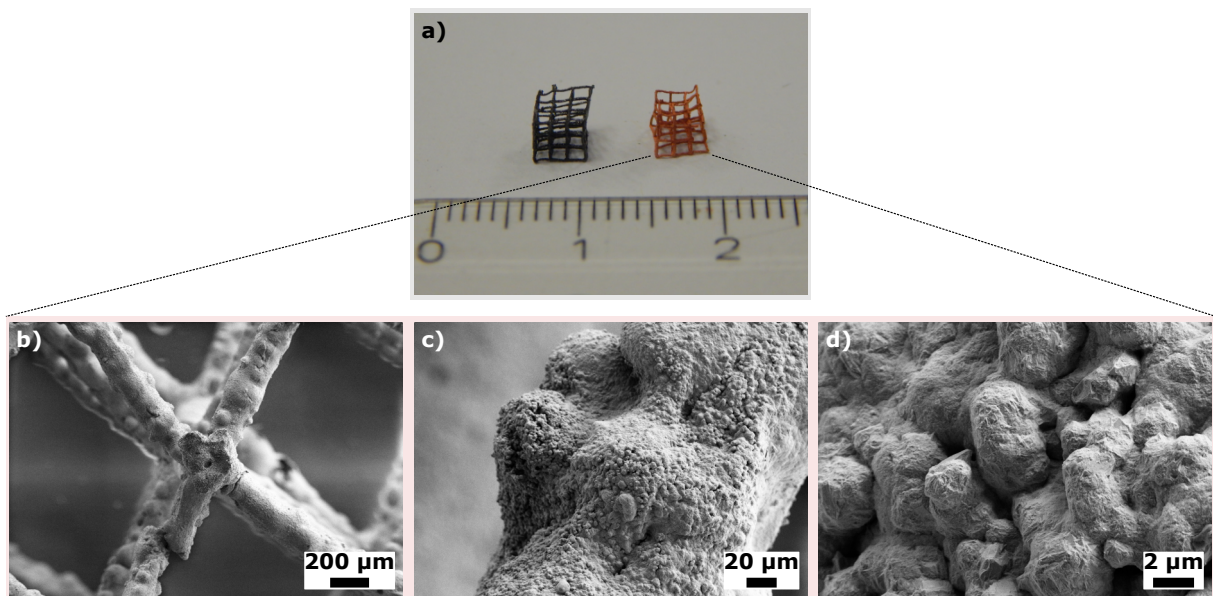
Figure 4.24: Electroplating of 3D printed carbon micro-lattice architectures. **(a)** Photograph of the 3D carbon architectures before and after electroplating with copper. The 3D carbon architectures are fabricated by stereo-lithography printing then carbonization in an inert environment. **(b-d)** SEM images of the deposited copper layer.

---

[3]3D laser stereolithography printing of the carbon micro-lattice architectures was done by *Monsur Islam*.

Figure 4.24a shows the 3D carbon structure before and after electroplating. The achieved 3D copper cube had a total surface area of $\approx 100\,\text{mm}^2$. Figures 4.24b-d present SEM images of the deposited copper. The deposited copper layer thickness was measured to be $\approx 2\,\mu\text{m}$.

4.5.3   Parallel electroplating[4]

The developed electroplating power source is compatible with the parallelization concept. A PBC was developed possessing eight current channels where each being separately and real-time controllable, as shown in Fig. 4.25. A self-constructed electroplating setup was prepared for parallel electroplating. The setup was build-out of four 3 L glass beakers, each equipped with a single copper anode and two wafers holders connected to the cathodes (power source channels). Holders for the electrical connections, thermometers, anodes, and cathodes (wafers) were cut of PMMA (Poly(methyl methacrylate)) sheets using a laser cutter (VLS2.30, Universal Laser Systems Inc.). The electrolyte allowed plating all of the eight wafers at room temperature at relatively high current densities of up to $4\,\text{A}\,\text{dm}^{-2}$.
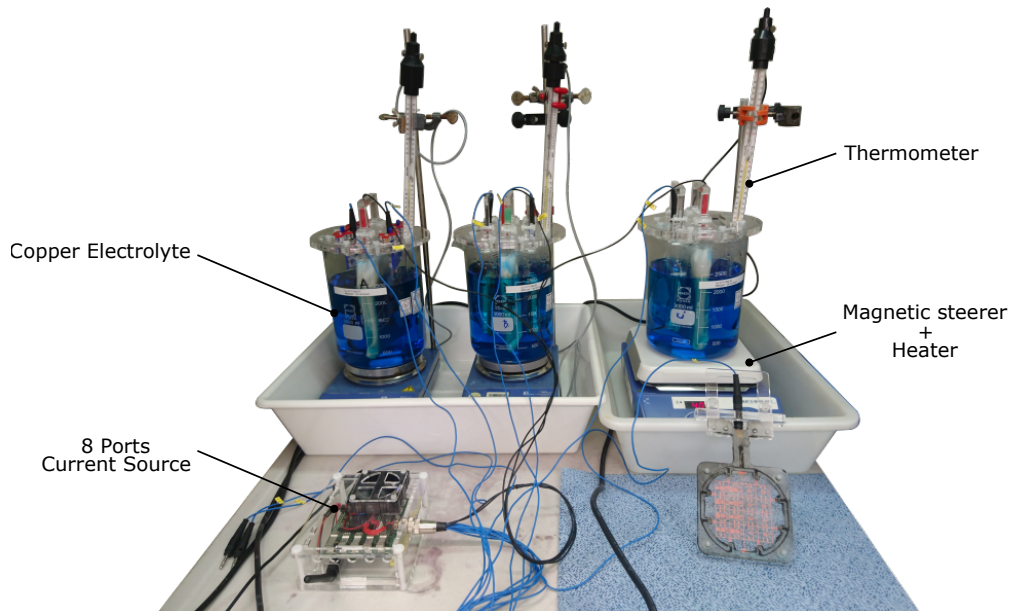
Figure 4.25: Electroplating setup for plating eight 100 mm wafers in parallel. The power supply with eight channels is presented in the foreground left, and a PMMA wafer holder is shown to its right. The figure is generated by *Markus V. Meissner*.

---

[4]The electroplating setup with eight channels shown here was designed and built by *Markus V. Meissner*.

Part II.

MRI Application - Interventional Magnetic Resonance Imaging (iMRI)
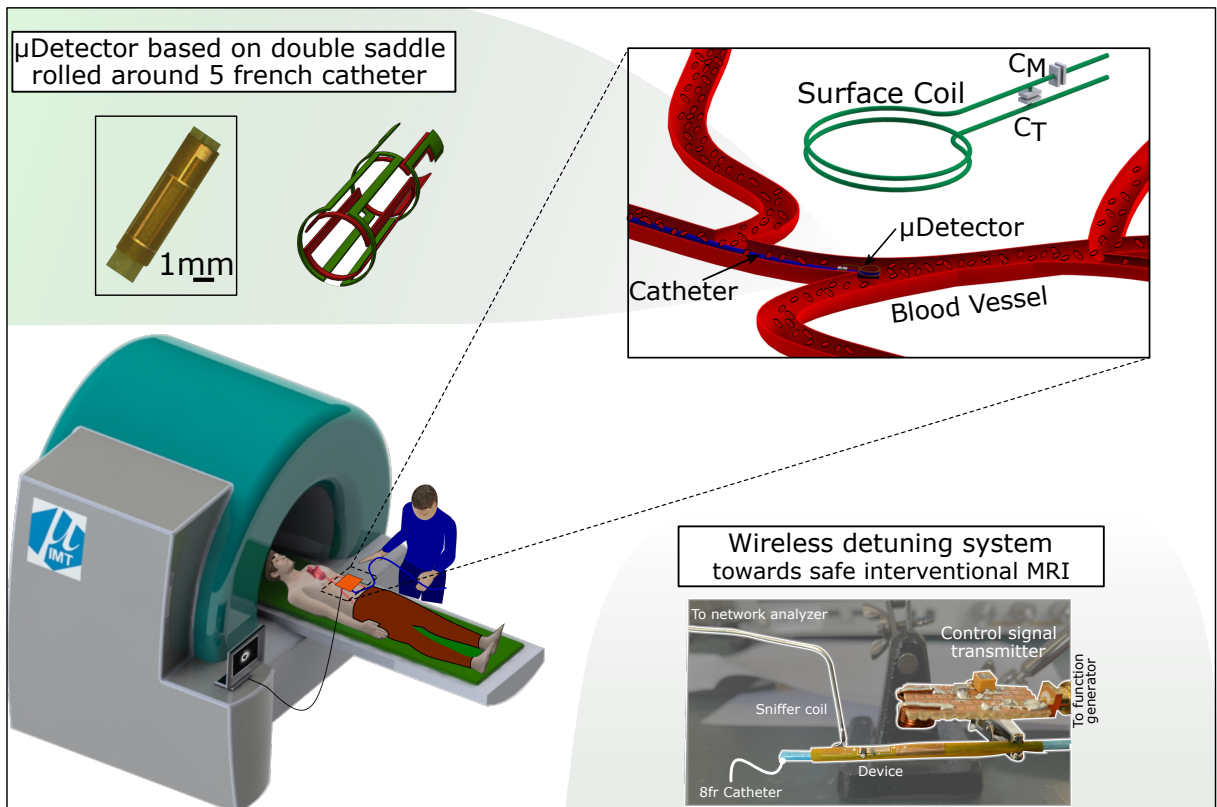
5 State-of-the-art: interventional Magnetic Resonance Imaging (iMRI)[1]

Catheter-based intervention is one of the effective medical methods used in treating and diagnosing cardiovascular diseases. It plays an essential role in the field of minimally invasive medicine [150, 151]. Over the past two decades, cardiovascular diseases have been reported as the leading cause of death globally, with more than seventeen million fatalities in 2017 surpassing all other medical causes combine [14]. Patients suffering from large vessel occlusion should be treated fast as it leads to death or long-term disability. Catheter-based endovascular embolectomy is an effective treatment where the doctors use a catheter under the visualized tracking approach to control its path through the vessels [152]. Hence, providing a surgeon with a real-time precise location of the catheter's tip within the patient's body is a prerequisite for further advancement of minimally invasive medical operations. Tracking the catheter can be achieved using real-time X-ray fluoroscopy. However, X-rays affect the patient and the medical staff with doses of potentially harmful ionizing radiation [153]. Moreover, tracking catheters using X-ray suffers from poor contrast of soft tissues, making the method unsuitable for complex interventional procedures [150].

Hence, tracking a catheter's tip within a magnetic resonance environment has been a topic of great attention during the past decade and has been considered a promising approach for interventional diagnosing and immediate treatment [154–156]. Several approaches have been developed to track catheters in an MR environment, categorized into passive and active techniques. The passive approaches depend on the magnetic susceptibility difference between the catheter and the body tissues, which results in a visualized location of the catheter [157]. Therefore, it requires either susceptibility artifacts or contrast agents [158]. Although passive approaches are easier to implement and cost-effective, they are less robust and lack reliability than other approaches [159]. The second approach is electrically active, where additional hardware such as resonators (coil ∥ capacitor) [160, 161] or RF antennas [162, 163] are placed on the catheter's tip resulting in a traceable visible spot in the MR image. The active approaches are divided into active and semi-active methods. In the active methods, the micro-resonators on the catheter tips are connected to the MRI scanner through a conductive wire for data transfer. On the other hand, the semi-active method eliminates conductive wires where the catheter's resonator provides a resonant inductive coupling effect, resulting in a wireless local signal amplification of the B_1 field.

However, installing an RF receiver coil of the MRI to the catheter still faces some unsolved issues concerning patient safety and catheter visualization, which has prevented this technology from finding widespread use. The excessive RF heating and high induced currents in the micro-resonator during transmission of the RF field can harm the patient by dangerously heating the surrounding tissues [164, 165] and may deliver an electric shock to the patient. The implanted conductive coil and transmission line inside the human body acts as an electromagnetic antenna [166], which is sensitive to both electric and magnetic fields, although the MRI detector should be sensitive only to the nuclear magnetic field.

---

[1]This chapter's text and figures were reproduced and adapted with permission from the author's published works [ON3] (CC BY 4.0, 2020 IEEE) and [ON6] (Copyright © 2019, IEEE)

5.1   Heating problem

Heating conductive electrodes or implants inside the human body during MRI procedures may lead to immediate and severe damage to the surrounding tissues. When subjected to a temperature above 44 °C, tissue injury will happen due to the disintegration of proteins. The alternating B_1 field is the electromagnetic field in MRI that contributes the most to the heating of conductive implants. The B_1 magnetic field generates an electric vortex field which induces eddy currents inside the conductive parts. This eddy current leads to direct heating of the conductive subject. The frequency-dependent skin effect defines the effective resistance, thus the conductor's thickness determines the heating generated by the eddy current.

When it comes to long conductive wires, the scattered electric field has a more significant impact. The B_1 fields induce surface currents into the conductive wire, resulting in a scattered electric field. The magnitude of the scattered electric field is defined by the length of the conductive wire, diameter, insulation material and thickness, and tip geometry [167]. The magnitude of the scattered electric field is magnified at the tip of the conductive wires, resulting in the maximum harmful heating at the wire's tip [167, 168]. This effect of the scattered electric field becomes very obvious when the wire length (L_{wire}) is in the range of the wavelength λ of the alternating B_1 field; $L_{wire} = \lambda/4, \lambda/2, \lambda, 3\lambda/2,...$etc. Park et al. [168] showed mathematically and experimentally that the resonant length (length at which maximum heating occurs) of a bare wire in a 1.5 T MRI scanner is 20 cm, while, for insulated wire, the resonant length exceeds 40 cm. Konings et al. [165] tested different lengths of conductive wire with the same configuration in a 1.5 T MRI scanner. The temperature rises from 37 °C to 72 °C by increasing the wire length from 45 cm to 85 cm.

A conductive material in an MR environment absorbs a certain quantity of the transmission power, leading to an increase in its temperature. The specific absorption rate (SAR) defines the quantity of the absorbed power per mass. The SAR distribution can be derived from the peak amplitude of the electric field (E) by [24]

$$SAR = \frac{\sigma|E|^2}{2\rho}, \tag{5.1}$$

where σ is the conductivity and ρ is the mass density. Equation 5.1 can be rewritten as a function of the parameters of the MR sequence (this simplified form is adapted from "From picture to proton, ch. 20.2 [24]")

$$SAR = \frac{\sigma\pi^2 r^2 f^2 B_1^2}{2\rho} D, \tag{5.2}$$

Where f is Larmor frequency which is in turn function in B_0, D is the duty cycle which is the fraction of the total scan time with RF field operating, and r stands for the sample size. The previous equation shows that SAR increases with the square of B_0 and B_1 magnetic fields. Moreover, SAR increases linearly with the number of RF pulses per cycle (duty cycle).

5.2 Active MR-catheter markers

This section presents an overview of the state-of-the-art MR-catheters, focusing on the introduced approaches for eliminating the long conductive transmission wires in MR-catheters to avoid the heating hazard. Ladd and Quick [169] used RF coaxial chokes for reducing the RF heating. An RF choke is a type of inductor that blocks high-frequency signals while it allows only low frequency or DC signals to pass. Several techniques could be employed to implement the chokes in a transmission cable, including winding loops around the cable, which add self-inductance to the system. Another possibility is adding discrete passive components like capacitors into the cable. However, windings and discrete passive components add challenges for interventional catheters due to their geometry constraints. An alternative is using a coaxial sleeve with a specific length ($\lambda/4$). Several coaxial chokes can be added within the transmission cable, where each choke participates in increasing the impedance and reducing the amplitude of the RF standing wave. Figure 5.1d shows a schematic diagram of two coaxial chokes in series integrated around the transmission line. In this design, a triaxial cable is used, where the chock is prepared by soldering the secondary shield to the inner shield and then a small segment of the secondary shield is removed after a length of $\lambda/4$. The other end of the secondary shield (chock) is left open. The coaxial chokes increase the impedance for the high-frequency currents flowing through the outside shield layer of the coaxial cable, eliminating unwanted currents. On the other hand, chokes do not affect the impedance within the conductor layer for low-frequency currents. After integrating a choke in the cable, the spot of the maximum electric field is shifted near to the choke, resulting in high impedance and reducing the standing wave. Consequently, the change in temperature is spatially distributed based on the chokes locations to avoid spots with high temperatures. In this approach, the catheter needs to be well insulated as it can deliver electric shock at the open end of the chocks.

Weiss et al. [170] reduced the electrical length of the conductive transmission wire by integrating miniaturized transformers within the wire, as shown in Fig. 5.1a. The conductive wire was divided into small segments, and the signal transfer between the segment was done using miniaturized transformers. The reduction of the conductive wire length restricts the induced electric field in the wire, thus reduces the generated heating. The miniaturized transformers were single loop transformers fabricated on a multi-layer PCB with a 127 μm gap between the two transformer coils. The results showed a reduction of the heat to a safe level. However, a loss in the transmission signal occurs but still sufficient for the active marker tracking purpose.

Syms et al. [171, 172] used thin-film magneto-inductive (MI) waveguides to transmit the signal instead of conductive transmission wire. The used MI waveguide had a periodic array of low-frequency resonators (LC circuits), as shown in Fig 5.1c. The LC circuits were structured on both sides of a thin-film substrate alternately, fixed around the catheter tube by the mean of heat-shrink tubing. The length of the elements was chosen to be short enough to protect the catheter against the external alternating B1 field and the induced electric fields. The system was developed to overcome the heat and orientation problems. The orientation problem is the loss of coupling of the catheter receiver during its movement because of bending or axial orientation.

Fandrey et al. [173] used laser light and optical fibers to transmit the MR signal instead of the conductive

wire to tackle the heating problem. However, the optical approach requires placing bulky components on the catheter's tip, which added another challenge to the iMRI system. The system consists of a resonant receiver circuit for acquiring the MR signal, an optical modulator on the catheter's tip, and the optical power supply. Figure 5.1b shows a schematic figure for the optical system for MR-catheter. The received MR signal is fed directly to the optical modulator that modulates the current via a laser diode. The power for the optical modulator on the catheter's tip is transmitted through another optical fibers. The fibers are located around the catheter tube. The resonator is passively decoupled using a pair of diodes on the catheter's tip. This technique ensured reliable tracking of the tip of the catheter and high contrast visualization. However, the optical method adds handling difficulties because of the mechanical connection between the scanner and the catheter using the optical fiber, where fibers manipulation, bending, or rotation should be avoided. Sarioglu et al. [174] tackled the drawback of the bulky components of the optical system by integrating metal-oxide-semiconductor photovoltaics. In addition, the interface circuit between the optical and electronic components was developed as an off-chip MEMS-based resonator array to reduce power consumption. A photovoltaics circuit as a power supply unit is also integrated to convert the input optical power to drive the CMOS chip. The CMOS chip is responsible for detecting the input signals then creates a PWM electrical current.
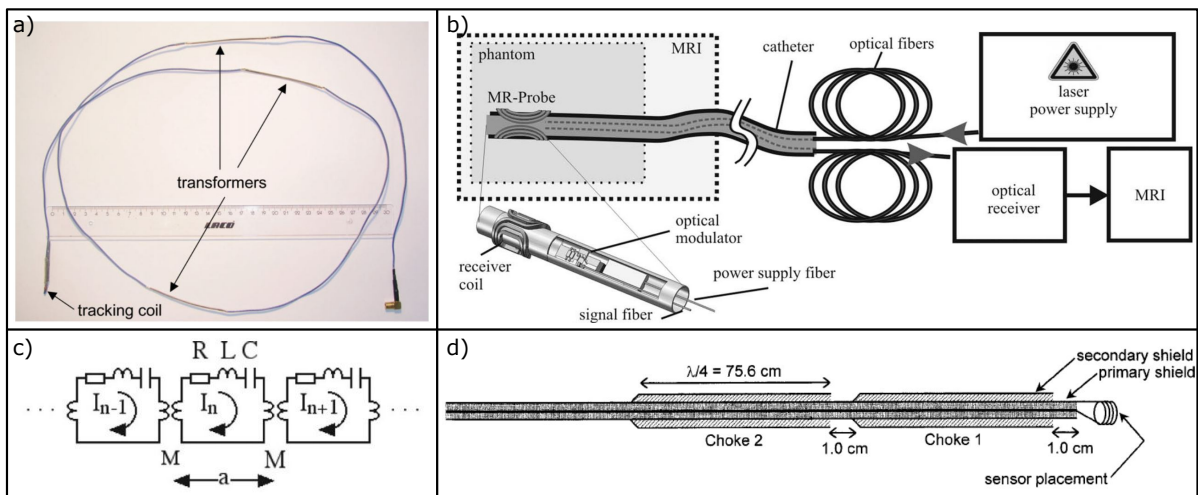
Figure 5.1: Examples of state-of-the-art signal transfer in MR-catheter. **(a)** Integrating miniaturized transformers to divide the conductive transmission wire into small segments, *reprinted from [170] with permission of John Wiley & Sons, Inc. (Copyright © 2005 Wiley-Liss, Inc.).* **(b)** Employing an optical system to transmit the MR signal instead of using conductive wire, *reprinted from [173] with permission of John Wiley & Sons, Inc. (Copyright © 2011 Wiley-Liss, Inc.).* **(c)** Utilizing thin-film magneto-inductive (MI) waveguides to transmit the MR signal, *reprinted from [172] with permission of IEEE (Copyright © 2013 IEEE).* **(d)** Using RF coaxial chokes to block the high-frequency currents, *reprinted from [169] with permission of John Wiley & Sons, Inc. (Copyright © 2000 Wiley-Liss, Inc.).*

5.2.1   Inductive coupling

An alternative approach for tracking the catheter is to wirelessly couple the resonator on the catheter's tip through inductive coupling to an RF surface coil outside the patient [175–179]. The surface coil is conventionally connected to the MRI scanner through a matching and tuning circuit, as shown in Fig. 5.2. A wireless coupling is implemented between the catheter's resonator and the surface coil to avoid any long conductive cables inside the magnet to overcome the heating problem. Tracking the catheter using inductive coupling has proven to be reliable, delivering high contrast visualization.

The micro-resonator on the catheter's tip is tuned to the Larmor frequency, so the exciting magnetic field results in high induced current into the micro-resonator. This current generates a local magnetic field whose flux depends on the coil geometry. The local magnetic field amplifies the MR signal and enhances the tracking image where the micro-coil is shown as a bright spot in the MR image. Consequently, the heat problem of the long wire connection between the catheter and the scanner is eliminated. The only source of heat is the induced current in the resonator.

Multiple surface coils (coils array) can enhance the acquired MR image, which can be post-processed using image processing techniques. The magnetic B_1 fields of the catheter's coil and the surface coil should be aligned for maximum coupling. Otherwise, the coupling decreases as the angle between the B_1 field increases, resulting in losing visibility in orthogonal B_1 fields. Recently, various micro-coil geometries have been adapted as a catheter's micro-resonator, including a surface loop coil, flat spiral coils, two opposing solenoids, a double helical inductors, and a surface loop coil. Figure 5.3 shows an overview of the previously implemented coils for MR-catheter. All proposed designs have fixed capacitance except for the design introduced by Ellersiek et al. [177], where a flexible resonant circuit was developed and fabricated, including a flat spiral coil and tunable capacitor. The tunable capacitor
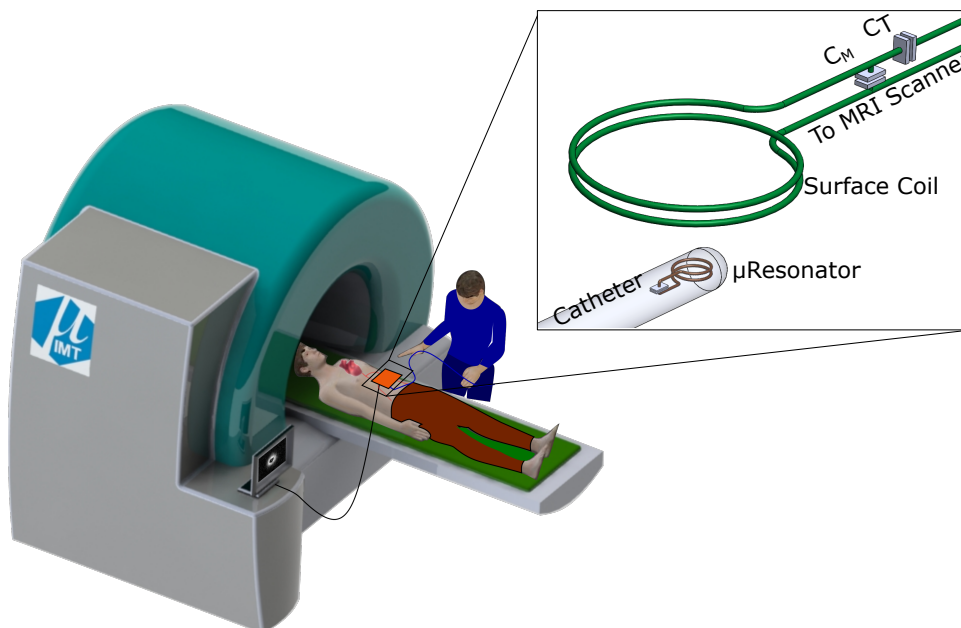
Figure 5.2: interventional Magnetic Resonance Imaging (iMRI) through inductive coupling for safe minimally invasive medical operation.

consists of a main capacitor and detachable capacitors. Calibration is performed manually by cutting parts of the detachable capacitor using a scalpel. After calibration, the resonant circuit is coated by a bio-compatible layer of Parylene-C then attached to the catheter.
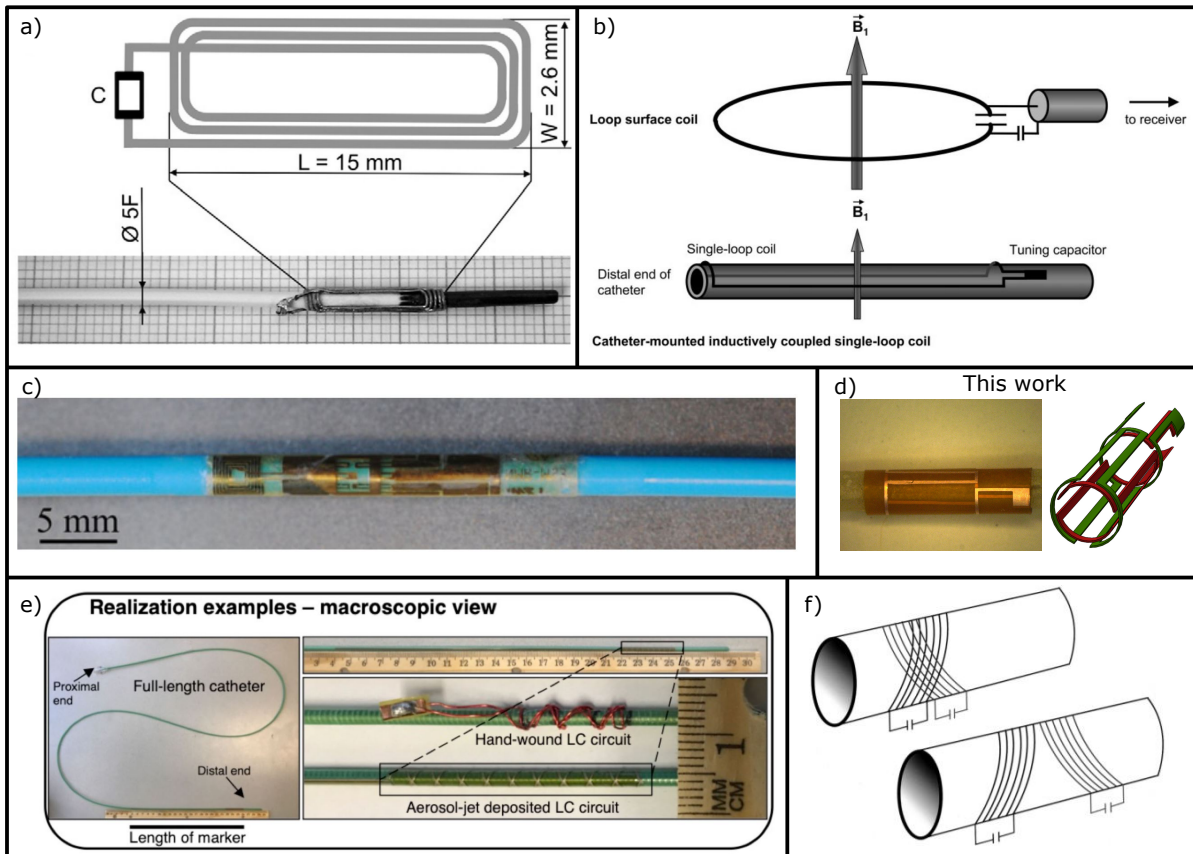
Figure 5.3: Examples of state-of-the-art MR-catheter using wireless inductive coupling. **(a)** A planar rectangular spiral coil attached to a tuning non-magnetic SMD capacitor fixed around the catheter using medical-grade heat-shrink tubing, *reprinted from [179] with permission of Elsevier (Copyright © 2014 Elsevier Inc.).* **(b)** A single loop coil attached to the tuning capacitor is placed around the catheter and coupled to the RF surface coil, *reprinted from [178] with permission of John Wiley & Sons, Inc. (Copyright © 2005 Wiley-Liss, Inc.).* **(c)** A spiral square coil with the capacitor fabricated on thin-film polymer and rolled around the catheter (the 2D structure of the resonator is shown in Fig. 5.5a), *reprinted from [177] with permission of Elsevier (Copyright © 2009 Elsevier B.V.).* **(d)** Two perpendicularly oriented saddle coils were deposited on a polyimide film and rolled around the catheter, *reprinted with permission from [ON3] (CC BY 4.0, 2020 IEEE).* **(e)** A double helix inductor on a polymer catheter achieved using aerosol jet deposition. *reprinted from [175] with permission of IEEE (Copyright © 2019 IEEE).* **(f)** Two separate resonators rolled at a 45° angle with the catheter's axis to decouple them. The resonator can be positioned either adjacent or on top of each other, *reprinted from [176] with permission of John Wiley & Sons, Inc. (Copyright © 2003 Wiley-Liss, Inc.).*

5.2.2   Marker designs

The developed markers (resonators) for the iMRI application should feature several functionalities, including bio-compatibility, sterilization, reliability and validity for tracking, and patient safety. The MRI active marker should be tuned at Larmor frequency [180]. Then during the RF excitation phase, the nuclear spins deflect from their equilibrium position with a flip angle proportional to the alternating magnetic field B_1. The MRI marker (resonant circuit on the catheter's tip) is coupled with the transmit coil, and RF current is induced through the micro-resonator coil. This current generates a magnetic field around the micro-coil that enhances the nuclear spins, enhancing the local magnetic field and the flip angle.

The MRI marker design is influenced by the main B_0 field orientation and amplitude which defines the Larmor frequency and the required orientation of the resonator's B_1 field; B_0 and B_1 fields should be perpendicular. Different shapes of resonant MRI markers are shown in Fig 5.4. For example, in the case of closed MR scanners, the B_0 field is parallel to the interventional instrument, so the saddle, spiral, and single loop coils are preferred. On the other hand, for open MR scanners, cylindrical loops are preferred as the B_0 field is perpendicular to the interventional instrument.

Additionally, for each application, the orientation, geometries, surface material, and stiffness of the interventional instrument define the coil design, fabrication technology, and the required adhesion material. For example, for soft intervention into the body, on the one hand, the catheter end should be soft to avoid damaging the blood vessels. On the other hand, it should be stiff enough to support push ability. Hence, the size of the micro-coil is important to support the catheter properties. Moreover, optimizing the coil's geometry defines its self-resonance frequency and quality factor.

The basic configuration of a resonant circuit consists of a coil and capacitor in parallel to tune the resonance frequency ($f = 1/\sqrt{LC}$). Using SMD capacitors is not preferred as they are bulky and not bio-compatible. Other approaches have been to integrate the capacitor, including a cylindrical or roll-up capacitor [177]. Multi-layer capacitors can also be fabricated along with the coil to increase the capacitor aspect ratio to be suitable for integrating on an interventional instrument [72], as shown in Fig. 5.5. Another good approach is using small capacitors with detachable connections [177], allowing editable capacitance for fine-tuning purposes.
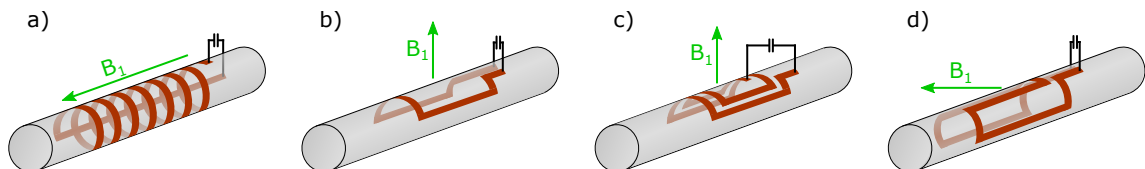
Figure 5.4: Different shapes of resonant MRI markers used for MR-catheters [180]. **(a)** Cylindrical coil. **(b)** Single-loop coil. **(c)** Spiral coil. **(d)** Saddle coil.

5.2.3   Marker fabrications

Different fabrication technologies have been considered for developing resonance markers around the catheter tube, including wire-winding, thin-film technology, inkjet-printing, hot embossing technology, and aerosol deposition process. Kaiser et al. have compared the different fabrication technologies for iMRI in their review paper [180]. The wire-winding technology is a simple 3D manufacture process where a wire is wound around a tube with the required geometry then soldered to an SMD capacitor. However, the wire-winding process faces many issues, including poor reproducibility, instrumentation diameter enlargement, restriction to cylindrical coils, and good fixation techniques.

Thin-film technology includes the patterning of the target 2D structure of a conductive layer on a carrier insulating film, then roll it around a tube to achieve the required 3D structure. This technology includes micro-fabrication methods such as spin coating, photoresist patterning, masked UV light exposure, etching, galvanization, and cleaning processes. On the one hand, thin-film technology provides accurate structures, flexible substrate, and high reproducibility. However, on the other hand, it is costly and requires expensive equipment.

The hot embossing fabrication process [181] is used to achieve a conducting structure onto a thermoplastic instrument using negative embossing stamps under suitable temperature and pressure. First, the stamp is pressed against a metallic foil that is mounted around the instrument. Then the stamp punches out the unneeded parts of the metallic foil, leaving behind the required structure. This technique provides high reproducibility of mechanically stable structures with low cost. However, the base instruments should be made of thermoplastic, and 3D structures can be challenging to be fabricated.

The aerosol-deposition [175] process is used to deposit catalytic nano ink to fabricate 3D structures directly on the instrument. This process can print conductive, insulating, and adhesive layers. Aerosol Jet deposition technology can deposit structures independent of the base substrate shape and material. However, the resulted structures have low mechanical stability, and the process requires high-cost materials.
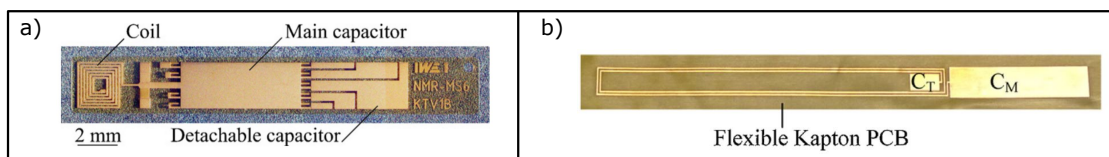
Figure 5.5: Examples of state-of-the-art fabricated capacitors for MR-catheter. **(a)** A manually editable tuning capacitor fabricated on a polymer substrate, *reprinted from [177] with permission of Elsevier (Copyright © 2009 Elsevier B.V.)*. **(b)** A fabricated fixed multi-layer tuning capacitor, *reprinted from [72] with permission of Elsevier (Copyright © 2015 Elsevier B.V.)*.

6 Novel wireless decoupling system[1]

Catheters can be visualized in the MR environment during minimally invasive surgery by locating a micro-resonator on the tip of the catheter. By tuning the resonator to the Larmor frequency of abundant nuclei and exposing it to the RF magnetic field, its motion can be tracked in real-time under direct image guidance. However, the conductive wires that connect the resonator to the MRI spectrometer, for signal transfer, tuning and matching, is known to cause dangerous tissue heating. A promising approach is to track the resonator wirelessly using a wired resonator outside of the body through inductive coupling. The matching and tuning network is then connected to the external resonator. The inductive coupling approaches face two challenges: i) during the RF excitation stage, a strong electric field is induced inside the MR-catheter resonator, leading to dangerous heating. However, the resonator should be sensitive only to the nuclear magnetic field during the receiving (sensing) stage. ii) As the catheter axial orientation changes during motion, the coupling between the MR-detector and the surface coil will be affected, which results in a difference in the catheter visibility. Visibility can be lost if the resonator and external coil fields B_1 are orthogonal. In this contribution, a novel wireless decoupling system is introduced where the resonance frequency of the resonator on the catheter tip can be tuned wirelessly. Consequently, the resonator's resonance frequency is controlled via a pulse sequence sent to an RF microelectronic system integrated with the detector coil to couple it during the acquisition stage. Moreover, a novel detector design is proposed based on two perpendicular miniaturized saddle coils that maintain constant coupling between the external coil and the MR-catheter detector at all axial orientations.

This chapter is divided into three main sections. The first section 6.1 explains the working concept of the wireless decoupling system. The second section 6.2 presents the technical details of the different electronic building blocks of the system proposed for decoupling the MR-catheter resonator wirelessly. Within this section, the fabrication and characterization of the developed system are also discussed. The third section 6.3 presents a novel double saddle coil for wireless tracking of the MR-catheter during interventions with orientation independence. This section discusses the modeling and design of the proposed double detector. Moreover, the performance of the detector is characterized using numerical simulations and confirmed with experiments.

6.1 System description

Figure 6.1 demonstrates an overall schematic diagram of a minimally invasive medical operation under iMRI through inductive coupling. It also shows a detailed illustration of the developed microelectronics system as well as the used MRI pulse sequence. The developed system for tracking the catheter tip consists of four resonators; two relatively big surface coil outside the body and two micro-resonators on the catheter tip inside the body. Each of the four resonators has a specific functionality:

---

[1]This chapter's text and figures were reproduced and adapted with permission from the author's published works [ON3] (CC BY 4.0, 2020 IEEE) and [ON6] (Copyright © 2019, IEEE)
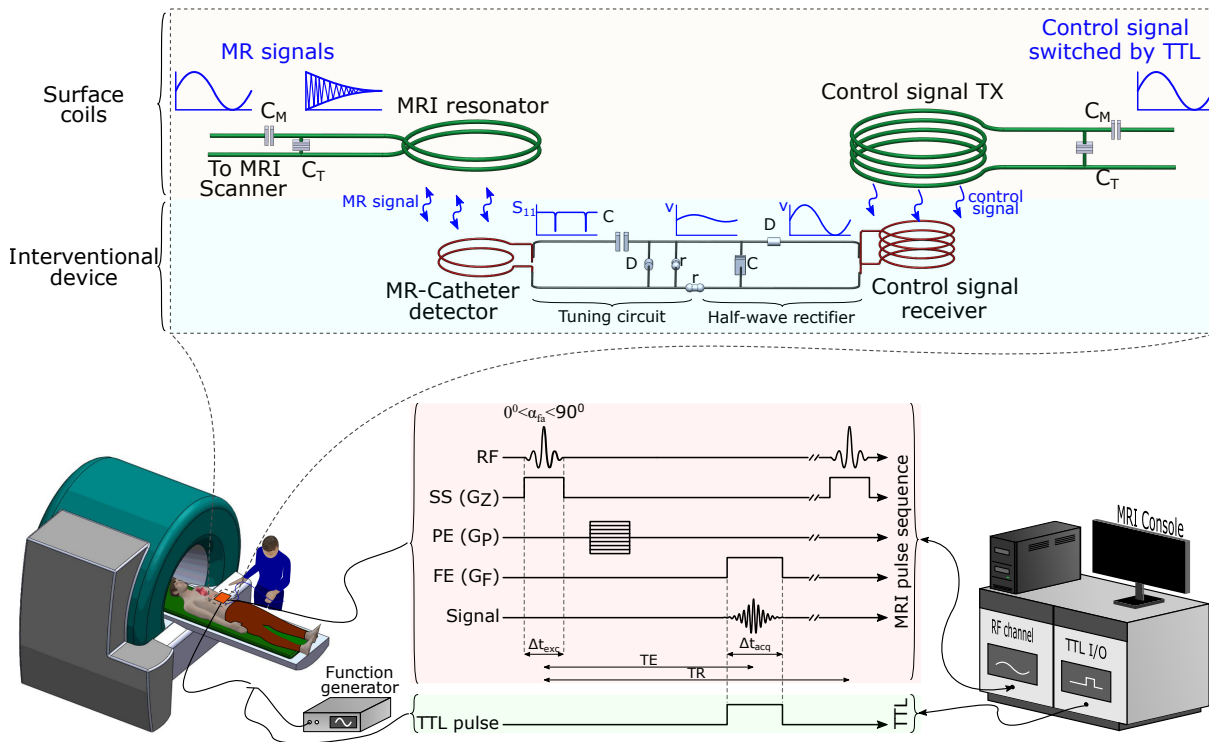
Figure 6.1: Overall schematic diagram of a minimally invasive medical operation under iMRI through inductive coupling with implementing wireless detuning system. [Bottom] The adapted MRI pulse sequence and RF connections. [Top] A detailed illustration for the developed micro-electronic system. Two surface coils are used, one coil to transmit and receive the MR signal and the other coil for transmitting a control signal. Two micro-resonators are positioned on the catheter tip, one resonator for collecting the nuclear magnetic signal to be visualized in the MR image. The other micro-resonator pickups the control signal to tune the first micro-resonator.

1. One of the two surface coils is tuned to the Larmor frequency and acts as the imaging coil where it is fed with the MRI pulse sequence from the spectrometer. This surface coil is used for generating the MR image and tracking the resonator on the catcher tip. This coil is referred to as the *"MRI surface coil"*.

2. The other surface coil is tuned to a resonance frequency below the Larmor frequency (1-10MHz). This coil is connected to a function generator through a switch controlled by a trigger pulse (TTL) generated by the MRI console's TTL input/output (I/O) unit. This surface coil is used for transmitting a control signal for tuning the detector on the catheter tip. This coil is referred to as the *"control signal transmitter"*.

3. One of the two resonators on the catheter tip is tuned to control signal's frequency as the control signal transmitter coil; thus, this resonator acts as a receiver for the control signal. In addition, this resonator is connected to a half-wave rectifier to generate a DC signal fed to a variable capacitor (varicap) to control the tuning frequency of the other MR-catheter resonator. This coil is referred to as the *"control signal receiver"*.

4. The other micro-resonator on the catheter tip is tuned to a frequency close to the Larmor frequency and is connected in parallel to the varicap. Hence, the DC control signal fed to the varicap can tune it to the Larmor frequency to be visible in the MR image. This coil is referred to as the *"MR-catheter detector"*.

Initially, the MR-catheter detector is not tuned to the Larmor frequency for considering fail-safe condition; therefore, no electric field is generated during the excitation phase, preventing the heating hazard. Then during the relaxation stage, a TTL pulse is sent by the MRI console, which switches on the control signal transmitter coil to transmit the control signal. Consequently, the control signal is picked up by the control signal receiver on the catheter tip. A half-wave rectifier generates a DC signal from the received control signal, which is then fed to a varicap to tune the MR-catheter detector to the Larmor frequency. Hence the MR-catheter detector becomes sensitive only to the nuclear magnetic field and could be visually detected in the MR image with eliminating the heating effect.

6.2   Wireless decoupling system

Figure 6.2 presents an equivalent schematic circuit of the developed wireless decoupling system. Three electric circuits represent the whole MR-catheter tracking system with the integrated wireless decoupling feature:

1. The equivalent circuit of the MRI surface coil (L_{S1}), as shown in Fig. 6.2 (shaded in blue). The coil is connected to the MRI scanner through the matching and tuning network (C_{M1} and C_{T1}). For connecting the coil to the MRI scanner, its impedance should match the transmitting cable impedance ($50\,\Omega$). Hence C_{T1} is used to tune the surface coil ($f_{L_{S1}} = 1/\sqrt{L_{S1}C_{T1}}$) and set the impedance real part to $50\,\Omega$, while C_{M1} eliminates the residual imaginary part.

2. The equivalent circuit of the control signal transmitting coil (L_{S2}), as shown in Fig. 6.2 (shaded in green). The coil is connected to a function generator through the matching and tuning network (C_{M2} and C_{T2}). The circuit possesses a switch (solid-state relay) controlled via the TTL pulse sent by the MRI console during the acquisition state.
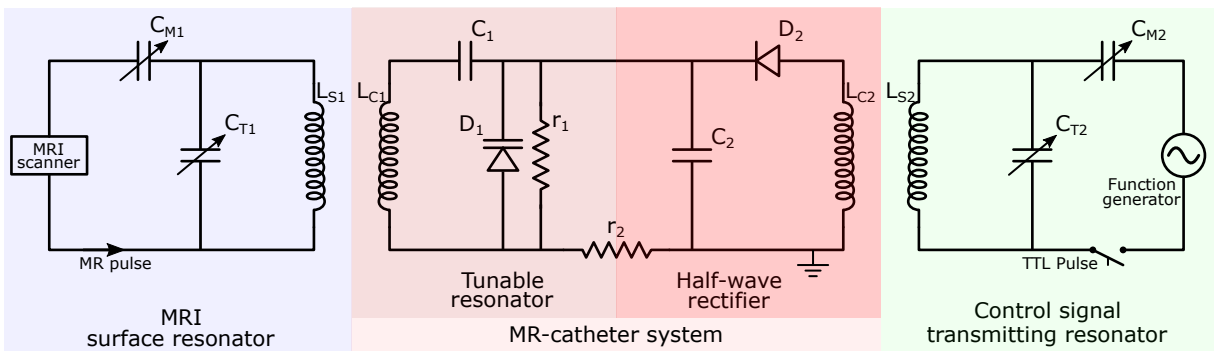
Figure 6.2: Equivalent schematic circuit of the wireless decoupling system for safe MR-catheter tracking. The equivalent circuits of MRI surface coil resonator [Blue], control signal transmitting resonator [Green], and wireless tunable detector on the catheter tip [Red].

3. The equivalent circuit of the wireless tunable detector on the catheter tip, as shown in Fig. 6.2 (shaded in red). The micro-resonator (L_{C2}) is tuned using D_2 and C_2 to the control signal's frequency to pick it up;

$$f_{Control} = F_{L_{S2}} = 1/\sqrt{L_{S2}C_{T2}} = F_{L_{C2}} = 1/\sqrt{L_{C2}(D_2C_2/D_2+C_2)}. \qquad (6.1)$$

The micro-resonator (L_{C1}) is tuned using D_1 and C_1 to a frequency close to the Larmor frequency to be coupled to the MRI surface coil during the acquisition stage to appear in the MR image;

$$f_{Larmor} = F_{L_{S1}} = 1/\sqrt{L_{S1}C_{T1}} = F_{L_{C1}} = 1/\sqrt{L_{C1}(D_1C_1/D_1+C_1)}. \qquad (6.2)$$

The D_2 and C_2 configuration create a half-wave rectifier. Hence it generates a DC signal from the received control signal, which in turn is fed to D_2 (varicap) to change the resonance frequency of the MR detector (L_{C1}). The resistance (r_2) is added to the ground line to isolate the electric fields of the two micro-resonators so that they do not interfere, i.e., r_2 should be in the MΩ range. The resistance (r_1) is added in parallel to D_2, so once the control signal is switched off, D_2 can dissipate the provided dc signal to the ground line and returns to its initial. The value of r_1 should be high enough to force the DC control signal to pass through D_2 during the tuning phase; i.e., r_1 should be in the MΩ range.

6.2.1   Fabrication of the wireless decoupling device

The whole microelectronics circuit on the catheter tip was fabricated using the thin-film fabrication processes described in Chapters 3 and 4. The dimensions of the fabricated device with its electronic components are defined mainly by the operating frequencies of the MR signal and control signal. The MR signal frequency is determined by the Larmor frequency. On the other hand, the control signal frequency could be adjusted to satisfy the fit to the application. The control signal should operate at a frequency away from the Larmor frequency to not interfere with the MR signal. Hence, in principle, the control signal could operate above or below the Larmor frequency. Operating above Larmor frequency provides the advantage of a low tuning capacitor (smaller dimension), but rectifying thin-film diodes are limited to low frequency. On the other hand, operating below Larmor frequency, the signal could be rectified using a thin-film diode, but the coil requires high capacitance for tuning. Therefore, an operating frequency of 20 MHz was chosen for the control signal to be rectified using a thin-film diode. In addition, the resonance frequency of the L_{C2} resonator is reduced to 20 MHz by increasing the coils' inductance (increase outer dimensions and the number of turns), as shown in Fig. 6.3a. For both resonators (MR-catheter detector and control signal receiver), a spiral surface coil was used. Table 6.1 summarizes the dimensions of both resonators with the experimentally measured inductance.

Based on the inductance of both resonators, the required capacitance was calculated to tune the resonator for the intended frequencies. The MR-catheter detector L_{C1} was designed to have a resonance frequency of 60 MHz (18 MHz above the Larmor frequency in a 1 T MRI scanner). Hence, considering the capacitance of D_1 of 62 pF, C_1 was designed (by setting the capacitor area and selected insulating material) to have a capacitance of 196 pF. The control signal resonator L_{C2} was designed to have a resonance frequency of 20 MHz (more than 20 MHz away from Larmor frequency in a 1 T MRI scanner). Hence,
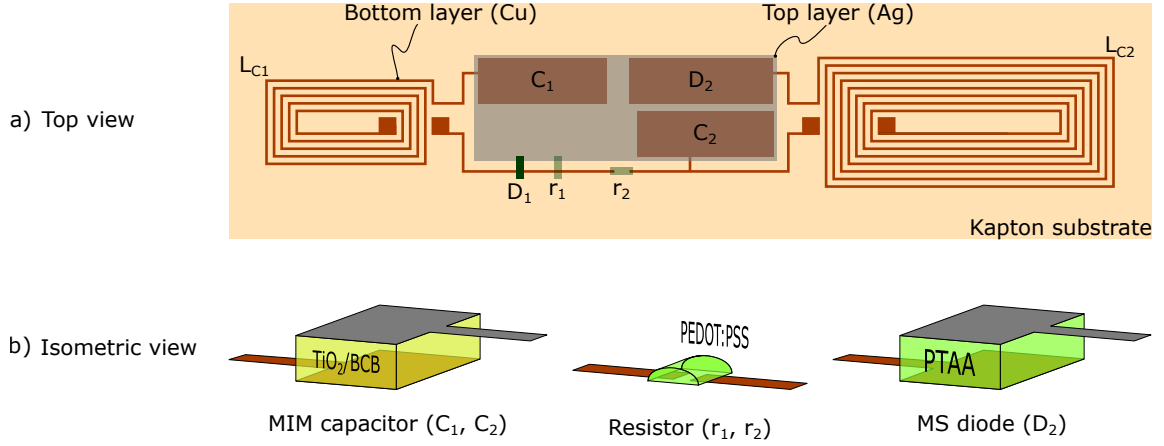
Figure 6.3: Schematic illustration of the designed electronic device for controlling the MR-catheter resonance frequency wirelessly. **(a)** Top view of the device with the bottom copper layer and top silver layer. **(b)** Isometric views of the capacitor, resistor, and diode.

the capacitance of C_2 and D_2 was designed to be 379 pF and 389 pF, respectively. Table 6.1 summarizes the designed dimensions and the expected values of the fabricated capacitors and diode.

The capacitors C_1 and C_2 were fabricated using the thin-film technology developed in Section 3.2, where an insulating film is inkjet-printed between two conductive layers. The rectifying diode D_2 was fabricated using the technology developed in Section 3.3, where a p-type semiconductor is spin-coated between two conductive sheets having different working functions (WF). The resistors r_1 and r_2 were fabricated by drop-casting of the conductive polymer PEDOT:PSS (Poly(3,4-ethylenedioxythiophene)-poly(styrenesulfonate), Sigma-Aldrich) between two discontinuous conductive traces. PEDOT:PSS polymer was employed to build the resistors as it possesses higher resistivity than most other inorganic material, resulting in the required MΩ resistance. Moreover, it can be processed in solution with stability in the ambient atmosphere. For the varicap D_2, a discrete component was used (BB640E6327HTSA1, Infineon). However, fabricating a varicap using thin-film technology is under investigation in our group.

Table 6.1: The geometrical dimensions and value of each electronic component included in the micro MR-catheter device.

Parameter	Geometrical dimensions	Value
MR-catheter detector (L_{C1})	L= 8.2 mm, W= 3.6 mm, W_{track}=150 µm, n= 5	146 nH[a]
Capacitor (C_1)	L= 3 mm, W= 2 mm, ε_0= 7, d= 1.9 µm	196 pF[b]
Control Signal RX (L_{C2})	L= 12.45 mm, W= 5 mm, W_{track}=150 µm, n= 8	362 nH[a]
Capacitor (C_2)	L= 5 mm, W= 1.2 mm, ε_0= 20, d= 2.8 µm	379 pF[b]
Capacitor (D_2)	L= 3 mm, W= 2 mm, ε_0= 3, d= 0.41 µm	389 pF[b]

[a] Measured experimentally using sniffer coil and network analyzer.

[b] Calculated according to: *Capacitance* $= \varepsilon_0 \varepsilon_r A / d$.

6.2.2 Experimental result of the wireless decoupling system

First, the bottom layer was inkjet-printed using silver ink on a 25 μm Kapton film. The bottom layer contains the two resonators (L_{C1} and L_{C2}), the bottom layer of the capacitors (C_1 and C_2) and diode D_2, and discontinuous lines for building the resistors (r_1 and r_2). The bottom layer was then electroplated with a 10 μm copper layer, as shown in Fig. 6.4a. The copper layer is required to reduce the RF resistance and provide a low WF material for the diode. Next, on top of the C_1 pad, an insulating layer is printed using BCB/TiO$_2$ composite ink (20wt.%, $\varepsilon_r = 7$) developed in Section 3.2. This ink was selected as C_1 has a relatively low capacitance (≈ 196 pF). On the other hand, for C_2, the composite ink BCB/TiO$_2$ (40wt.%, $\varepsilon_r = 20$) was used as it has relatively high capacitance (≈ 379 pF). Then, on top of the diode D_2 pad, a layer of the PTAA semiconductor was spin-coated (measured thickness= 410 nm, $\varepsilon_r = 3$). Consequently, on top of the insulating and semiconductor layers, a silver layer was inkjet-printed. Then, the resistors were achieved by drop-casting of the PEDOT:PSS polymer. Figure 6.4b presents the final device before rolling around the catheter tube. Finally, the device was rolled around an 8 fr catheter tube.

The measured tuning frequency of the MR-catheter resonator and control signal receiver resonator were 56.5 MHz and 23 MHz. Figure 6.5 presents an experimental setup to verify the functionality of the fabricated device for wireless tuning. First, a macro resonator (mimic L_{S2} in Fig. 6.2) tuned to 23 MHz and connected to a function generator placed 1 cm away from the control signal receiver coil L_{C1}. Moreover, a sniffer coil was positioned facing the MR-catheter detector L_{C1} and connected to a network analyzer (Agilent E5071C) for measuring the detector resonance frequency. The sniffer coil enables detecting the resonance frequency of a resonator without any direct wire connections [182, 183]; a description of the sniffer is attached in appendix C.

The plot in Fig. 6.5 shows the measured reflection coefficient (S_{11}) of the sniffer coil. Each peak represents the resonance frequency of the MR-catheter detector at different voltage levels supplied to the control signal transmitter coil via the function generator. Thus, the developed system successfully tuned the resonance frequency of the MR-detector wirelessly, which proves that it can decouple the resonator inside the patient wirelessly. The resonance frequency could be tuned within a 15 MHz range equivalent to a 7 V range of the control signal amplitude. Increasing the control signal amplitude over 7 V

a) Bottom layer

Bottom Copper layer (inkjet-printing + electroplating)

Top silver layer

b) Full device

C_1 D_2
C_2
D_1
MR detector r_1 and r_2 Control signal receiver
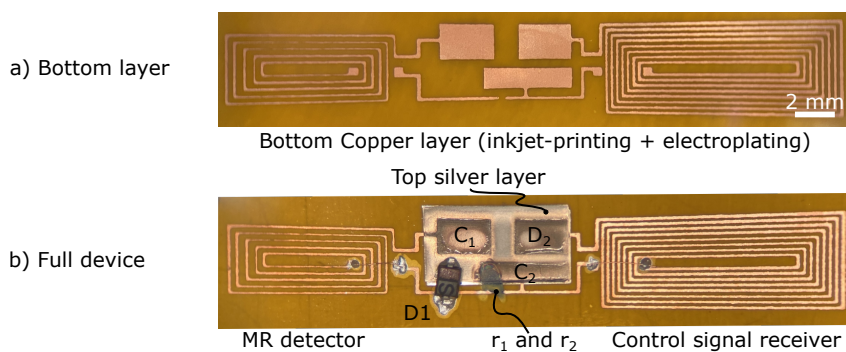
Figure 6.4: Fabricated device for wirelessly tuning the MR-catheter detector resonance frequency. **(a)** Bottom layer achieved by silver inkjet-printing and copper electroplating. **(b)** Full device after depositing capacitors insulator, diode semiconductor, top silver layer, and resistors conductive polymer.
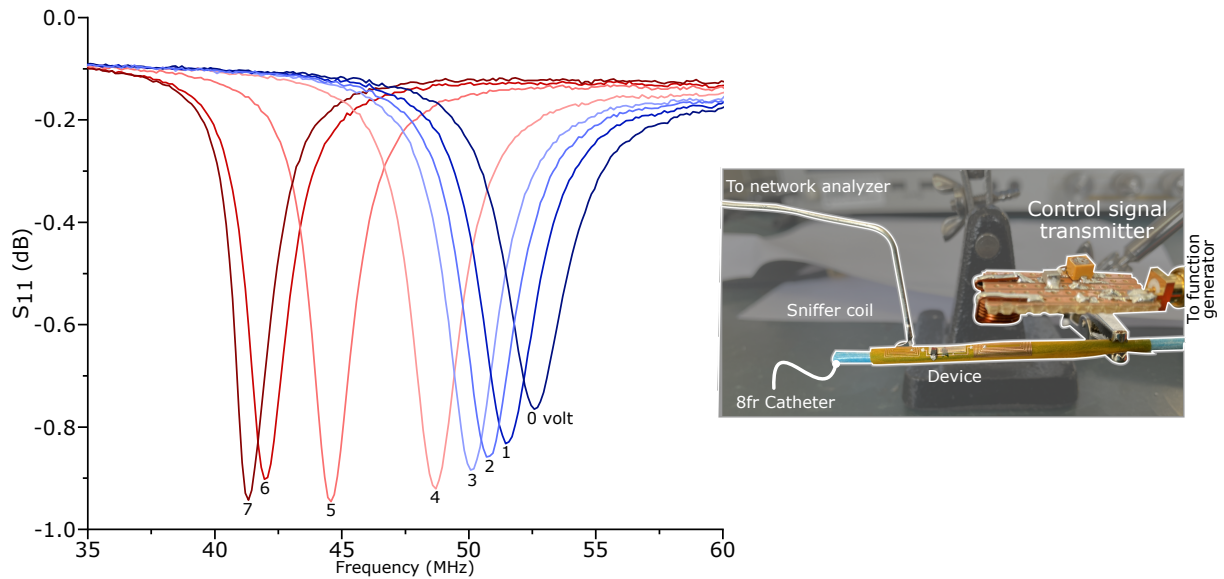
Figure 6.5: Experimental results of tuning the MR-catheter detector wirelessly. **(a)** Reflection coefficient of the sniffer coil, where each peak represents the MR-catheter detector resonance frequency at different amplitudes of the control signal. **(b)** Photo for the testing setup.

did not further change the resonance frequency, indicating that the varicap reached its limit. It was observed that as the amplitude of the control signal increases, the resonance frequency decreases, which indicates that the varicap D_1 capacitance increases with the control signal. The increase in the varicap capacitance implies that it is supplied with a negative voltage. This is because the D_2 configuration (silver-PTAA-copper) cuts the positive part of the control signal and rectifies the negative part of the signal. Nevertheless, if it is required that the resonance frequency increase with the control signal, the diode configuration could also be inverted (copper-PTAA-silver). However, this was done to simplify the fabrication process; otherwise, more than two printed conductive layers will be required. Moreover, the working principle of the system is still valid.

The introduced fabrication process's overall yield is relatively low, out of a batch of 20 devices, only four of them work as expected. This is due to the complexity of the device and the involvement of several materials (conductor, semiconductor, insulator) in the fabrication process. The main problem with inkjet-printing that each device is fabricated separately, and the operators skills significantly affect the result. Hence, one solution would be utilizing a different process compatible with mass production where the operators skill is marginalized, such as screen printing or roll-to-roll processes.

6.3 Double-saddle micro-resonator

In the introduced system, the catheter tip is being tracked inside the patient by wirelessly coupling a micro-resonator on the catheter tip with an outside surface coil through inductive coupling. The surface coil in this system is connected to the MRI scanner through a matching and tuning network. The maximum coupling between the micro-resonator and the surface coil occurs when their B_1 magnetic fields are aligned. At this arrangement, with both B_1 fields aligned, the maximum visibility of the catheter tip in

the MRI scanner is achieved. However, as the catheter axial orientation changes during the medical operation, the resonator's visibility varies and can be lost when the B_1 fields of the catheter micro-resonator and the surface coil are approximately orthogonal [176, 178]. Additionally, as the magnetic coupling changes with the catheter motion and orientation, the entire system demands to be re-matched and tuned.

In the following subsections, the design and fabrication of a micro-resonator based on a double saddle coil is proposed. The developed micro resonator maintains almost constant maximum coupling between the B_1 fields of the micro-resonator on the catheter tip and the external surface coil throughout the entire range of axial orientations.

6.3.1   Modeling and simulation of inductive coupling for iMRI

An RF resonator mainly consists of an inductor connected in parallel to a capacitor. For a lumped-parameter RF resonator, the angular resonance frequency ω_0 depends on its capacitance C and inductance L and is given by $\omega_0 = 1/\sqrt{LC}$. When the coils of two RF resonators are in close proximity to each other, where the magnetic field generated by one coil cuts the loops of the other coil, they turn to be inductively coupled and share a mutual inductance M_{12}, as shown in Fig. 6.6. Depending on the coupling strength, the resonance frequency of each of the two inductively coupled resonators is shifted away from its initial value. If both of the RF resonators are tuned to the same initial resonance frequency ($\omega_0 = \omega_{01} = \omega_{02}$), then coupling will split this frequency, resulting in two frequencies shifted $\omega_{1,2}$ to the left and right of the initial value,

$$\omega_{1,2} = \frac{\omega_0}{\sqrt{1 \pm K}}, \tag{6.3}$$

where K is the inductive coupling coefficient, which depends on the mutual inductance between the two coils and is given by $K = M_{12}/\sqrt{L_1 L_2}$. Applying voltage to one of the two inductively coupled resonators (V_S) induces a voltage in the other resonator (V_{OUT}), as shown in Fig.6.6:

$$V_{Out} = V_S \frac{Z_2 j\omega M_{12}}{Z_1 Z_2 + (j\omega M_{12})^2}, \tag{6.4}$$

where Z_1 and Z_2 are the impedance of the two resonators. Equations 6.3 and 6.4 are driven in appendix C. Agilent's advanced design system (ADS) software was used to simulate the frequency splitting for a pair of inductively couple RF resonators. The two simulated resonators were identical (R= 1 Ω, L= 50 nH,
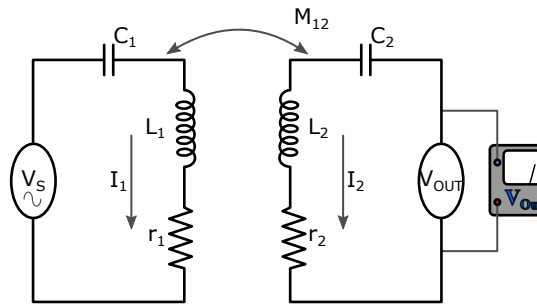
Figure 6.6: Equivalent schematic circuit of two inductively coupled RF resonators.
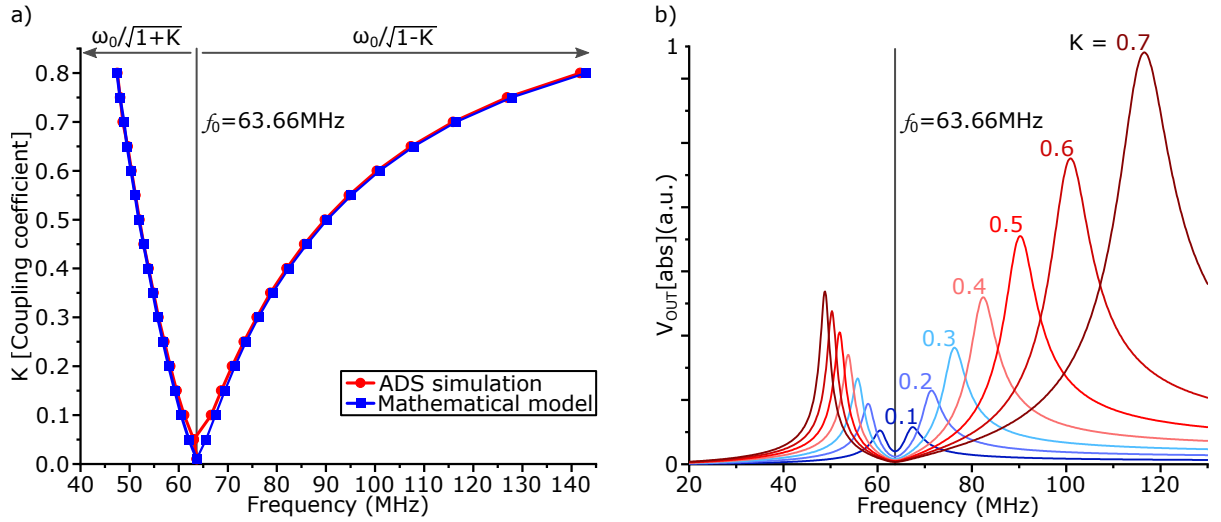
Figure 6.7: Resonance frequency splitting due to inductive coupling. **(a)** Degree of the resonance frequency splitting versus coupling coefficient (K), comparing the mathematical model is compared to the ADS simulation. **(b)** The induced output voltage at different K, labeled in the figure.

C= 125 pF) with an angular resonance frequency of $\omega_0 = 63.6$ MHz, a photo of the ADS simulation environment is attached in appendix C. The voltage supplied to one of the two resonators was set to unity, and the coupling coefficient (K) was swept. Figure 6.7b shows a comparison between the simulation results and the mathematical model. Figure 6.3b illustrates the shape of the induced voltage in the other resonator at different coupling confidence using Equation 6.4. The figure shows the induced voltage reduction as the coupling decreases.

Tracking catheter using a single coil is not reliable due to the impact of the catheter axial orientation on the catheter visibility. The coupling coefficient changes as the catheter's axial orientation varies with respect to the static surface receiver coil during interventions. Hence, the entire system needs to be re-tuned and matched with the catheter motion and orientation. Moreover, the visibility can be lost if the B_1 fields of the catheter-detector and surface coil become orthogonal. Therefore, a novel micro-detector is introduced based on two orthogonal saddle coils, as shown in Fig. 6.8a. The proposed detector maintains near-constant coupling with the surface coil under the entire range of the catheter axial orientations. The two saddle coils are arranged to have their B_1 fields orthogonal, which effectively decouples them. The two coils are connected in series and tuned by a single capacitor to the Larmor frequency, as illustrates in the equivalent schematic circuit in Fig 6.8b.

The finite element analysis software COMSOL multiphysics was used to gain insight into the B_1 field distribution generated by micro-detector in the space around the catheter. Additionally, the simulation was utilized to evaluate the angular dependence of the coupling between the micro detector and the surface coil. Two simulation scenarios were considered:

1. In the first simulation model, a micro-saddle detector was excited using a $50\,\Omega$ port, and the magnetic flux density was plotted around the detector. Two micro-detector designs were simulated based on single and double saddle coil. In each case, the perimeter gap (see Fig. 6.8 for
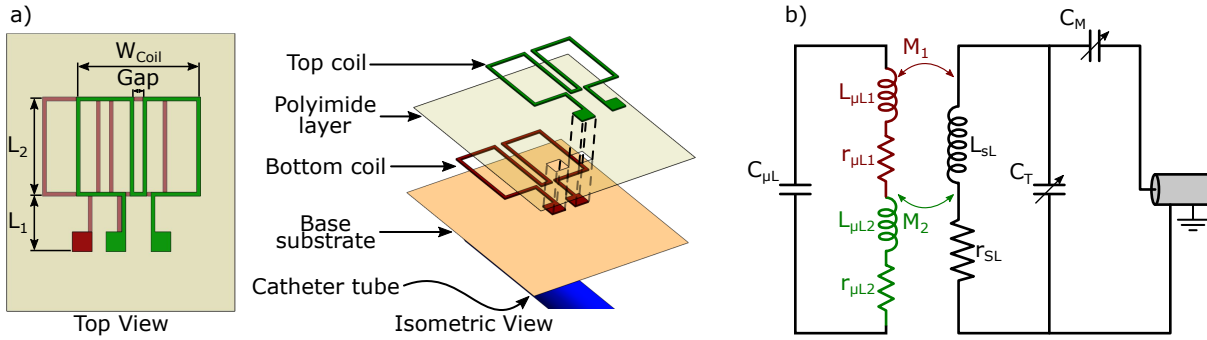
Figure 6.8: Double saddle coil for MR-catheter tracking through inductive coupling. **(a)** CAD-drawing illustrating the design of the double saddle coil. **(b)** Equivalent schematic circuit for a tuned double saddle detector inductively coupled to a surface pickup coil.

description) between the saddle's two square loops was swept to achieve the best magnetic field distribution.

2. In the second simulation model, the excitation port was connected to a stationary surface coil, and the micro-detector was connected to a port for measuring the induced voltage, as shown in Fig. 6.10. Single and double saddle micro-detectors were considered, and in each case, the three possible relative orientations between the surface coil and the micro-detector (roll, pitch, and yaw) were swept from $0°$ to $360°$.

The COMSOL radio frequency module was used for both simulation models, and simulations were run at a 63 MHz excitation frequency. As part of the simulation environment, the micro-detector was positioned inside a box-shaped domain to represent the surrounding sample (water), which was then located inside a bigger box-shaped domain to mimic the ambient air. A radiation boundary condition was employed to act as an absorbing layer to prevent back-scattering. The free tetrahedral mesh was refined to resolve the modeled structures correctly, as shown in Fig. 6.10a.

Figure 6.9 summarizes the results of the first simulation scenario. The results revealed that the micro-detector with a double-saddle provides more magnetic flux sources around the detector than the single-saddle detector. The distribution of the generated magnetic field around the detector can be manipulated by varying the perimeter gap between the saddle coil's two square loops. By setting the detector dimensions to the values listed in Table. 6.2 and sweeping the gap, it was found that the best homogeneity for the magnetic field was obtained at a gap of $450\,\mu m$. Hence, a gap value of $450\,\mu m$ was used for further simulations and fabrication.

Figure 6.10b-d summarize the results of the second simulation scenario. The variation in the induced voltage in the micro detector with the change in the relative axial orientation is shown in Fig. 6.10b. In the case of a single saddle coil, the coupling between the micro-coil and the surface coil was maximum when their B_1 fields were aligned, and as the relative angle between the B_1 fields increases, the coupling decreases. Accordingly, no coupling was observed (i.e., no voltage induced in the micro-coil) when an orthogonal position was taken. On the other hand, for a double saddle coil, the coupling remained constant over the entire range of relative axial orientations, with values alternating above the single
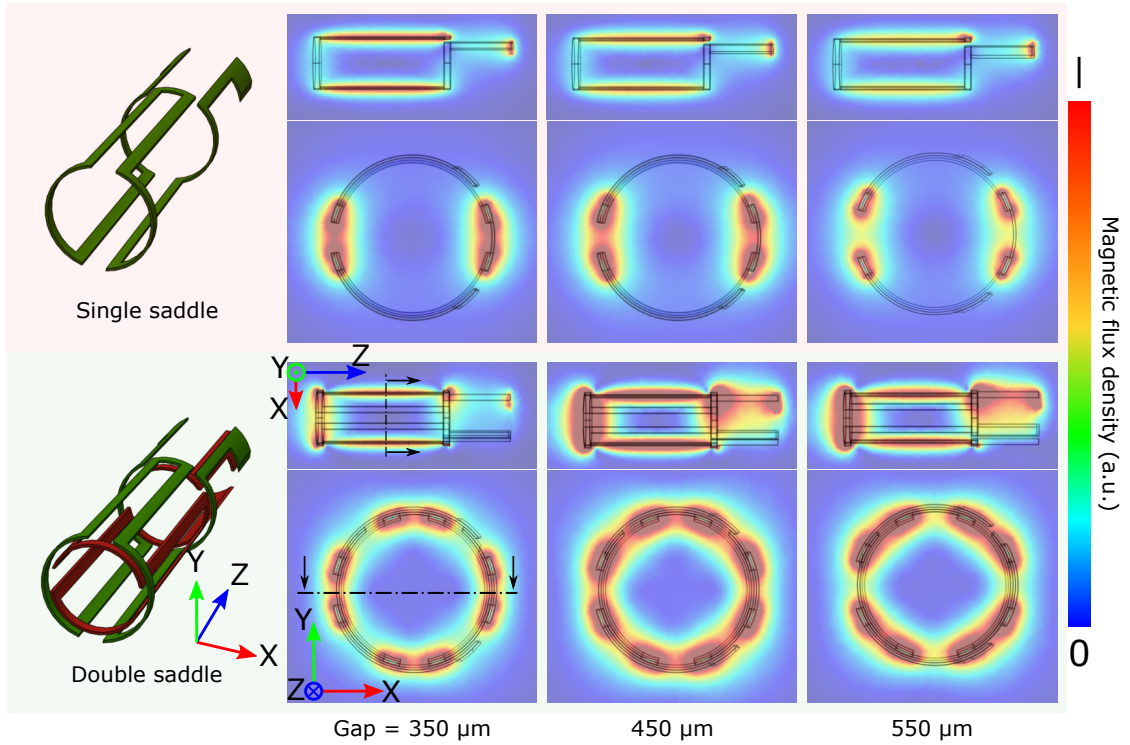
Figure 6.9: The simulated magnetic field generated the micro-saddle detectors excited at 63 MHz. The top row demonstrates the magnetic field distribution generated by a single saddle coil, while the bottom row presents the magnetic field generated by a double saddle detector. For each case, the magnetic field direction is presented at two different cross-section views, one perpendicular to the coil's axis (XY-plane) and the other along its axis (XZ-plane). In addition, the magnetic field direction is plotted at different perimeter gaps to deduce the change in the magnetic field distribution with the gap.

saddle coil's maximum value. This is because the total coupling of the whole double saddle detector is the summation of the coupling of each of the single saddle coils within the double saddle detector with the surface coil. Thus, a coupling reduction of a single saddle element is accompanied by a coupling increase in the other saddle element. The variation in the induced voltage in the micro detector with the change in the relative angle between coil axes shown in Fig. 6.10c. For both double and single saddles, the maximum coupling occurs when the surface coil axis and the saddle coil axis are orthogonal, and minimum coupling occurs when the two axes coincided. The change in the coupling as the micro detector

Table 6.2: Geometrical dimensions of the double saddle coil used for MR-catheter tracking.

Parameter	value
Coil length ($L_1 + L_2$)	8 mm
Detection region length (L_2)	5 mm
Coil width (W_{Coil})	5 mm
Gap	450 µm
Track width (W)	200 µm
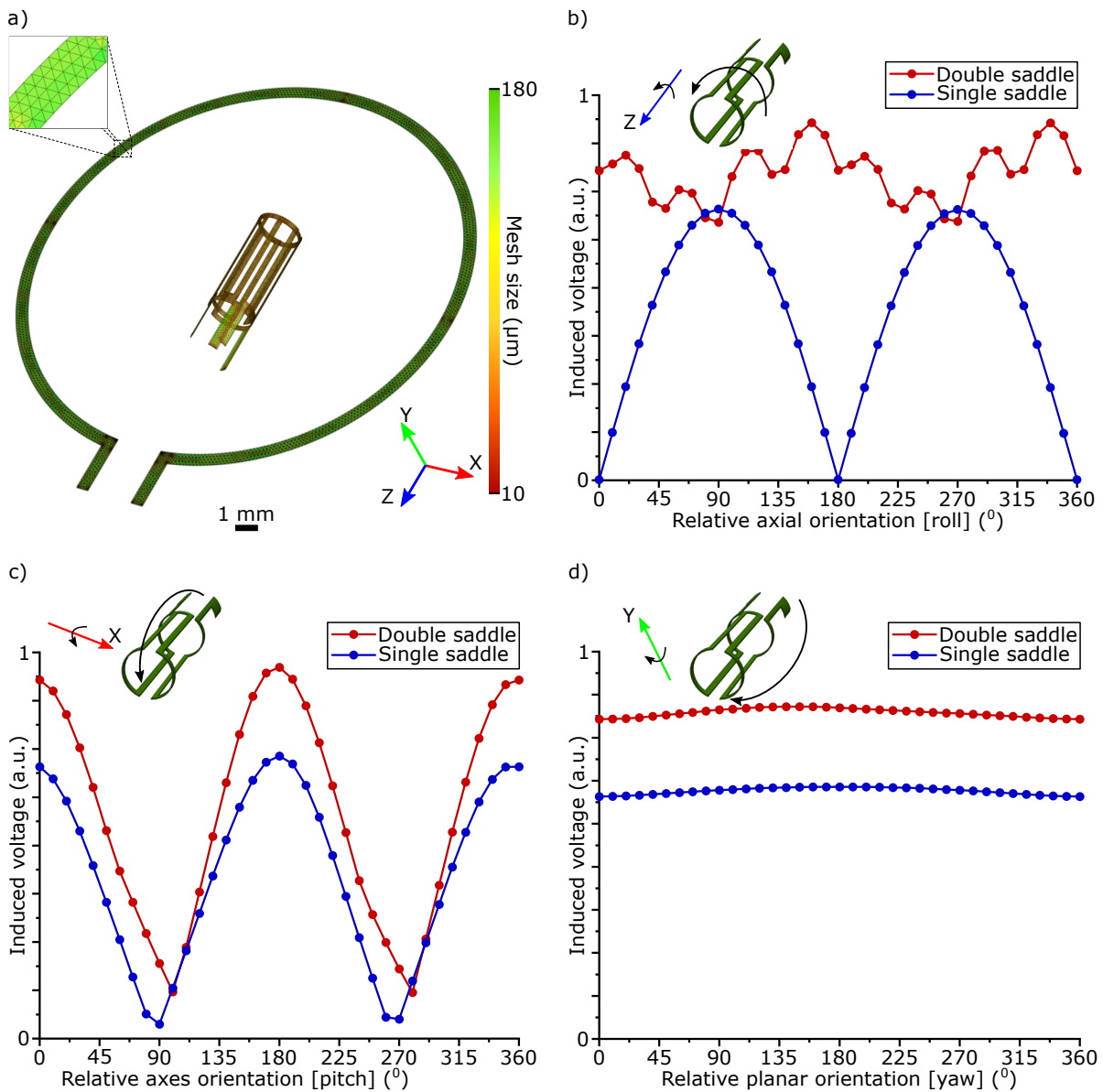
Figure 6.10: Simulation results of the voltage induced in a catheter micro-saddle coil due to inductive coupling with a surface coil at different relative orientations. **(a)** The simulation model of a micro-saddle coil positioned within a stationary single loop surface coil. The diagram illustrates the refined tetrahedral mesh applied for the numerical model. The plots illustrate the voltage induced in the micro-saddle coil caused by the surface coil as a function of the three orthogonal relative rotations: **(b)** Relative axial orientation of between the saddle and surface coil (saddle rotation around the Z-axis), **(c)** Alignment of the axes of micro-saddle and surface coil (saddle rotation around the X-axis), and **(d)** Rotation of the saddle coil in the plane of the surface coil (saddle rotation around Y-axis).

orient in the 2D plane is shown in Fig. 6.10d. The orientation of the micro-detector in the 2D plane does not affect the coupling.

During invasive medical procedures using MR catheter, it is expected that the catheter is intensively subjected to rotations along its axis and turns in the surface coil's plane (along the length of a laying body, and across its width). On the other hand, the angle between the micro-coils and the surface coil

axes rarely varies with wide angles (into the depth of the body). Therefore, the proposed micro-double saddle coil is considered to be a highly suitable detector for the MR-catheter application.

6.3.2 Fabrication of the double saddle resonator

Building a micro-double saddle detector around a slender catheter tube is challenging as it demands a micro-fabrication process for creating multi-layer structures in the 3D. The fabrication is done by 2D patterning of conductive layers separated by a thin flexible polymer film. Then the polymer film with the conductive layers is rolled around the catheter tube to achieve the 3D structure. The conductive layers 2D patterning has been performed utilizing two different techniques: inkjet-printing and photolithography process. Direct inkjet-printing onto an unstructured substrate is an efficient and fast prototyping process but has a low resolution (above 50 μm). On the other hand, the photolithography process required expensive instrumentation but offers a high resolution and suitable for mass production.

Photolithography process

Fabricating the double saddle coil using the photolithography process was conducted in three main steps, as explained in Fig. 6.11a. The first step was done by chemical wet etching to pattern the bottom saddle coil on a 25 μm Kapton film (Fig. 6.11a(i)). Subsequently, the second step was done by structuring a liquid photosensitive polyimide on top of the bottom saddle to create the separation layer, including via that connects the top and bottom metal layers (Fig. 6.11a(ii)). Lastly, the third step was done by lift-off process to deposit the top saddle coil on top of the separation layer (Fig. 6.11a(iii)). The three performed processes (wet etching, photosensitive polyimide, and lift-off) are explained in detail in the photolithography Subsection 3.1.1 in the micro-fabrication Chapter 3.

Inkjet-printing process

The inkjet-printing of silver metal onto unstructured Kapton film is explained in detail in the inkjet-printing Subsection 3.1.2 in the micro-fabrication Chapter 3. Kapton film with a thickness of 25 μm was
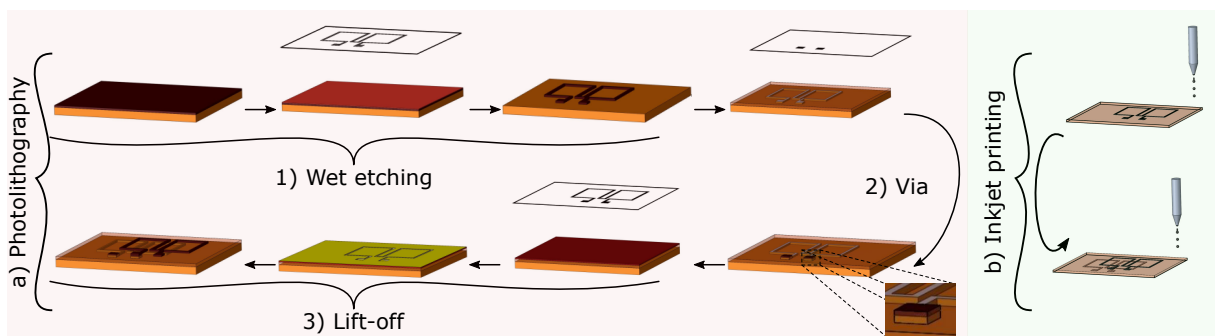
Figure 6.11: Schematic illustration of the two micro-fabrication techniques used for developing a micro-double saddle coil. **(a)** Photolithography process consists of three main fabrication steps: (1) Wet etching for patterning the bottom saddle coil, (2) Structuring photosensitive liquid polyimide for creating a separation layer possessing via, and (3) Lift-off process for depositing the top saddle coil. **(b)** Inkjet-printing of silver ink on both sides of a Kapton film.
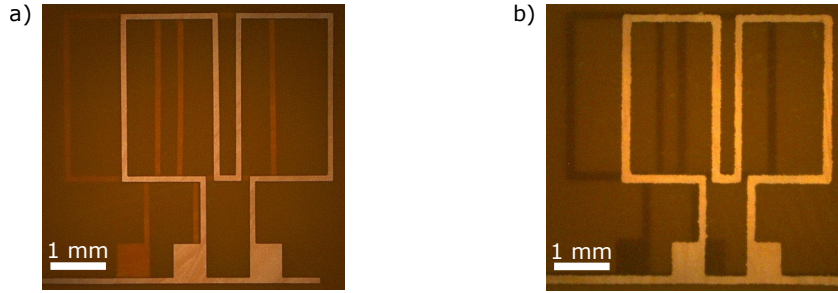
Figure 6.12: Microscope images of the 2D patterned micro-double saddle coil. The coils are fabricated by **(a)** Photolithography process and **(b)** Inkjet-printing.

used. Printing of the double saddle was done in two steps, as shown in Fig.6.11b. The first silver layer was printed, then the Kapton substrate dried at 90 °C for 15 min using a hot plate. Subsequently, the Kapton substrate was flipped over, and after printing the second layer, it was dried again at 90 °C for 15 min. Lastly, the device was sintered in an oven at 150 °C for 1 h.

The thicknesses of the conductive layers deposited using either inkjet-printing or lift-off process are within a few hundreds of nm. However, for RF applications, a minimum thickness of the conductive track is required according to the operating frequency to provide low RF resistance. Therefore, the thickness of the tracks was increased by electroplating to $\approx 10 \mu$m using the home-built electroplating setup discussed in Subsection 4.3.3 in the electroplating Chapter 4. Finally, the Kapton film with the double saddle coil was rolled around a 5 fr catheter tube. Figure 6.12 shows microscopic images of the 2D patterned micro double-saddle coil achieved by the photolithography process and inkjet printing.

6.3.3   Experimental results of the double saddle resonator

The enhancement in MR-catheter tracking provided by the proposed micro-double saddle coil was verified by conducting two experiments. The first experiment was done to characterize the inductive coupling between the micro-saddle coil and the surface coil at various relative axial orientations. The second experiment was done to map the B_1 field of the micro-saddle coil within an MRI scanner.

An experimental setup was created from laser-cut PMMA sheets to characterize the inductive transmission coefficient between a micro-detector immobilized on a catheter tip and a primary stationary surface resonator, as demonstrated in Fig. 6.13. The primary surface coil (radius = 2 cm) was connected to a network analyzer through a matching and tuning network $((L_{Coil} \parallel C_M) - C_T)$ containing variable capacitors. The catheter tip with the micro-detector was adjusted to face the center of the primary surface coil at a distance of 2 cm. The catheter axial orientation was actuated utilizing a stepper motor actuator (step motor 28byj-48) controlled using a microcontroller (Arduino-Uno board) through a motor driver board (ULN2003APG).

The experiment was carried out twice, the first run with a single saddle coil and subsequently the second run with a double saddle coil. The primary stationary surface coil was tuned to 63 MHz resonance frequency and matched to 50 Ω. The single saddle coil had a measured inductance of 16 nH and was tuned
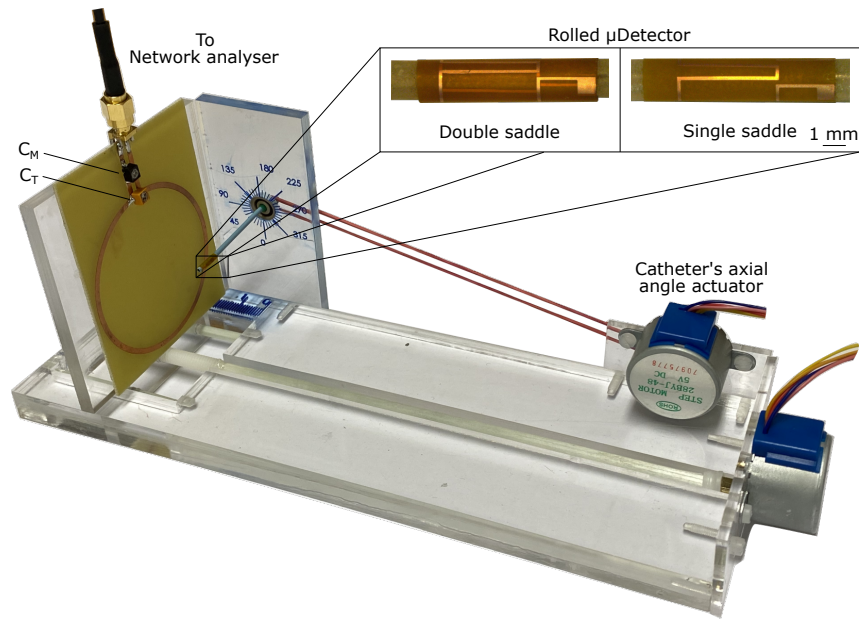
Figure 6.13: Experimental setup used to characterize the inductive coupling strength between a stationary scale primary coil and a rotatable micro-detector.

to a resonance frequency of 63 MHz by a 390 pF capacitor (SMD capacitor 0402). In contrast, the double saddle coil (two single coils connected in series, $L_{double} = 2 \times L_{single}$) was tuned to the same resonance frequency by a 190 pF capacitor. The capacitance required for tuning the double saddle is almost half of the capacitance used for tuning the single saddle; this is because the double coil's inductance is twice that of the single coil ($f = 1/\sqrt{LC}$). The primary coil's reflection coefficient (S_{11}) was recorded at different relative axial orientations (swept from 0° to 90° with a step of 10°) with the micro-detector immobilized on the catheter tip. The relative axial orientation range from 0° to 90° was enough to fully characterize the coupling coefficient due to the symmetric structure of the saddle coils.
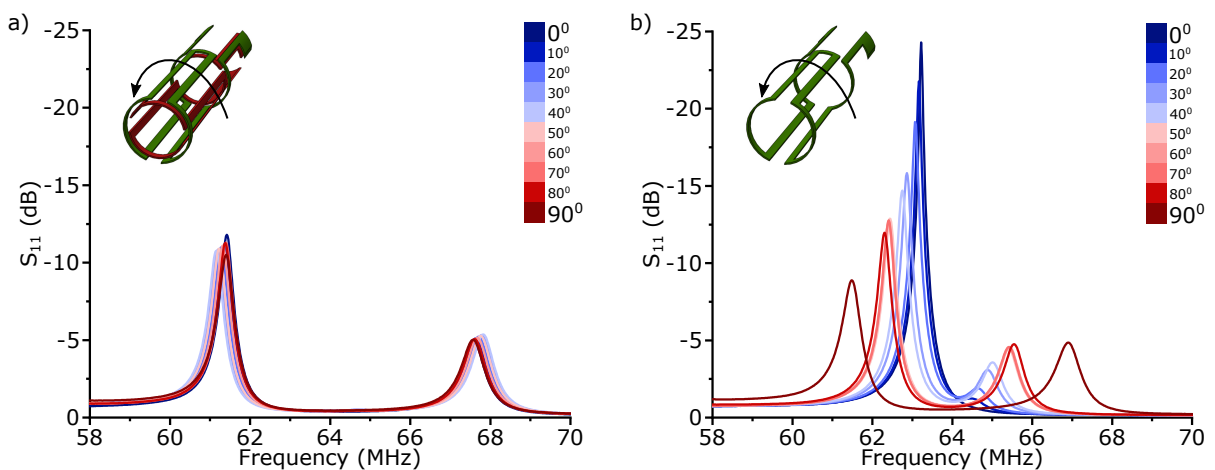
Figure 6.14: Measured reflection coefficient (S_{11}) curves of a stationary primary resonator due to coupling with micro-saddle detector. The S_{11} curves demonstrate the resonance frequency splitting of a stationary resonator tuned at 63 MHz due to inductive coupling with **(a)** Micro-double saddle coil and **(b)** Micro-single saddle coil both tuned at 63 MHz.
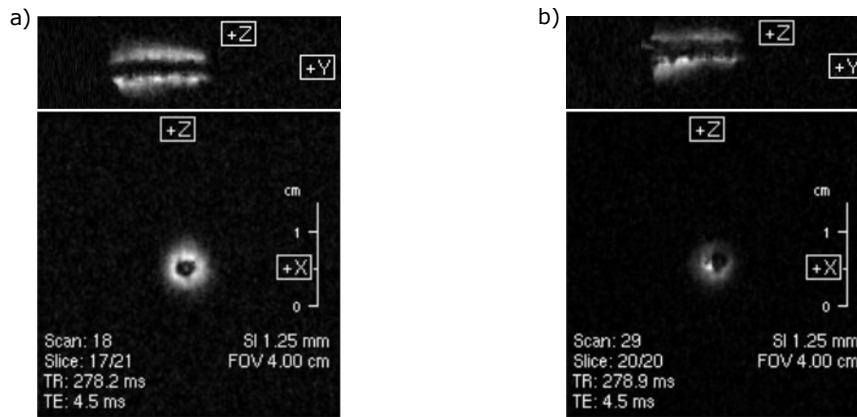
Figure 6.15: Mapping the B_1 fields of **(a)** A micro-double saddle coil and **(b)** A micro-single saddle coil in a 1 T MRI scanner.

Figure 6.14 presents the experimental results of the inductive coupling characterization. The practical results match the COMSOL simulation results in Fig. 6.10b; The coupling between the primary surface coil and the single saddle coil decreases as the relative angle between their magnetic B_1 fields increases. Furthermore, when the B_1 fields were nearly orthogonal, the reflection coefficient curve showed no splitting in the resonance frequency, confirming that no inductive coupling occurred (Fig. 6.14b). In contrast, for the double saddle coil, the inductive coupling between the surface resonator and the micro-detector was maintained at a near-constant profile for the entire range of the relative axial orientations (Fig. 6.14a).

The magnetic B_1 fields of the micro-saddle coils were mapped utilizing a low field MRI scanner (Bruker ICON, $B_0 = 1$ T). As revealed in Fig. 6.15a, the double saddle coil generated a homogeneously distributed magnetic field surrounding the catheter tube, confirming the simulated magnetic field distribution in Fig. 6.9. The MR images had a slice thickness of 1.25 mm, a field of view (FoV) of 20 mm × 20 mm, with an imaging matrix size set as 128 × 128 using echo time (TE) = 4.5 ms, repetition time (TR) = 278 ms, a flip angle of 40°, and using four averages.

Part III.

NMR Application - Automated High Throughput Nuclear Magnetic Resonance
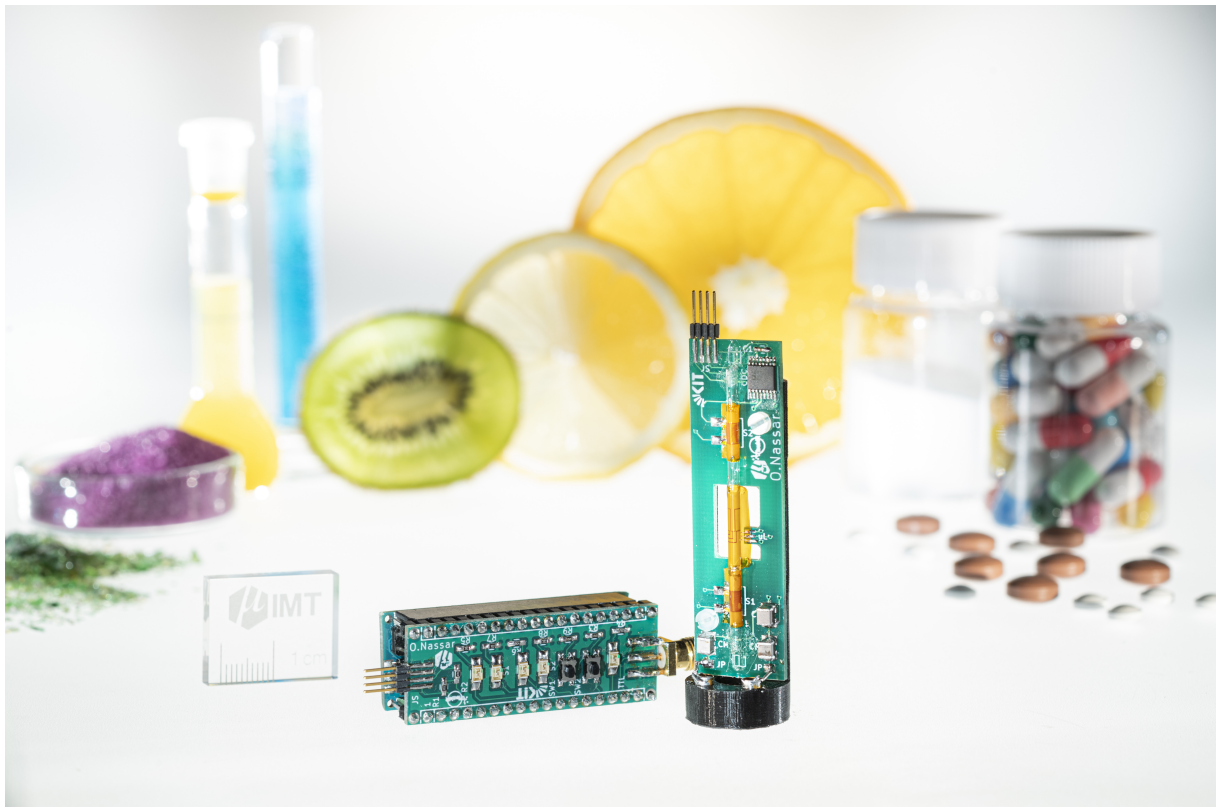
7 State-of-the-art: high throughput NMR spectroscopy[1]

NMR spectroscopy is an information-rich analytical method utilized for characterizing materials by determining and quantifying molecular structure. NMR is an attractive screening tool as: i) it offers broad chemical coverage; ii) it is a non-destructive technique, permitting further upstream analytics; and iii) it does not require significant sample preparation. The NMR technique measures the response of a sample's spins to a polarizing static magnetic field (B_0) and an excitation RF magnetic field (B_1), which generates a small electrical signal in an RF resonant detector. The polarizing B_0 field is provided by an external magnet, while the B_1 excitation field is commonly generated by the RF detector itself, as explained in detail in Chapter 2.

A standing challenge facing the present NMR technique is that it is generally limited to single sample measurements under low throughput conditions. Therefore, there is a disconnect between applications that require large parameter spaces screening and the opportunity to take advantage of this information-rich method. By addressing the NMR throughput challenge, it could lead to a significant push to diverse fields, including drug discovery screening, clinical analysis, chemical process monitoring, bio-fluid metabolomics, and food analysis.

Consider the field of drug discovery as an example; NMR can resolve the binding of drugs to pathogens and can be used for screening compound libraries to investigate the molecular interactions with target proteins [15, 16]. Pharmaceutical companies have molecular libraries containing millions of compounds, which is ever-increasing as new molecules are being synthesized utilizing combinatorial methods. For example, Pfizer, Inc. maintains 4 million compounds inside their molecular library that can be used for analyzing potential medicines, as reported in 2017 [17]. Hence, the development of high throughput NMR methods is a must to enhance the screening efficiency of these massive and ever-increasing molecular libraries.

7.1 High throughput NMR approaches

For the last decades, developing high throughput NMR techniques has been addressed extensively with the goal to involve this powerful technique in screening these large compound libraries. For a fully automated NMR measurement, several steps should be controlled [184]. The NMR spectroscopy process involves sample preparation, transferring the desired sample into the magnet, adjusting the NMR instrument (tuning, matching, shimming), performing the measurement, transferring the sample outside the magnet, and processing the data. Several approaches have been developed, which can be divided into three main concepts: i) automated sample changers; ii) probe with multi RF coils; and iii) flow-based NMR systems.

---

[1]This chapter's text was partially reproduced and adapted from the author's published work [ON5] (CC BY 4.0, 2021 Springer Nature)

7.1.1   Automatic sample changer

The first approach to be discussed is the automated sample changer systems. This approach was developed to analyze multiple samples with avoiding the manual samples changing as possible, i.e., overnight or weekends. The system possesses a sample preparation holder where each sample is physically separated to avoid cross-contamination. The sample holder is connected to the NMR magnet to transfer each sample individually using a pneumatic control system. Automated sample changers provides the user with easy and safe access to the NMR magnet without the need for ladders or steps. This automation approach allows users to access and automated operation overnight, which enhances the NMR spectroscopy throughput. Besides the automation process, manual control for the sample handling system is usually possible using a push button. Therefore, automated sample changer systems have been adequate for individual NMR glass sample tubes. However, this approach automates only the sample transfer into and outside the NMR magnet. The throughput is still limited by the NMR instrument re-adjusted (tuning, matching, shimming) after each sample exchange.

Since the automated sample changer was first introduced, it has been enhanced and developed where commercial automated changers are now available and capable of queuing up to ~ 500 samples for the NMR measurement [184, 185]. For illustrating the capability of the automated sample changers, two examples of commercially available systems are discussed below. The first example is for a sample changer system provided by Brucker [186], a photo of the system is shown in Fig. 7.1a. The sample holder possesses 24 or 60 sample positions compatible with various NMR sample tube lengths and diameters. The system can be connected to almost all Brucker's NMR magnets. The system has the distinction of being vibration-free and has no RF interference effect on NMR coils. Two versions of the systems are provided to control the samples set-point temperature, heated and cooled version. The heated version has a temperature range from room temperature up to $125\,°C$; thus, liquid polymers could be analyzed. On the other hand, the cooled version has a temperature range from $4\,°C$ up to $40\,°C$, which is appropriate for analyzing various samples such as protein or biofluid solutions.

a)   b)
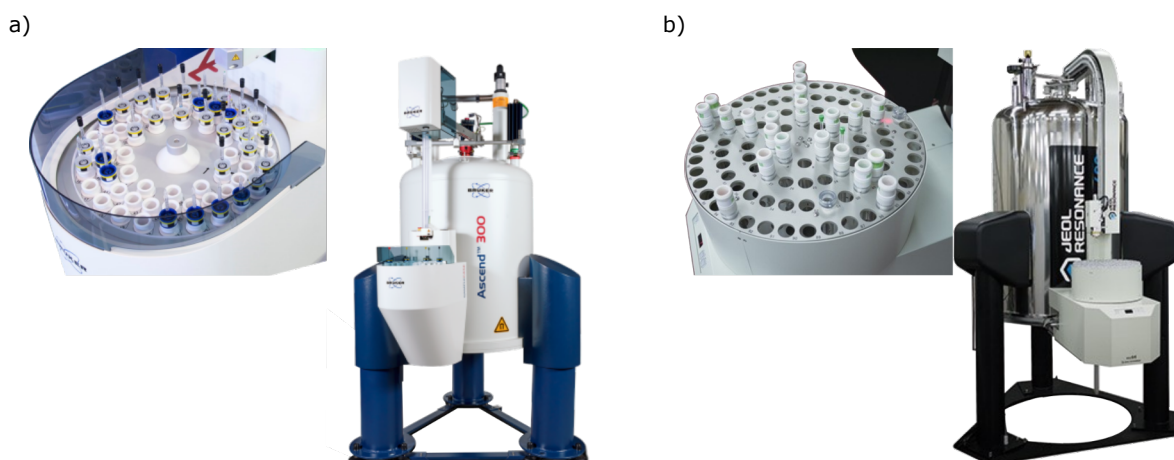
Figure 7.1: Examples of the commercially available automated NMR sample changer systems. *The pictures are reprinted from the companies' websites [186, 187].*

The second example is the ASC24 system provided by JEOL [187], a photo of the system is shown in Fig. 7.1b. Several versions of the sample holder are available that possess 30, 64, or 100 sample positions. The sample changer is at the same height as the user, so no need for ladders or steps. Besides, there is a top-loading sample changer version installed on the top of the NMR magnet to save space. A manipulator controls the sample for insertion and ejection through an NMR magnet. The automatic sample changer comes with several advantages, However, the main drawback of these systems is that it requires NMR instrument readjustment after the insertion of each sample, such as tuning and matching of the RF coils and shimming of the main magnet.

7.1.2 Parallel detectors

Developing NMR probes with multiple RF coils has been considered a practical approach for enhancing the NMR spectroscopy throughput. Instead of using a single RF detector to acquire an NMR spectrum from a single sample, a probe with multiple RF detectors could be designed to excite and acquire signals from various sample volumes simultaneously. Commonly, the reported multiple-coils probes have been designed in a way that each RF coil is warped around a capillary where the sample is located.

Sample excitation and NMR signal acquisition have been conducted following two main approaches using parallel coil NMR probes. The first approach is attaching all coils to a single resonant circuit, and a gradient field is applied during sample excitation to provide spatial frequency dependence. Thus, one receiver is used to acquire the NMR signal from the multiple coils, and each sample's signal is separated based on the frequency shift introduced by the gradient field. This approach provides the advantage of simple hardware construction. MacNamara et al. [188] introduced a four coils NMR probe, shown in Fig. 7.2a. The four coils are connected in parallel and attached to a single resonance circuit with trimmer capacitors; the circuit is located beneath the sample region. To differentiate the acquired signal based on the sample location, a static linear field gradient has been applied in the direction of the B_0 field by changing the shim power supply.

The other approach is providing a separate resonant circuit for each coil to excite and detect signals separately with avoiding RF interference and coupling between the coils. Fabricating several RF receivers adds to the system hardware complexity and cost. Wang et al. [189] introduced an eight coils probe head developed with an interface to four receiver channels spectrometer, shown in Fig. 7.2b. The eight coils have been divided into two groups (four coils each) where data from one group are acquired at a time. For designing an eight coils probe to fit into the NMR magnet homogeneous region, the impedance matching circuits have been designed to be away from the coils. This design reduces the efficiency of the RF coils, but a compromise for enhancing the filling factor was considered. Additionally, sufficient grounding and proper shielding between the coils' circuits were required to avoid RF cross-coupling and interference as much as possible.

An application for the multiple coils principle is NMR detection for continuous-flow capillary electrophoresis (CE) [190]. Capillary electrophoresis is a powerful separation method for a mixture of various samples by exposing them to a transient electric field. Although no physical separation, NMR measurement can be conducted based on the different electrophoretic mobility of the different sam-

ples [191]. Wolters et al. [190] introduced a two coils probe that has been used with performing CE NMR spectroscopy. Figure 7.2c shows a schematic illustration of the CE/NMR system with multiple coils. The system possesses a single separation capillary connected to multiple outlets, where each outlet has a coil with its detecting circuit. The coils' circuits are attached to an electromagnetic relay switch to determine which coil is connected to the transmit/receive channel, i.e., one coil is active at a time. Hence, continuous CE flow sequentially direct sample flow into the various outlets, and cycled stopped-flow detection process is conducted between the multiple NMR detectors.

In principle, the number of coils in multiple coil probes can be scaled up to increase the throughput, nevertheless, a limitation arise from the small volume of the homogeneous B_0 field inside the NMR magnet. The design of the coils and the minimum coils spacing should be considered to avoid RF cross-coupling and interference that could result in signals bleed between neighboring coils, i.e., exciting a specific coil can generate an RF signal in the adjacent detecting coil. These challenges could be addressed in several ways, such as; considering only one active coil and de-tuning the inactive neighboring coils or using different frequency adjustments for the various coils.
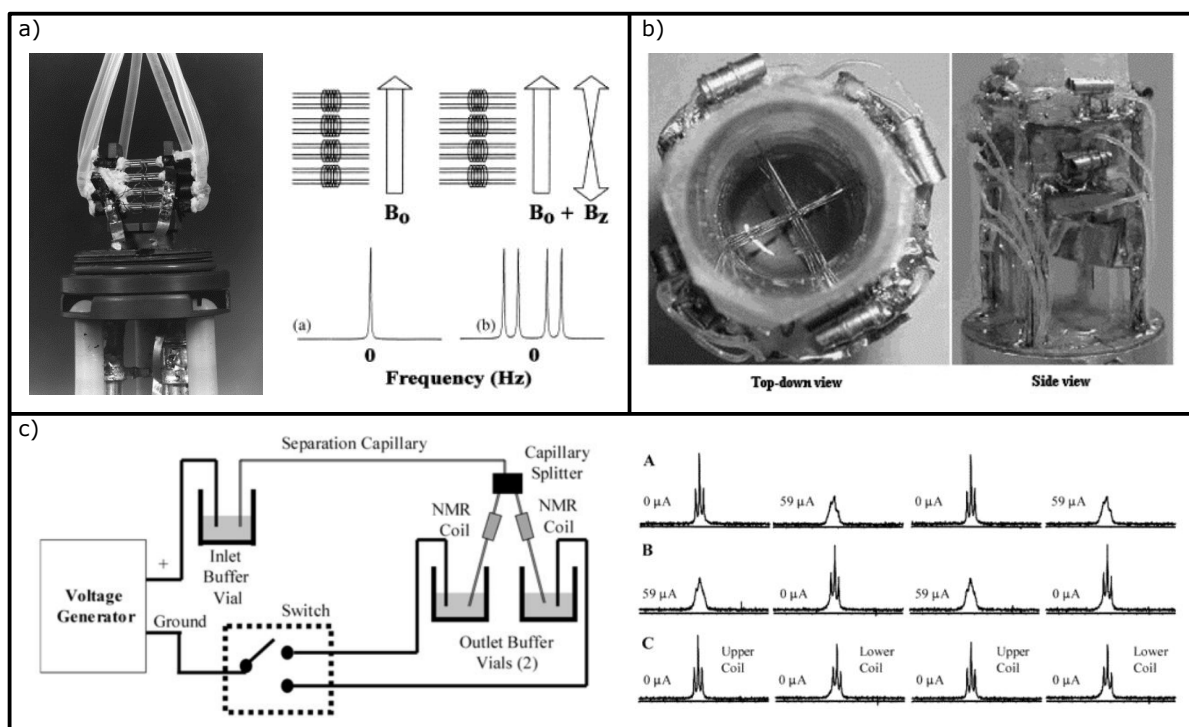
Figure 7.2: Examples of state-of-the-art multiple parallel coil NMR probes. **(a)** NMR probe head with four parallel flow-through coils [Right]. Spatial frequency encoding is considered for using single resonance circuit [Left], *reprinted from [188] with permission of Elsevier (Copyright © 1999 Elsevier Science B.V.).* **(b)** NMR probe head with eight parallel RF coils. Each coil has its own resonant circuit, *reprinted from [189] with permission of Elsevier (Copyright © 2004 Elsevier Inc.).* **(c)** Schematic illustration of the CE/NMR system with two micro-NMR RF coils [Right]. The results [Left] show that system with multiple coils and CE flow could separate the spectra, as shown in (A) and (B). On the other hand, without CE, the spectra are overlapped, as shown in (C), *reprinted with permission from [190], Copyright ©2002 American Chemical Society.*

7.1.3 Flow-based NMR

Flow-based NMR systems have also been considered to achieve high throughput NMR spectroscopy [192, 193]. Flow-based NMR spectroscopy is done by transferring a sample from outside the magnet through the NMR detector using fluidic tubes. Several liquid handlers are available commercially (e.g., multiple probe 215 liquid handler provided by Gilson Inc [194]), or even standard syringe pumps can be used to inject the sample into the inlet of the flow-injection probe. After analyzing the sample, it is transferred out of the magnet, and the following sample is injected without the need for hardware disassembling. Solvents can be used between every two successive samples for the rinsing purpose of the probe's tube to avoid cross-contamination. The main advantage of the flow-based approach is that the NMR instruments should be adjusted once (shimming, matching, and tuning) for the first sample, and no need for re-adjustment.

Rehbein et al. [195] introduced a flow probe with a double resonance solenoidal detector having an active detection volume of $2\,\mu L$ used for capillary HPLC-NMR spectroscopy coupling, a picture of the probe head and the whole system is shown in Fig. 7.3a. The NMR RF coil is warped directly around a horizontal capillary (OD/ID, 1.5/0.8 mm) attached at both ends to vertically oriented flow tubes. The NMR detector is immersed in a fluorinated oil (FC-43) to match the susceptibility miss-match between air and copper. By using the introduced system, NMR spectroscopy can be done in a continuous-flow or stopped-flow measurement. The advantage of the stopped-flow method is that the NMR acquisition time could be increased leading to a greatly enhanced SNR. Also, with this method, it is possible to record 2D correlation NMR spectra.

Carret et al. [10] introduced a flow-based device that is compatible with any commercial NMR probe head, a picture of the device is shown in Fig. 7.3b. The device possesses a micro-coil with an inlet and outlet for the sample flow. The NMR signal is transferred from the micro-coil to the NMR system detector through induction coupling.

Macnaughtan et al. [196] introduced a system where a multiple coil probe is combined with flow-based NMR spectroscopy, a picture of the system is shown in Fig. 7.3c. The system injects four samples simultaneously into four coils installed on a probe head using a liquid handler possessing four controllable syringe pumps. The time consumption is improved by a factor of four compared to a single flow-through system. The four micro-solenoidal detectors were connected in parallel and attached to a single resonance circuit with two variable capacitors for tuning and matching. NMR analysis was performed based on the chemical shift imaging or selective excitation between the four NMR detectors [197].

The flow-based approach has proven to be a reliable alternative to enhance the NMR spectroscopy throughput, with additional enhancements by developing probes with multiple RF NMR detectors. However, flow-based NMR spectroscopy faces mainly two challenges:

1. A challenge to be considered while using a flow-based NMR system is the cross-contamination because of the tiny solvents droplets that remain in the flow junctions dead volume inside the tubes due to the tubes' inner diameter mismatch. This issue could be addressed by using proper fittings and avoiding inner diameters mismatch. Additionally, tube rinsing can be done using solvents

such as D_2O and H_2O. D_2O is a good solvent choice to decrease the ^1H solvent signal, but H_2O could be used instead due to cost considerations. Another practical rinsing approach uses air or nitrogen between various samples transfer, but it is a time-consuming process [193].

2. Another common challenge facing the flow-based approach is the relatively large dead volume in the flow tubing feeding the micro-NMR detector. Since the NMR detector is invisible inside the NMR magnet and to make sure that the sample is filling the NMR detector, the sample needs to be visible at both inlet and outlet of the NMR system, resulting in overall inefficient use of the sample.
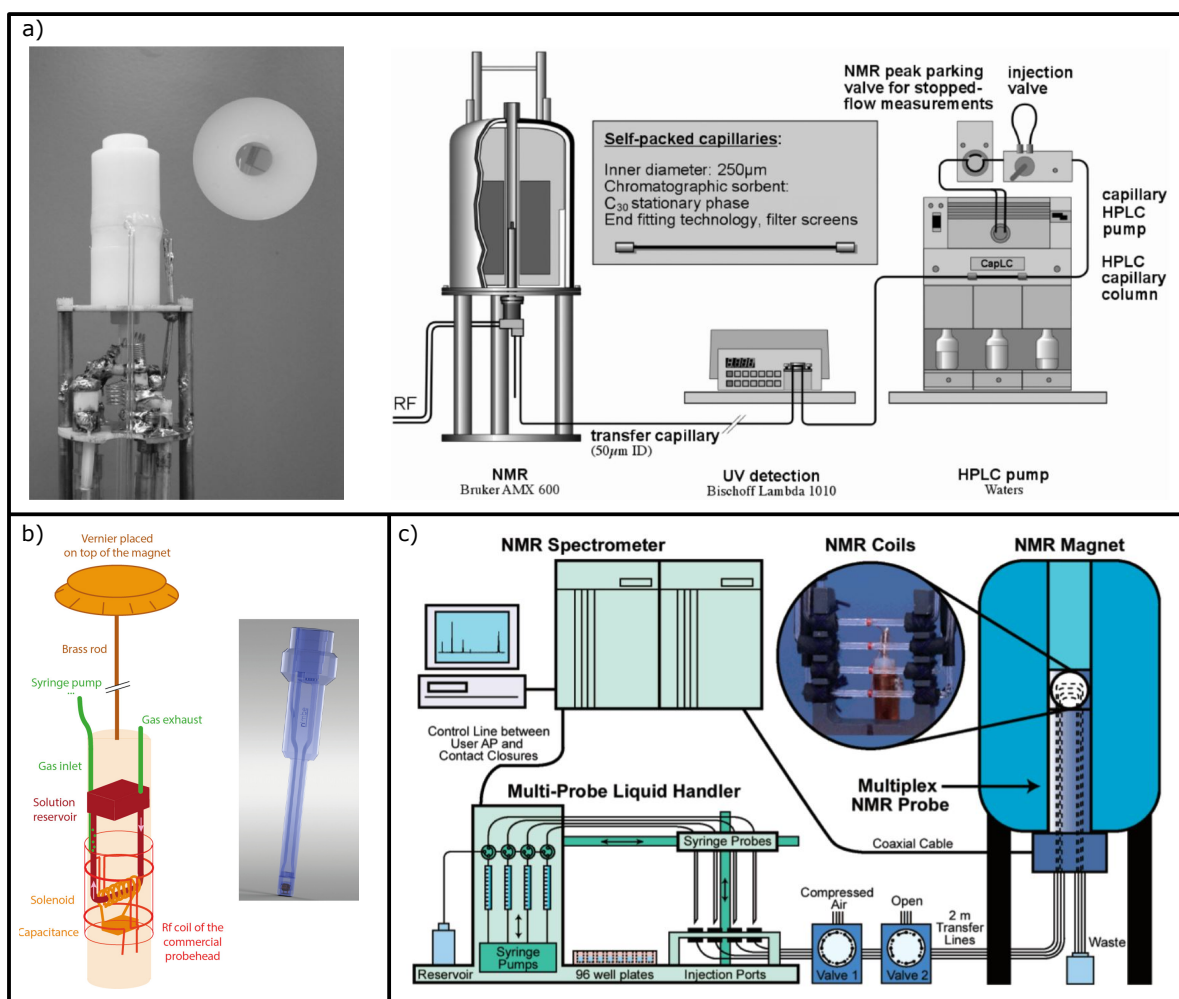
Figure 7.3: Examples of state-of-the-art flow-through NMR probes. **(a)** A probe head possessing a micro-solenoidal coil for flow-based NMR spectroscopy [Left]. Schematic illustration for a capillary HPLC-NMR spectroscopy coupling system, *reprinted from [195] with permission of John Wiley & Sons, Inc. (Copyright © 2007 WILEY-VCH Verlag GmbH & Co. KGaA)*. **(b)** Schematic illustration for a flow-based NMR device that is compatible with commercial NMR probe heads. *reprinted with permission from [10], Copyright ©2018 American Chemical Society*. **(c)** Schematic illustration for a system combining multiple coil probe with flow-based NMR spectroscopy, *reprinted with permission from [196], Copyright ©2003 American Chemical Society*.

7.2   Adapted approach

The sample exchange phase during an NMR experiment is not necessarily the only time-consuming step. NMR spectroscopy is famous for its high resolution, with spectral line widths in ppb. This is because nuclear spins have relatively long relaxation periods, typically in the term of seconds for hydrogen nuclei in the liquid state. The relatively lengthy re-equilibration delay results in restricting the number of times an NMR experiment can be replicated. This recycling delay can be eliminated under the flow-based approach as freshly polarized samples are continuously transferred into the NMR-coil detection volume, avoiding the need for re-equilibration. This is particularly significant when the target nuclei have relatively long relaxation time constants [10]. Combining the lengthy recycle times with the insensitivity of NMR spectroscopy results in the NMR being a low throughput technique. Hence, in situations where sample exchange and recycle delay become time-limiting processes, a flow-based approach will outperform the traditional sample handling technique and enhance throughput.

Therefore, a flow-based NMR spectroscopy is adapted here to enhance the NMR throughput. Instead of exchanging individual sample containers traditionally, a flow-through NMR system can be used to deliver a series of concentrated sample plugs separated by an immiscible fluid from outside the magnet through the NMR detector. This two-phase flow eliminates the dead volume but requires continuous online measurement to track the sample plug's position and velocity to ensure that the target sample fills the NMR detection volume. In this contribution, a novel flow-based NMR system is introduced. The flow system features: i) integrated capacitive sensors for sample position and velocity measurements; and ii) a micro-saddle coil for NMR spectroscopy. This flow system enables fully automated NMR spectroscopy while taking advantage of the improved experimental time per sample due to continuous sample flow. The system is discussed in detail in the next Chapter 8.

A flow-based NMR spectroscopy is extremely attractive when target sample quantities are small; instead of dealing with poor filling factors or diluting samples using standard NMR hardware, microfluidic technologies and micro-NMR techniques can be used. The following subsections provide an overview of the state-of-the-art micro-NMR detectors and flow sensors.

7.3   Micro-NMR detectors

The RF coil is the core element of the NMR system, allowing interaction of measurement device with the target sample magnetization. In this part of the thesis, 'coil' refers to any device capable of generating and detecting magnetic fields. The topology and design of the RF coil have a significant impact on the NMR measurement. This section provides an overview of various NMR coils, which can be divided into two main categories: volume and planar.

7.3.1   Volume coils

There are many shapes of the volume coils, such as solenoidal and Helmholtz coils. Volume coils have better field homogeneity than planar coils. In the case of analyzing samples that can be cast into a

cylindrical shape, such as liquids or powders, volume coils are the proper choice since the probe volume can be filled optimally, resulting in a high filling factor and sensitivity.

Solenoidal coil

Solenoidal coils have the classic topology represented by helically wrapped thin conductive wire around a cylinder used as a mechanical support for the coils. A schematic of the solenoidal coil is shown in Fig. 7.4a. In the case of NMR application, the supporting cylinder is a capillary that holds the sample during the measurement. Solenoidal coils are attractive for micro-NMR applications due to their several
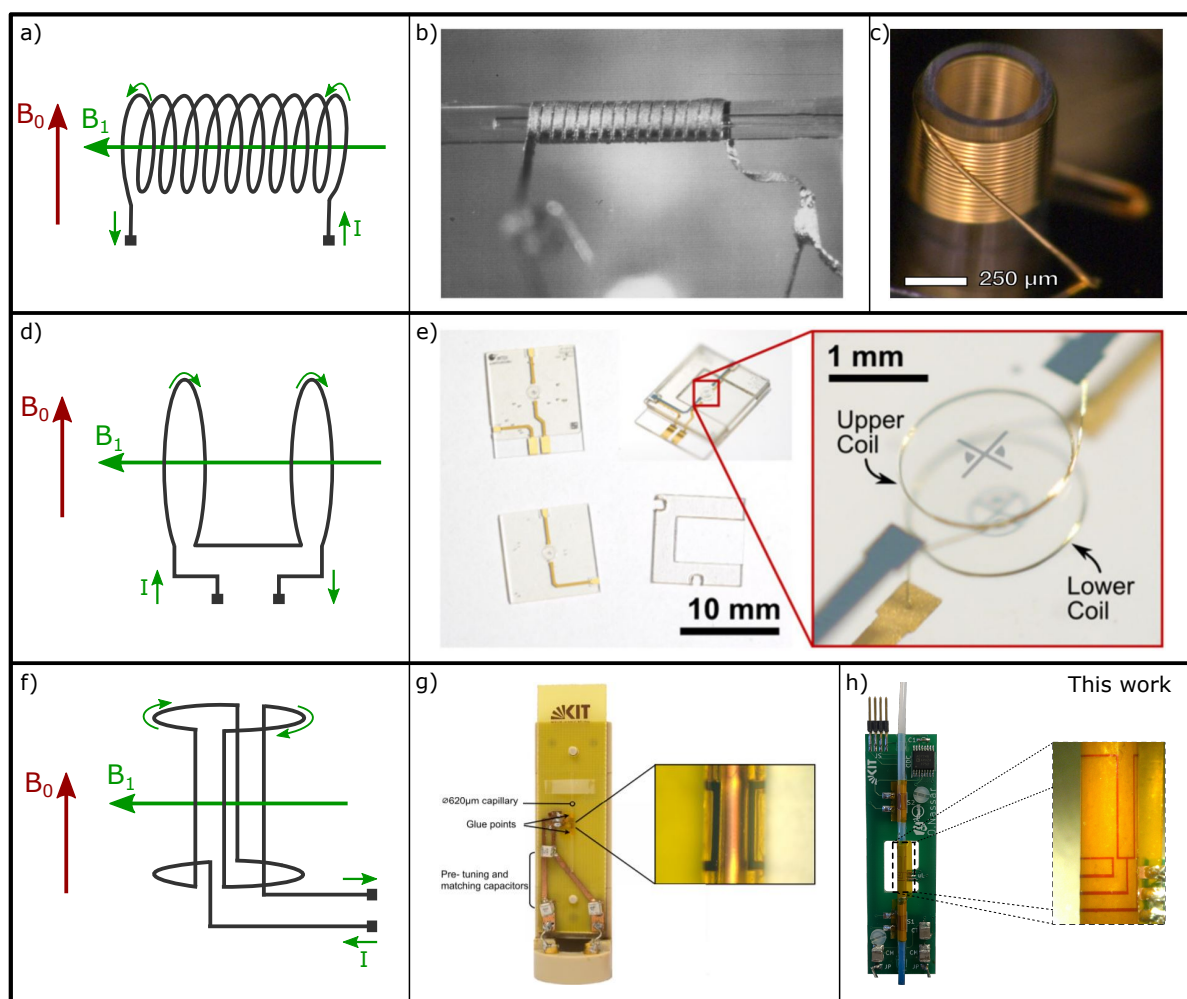
Figure 7.4: Examples of state-of-the-art volume NMR coil. **(a)**, **(d)**, and **(f)** Schematic illustration for the solenoidal, Helmholtz, and saddle coils, respectively. The schematic illustrations show the B_0 and B_1 fields' expected orientations. **(b)** and **(c)** Examples for micro-solenoidal coils. **(b)** *Reprinted from [198] with permission of AIP Publishing (Copyright © 1997 AIP.)*, and **(c)** *reprinted from [199] with permission of Elsevier (Copyright © 2009 Elsevier B.V.)*. **(e)** Example for micro-Helmholtz coil, *reprinted from [200] with permission of IOP Publishing (Copyright © 2014 IOP Publishing Ltd)*. **(g)** and **(h)** Examples for micro-saddle coils. **(g)** *Reprinted from [143] with permission of IOP Publishing (Copyright © 2017 IOP Publishing Ltd)*, and **(h)** *reproduced from the author's published work [ON5] (CC BY 4.0, 2021 Springer Nature)*.

advantages including high filling factor, high sensitivity, ease of electric decoupling, highly uniform magnetic field within the coil's core, and easily manufactured on the micro-scale [201].

However, integrating solenoidal coils into an NMR system faces some issues. The first drawback is the sample handling, especially in flow-based spectroscopy, since the coil should be transversely located inside the NMR magnet. Another drawback is that the NMR magnet homogeneous B_0 field needs to penetrate through the coil's tracks before it polarizes the sample. This leads to the distortion of the B_0 field due to the susceptibility mismatch of different material interfaces, resulting in broader NMR signals. There are several approaches to overcome this challenge, for example, adding susceptibility materials for matching purposes [202].

The coil efficiency (B_1/I) is the coils ability to produce a magnetic field from a unit current which also expresses the detector ability to convert the NMR signal into a voltage signal [27]. Solenoidal coil efficiency depends on the number of turns and the coil diameter [28],

$$\frac{B_1}{I} = \frac{\mu_0 \, N_C}{d_C \sqrt{1 + (h_C/d_C)}}, \tag{7.1}$$

where N_C is the number of turns, d_C is the coil diameter, and h_C is the coil height. The previous equation shows that decreasing the coil diameter, with maintaining a constant h_C/d_C ratio, increases the coil efficiency. Hence, solenoidal coils on the micro-scale were developed using MEMS fabrication techniques [203].

Helmholtz coil

The basic shape of a Helmholtz coil is a pair of identical circular coil loops which are placed apart with a distance equivalent to the radius of the coil loop with a common axis. A schematic of the Helmholtz coil is shown in Fig. 7.4d. The two loops are electrically connected in series so that the same current passes through them in the same direction to generate a homogeneous B_1 field in the center.

The main advantage of Helmholtz coils over solenoidal coils is the homogeneity and direction of the B_1 field, which aligns the coil loops with the B_O field. Hence, the B_0 field does not penetrate several material interfaces as in the case of solenoidal coils, reducing B_0 field distortion. Moreover, the Helmholtz coil orientation inside the B_0 field results in more convenient sample handling, especially in flow-based NMR, where there is no need to remove the probe head to exchange the sample. Helmholtz coils can be fabricated using the MEMS technologies, where each of the two loops could be considered as a planar structure and then connected together [200, 204]. But, the Helmholtz coils have lower sensitivity than the solenoidal coils [27].

Saddle coil

Saddle coil is a special type of a Helmholtz coil, where the coil loops take a cylindrical arrangement other than the planar arrangement in classical Helmholtz coils. A schematic of the saddle coil is shown in Fig. 7.4f. The cylindrical geometry maximizes the coil's filling factor, thus, saddle configuration for NMR is an appealing possibility for tube-based NMR experiments. For better magnetic field homogeneity, it was shown that the angular width for each coil loop should be $\approx 120°$, and the separation arc in between the loops should have angular width of $\approx 60°$ [205].

Saddle coils feature similar advantages as Helmholtz coils regarding B_1 field homogeneity and direction,

as previously discussed. Moreover, they provide ample sample space, so an easier sample handling that is compatible with stationary and flow-based NMR.

The main challenge facing the saddle coil is the fabrication at the micro-scale due to the 3D configuration. In 2018 Wang et al. [143] introduced a robust micro-fabrication process for developing a micro-NMR saddle coil with an active sample volume of 82 nL. The developed process was to pattern 2D conductive layer onto a thin planar polyimide film then rolling it around a glass capillary to achieve the 3D structure. The supporting glass tube was used as a microfluidic sample chamber.

7.3.2   Surface coils

Surface coils are the second group of coils beside the volume coils. Surface coils have simple structures that can be efficiently designed and optimized compared to the volume coils. 2D planar coils could be easily fabricated at the micro-scale using standard lithography or fast prototyping techniques such as inkjet-printing [206]. The main advantage of the surface coils is locating the sample on the top of the probe instead of inside of it, which means more straightforward sample handling and larger available sample space. Planar spiral and striplines are wide-used arrangements in MR applications.

Planar spiral coils

Planar spiral coils have been developed to offer small NMR detectors with high sensitivity and a straight-
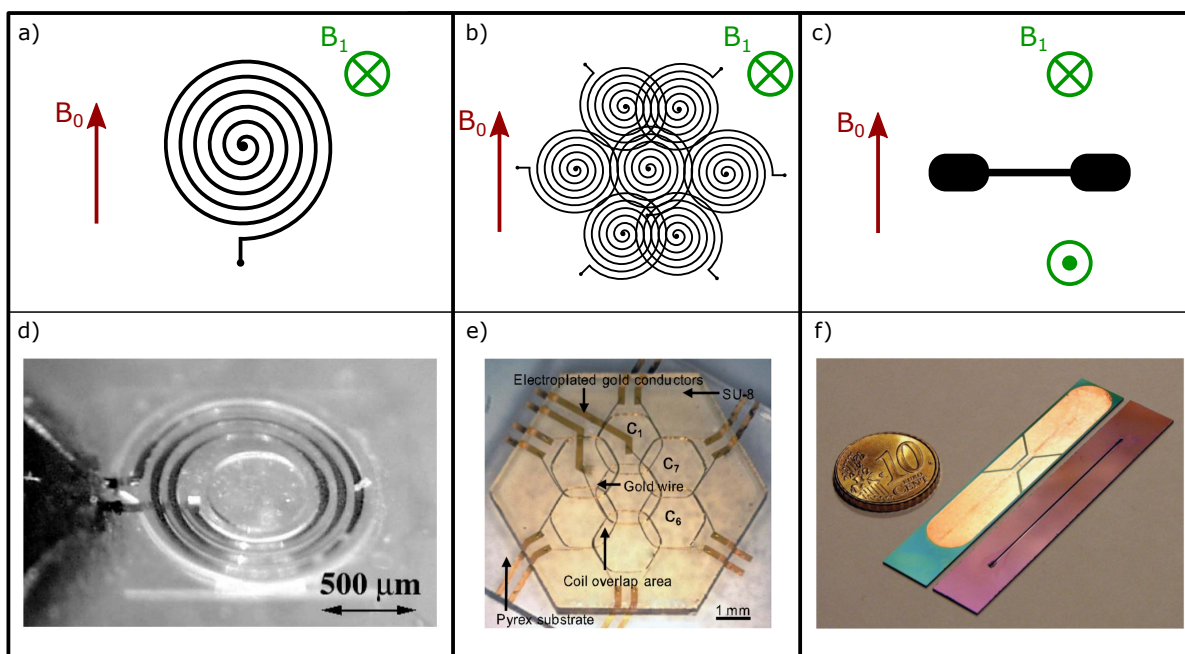
Figure 7.5: Examples of state-of-the-art surface NMR coil. **(a)**, **(b)**, and **(c)** Schematic illustration for the spiral planar, phased array, and striplines, respectively. **(d)** Example for micro-planar NMR coils, *reprinted from [206] with permission of Elsevier (Copyright © 2002 Elsevier Science B.V.).* **(e)** Example for phased array coils, *reprinted from [207] with permission of IEEE (Copyright ©2011 IEEE).* **(f)** Example for stripline, *reprinted from [208] with permission of AIP Publishing (Copyright © 2008 AIP).*

forward sample handling. A schematic of the planar spiral coil is shown in Fig. 7.5a. The magnetic field of the planar coils is not uniformly distributed in space; the magnetic B_1 field strength drops with distance from the coil surface. Hence, it is important to consider the sample location (volume of interest) with respect to the coil structure [209]. Moreover, a field distortion is introduced by the electrical bridge between the outermost and innermost winding to create a closed-loop.

In the beginning, Stocker et al. [210] developed a rectangular planar micro-coil that was successfully employed to acquire NMR spectra of liquid samples. Later Dechow et al. [211] introduced micro-coils of gold tracks fabricated on gallium arsenide substrate with inner diameters ranging from $50\,\mu m$ to $400\,\mu m$ to serve samples with nL volumes. In 2015, Grisi et al. [212] introduced a single transceiver chip with dimensions of $1\,mm^2$, which features an integrated planar micro-coil. Montinaro et al. [213] used this chip to design 3D micro-channels to analyze sub nL samples using NMR spectroscopy. Commercial micro planar coils have been provided by Bruker BioSpin (Billerica, MA and Fällanden, Switzerland), which were used to interface digital microfluidics with NMR micro-coils to manipulate droplets [214]. Lee et al. [215] introduced a phased array micro coils configuration to increase the field of view (FOV), schematic for phased array coils is shown in Fig. 7.5b. A phased array is a configuration of multiple planar coils with a carefully designed defined overlap where the mutual inductance between the neighboring coils is canceled [207, 216]. This configuration is valid for samples with a large area or several parallel samples with minimal interference in between. Davoodi et al. [217] developed a broadband micro spiral coil that could acquire NMR spectra over a wide range of frequencies (125–$500\,MHz$ in an $11.74\,T$ NMR magnet) without the need for a tuning interface circuit.

Striplines

Striplines or micro slot coils have a very simple structures; they are made od a single planar lines that can be easily fabricated using micro-fabrication technologies. A schematic of the stripline is shown in Fig. 7.5c. It operates as a wave-guide with geometrical dimensions that determine the resonance frequency, such as the conductive strip's geometries and the substrate's relative permittivity. Additionally, its magnetic field B_1 is proportional to the substrate (dielectric) thickness [218]. The matching circuit interface connected to the stripline significantly affects its quality factor because of the thermal noise arise by the lumped components. This problem was raised while developing a lumped-element planar strip array (LPSA) to enhance parallel MRI imaging and decrease the scan time [219].

Several approaches have been developed to benefit from the simple stripline structure and high sensitivity. The volume microstrip approach has been developed as a microstrips transmission line (MTL) to develop MR imaging of the human head [220]. In addition, this volume approach was also applied by using double microstrips for achieving a uniform magnetic field within the volume of interest and better SNR. Moreover, they were able to analyze flat samples such as cell layers [221]. Another approach to enhance the stripline magnetic field homogeneity is adding two metal planes to force the field line to be parallel to the planes, which enlarge the volume with a homogeneous magnetic field [222]. Striplines have been utilized for analyzing living cells like cancer cells, where a microfluidic device was developed to hold the sample then placed on the top of a micro slot detector to perform the NMR analysis [1].

7.4 Flow sensors

Developing microfluidic-compatible NMR devices has drawn significant attention in recent years. Microfluidic devices have been used in high-field NMR spectroscopy (^{1}H resonant frequency > 200 MHz), often integrating flow for biological sample monitoring [1–3], chemical reaction tracking [4–8], sensitivity enhancement techniques [9–12], and most recently, electrochemical functionality [13]. Except for the digital microfluidic approach [8, 223], the target sample in these examples has always been transferred from outside the magnet without considering the sample handling situation. For flow-based NMR spectroscopy, sample loading is done from outside the NMR magnet. Thus, eliminating dead volumes in filling transfer lines (often a few meters in length) before the sample reaches the NMR detector is the challenge. The feading dead volume can be converted into a multi-sample queue using two-phase flow, achieving high throughput by taking advantage of microfluidic technologies. Hence, online tracking of the sample position and velocity must be addressed to ensure each NMR signal acquisition is synchronized to the target sample.

Fluids in microfluidic applications are commonly detected by employing either optical or electrical sensing systems, examples of state-of-the-art flow sensor are shown in Fig. 7.6 . Electrical sensing is appealing for two-phase flow since samples are usually optically similar. Moreover, aqueous samples have a dielectric constant at least an order of magnitude different from standard immiscible oil. Hence, electrical sensing is an excellent candidate for two-phase plugs flow detection.

7.4.1 Optical sensors

An optical sensing system consists mainly of an optical source, optical detector, and wave-guides to guide the light beam. Several optical sources have been used, e.g., semiconductors laser sources, based on amplifying the stimulated emissions. Each laser has specific parameters such as the operating wavelength, single or multiple modes, and beam quality; the parameter of the laser is selected based on the application. Several optical detectors have been utilized, such as photo-diodes, photo-multiplier tubes (PMT), and charged coupled devices (CCD). The optical detector is used to receive the optical signal and detect the change in the signal intensity corresponding to a parameter of the sample. The detector converts the change in the light intensity to an electrical signal to be analyzed.

Optical sensing systems are widely used for medical, cosmetic, and food industries. Nguyen et al. [224] developed an optical sensing system to control droplet size in a microfluidic droplet-based system. The laser source was located above the micro-channel and a photo-diode detector on the other side of the channel. The laser light intensity varies as a droplet crosses the light beam due to diffraction and absorption. As a result, the size and the shape of the droplets can be recorded. Camer et al. [225] developed an optical sensing system for counting formed droplets in a dripping system. The optical system was built around a transparent rectangular-shaped flow channel with a width of 2.5 mm. A 760 nm laser source is located on one side of the channel, and a detector is located opposite it. The detector senses the interruption of the laser beam whenever a drop crosses it and transmits electrical data with a frequency of 200 kHz. Additionally, a CCD camera is used to monitor the drop breakup during dripping.

The optical methods have the advantage of being a non-invasive sensing technique, extending the flexibility in sample handling. However, the main challenge is that the target samples are often optically similar. Other than the optical sensing system, the sensing element of the electric sensors can be easily fabricated using the standard lithography process within microfluidic devices.

7.4.2 Electrical sensors

Flow electrical sensors are mainly based on changing the impedance of the sensor corresponding to a change in the physical properties of the material in their vicinity. The commonly used flow electrical sensors could be categorized into resistive and capacitive sensors. Capacitive sensors provide an output signal based on the target sample dielectric constant, while resistive sensors sense the samples based on their thermal conductivity.

Resistive sensors

Resistive sensors are thermosensitive sensors, where the resistance changes with the change of the temperature. By applying a constant potential difference across the resistive sensor, its temperature settles
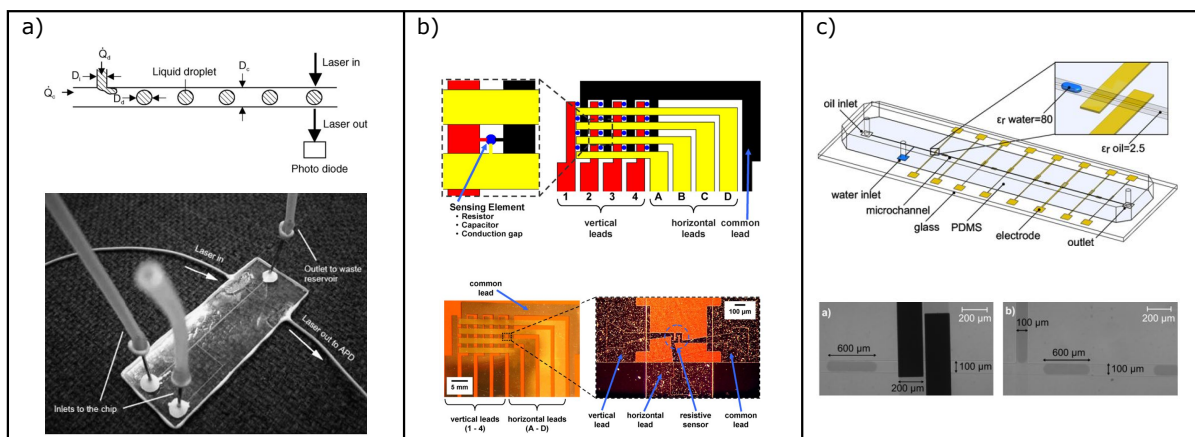
Figure 7.6: Examples of state-of-the-art flow sensor. **(a)** Liquid droplets detection using an optical system. [Top] Schematic illustration of the system, and [Bottom] microfluidic device with the flow optical detecting system, *reprinted from [224] with permission of Elsevier (Copyright © 2005 Elsevier B.V.).* **(b)** Multiplexed arrays (4 × 4) of capacitive and resistive sensors for sensing the flow of liquid plugs. The resistance of the resistive sensors (thin-film serpentine resistors) varies according to the thermal conductivity of the liquid in contact. [Top] Schematic illustration of the multiplexed sensors, and [Bottom] microscopic image of the resistive sensors, *reprinted from [226] with permission of Elsevier (Copyright © 2008 Elsevier B.V.).* **(c)** Microfluidic device integrating capacitive sensors (coplanar electrodes) positioned beneath a flow channel with a thin insulation layer to prevent direct contact with the target fluids. The capacitance of the sensor changes according to the permittivity of the flowing fluid. [Top] Schematic illustration of the microfluidic device with an array of the capacitive sensors, and [bottom] microscopic image of the coplanar capacitive sensor, *reprinted from [227] with permission of Elsevier (Copyright © 2011 Elsevier B.V.).*

at constant temperature based on its temperature coefficient of resistance (TCR) and the surroundings thermal conductivity. When samples with different thermal conductivity, or samples of the same liquid flowing at different velocities, flow over the resistive sensor, the sensor's temperature varies correspondingly, changing the sensor's resistance and thus the output current.

Several studies have employed resistive sensors in droplet detection [226, 228]. However, The main limitation of the resistive sensor is that the target fluid should come in direct contact with the sensor to change its resistance. This direct physical contact between the sensor and the sample could lead to sample's temperature fluctuation and cross-contamination.

Capacitive sensors

The capacitive sensor is a suitable choice for most microfluidic applications. In general, the capacitance of a capacitive sensor changes according to the change in the insulator dielectric constant or the capacitance dimensions. Capacitive sensors are suitable for various applications such as position, angle, pressure, and fill level measurements. The sensor configuration is optimized according to the application, e.g., in the case of fill-level capacitive sensors, the sensor configuration depends on whether the fluid is conductive or non-conductive [229]. For conductive fluid, the fluid is considered as counter electrode, and an insulated electrode is immersed into the liquid with a single conductive electrode. On the other hand, for non-conductive fluids, the fluid is considered the dielectric insulator between the two inserted conductive electrodes. Soenksen et al. [230] developed a capacitive sensor to monitor and control a fluid height without direct contact with the fluid. Elbuken et al. [227] developed a planar interdigitated capacitive sensor for measuring droplets' size and speed. Ghafar-Zadeh and Sawan [231] developed a hybrid microfluidic/CMOS capacitive sensor. The design of the sensing part is based on interdigitated electrodes (IDC), where the system output signal varies according to the dielectric constant of the material in contact.

Capacitive sensors feature several advantages including high sensitivity, no physical contact or interference with the sample, small temperature influence, and good stability and reproducibility. In contrast, they feature some drawbacks such as the electrical connection influences the output reading (i.e., interfacing electronic should be located near it), sensitivity to humidity and dust, and sometimes shielding is required to avoid susceptibility for interfering signals.

8 Automated high throughput NMR system[1]

This chapter presents a thorough description of the design, characterization, and fabrication of a fully automated high throughput NMR system. Automating the NMR spectroscopy is achieved by combining microfluidic technologies with thin-film micro-NMR detectors. The system is based on the concept of flow-based NMR spectroscopy, where plugs of the target samples are loaded into a flexible microfluidic tube separated by an immiscible fluid. The flexible tube is fed through a glass capillary with a micro-NMR detector, and flow sensors are rolled around it and placed in the isocenter of an NMR magnet. The arrangement of successive plugs of samples and immiscible fluid is kept under continuous flow. The flow sensors detect the aqueous-oil interfaces and synchronize the NMR spectroscopy acquisition via a microcontroller. The system possesses a pair of flow sensors that allows the system to operate regardless of the flow velocity and the plug volume.

This chapter is divided into four sections. Section 8.1 explains the technical details for the different components of the automated NMR system. Within this section, the control system's hardware connections and software algorithms are presented. Section 8.2 discusses the design, optimization, and characterization of the micro-NMR detector. Section 8.3 discusses the design, optimization, instrumentation, and validation of the flow sensing system. Section 8.4 introduces a robust thin-film micro-fabrication process used for fabricating the micro-detector and flow sensors.

8.1 System description

Figure 8.1a presents an overall schematic of the hardware components of the actively synchronized NMR system, with a detailed illustration of a custom-built NMR probe head in Fig. 8.1b. The primary part of the automated NMR system is a custom-built NMR probe head. The probe head is built from a 3D printed holder (see Appendix D for the holder's working drawing) supporting a PCB that possess three substantial modules:

1. **A micro-NMR detector** attached to pre-tuning and matching capacitors.

   The pre-tuning and matching network is built from three non-magnetic capacitors (S111DUE, Johanson Technology) soldered directly on the PCB, having a balanced configuration of $C_{M,PCB} - (L \parallel C_{T,PCB}) - C_{M,PCB}$. The capacitor values can be modified to adjust the resonance frequency of the micro-NMR detector so the NMR spectroscopy could, in principle, be performed on any NMR-sensitive nucleus. This tuning and matching configuration is discussed previously in detail in Subsection 2.4.3, where $C_{T,PCB}$ is used to tune the NMR detector to ^{1}H NMR frequency, and $C_{M,PCB}$ is used to match the circuit to $50\,\Omega$ to guarantee signal transfer and prevent signal reflection.
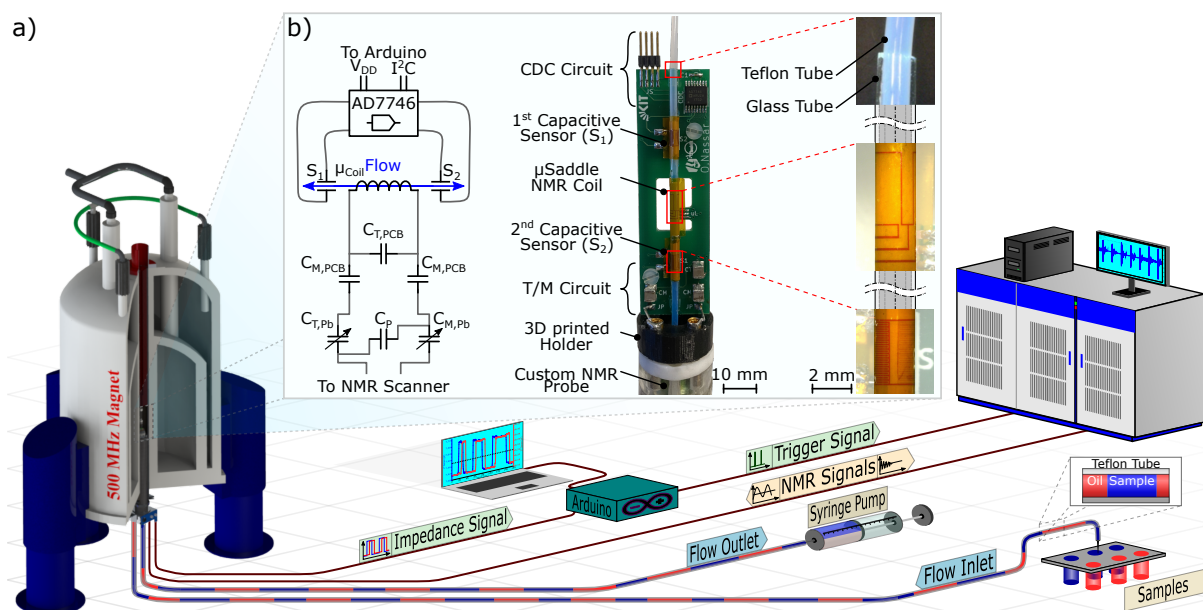
Figure 8.1: Overall diagram of the fundamental elements of the novel high throughput NMR experimental setup. **(a)** A microfluidic Teflon tube (OD/ID, 1.6/1 mm) is utilized to transport a sequence of plugs of various samples separated by an immiscible fluid through a custom-built NMR probe installed in an 11.7 T NMR magnet. A syringe pump is used to regulate the flow from outside the NMR magnet. A microcontroller is used to drive a pair of flow sensors integrated on the probe head to determine the samples' velocity and location and synchronize the NMR data acquisition. **(b)** Photograph of a customized probe head installed on the NMR probe. The probe head consists of a PCB supported by a 3D printed holder. The PCB possesses a micro-NMR coil with a pre-tuning and matching network, two flow sensors with their interface electronics, and a glass capillary (OD/ID, 2.15/1.72 mm) through which the flexible sample flow tube is fed. Right: microscopic images for the micro-NMR detector, the IDC sensor, and the insertions of the Teflon tube inside the glass capillary. Left: schematic diagram of the equivalent electronic circuit in the NMR probe.

2. **Two capacitive flow sensors**, before and after the micro-NMR detector, electrically connected to a capacitance-to-digital converter (CDC) microchip to convert the sensors' reading to digital data to be transferred outside of the magnet.

   Two sensors were used to enable velocity calculation, where the total separation distance between them is set to 30 mm. The two sensors are flanking the NMR detector with a separation of 10 mm w.r.t. the detector so that the NMR automated spectroscopy is independent of the flow direction. The capacitive sensors' readings were transferred to a microcontroller unit (MCU) located outside the NMR magnet via the CDC integrated circuit (IC). In addition, a digital pin of the MCU was connected to the triggering signal input-output unit (TTL I/O) of the NMR spectrometer console to synchronize NMR experiment acquisition.

3. **A glass capillary** with the micro-NMR and the flow sensors rolled around to contain the flexible microfluidic tube holding the flow.

   The flexible microfluidic tube (OD/ID, 1.6/1 mm) holding the sequence of samples was fed from

outside of the NMR magnet through a customized NMR probe and the glass capillary (OD/ID, 2.15/1.72 mm). This arrangement of fitting the flow tube inside the glass capillary provides several advantages:

(a) On the hardware side, it gives durability to the probe head as it prevents the interaction between the user and the sensors or detector. It avoids the cross-contamination of the probe head's glass capillary as there is no direct contact with the samples; therefore, the probe head can be used multiple times with a long life span.

(b) On the experiment preparation side, the sample's preparation is done effortlessly as the tube can be loaded with the required samples and later is into through the NMR setup.

(c) On the microfluidic side, it avoids the presence of any fluidic junctions, preventing flow disturbance which creates air bubbles or leads to the interference of the oil plugs inside the sample plug.

(d) On the NMR side, it increases the gap between the sample and the NMR detector's tracks where the magnetic fields are distorted, consequently, confine the sample to the volume with the most homogeneous magnetic fields.

The probe head's polylactic acid (PLA) material and the FR-4 of the PCB were eliminated next to the micro-NMR detector as they are a source of background signal and affect the homogeneity of the magnetic field. The probe head was designed to be compatible with market available micro-imaging NMR probe and a triple-axis micro-gradient sleeve (Bruker). Hence, the system is compatible with pulsed-field gradient (PFG) sequences for the magnetic resonance imaging (MRI) experiments.

The probe head is connected to the ^{1}H channel of the custom-built NMR probe. The design of the NMR probe is adopted from commercial probes. The main addition in the developed probe is four built-in pipes inside the probe, allowing fluidic and electrical access to the probe head. Like other commercial probes, the probe posses two trimmers (0.5 - 10 pF, TG 092 ROHS, EXXELIA) connected in series to the probe head for fine-tuning and matching. The trimmers can be mechanically adjusted using glass fiber rods from outside the magnet. Figure 8.2 shows the configuration of the tuning and matching network in the probe and the probe head. The fixed capacitor C_P is added to the probe's circuit to set one
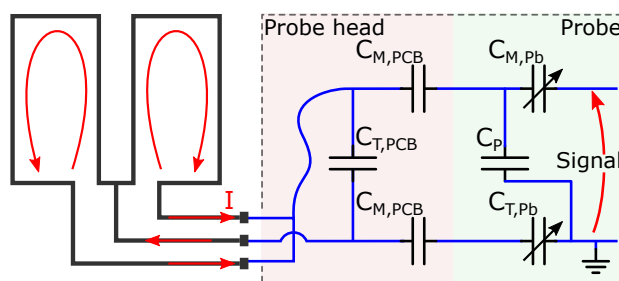
Figure 8.2: Electrical RF tuning and matching network in the NMR probe. The saddle coil's three-terminals are connected in a way to keep the electrical current flowing in the opposite direction in the two loops so that their magnetic field constructively interfere in the coil center. The probe head has fixed capacitors for pre-tuning and matching, and the probe has trimmers for fine-tuning and matching.

of the trimmers in parallel with the probe head circuit to enable the tuning functionality; this electrical configuration is discussed in detail in Subsection 2.4.3. The probe was designed to locate the micro-NMR detector in the NMR magnet isocenter (the region with the magnet's highest homogeneity). Locating the micro-detector in the isocenter enables the spectrometer shim system to correct the static B_0 field's minor deviations within the detection volume. A 3D CAD model of the probe is available in Appendix D.

The train of samples was kept underflow using a syringe pump positioned outside of the NMR magnet. Loading the microfluidic tube with the samples was done manually and automatically, as discussed in Subsection 8.1.2.

8.1.1   Control system

Figure 8.3 presents a schematic diagram of the hardware components of the automated NMR control system. As the train of aqueous plugs and oil plugs flow through the capillary tube with the flow sensors, a difference in the sensors' capacitance is detected. The change in the capacitance results from the different effective dielectric interacting with the sensor's electric fringe field. The changes in the capacitive sensor's values are then sensed by the MCU, which in turn synchronizes the NMR acquisition to collect the spectrum for each plug separately. The MCU sends the digital triggering signal (TTL) via a DIO pin (high = 5 V, Low = 0 V) to the TTL I/O unit of the NMR console. Hence, during the automatically synchronized NMR experiment, two software algorithms are executed in parallel. One algorithm on the MCU responsible for sending the TTL signal based on the flow interface. The other algorithm is the pulse sequence program on the NMR acquisition software (TopSpin 3.5pl2, Bruker BioSpin) to receive the TTL signal and increment the FIDs to save the spectrum from each plug on a different memory location.

Figure 8.4 presents a flow diagram for both algorithms, the source codes of the two algorithms are attached as supplementary material in Appendix D. On the NMR pulse program side, the acquisition
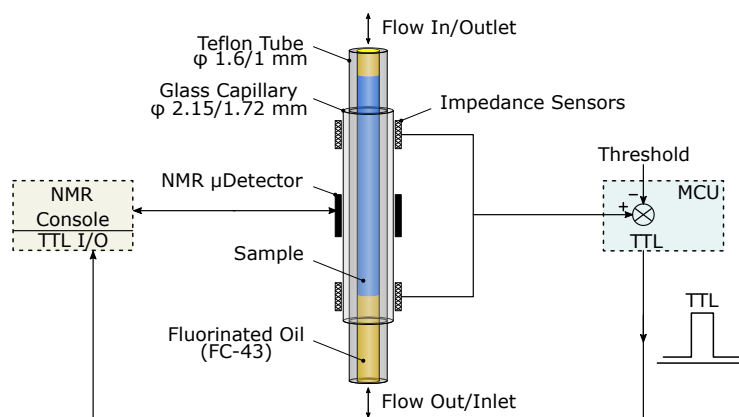
Figure 8.3: Schematic diagram demonstrating the main hardware elements of the control system. The NMR data acquisition is synchronized by the microcontroller, which sends the TTL signal to the NMR spectrometer console's TTL I/O unit. The microcontroller generates the TTL pulse according to the values of the flow sensors.

software starts collecting the NMR scans of the first FID following the system start. Following each collected scan, the NMR acquisition software checks the triggering input signal value sent from the MCU on the TTL signal pin in the NMR consol TTL I/O unit. If the TTL signal is low (0 volts), the spectrometer accumulates the collected scan to the current FID. In case the TTL signal is high (5 volts), the current FID is saved to the disk after adding the last NMR scan and then initiates the next FID measurement. Meanwhile, on the MCU side, the program monitors the capacitance values of the two sensors simultaneously. Once the measured capacitance value of either of the two sensors overrides a user-set threshold value, the current time is recorded (t_1). Additionally, a TTL signal is sent from the MCU'S DIO pin to the TTL pin in the TTL I/O unit of the NMR console after a delay (d). Subsequently, the MCU monitors the other sensor's capacitance value until it overrides the threshold value, and then it records the time (t_2). Afterward, the MCU monitors the first sensor's value until it becomes lower than the threshold level, after which the MCU sends a TTL signal after a delay (d). Consequently, for each plug, the NMR TTL I/O unit receives two triggering pulses, the first TTL pulse when a sample plug enters the NMR micro-detector (start new NMR FID acquisition) and the second TTL pulse when it leaves the micro-detector (save the current NMR FID). Afterward, the MCU monitors both sensors' capacitance
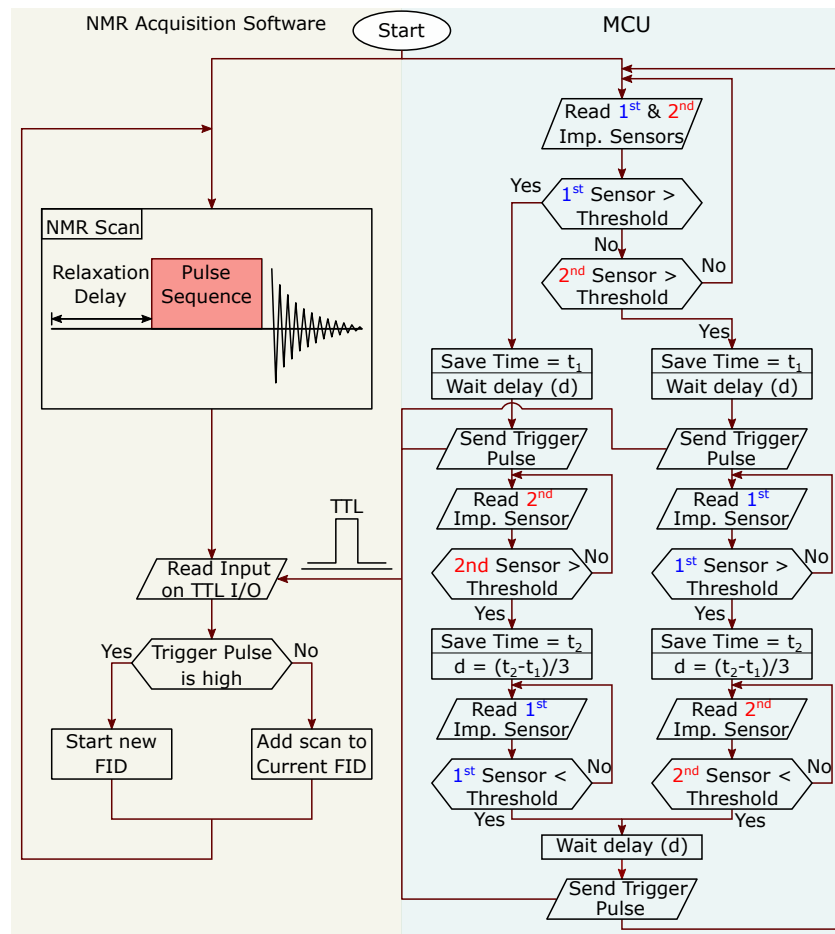
Figure 8.4: Flow chart illustrating the executed algorithms on both the MCU and the NMR acquisition software. During an automated NMR experiment, the two algorithms run in parallel. The algorithm on the MCU triggers the NMR pulse sequence to increment the FID based on the sample presence.

value in a threshold detection loop, waiting for the next plug. This control algorithm results in saving the NMR scans collected for each sample in a different FID. At the beginning of each loop, the MCU monitors both sensors' capacitance values to maintain the flexibility of running the NMR experiment in a bidirectional flow.

The triggering signal is always sent from the MCU to the NMR TTL I/O unit after a time delay (d) to ensure that the sample plug either reached or entirely left the NMR micro-detector. The delay (d) is calculated base on the times (t_1 and t_2) recorded during the flow using Equation 8.1, taking into consideration the separating distance between the flow sensor and the NMR detector of 10 mm, the total gap between the two flow sensors of 30 mm. The initial value of the time delay d is set to zero and updated after the MCU measures each plug's velocity. Hence, a dummy plug is usually added at the beginning to determine the time delay's first value, which depends on the flow velocity.

$$d = \frac{t_2 - t_1}{3}. \tag{8.1}$$

On the one hand, to guarantee that the NMR spectrometer captures the triggering pulse, the pulse width (t_{TTL}) needs to be longer than the summation of the NMR scan's acquisition time (T_{AQ}) and relaxation delay ($D1$). On the other hand, the TTL pulse width must also be shorter than twice the summation of acquisition time and the relaxation delay; otherwise, it will be captured twice by the NMR spectrometer:

$$(T_{AQ} + D1) < t_{TTL} < 2 \times (T_{AQ} + D1). \tag{8.2}$$

8.1.2   Sample loading

Filling the microfluidic tube with the samples can be done manually or automatically. In both filling regimes, the same sequence was adopted as follow:

1. The microfluidic tube was fed through the NMR probe and the glass capillary on the probe head.

2. The syringe pump was connected to one terminal of the tube, while the other tube's terminal was left open.

3. The syringe and the whole tube were initially filled with the oil used for separating the sample to avoid any air gaps, which hindered the flow's stability.

4. The tube's open terminal was transferred to the first sample reservoir, and the syringe pump is switched on to draw the sample with a pre-adjusted volume.

5. The tube terminal was then moved to the separating oil reservoir, where at first a small portion of the sample is pumped out to ensure no air bubbles are introduced in the line, and then draw the oil plug.

6. Then, the tube's terminal is moved to the next sample, and so on.....

After each filling step, the tube's terminal was immersed in a pure deionized (DI) water reservoir for cleaning to avoid cross-contamination. Once all sample plugs are loaded in the tube, the flow was continuously switched on for the NMR acquisition.

In the manual filling regime, the motion of the tube's terminal between the different reservoirs and the synchronization of the syringe pump were both done by the user. On the other hand, in the automatic filling regime, a robotic arm was used to move the tube's terminal. A MCU was used to control the syringe pump and synchronize it with the robotic arm motion. An overview of the components of the automatic filling is illustrated in Fig. 8.5.

The automatic loading system consists of an MCU (Arduino Mega 2560 and customized Arduino shield), a robot arm (UR3e, UNIVERSAL ROBOTS), a syringe pump (Fusion 200-X Touch, KR Analytical), and a router. This shield contains a Wi-Fi module (ESP8266), a serial-RS232 converter, a switch for resetting the controller, and an LED to indicate the current controller activity. The MCU is connected to the syringe pump via a DB-9 serial connector, through which the pump receives the required commands to change pumping settings. The router is used as a message queuing telemetry transport (MQTT) host, through which the communication between the MCU and the UR3e robot arm is achieved wirelessly.

The user interface to control the automated loading system comprises three programs that all run on a computer and are connected to the MCU. The user interface allows the researcher to program the system's pumping sequence and know its progress. These programs include: i) an excel workbook that serves as the front-end where the user can set up the experiment sequence; ii) a python file that runs in the Windows shell, takes the input from the excel file and sends the control signal to the pump and the wifi module; and iii) a program to monitor the MQTT client. A description of the user interface provided in Appendix D.
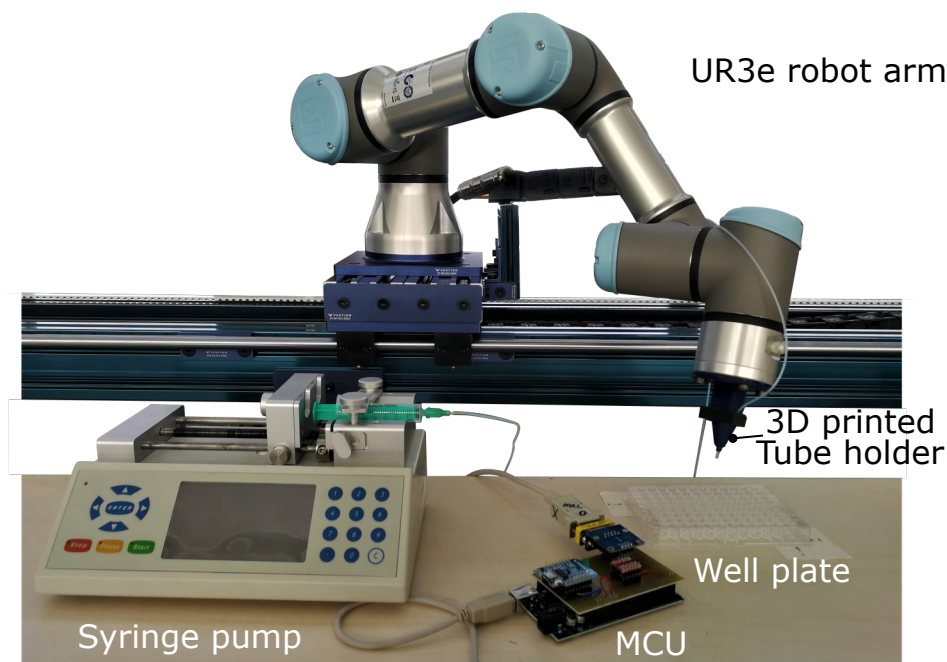
Figure 8.5: Overview of the hardware components of the automated plugs loading system.

8.2 Micro NMR-detector

8.2.1 Detector design and optimization

The topology of an MR coil is typically defined based on the application and the target sample type. In general, volume coils are favored for NMR applications where the samples are chemical solutions or suspensions. In contrast, planar coils might be the choice for MRI applications where the samples have arbitrary shapes as tissues and animal organs. Key design considerations to maximize the performance (sensitivity and spectral resolution) for an MR detector are: i) the strength and homogeneity of the excitation magnetic B_1 field generated by the RF coil; and ii) the impact of the MR coil conductive tracks on the homogeneity of the primary static magnetic B_0 field. The performance of the B_1 field has a direct impact on the measurement sensitivity. The B_0 field homogeneity deviates within the RF region due to a magnetic susceptibility mismatch between material interfaces, directly impacting the MR signal spectral resolution. An MR coil with a slight deviation in the B_1 field homogeneity is acceptable in MRI applications even though this will affect the image contrast. On the other hand, for NMR spectroscopy, any deviation in the coil performance means wasted signals which can be a problem with low concentrate samples. Hence for NMR spectroscopy, the RF coil needs to be carefully optimized.

For the presented flow NMR application, a saddle coil geometry has been adapted for its advantages. Saddle coil is one of the most used geometries in NMR spectroscopy. A saddle coil is a special case of a Helmholtz coil; it is built out of two square loops facing each other and arranged in a cylindrical manner, as shown in Fig. 8.6.

The homogenous B_1 field generated by the saddle coil is in the center of the arrangement and is perpendicular to the coil structure, making it very suitable for the flow-based NMR applications. Finite
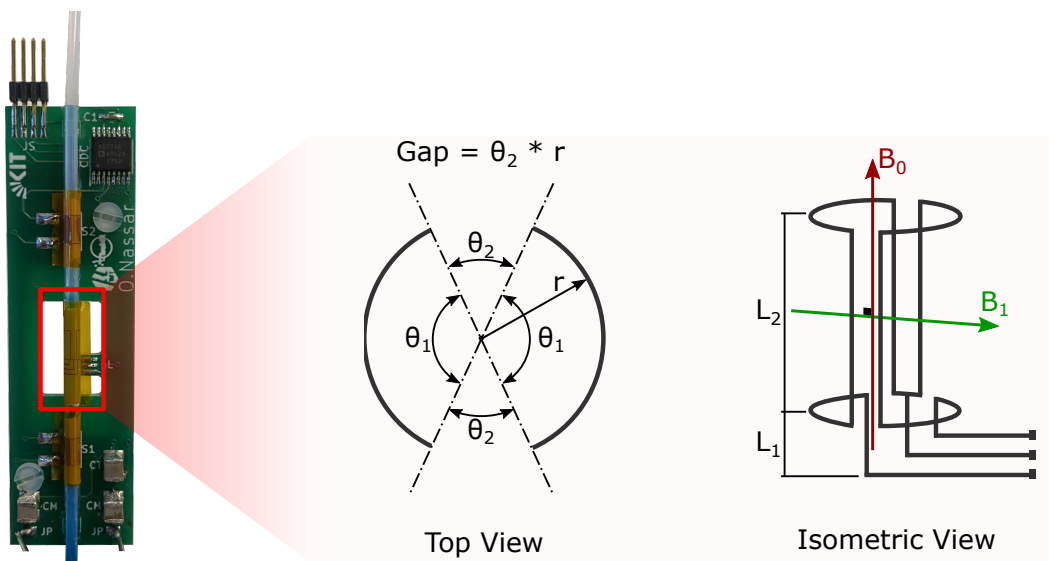
Figure 8.6: Photograph (left) and schematics diagram of a micro-saddle coil. Design parameters of the saddle coil include the perimeter gap between the two square conductor loops, the length of the coil detection region (L_2), and the length of the electric power leads (L_1).

element simulations were performed for the magnetic field generated by the coil. The simulation results in Fig. 8.7 show the magnetic field orthogonality with the coil loops. Since the B_1 field should be orthogonal to the B_0 field, the coil is oriented along the axis of the B_0 field. Therefore, the flow tube can be easily fed along the magnet's axis, making the sample handling comfortable. Moreover, in this arrangement, the B_0 field needs to cross fewer material interfaces near the RF detection region, making re-shimming of the coil more manageable. A solenoidal coil has a much higher filling factor than a saddle coil; nevertheless, its B_1 field is along its axis, which places it perpendicular to the B_0 field. Hence, for a solenoidal coil shimming and flow tube feeding can be a big challenge.

Finite element simulations using COMSOL Multiphysics software were performed to optimize the micro saddle coil geometrical dimensions of the saddle coil. The optimization aims to select the coil geometrical dimensions in a way to enhance the generated radio frequency field B_1 per unit current while maintaining the static B_0 and RF B_1 fields as homogeneous as possible. In the simulation model, a micro saddle coil geometry was constructed around two concentric tubes to model a glass capillary and a Teflon tube filled with water. The saddle coil with the glass and Teflon tubes was located inside a cylinder-shaped domain to model the surrounding air. Two simulation scenarios were considered:

1. The first scenario aims to calculate the coil sensitivity and the RF B_1 field homogeneity. The COMSOL radio frequency module (electromagnetic waves, frequency domain) was utilized in this model. The saddle coil was attached to a $50\,\Omega$ port for excitation by a 1 A signal at 500 MHz. In this simulation model, a radiation boundary condition that acts as an absorbing layer was implemented to prevent back-scattering. The B_1 field generated by the coil inside the water domain was deduced, and the coil sensitivity η_{RF} was calculated with Equation 2.31, taking into consideration the coil high-frequency resistance R and the driving electrical power P.

2. The second scenario aims to check the coil conductive tracks' effect on the static B_0 field homogeneity. The COMSOL AC/DC module (magnetic fields, no currents) was utilized. An external static magnetic field of 11.7 T was applied along the tubes' axis.

In both simulation scenarios, the coil had a track width of $100\,\mu m$ with L_1 and L_2 of 2 mm and 4 mm, respectively (see Fig. 8.6 for description). Additionally, the gap between the saddle coil two rectangular
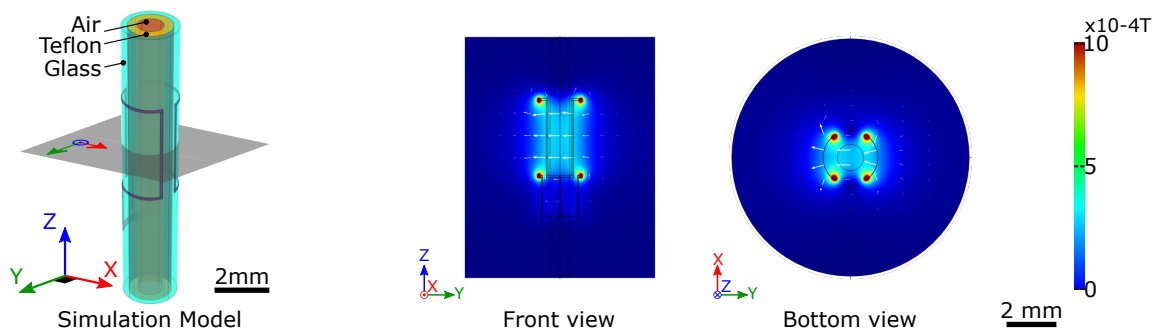
Figure 8.7: Simulated saddle coil model (left) and the resulted magnetic field (right). The simulated magnetic B_1 fields of the saddle coil's two loops are pointing in the same direction, and thus they constructively interfere in the coil center (sample region).

loops (θ_2) was swept to obtain the best performance (highest sensitivity with the most homogeneous B_0 and B_1 magnetic fields). The gap was swept in a way that the gap perimeter ($\theta_2 \times r$) changed from 100 µm to 1300 µm at steps of 100 µm. The simulation results are presented in Fig. 8.8, the coil sensitivity and the static B_0 field homogeneity are plotted versus the gap perimeter (arc distance between the rectangular loops). Furthermore, the B_0 and B_1 magnetic fields distribution are illustrated at different gaps.

The simulation results reveal that for a saddle coil, conductive tracks with a high degree of symmetry not only enhance the B_0 and B_1 magnetic fields homogeneity but also increase the sensitivity. According to the simulation study, a gap of 700 µm (equivalent to θ_2 of 37.3°) was selected for the coil fabrication. The full geometrical dimensions of the implemented saddle coil are summarized in Table 8.1. The fabrication process can be found in micro-fabrication Section 8.4.
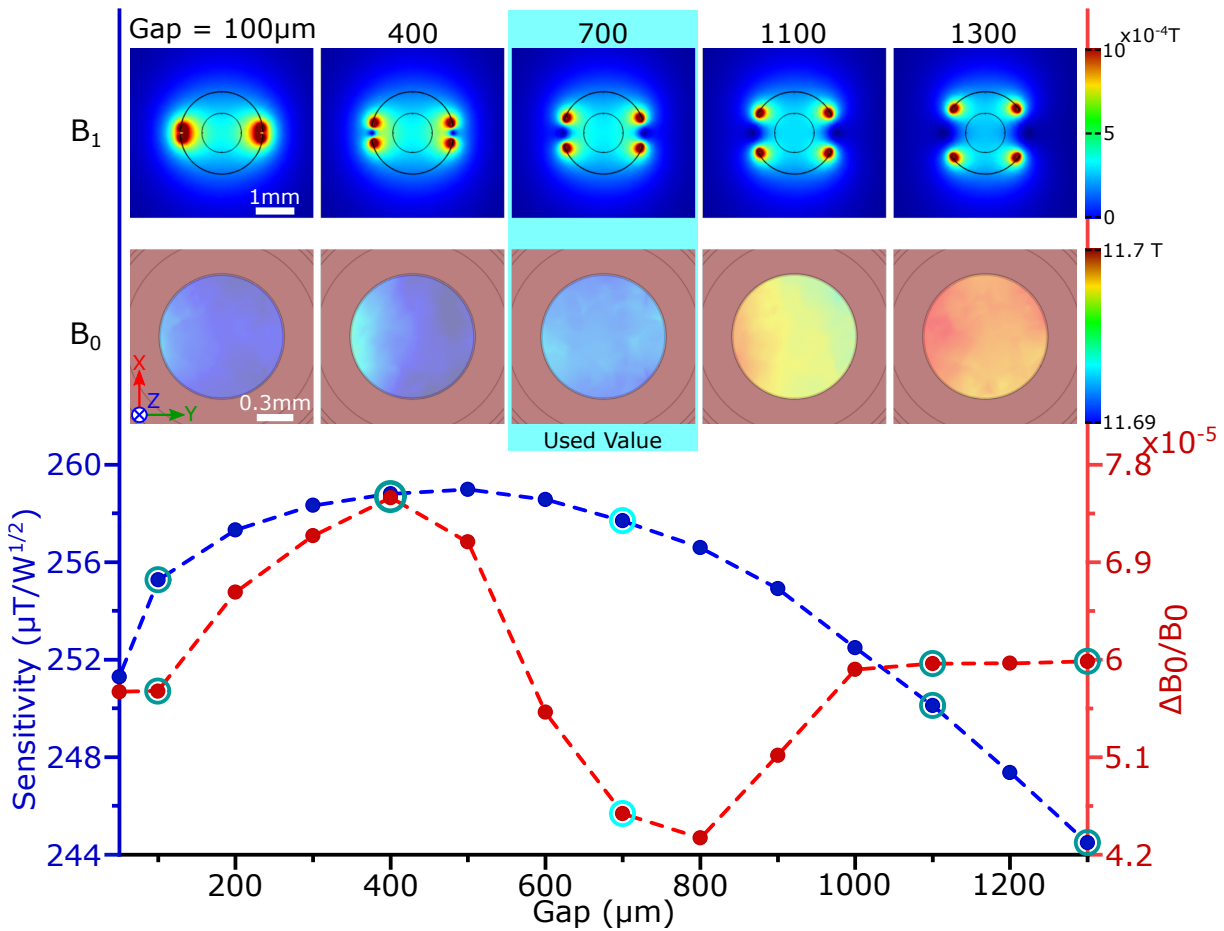
Figure 8.8: Finite element simulation (COMSOL Multiphysics) studies the effect of changing the perimeter gap between the saddle coil's loop on the coil sensitivity and the B_0 magnetic fields' homogeneity. The graph is the simulated coil sensitivity and the simulated B_0 homogeneity versus the gap between the saddle coil's loop. The B_0 and B_1 field top view profiles at a cross-section in the center of the saddle coil are plotted for different gap values (Top).

Table 8.1: Geometrical dimensions of the integrated saddle coil in the custom-built NMR probe head.

Parameter	value
Track thickness (t)	9 µm
Track width (W)	100 µm
Coil length ($L_1 + L_2$)	6 mm
Detection region length (L_2)	4 mm
Radius (r)	1.075 mm

8.2.2   Detector characterization

The fabricated micro-saddle coil was evaluated following the different evaluation approaches summarized in Table 2.1 in the MR characterization Subsection 2.4.4.

With a rolled-up micro-saddle coil connected to the custom-built probe, pre-matching and tuning was accomplished by adjusting the capacitors soldered on the probe head's PCB and validated using a network analyzer (Agilent, E5071B). The reflection coefficient S_{11} was used to check the resonance of the resonator. The coil was consecutively tuned to 500 MHz, the ^{1}H proton resonance frequency (Larmor frequency) at 11.7 T, and matched to 50 Ω, as shown in Fig. 8.9. By knowing the bandwidth at -3 dB ($\Delta f_{-3\,dB}$) of the resonance frequency (f_0) and substituting in Equation 2.35, the loaded quality factor for a batch of fabricated coils was measured to be $Q_P = 50 \pm 2$.

The probe head was characterized using NMR spectroscopy measurements conducted using an AVANCE
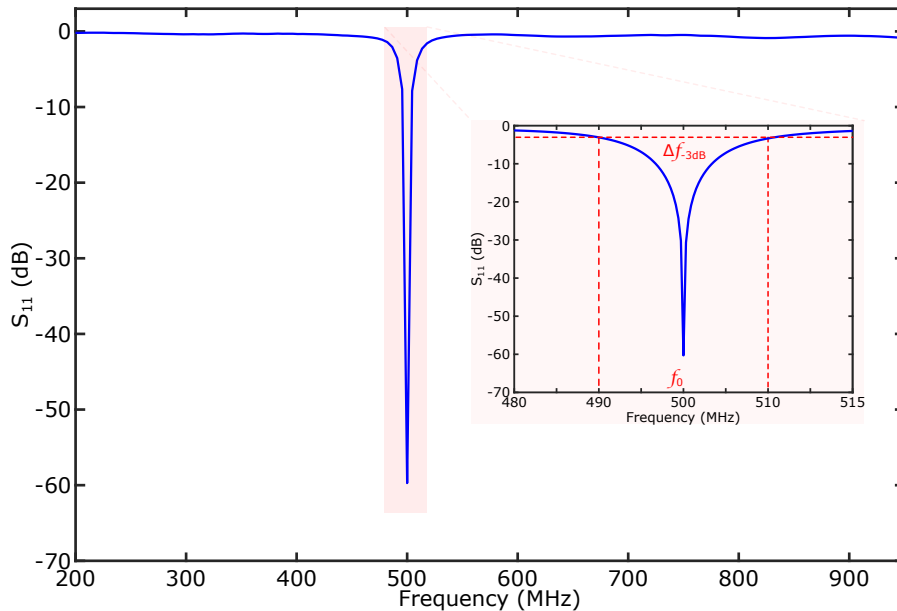
Figure 8.9: Measured reflection coefficient S_{11} of a micro-saddle coil. The coil is connected to the custom-built NMR probe and filled with an aqueous sample, tuned at 500 MHz and matched to 50 Ω. The bandwidth at -3 dB was measured to be approximately 20 MHz, resulting in a loaded quality factor of ~ 50.

III 11.7 T NMR system (^{1}H resonance frequency 500 MHz, Bruker BioSpin) under stationary (non-flowing) conditions. The coil was filled with a test sample (30 mM TSP dissolved in deionized (DI) water) using a Teflon tube with an inner diameter of 1.0 mm, yielding an active sample volume of 3.14 μL. FWHM of the ^{1}H NMR water resonance was used to evaluate the spectral resolution (Fig. 8.10, red spectrum), with the micro-coil yielding a line-width of 1.25 Hz. The excitation B_1 magnetic field performance was assessed by acquiring a nutation spectrum (a series of ^{1}H NMR spectra at fixed supplied power of $P = 1$ W, varying the excitation pulse width from 1-105 μs, in increments of 5 μs (Fig. 8.10, blue spectra). The nutation spectrum envelop time period was measured to be $T_{nut} = 204$ μs (90° flip angle achieved at 51 μs), thus the nutation frequency was calculated to be $f_{nut} = 4.9$ kHz.

The B_1 field strength was calculated using Equation 2.33 to be $B_1 \approx 230$ μT (^{1}H gyromagnetic ratio $\gamma_{^1H} = 42.756$ MHz T^{-1}, angle between the B_1 and B_0 fields $\theta = 90°$). Thus, the micro-coil sensitivity (η_P) was calculated using Equation 2.31 to be approximately 230 μT$/\sqrt{W}$, comparable to the simulation result in Fig. 8.8.

Additional electronic components (sensors, AD7746, and MCU) were added to the NMR system for realizing a synchronized NMR spectroscopy. These hardware components come with the cost of adding noise to the NMR signal, as illustrated in Fig. 8.11. A single scan ^{1}H NMR spectroscopy was performed on a stationary (non-flowing) sample (250 mM sucrose and 30 mM TSP in DI water) before and after powering up the periphery sensing components, leading to a reduction of the SNR by 55%, so that the $nLOD_\omega$ increases from 1.19 nmol s$^{1/2}$ to 2.18 nmol s$^{1/2}$. Nevertheless, the NMR probe head sensitivity was comparable to other micro-coils, even with the added noise [30]. The measured sensitivity
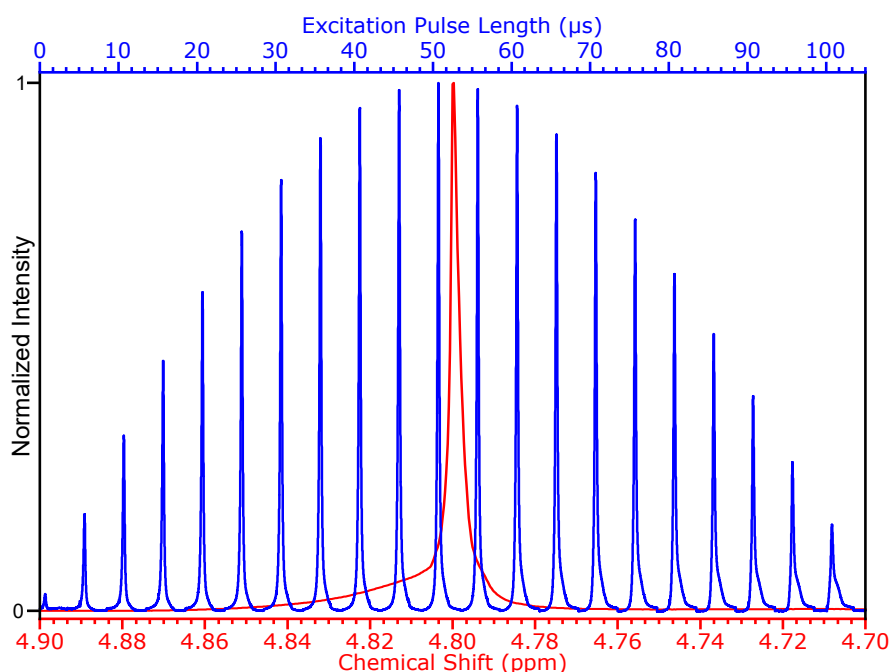
Figure 8.10: Characterization of the NMR micro-saddle coil. Measurements were performed using a micro-saddle coil at 500 MHz NMR magnet. The graph shows the NMR spectrum of water (red, lower scale) and NMR Excitation pulse nutation spectrum (blue, upper scale). The time delay between successive nutation measurements was 10 s.
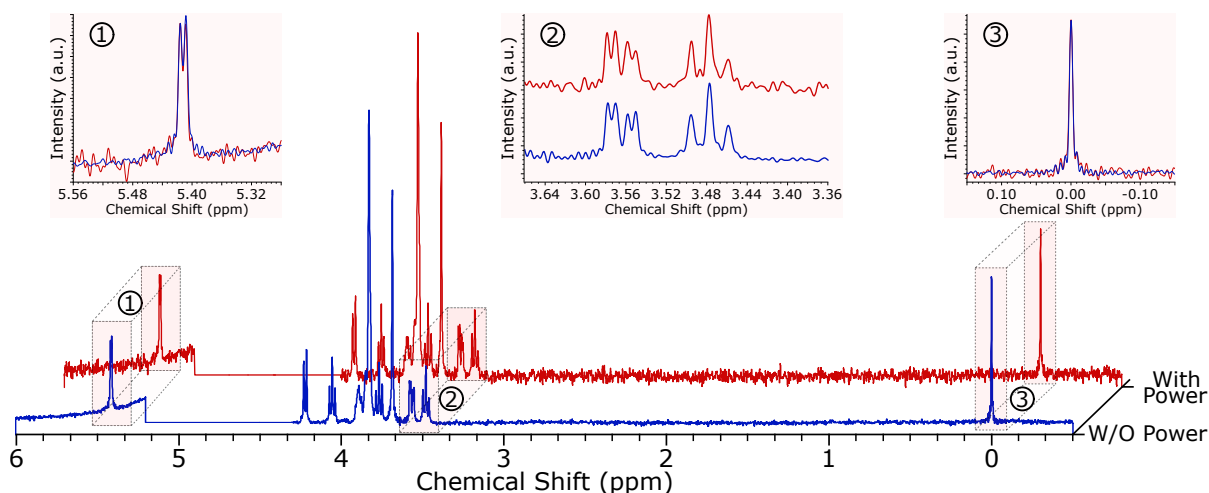
Figure 8.11: Comparison of a single-scan ^{1}H NMR spectra without (blue) and with (red) connecting the electrical power to the flow sensors' electronics interface. In this experiment, the sample was stationary (250 mM sucrose and 30 mM TSP dissolved in DI water). SNR was noted to decrease by $\sim$55 % after connecting the power for the electronics interface. The regions between 5.56 - 5.28 ppm, 3.68 - 3.36 ppm, and 0.15 - -0.15 ppm are re-plotted in red boxes for illustration. The water peak's intensity (5.2 - 4.3ppm) was set manually to zero.

of 1.19 nmol s$^{1/2}$ is at a 500 MHz static magnetic field. To facilitate comparison with other reported micro-coils, the sensitivity needs to be scaled to 600 MHz, which is then converted to 0.86 nmol s$^{1/2}$. For context, Finch *et al.* showed a sensitivity of nLOD$_\omega$(600 MHz) 1.57 nmol s$^{1/2}$ using their optimized stripline micro-detector [232]. Even with the noise added with the active flow-sensing elements in operation (yielding nLOD$_\omega$(600 MHz) 1.58 nmol s$^{1/2}$), the NMR detector performance is adequate.
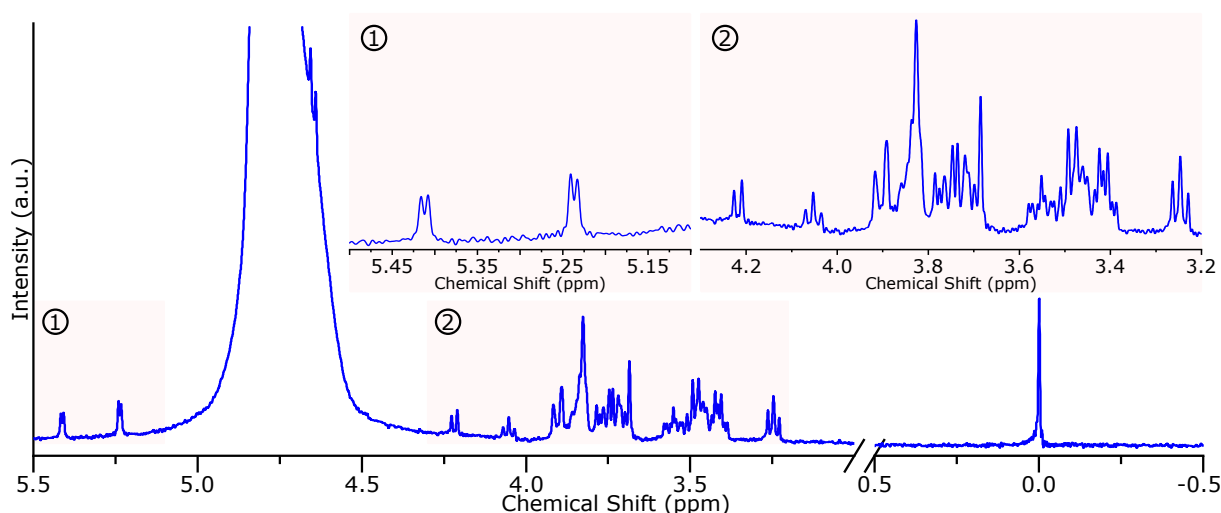
Figure 8.12: Single-scan ^{1}H NMR spectra of a stationary sample (300 mM glucose, 75 g L^{-1} coloring powder, and 30 mM TSP dissolved in DI water). In this experiment, the electrical power was not connected to the flow sensors' electronic interface. The regions between 5.5 - 5.1 ppm and 4.3 - 3.2 ppm are re-plotted in red boxes for illustration. The spectral region between 3.0 - 0.5 ppm (free region) was eliminated for clarity.

139

A test sample was prepared with 300 mM glucose, 75 g L^{-1} coloring powder, and 30 mM TSP dissolved in DI water to characterize the SNR of the flow NMR system. The characterization results are presented in the next Section 9.2. The coloring powder is added to the sample to visually separate the sample plugs from the transparent immiscible oil plugs. A single scan ^{1}H NMR spectroscopy of a stationary sample is shown in Fig. 8.12. The anomeric glucose hydrogen signal J-coupling could be resolved to $\sim 50\,\%$ from baseline. For comparison, Finch *et al.* demonstrated $\sim 85\,\%$ from baseline resolution of the same signal using the stripline micro-detector [232].

8.3   Capacitive Sensor

8.3.1   Sensor design and optimization

Interdigitated capacitive sensors (IDC) were used for detecting the flow, illustrated in Fig. 8.13. Interdigitated electrodes are sensitive to differences in material permittivity, interfering with its fringe field by modulating the sensor capacitance. Flow sensing dependent on capacitance calculation has several appealing characteristics: i) the non-invasive measurement avoids sample contamination; and ii) it requires low power minimizing temperature fluctuations. Figure 8.13 presents a 2D layout of the interdigitated electrodes and the expected fringe field lines within a rolled sensor detection region. The fringe field is directed toward the flow by rolling the sensor around the flow capillary. Rolled IDC sensors have improved sensitivity to differences in dielectric constants and are much more compact than conventional co-planar capacitive sensors.

The strength and uniformity of the electric field generated by the sensor define its sensitivity and performance. Improving the sensor sensitivity can be achieved by optimizing the interdigitated sensor geometrical dimensions to enhance the sensor generated electric field. To optimize the flow sensor performance, the sensor total width (W_S), and the gap between the electrodes (G) were explored (Fig. 8.14). Optimization was done by simulating the capacitive sensor's generated electric field using finite element
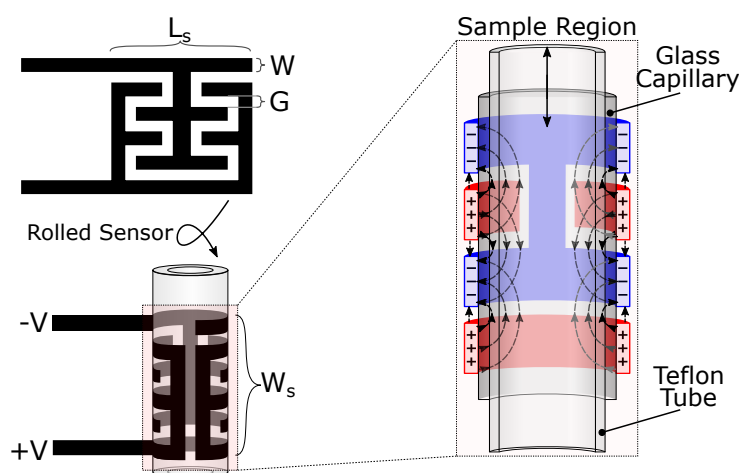
Figure 8.13: 2D schematic layout of the interdigitated capacitive sensors (IDC) and the expected fringe field generated by the sensors after rolling around the glass capillary.

simulation. In the simulation model, the interdigitated sensor was constructed around two concentric tubes to model a glass capillary and a Teflon tube filled with air and placed in an air-like environment. The simulated sensor was excited with a sinusoidal signal of 5 V at 32 kHz (mimicking the existing system parameters), and the sensor generated electric field was plotted. The simulated sensor had a total width $W_S = 3.725$ mm, a gap of $G = 25$ μm, the number of sensing electrodes $N = 30$, each with a width of $W = 100$ μm, and a length of $L_S = 6.6$ mm (slightly less than the outside circumference of the glass capillary 6.75 mm).

Figure 8.14a shows the effect of the gap width between the electrodes (G) on the generated electric field. The gap width was swept from 10 μm to 100 μm at steps of 10 μm. Subsequently, the electric field strength at the sensor center was plotted against the gap, as shown in Fig. 8.14a. Reducing the gap width increases the generated electric field strength and hence increases the sensor's sensitivity as in the case of co-planar interdigitated capacitive sensors [233]. Figure 8.14b demonstrates the effect of the capacitive sensor overall width (W_S) on the generated electric field. The sensor width was swept from 2 mm to 5 mm with a step of 0.5 mm. Subsequently, the electric field strength at the sensor center was plotted against the sensor width, as shown in Fig. 8.14b. On the one hand, expanding the sensor sensing region by increasing the sensor's width along the glass capillary increases the generated electric field's strength and increases sensors sensitivity. On the other hand, the sensor width should be minimized to reduce the sensor's settling time. Increasing the number of sensing electrodes (N) within the sensor improves the generated electric field homogeneity and hence the smoothness of the signal [227]. According to the simulation results and considering fabrication complexity to not select dimensions below 25 μm, several
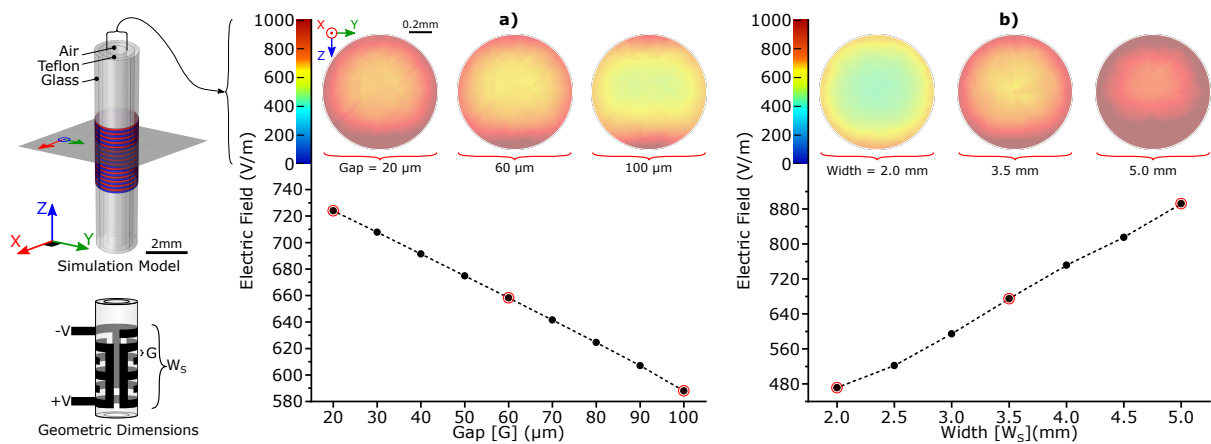
Figure 8.14: Finite element simulation (COMSOL Multiphysics) studies the impact of varying the gap between the IDC sensor's fingers (G) and the sensor total width (W_S) on the produced electric field inside the sensor. **(a)** Gap dependence: The electric field at the sensor center is plotted versus the gap (bottom). Top view profiles of the electric field at a cross-section in the center of the sensor are plotted for different gap values of 20 μm, 60 μm, and 100 μm. The electric field generated by the sensor decreases as the gap between the fingers increases. **(b)** Width dependence: The electric field at the sensor center is plotted versus sensor width (bottom). Top view profiles of the electric field at a cross-section in the center of the sensor are plotted for sensors with widths of 2 mm, 3.5 mm, and 5 mm. The electric field generated by the sensor increases as the sensor width increases.

Table 8.2: Geometrical dimensions of the integrated flow IDC sensor in the custom-built NMR probe head.

Parameter	value
Sensor's width (W_S)	3.725 mm
Number of electrodes (N)	30
Gap between electrodes (G)	25 µm
Electrode's width (W)	100 µm
Sensor's length (L_S)	6.6 mm

design iterations were tested. The selected dimensions of the interdigitated sensor implemented in the NMR probe head are summarized in Table 8.2.

The electric field generated by the implemented sensor is simulated. The domain inside the Teflon tube was modeled using, the relevant parameters, once for water ($\varepsilon_r = 80$) and again for the separating oil FC-43 ($\varepsilon_r = 1.9$). The electric field within the detection volume is lower in water than in FC-43 due to the relatively high dielectric coefficient of water compared to FC-43, as shown in Fig. 8.15. This variation in the sensor electric field leads to the change in the interdigitated sensor capacitance, which is then sensed to detect the solutions' interface. The capacitance instrumentation technique is discussed in the following Subsection 8.3.2.
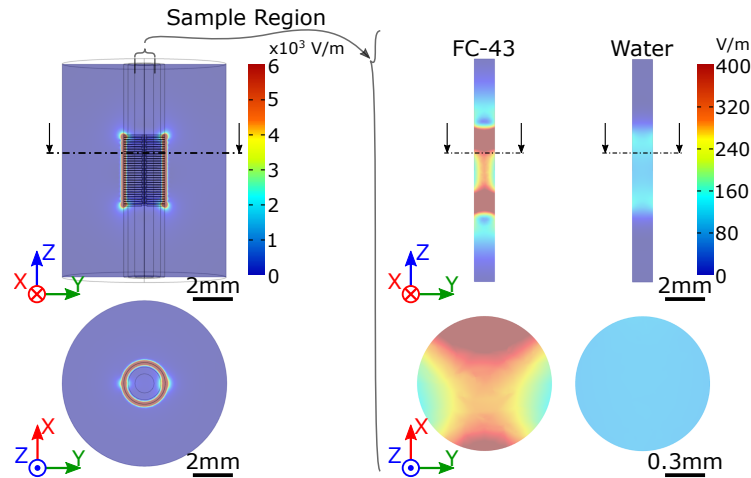
Figure 8.15: Finite element simulation (COMSOL Multiphysics) illustrating the electric field profile inside the IDC sensor (water and FC-43 oil as examples). Left: an overview of the whole sensor, right: focusing on the target sensing region inside the Teflon flow tube.

8.3.2   Sensor instrumentation and characterization

The IDC sensor capacitance was read-out utilizing an off-the-shelf capacitance-to-digital converter (CDC) microchip (AD7746, Analog Devices). The AD7746 microchip is a high resolution sigma-delta ($\Sigma - \Delta$) CDC that posses two separate single-ended measurement channels, each of 24-bit resolution. The full-

scale capacitance of each of the CDC's channels is $\pm 4\,\text{pF}$ from an internal set reference value (0-17 pF). The CDC measurement has an accuracy of 4 fF and a resolution down to 4 aF. The AD7746 chip provides two built-in excitation sources (up to 5 V at 16 or 32 kHz) and amplifying/filtering circuits. The sampling rate of the CDC can be set between $9.1 - 90.9\,\text{Hz}$ resulting in root-mean-square (RMS) noise levels of $4.2 - 40\,\text{aF}$.

The AD7746 chip has a 16-lead TSSOP (Thin Shrink Small Outline Package) configuration ($4.5 \times 5\,\text{mm}$), enabling integration on the NMR probe head's PCB. Each of the two capacitive flow sensors was attached to a separate measurement channel of the CDC, via a positive capacitance input pin (CIN 1/2 (+)) and an excitation pin (EXC A/B) leveraging the single-end measurement. The excitation signal was set to 5 V at 32 kHz, and the CDC's sampling rate was set to 9.1 Hz. The PCB's conductive tracks connecting the capacitive sensors to the CDC chip were kept as far as possible from each other to limit cross-coupling between the two sensors. The CDC's digitized capacitance measurements were transmitted via I²C serial communication to a microcontroller outside the NMR magnet, as shown in Fig. 8.16. An Arduino board was used as an off-the-shelf MCU. Two Arduino shields have been developed compatible with Arduino Uno and Micro modules. The schematic designs and photographs of each of the two Arduino shields are provided in Appendix D. The Arduino shield was used to connect the I²C wires from the CDC to the Arduino board; it additionally featured LEDs for visual feedback and push-buttons for triggering the NMR experiment manually. The performance of the two microcontrollers (Arduino Uno and Micro) was observed to be equivalent.

The instrumentation system's functionality to detect permittivity differences was validated by sensing the capacitance read-outs in the presence of various solvents, summarized in Fig. 8.17. The developed system was efficiently able to differentiate between toluene ($\varepsilon_\text{r} = 2.38$) and the fluorinated oil FC-43($\varepsilon_\text{r} = 1.9$)
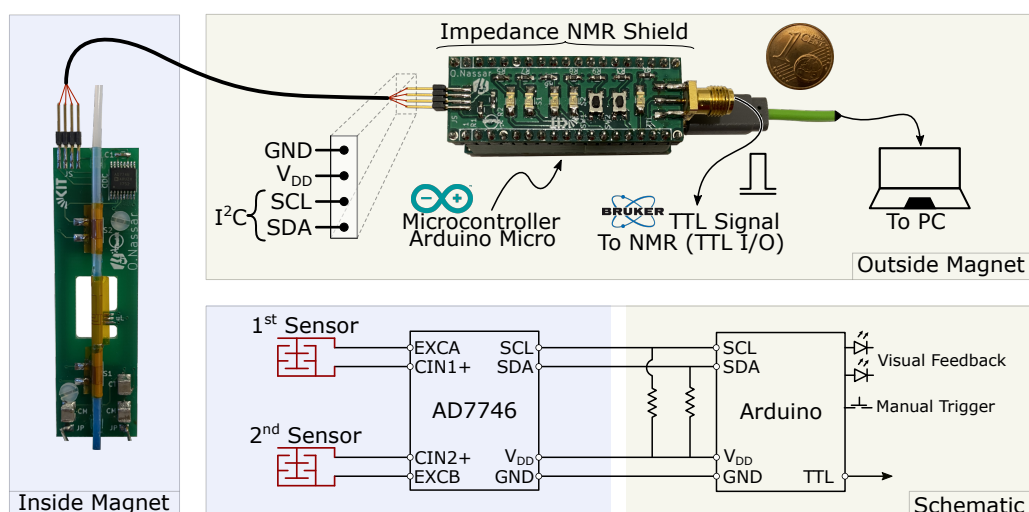
Figure 8.16: Electronic hardware components implemented for realizing the automatically triggered NMR experiment. Each of the two IDC sensors is connected to an input channel of a CDC microchip on the NMR probe head. The digitized sensors' readings are transferred to an MCU outside the NMR magnet over an I²C communication. An Arduino shield is developed comprising I²C interface, push-buttons for manual triggering, LEDs for visual feedback, and TTL signal interface.

used for samples separation. Also, a difference in capacitance measurement was observed between air and FC-43, opening the possibility of air-bubble detection. The measurement system's sensitivity was independent of the magnetic field, with only a constant offset of +0.3 pF observed with the sensor located in the NMR magnetic field. This capacitance offset could be compensated by re-calibrating the CDC IC, but since the offset does not affect the working principle of the system, this re-calibration was not performed. The measurement system's sensitivity to a difference in relative permittivity was determined to be $\Delta \varepsilon_r = 0.2$.

The developed measurement system features two flow sensors to enable flow velocity measurement and bi-directional NMR flow synchronization. The system accuracy to measure the velocity was character-ized by loading the line with plugs of colored aqueous samples separated with the fluorinated oil FC-43 and recording the flow using a camera (60 fps). The plug velocities were extracted from the recorded video data using motion analysis software (Kinovea), which were then compared to the velocities mea-sured by the developed system. The velocity measured by the system was within 4% of the camera results. The velocity characterization experiment was done outside of the NMR magnet to enable video recording.

Validating the sensors capability to synchronize NMR data acquisition was achieved by loading the flow tube with a line of three aqueous sample plugs separated by FC-43 oil. The three sample plugs are of different volumes and glucose concentrations, but all flowing at $4\,\mathrm{mm\,s^{-1}}$. Figure 8.18 demonstrates the sensors reading from the three aqueous sample plugs. The results reveal that a capacitance change above 100 fF is generated by the aqueous solutions separated by FC-43 plugs. Therefore, the capacitive sensor SNR is satisfactory even when the CDC microchip operates at the highest sampling rate of 90 Hz (RMS noise of 40 aF). As can be observed from the sensors measurements, the capacitance reading between the two flow sensors was not identical. The measured capacitance variation between the aqueous samples
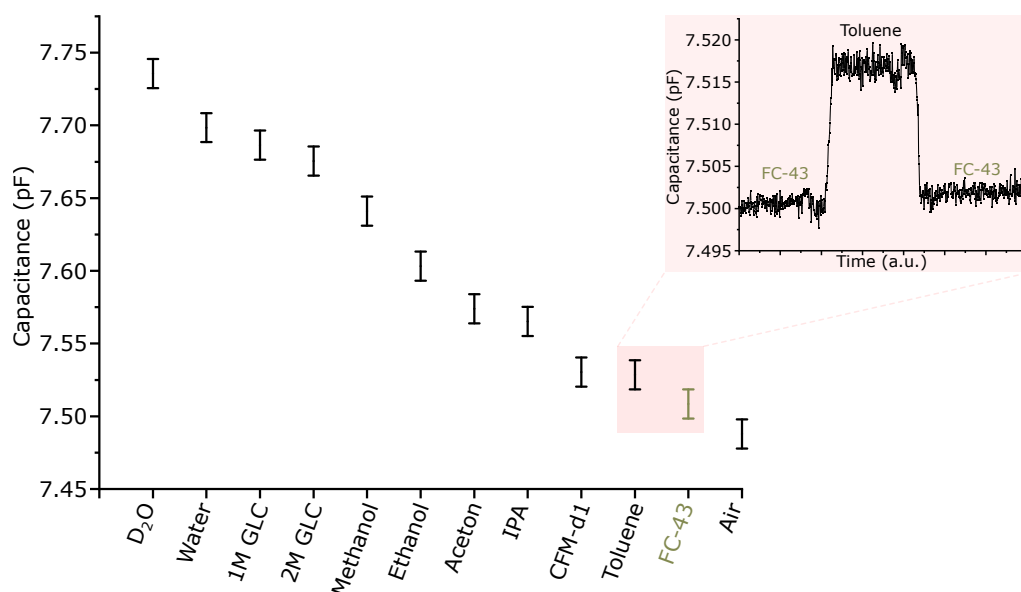
Figure 8.17: IDC sensor measured capacitance when filled with different solutions. The error in the capacitance measurement arises from the CDC chip's noise ($\pm\,0.03$ pF). The system is efficiently capable of differentiating toluene ($\varepsilon_r = 2.38$) from FC-43 ($\varepsilon_r = 1.9$) (inset).
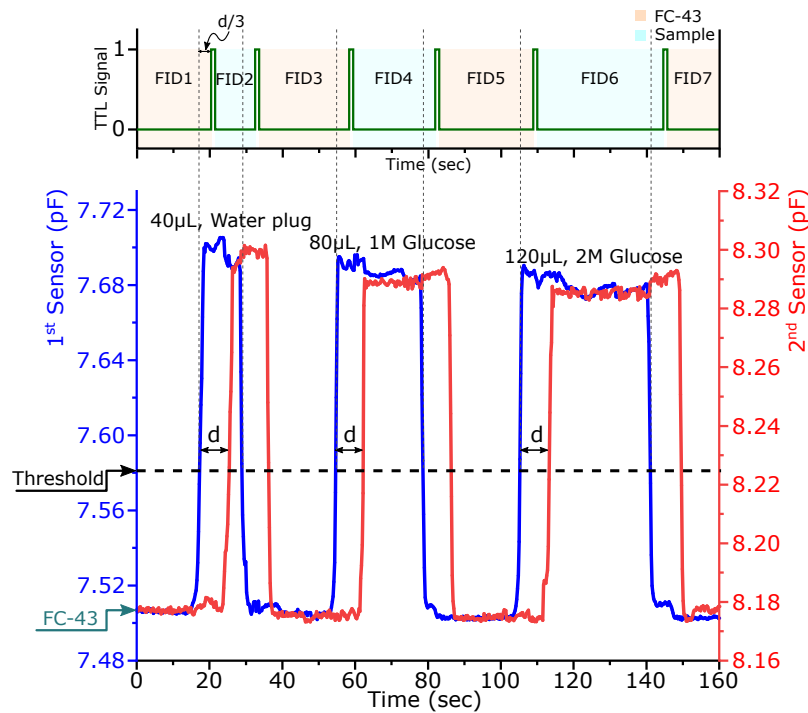
Figure 8.18: Output readings of the flow sensors during a triggered NMR experiment. The experiment was performed on three plugs of different volumes ($40\,\mu$L, $80\,\mu$L, and $120\,\mu$L) and different glucose concentrations ($0\,$M, $1\,$M, and $2\,$M) separated by plugs of FC-43 ($80\,\mu$L). In this experiment, the plugs were flowing at a velocity of $4\,\mathrm{mm\,s}^{-1}$. The MCU sends the TTL signals to the NMR console's TTL I/O unit after a calculated delay (*d*/3). This guarantees that a new NMR acquisition starts once the sample enters the NMR detection region. The time delay (*d*) is calculated using the sample's velocity measured by the capacitive sensors (top).

and the FC-43 oil for the 1$^{\text{st}}$ sensor was $\sim 190\,$fF (closer to the CDC IC) and $\sim 120\,$fF for the 2$^{\text{nd}}$ sensor. The difference between the two capacitive sensors can be attributed to the fabrication tolerances and the variation in proximity between each sensor and the CDC microchip, where long tracks build up parasitic capacitance. Nevertheless, the system working principle is not affected by the variation in the flow sensors readings since an individual threshold value could be set for each sensor.

The sensors performance was comparable to other systems utilizing the same sensing principle, even with the parasitic capacitance effect [227, 234]. A sensitivity advantage was achieved by rolling the flow sensors around the flow tube compared to planar IDC sensors [227] and capacitive sensors with less filling factor [234]. The signals acquired from the CDC microchip for the two flow sensors are sufficiently distinct that a robust triggering algorithm could be developed, as described previously in control system Subsection 8.1.1.

8.4 Micro-fabrication

The fabrication process used for realizing the micro-saddle NMR detector and the interdigitated capacitive flow sensors around a slender glass capillary with an outer diameter of 2.15 mm consist of two main

steps, as shown in Fig. 8.19. The first fabrication step was 2D patterning of a conductive layer in the form of the detector and the sensor on a flexible polymer film. The second fabrication step was rolling the 2D structured film around the slender glass capillary, thereby realizing a 3D conductive structure around the glass capillary.

The conductive layer 2D patterning was achieved following a standard wet-etching photolithography process suitable for mass production at the wafer scale. A 25 µm Kapton film covered from a single side with a 9 µm copper layer (AkaFlex KCL 2-9/25 HT, Krempel GmbH) was utilized as the base substrate for the photolithography process. Kapton was used due to its magnetic susceptibility, which is close to that of water [48]. A conductive copper layer of 9 µm provides the requisite conductor skin depth at 500 MHz, ensuring the minimal electrical resistive losses of the NMR detector. The wet-etching fabrication process is discussed in details in Section 3.1. After the 2D patterning process, the NMR saddle coil and flow sensors were cut from the Kapton film (a photograph of the entire wafer with a batch of detectors and sensors is provided in Appendix D). After rolling the film around the glass capillary (OD/ID, 2.15/1.72 mm, borosilicate glass, Hilgenberg GmbH), it was fixed using epoxy glue (UHU-Plus). The glass capillary with the NMR detector and flow sensors was glued to the probe head PCB using the same epoxy.

The fabrication process's overall yield is very high (nearly 100%), owing to the standard processes used. After multiple uses, no failures in the glue holding the film to the capillary were observed or in the glue holding the capillary to the PCB. If necessary, adhesion could be enhanced using a low temperature cure liquid polyimide such as LTC9300 provided by FUJI-FILM. The liquid polyimide can be applied and then hard-baked inside an oven at 200 °C for 180 min, then it will be converted into a film, resulting in a solid fixation of the structures.
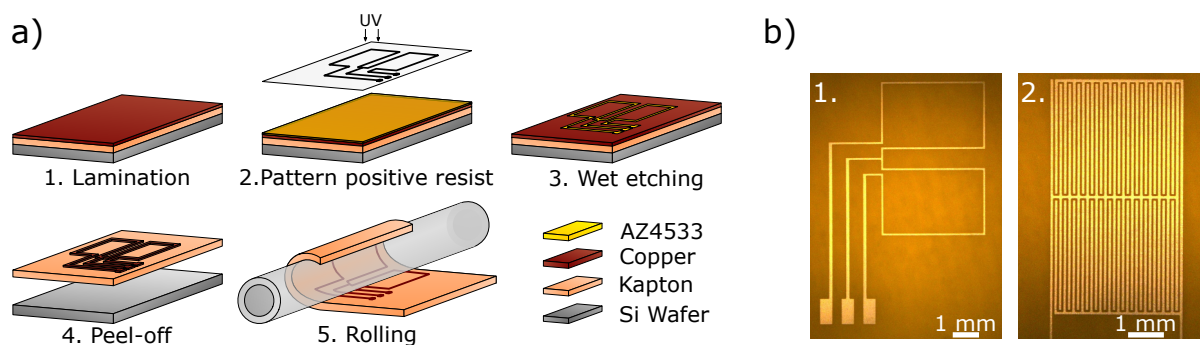
Figure 8.19: Schematic illustration of micro-fabrication process of the micro-saddle coil and IDC sensor. **(a)** Five steps categorized in two processes. First process: a wet etching photolithography process: (1) Substrate preparation by laminating 25 µm Kapton film covered with a 9 µm copper layer on a silicon wafer, (2) Patterning of a positive photoresist (AZ4533) layer using UV lithography, (3) Etching the exposed regions of the copper layer; and (4) Peeling off the Kapton film from the silicon wafer. Second process: (5) Rolling the Kapton film with the patterned conductive layer around the glass capillary. **(b)** Microscopic images of the 2D patterned conductive layer in the shape of (1) Saddle coil and (2) IDC sensor.

9 Automated flow NMR results[1]

This chapter presents the results of the different experiments performed using the developed system for automating the NMR spectroscopy. This chapter is divided into four sections. Section 9.1 describes the material used for the NMR experiment as well as the sample preparation. Additionally, Within this section, NMR spectroscopy data processing is explained. Sections 9.2 and 9.3 present the experimental result for characterizing the automated flow-based NMR system where the system SNR was expressed as a function of the sample velocity, volume, and analyte concentration. Section 9.4 demonstrates the results of automating the NMR screening of various commercial beverages as a piece of evidence that the system can efficiently automate NMR spectroscopy on different samples.

9.1 Sample preparation and NMR spectroscopy

A 4.5 m microfluidic tube was fitted through the customized probe head and used for sample flow. The used tube is made out of polytetrafluoroethylene (PTFE) (OD/ID, 1.6/1 mm, S1810-12, Bohlender GmbH), which provides the required flexibility to be fitted through the NMR system. The Fluorinert oil FC-43 ($> 99\%$, 3M^{TM} Fluorinert Electronic Liquid) is used for separating the target sample plugs and was purchased from Ionic Liquids Technologies (IOLITEC) GmbH. FC-43 oil is commonly used in many electronic and chemical applications because of its technical properties [235]. It is a perfect candidate for separating the target sample plugs within a microfluidic channel: i) it is chemically inert, thermally stable with low toxicity, making it compatible with the Teflon tube and various target samples, ii) it is immiscible with many popular NMR solvents, iii) its viscosity is relatively low (4.7 mPa s) and therefore flows easily inside the microfluidic channels, and iv) its electrical resistivity is relatively high $(3.4 \times 10^{15} \, \Omega \, \text{cm})$ preventing static charges.

The test sample used for characterizing the flow system SNR presented in Section 9.2 was prepared as 300 mM glucose, 75 g L^{-1} food coloring powder, and 30 mM TSP dissolved in deionized (DI) water. The glucose concentration series from 1 mM to 1 M presented in Section 9.3 was prepared using 50:50 DI water : D$_2$O. D-glucose, 3-(trimethylsilyl)- propionic-2,2,3,3-d4 acid sodium salt (TSP), and deuterium oxide (D$_2$O, 99.9% deuterium, Sigma Aldrich) which were purchased from Sigma-Aldrich. A market-available food coloring powder (Brauns Heitmann) was used. The beverages used in the automated NMR experiment represented in Section 9.4 were a selection of commercial beverages that were privately donated. Beverage samples were prepared by adding 1 mL of 5 mM TSP in D$_2$O to 3 mL of the beverage ([TSP]$_{final}$ = 1.25 mM).

NMR experiments were conducted on an 11.7 T wide-bore AVANCE III NMR spectrometer (^{1}H resonance frequency 500 MHz). The customized flow-sensing probe head was installed on a custom micro-imaging NMR probe and is therefore fully compatible with magnetic resonance imaging (MRI). The NMR pulse sequence was a modified version of a conventional single-pulse experiment, including the

---

[1]This chapter's text and figures were reproduced and adapted from the author's published work [ON5] (CC BY 4.0, 2021 Springer Nature)

trigger signal control. For a typical FID, the number of collected points was 5998 over a spectral width of 10 kHz, using a recycle delay of 0.1 s. For the beverage NMR experiments in Section 9.4, the number of collected points was raised to 12014. In all synchronized NMR experiments, FIDs were collected in a pseudo-2D NMR experiment, which was later separated and processed individually after the NMR experiment for all plugs was completed. Each FID was zero-filled by a factor of 2 prior to the Fourier transformation and multiplied by an exponential function equivalent to a line broadening of 0.3 Hz. After separating each spectrum, it was referenced to TSP (0 ppm), and the phase and baseline were corrected.

9.2   NMR characterization - varying sample volume and flow rate

Characterizing the NMR performance was done by observing the acquired SNR using the automatic and manual acquisition of NMR data. Two series of experiments were done using the same test sample:

1. In the first series of experiments, the sample plugs' volumes were kept constant, and the velocity of the flow was varied from $4\,\mathrm{mm\,s^{-1}}$ to $30\,\mathrm{mm\,s^{-1}}$. A series of sample volumes were examined (120, 80, and 40 μL) where all the three sample plugs were loaded into the flow tubing, separated by 80 μL of FC-43. NMR acquisition was automatically synchronized, employing the capacitive detection of the oil-aqueous interface.

2. In the second series of experiments, the sample volume was varied from 40 μL to 160 μL, in increments of 20 μL under constant flow rate. A series of flow rates were also examined (4, 8, and $12\,\mathrm{mm\,s^{-1}}$) where all the sample plugs (separated by 80 μL of FC-43) were loaded into the flow tubing. NMR acquisition was automatically synchronized, employing the capacitive detection of the oil-aqueous interface.

For manual triggering, a single sample plug was loaded into the flow tubing, bordered by FC-43. NMR acquisition was started and stopped manually when the sample entered and exited the probe. As a metric of NMR performance, the SNR of the TSP signal (0 ppm) was considered under each test condition. The normalized limit of detection (nLOD$_\omega$) was then calculated, as explained previously in Section 2.4.4, for the spectrum of each case based on the SNR of the TSP signal. The acquisition time for a single scan NMR experiment was set to be 0.299 s with the NMR detector sensitive volume of 3.14 μL.

The experimental results of the first series of the NMR experiments, where the sample flow rate was varied, are presented in Fig 9.1a and b. The developed triggering system acquires and stores the time domain NMR signal (FID) separately, as shown in Fig. 9.1a. The flow rate was incremented after the NMR spectroscopy for an oil-sample plug pair was completed. The velocity values reported in the results are the values calculated by the MCU using the acquired capacitive sensor signals. The system performance proves that the developed system could robustly differentiate the oil from aqueous signals. The TSP signal SNR was calculated in the frequency domain after applying the Fourier transformation to the FID.

The SNR at the different velocities for various volumes is plotted in Fig. 9.1b and d, and selected spectra are plotted in Fig. 9.3a. As the results reveal, the NMR spectrum's SNR decreases as a function of the
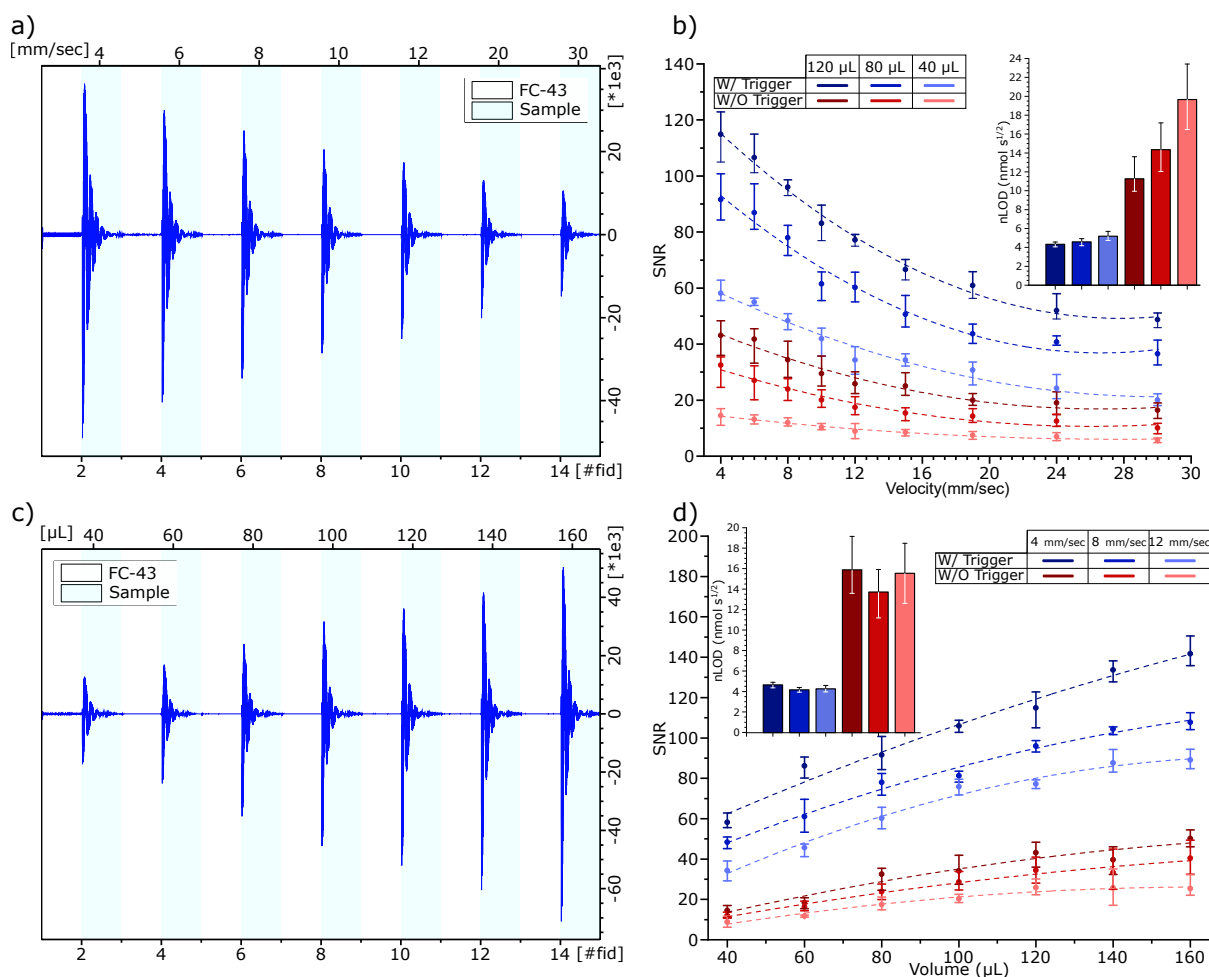
Figure 9.1: Performance of the automated flow-based NMR experiments under varying sample volumes and flow velocities. **(a)** Measured FID of seven sample plugs (80 µL) separated by FC-43 oil plugs (80 µL) with varying the flow rate. **(b)** The relationship between TSP peak SNR (0 ppm) and the sample velocity measured by the dual IDC sensors. The sub-figure shows the nLOD_ω at each sample volume (mean ± standard deviation over all tested flow velocities). **(c)** Measured FID of seven sample plugs separates by FC-43 oil plugs with varying the sample volume. The flow velocity was kept constant at $8 \, \text{mm}\,\text{s}^{-1}$, and the oil plugs volume held constant at 80 µL. **(d)** The relationship between TSP peak SNR (0 ppm) and the sample volume measured by the dual IDC sensors. The sub-figure shows the nLOD_ω at each sample velocity (mean ± standard deviation over all tested sample volumes). In (b) and (d), each data point represents the mean ± standard deviation of the NMR experiment performed in quadruplicate. The data were fit using the damped least-squares method to a 2nd order polynomial.

sample flow rate, as expected, since increasing the flow rate reduces the sample residence time in the NMR detector's detection region. The SNR was continuously enhanced using the developed automated synchronized system as compared to manual triggering. Consequently, approximately improvements by factors of 2.5, 3.0, and 4.0 in the spectra SNR was observed for sample plug volumes of 120 µL, 80 µL, and 40 µL, regardless of the sample flow velocity. The nLOD_ω calculated from the SNR is plotted in the inset of Fig. 9.1b. The performance under the automated triggering system is four-time better than the previous micro-saddle coil results [143], with a value of 4-5 nmol s$^{1/2}$.
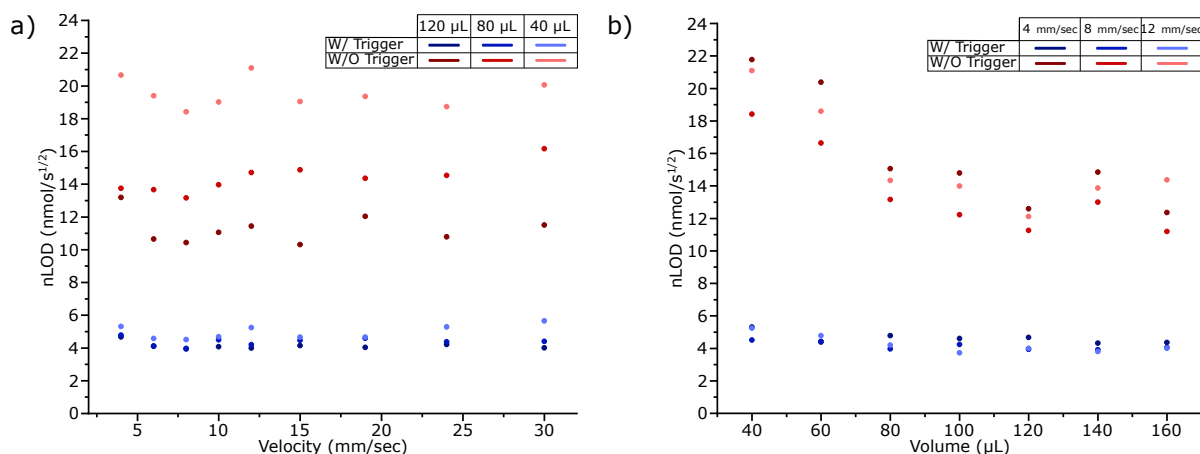
Figure 9.2: NMR system's sensitivity under varying sample flow rates and volumes. **(a)** The change in the normalized limit of detection ($nLOD_\omega$) with the sample velocity. Under automatic triggering conditions, The $nLOD_\omega$ alters within a small range over the enter range of tested velocities for a given sample volume. Under manual triggering conditions, the $nLOD_\omega$ increases as the volume of the sample decreased due to the increased signal contribution from the FC-43 oil signal (noise). **(b)** The change in the normalized limit of detection ($nLOD_\omega$) with the sample volume. Under automatic triggering conditions, the $nLOD_\omega$ is minimally enhanced by increasing the sample volume. Under manual triggering conditions, the $nLOD_\omega$ is enhanced by increasing the volume of the sample as the contribution of the oil signal is reduced. The mean $\pm$ standard deviation of the data presented here are plotted in Fig. 9.1.

As the results reveal, the $nLOD_\omega$ under manual triggering conditions increases as the sample volume decreases due to the increased contribution of the FC-43 oil signal (essentially noise) to the FID. The experimental results of the second series of the NMR experiments, where the sample plug volume was varied, are presented in Fig 9.1c and d. The FID signals of seven oil-sample FID pairs are shown in Fig. 9.1c, the volume of the sample plugs was incremented while the volume of the FC-43 oil plugs was held constant at $80\,\mu L$. The expected enhancement in the SNR of the TSP with increasing the sample volume is illustrated in Fig. 9.1d (selected spectra are plotted in Fig. 9.3a). The triggering system, once again, yielded a systematic SNR enhancement in comparison to the manual triggering condition, approximately by factors of 2.5, 3.0, and 4.0 for plugs velocities of $4\,\mathrm{mm\,s^{-1}}$, $8\,\mathrm{mm\,s^{-1}}$, and $12\,\mathrm{mm\,s^{-1}}$ regardless of sample plug volume. The enhancement in the NMR sensitivity when implementing the automated triggering system, as well as the micro-NMR detector performance, is further confirmed by the calculated $nLOD_\omega$ for each flow rate (inset, Fig. 9.1d). The calculated $nLOD_\omega$ and at each flow velocity are plotted in Fig. 9.2b.

A balance should be realized between the sample volume, flow rate, SNR, and spectral resolution to enhance the NMR throughput. Increasing the samples flow rate with keeping all other parameters constants result in the degradation of SNR and spectral resolution, as illustrated in Fig. 9.3. On the other hand, increasing the sample volume enhances SNR and spectral resolution. Increasing the flow rate reduces the NMR measurement time, leading to less noise averaging over the accumulated signals. Simultaneously, increasing the flow rates allows a bigger fraction of the excited sample to leave the NMR detection region during NMR signal acquisition. Consequently, the FID is artificially shortened and manifesting as
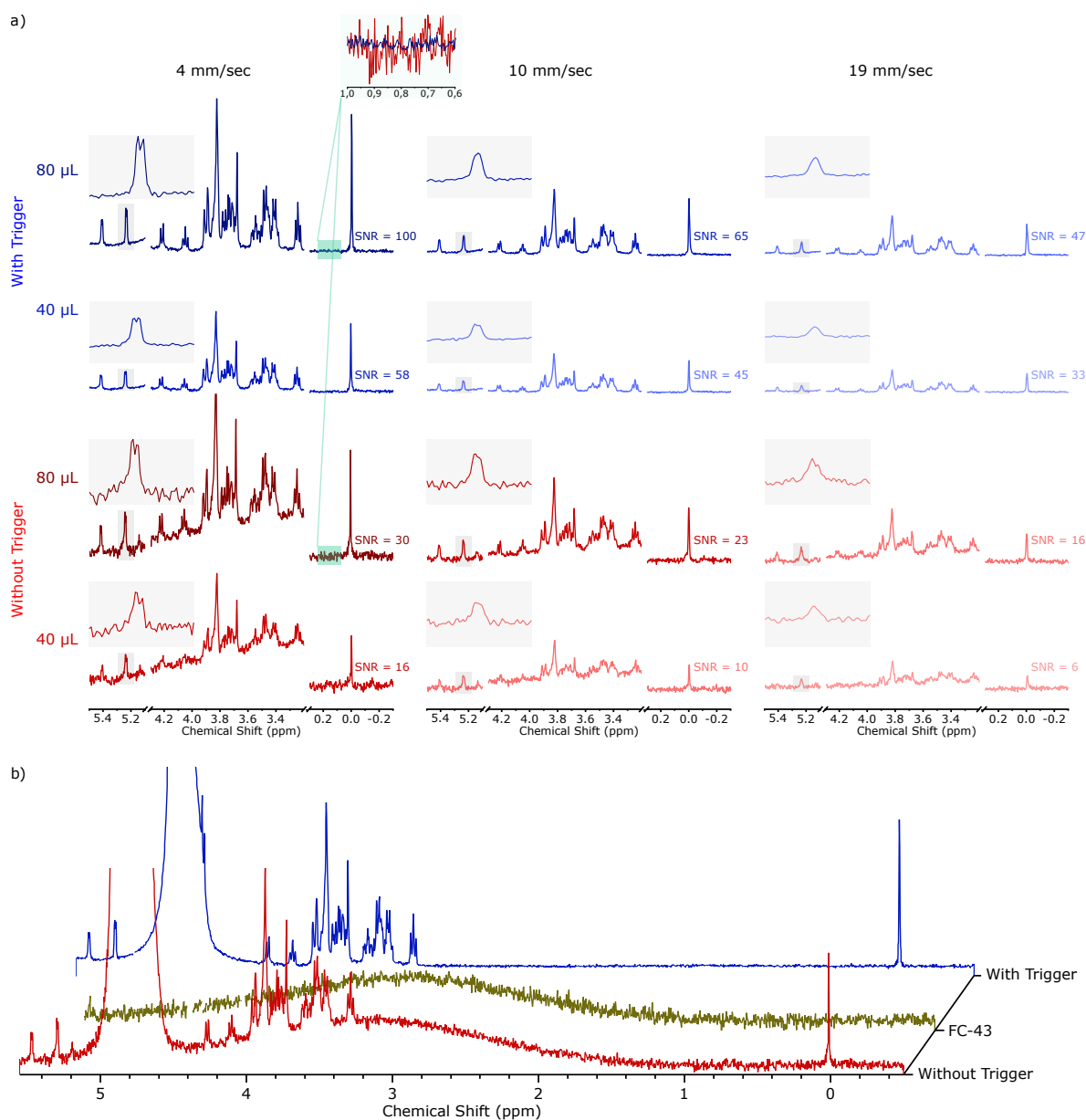
Figure 9.3: Selected ^{1}H NMR spectra resulted from the flow NMR spectroscopy experiments on a test sample (300 mM glucose, 75 g L^{-1} coloring powder, and 30 mM TSP dissolved in DI water) with varying the sample volumes and flow rates (SNR of all extracted data are plotted in Fig. 9.1). **(a)** The SNR of TSP peak (0 ppm) for each spectrum is noted next to the signal. A focused view of the glucose anomeric proton (5.2 ppm) is located next to each spectrum in a gray box for spectral resolution comparison. The water signal (5.1-4.3 ppm) was eliminated for clarity. The baseline distortion in the spectra with a manual triggering system results from signal accumulation from the FC-43 oil phase (noise). **(b)** Representative full ^{1}H NMR spectra of a 120 μL sample plug flowing at velocity of 4 mm s^{-1}. The blue spectrum is obtained with the auto triggering system. In contrast, the red spectrum is obtained with manual triggering. The automatic triggering system eliminates the noise contribution from the oil phase.

a rise in the apparent relaxation time T$_2$, results in broadening the spectral line as shown in Fig. 9.3. At extremely high flow rates, the whole excited part of the sample leaves the detection volume before NMR signal acquisition is completed, therefore adding more noise into the collected signal.

9.3   NMR characterization - concentration limit of detection

The dependence of the developed automated NMR spectroscopy system on the sample concentration was estimated by loading the flow tube with a series of nine aqueous samples spanning a glucose concentration range from 1 mM to 1 M. The aqueous sample plugs with different glucose concentrations had a volume of 120 μL and were separated by FC-43 oil plugs with a volume of 80 μL. The automated flow NMR experiment was done at two different flow velocities $6\,\mathrm{mm\,s^{-1}}$ and $10\,\mathrm{mm\,s^{-1}}$.

The results of the concentration experiment are summarized in Fig. 9.4. The automated NMR triggering system, as with previous experiments, could efficiently separate signals from aqueous plugs and oil plugs, as shown in the FID signals in Fig. 9.4a. The relation between the SNR of the glucose anomeric hydrogen signal (5.1-5.3 ppm) and the glucose concentration is plotted in Fig. 9.4b for the two flow rates tested. Selected NMR spectra for these auto synchronized experiments are plotted in Fig. 9.4c. The NMR signal SNR has a linear relation with the sample concentration ($R^2 > 0.99$). The SNR is greater at a lower flow velocity of $6\,\mathrm{mm\,s^{-1}}$ versus the higher flow velocity of $10\,\mathrm{mm\,s^{-1}}$, considering the samples at lower velocity have a longer residence time in the NMR coil detection region, allowing greater signal accumulation. The total experimental time required by the automated flow-based NMR system to acquire the NMR signal of all oil and aqueous plugs (18 measurement in total) was 6.1 min and 3.6 min, or effectively 25.5 s and 15.3 s per aqueous sample at flow velocities of $6\,\mathrm{mm\,s^{-1}}$ and $10\,\mathrm{mm\,s^{-1}}$.

Obtaining the relation between SNR and sample concentration is suitable for examining the sample plugs' cross-contamination. After loading the line with the nine aqueous samples, the measurements were performed in four consecutive runs after reversing the flow direction (i.e., all plugs signal were acquired in one flow direction followed by reversing the sample flow direction and repeating the measurements). Hence, the linear plot between the SNR and concentration after repeating the measurement four-time confirms that there was no cross-contamination of the Teflon tube or between the different sample plugs.

Employing a plug flow approach will always raise the issue of cross-contamination. In the case reported here of aqueous samples and FC-43 plugs flowing in a Teflon tube, cross-contamination was not recognized at the NMR detection limit. However, in situations where cross-contamination may be problematic, one could introduce additional solvent plugs to clean the flow line.

9.4   Automated sample throughput - beverage application

The developed system functionality was validated on a set of samples beyond simple test solutions. The flow tube was loaded with seven samples of different beverages and separated by FC-43 oil plugs. Each beverage sample plug had a volume of 120 μL, and the FC-43 oil plugs had a volume of 80 μL, and the NMR spectroscopy was done at a flow rate of $4\,\mathrm{mm\,s^{-1}}$.

The total experimental time of the NMR signal acquisition under these conditions was 7 min with effectively 38.3 s acquisition time per beverage sample. Figures 9.5a and b demonstrate the resulting FID and spectra of all samples. TSP was added to the samples with a target concentration of 1.25 mM to facilitate

referencing the resulted spectrum. However, it was observed from the results that the solubility of the TSP within the beverages was sample-dependent, and therefore the TSP signal could not be utilized for
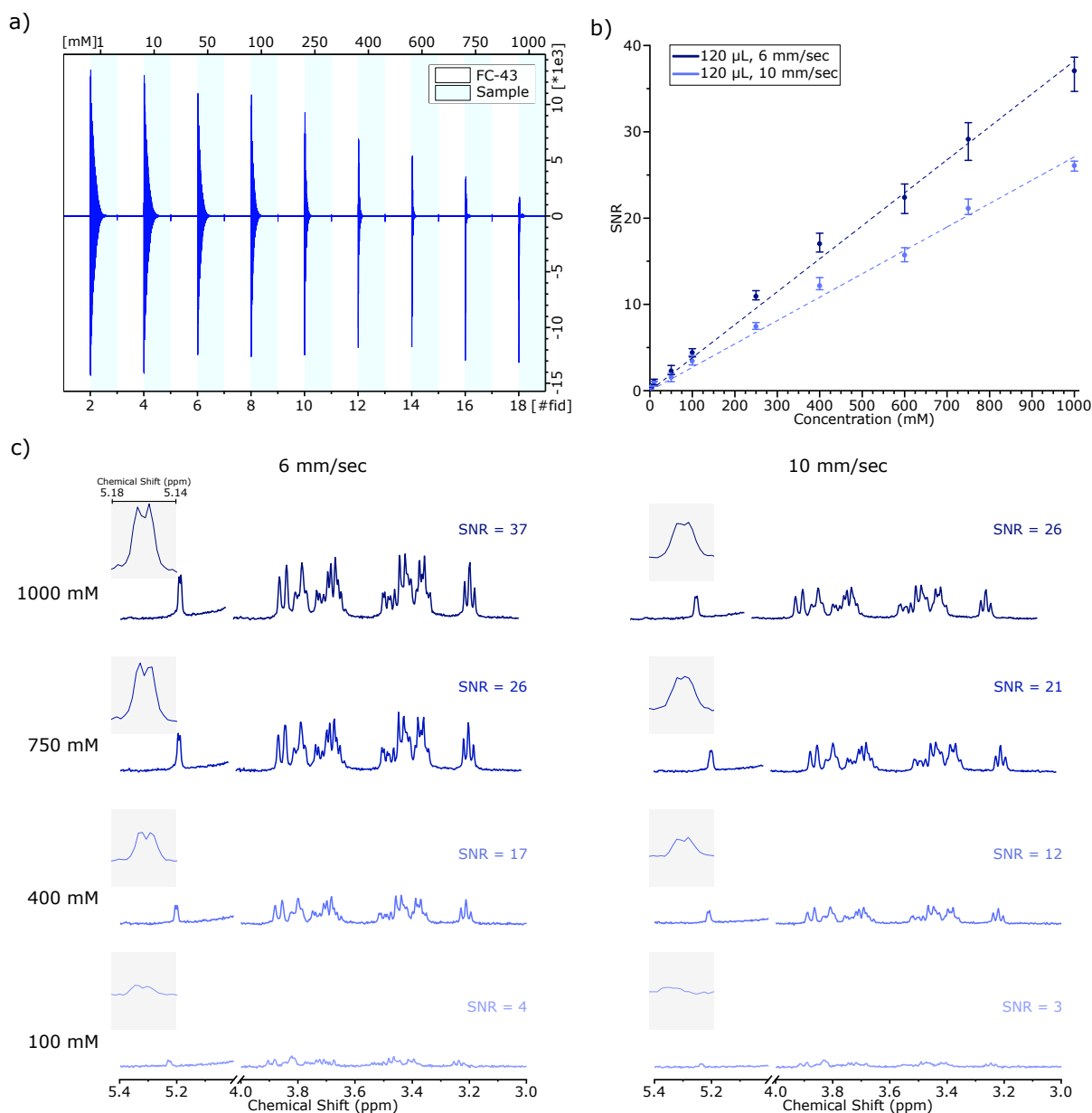
Figure 9.4: Performance of the automated flow-based NMR experiments under varying sample concentrations. **(a)** Automatically measured FID signals of nine aqueous sample plugs ($120\,\mu L$) separated by FC-43 oil plugs ($80\,\mu L$). flowing at $10\,mm\,s^{-1}$. The aqueous samples contained glucose concentrations ranging from $0.001\,M$ to $1\,M$. **(b)** The SNR (calculated using the glucose anomeric hydrogen signal (5.3-5.1 ppm)) versus glucose concentration under two flow velocities. Each data point is the mean $\pm$ standard deviation of the NMR experiment performed in quadruplicate. The Linear data fit (dashed lines) had $R^2 > 0.99$ in both cases. **(c)** Selected ^{1}H NMR spectra from the automated flow NMR spectroscopy experiments with varying the glucose concentrations dissolved in DI water. The water signal (5-4 ppm) was eliminated for clarity. The glucose anomeric proton's SNR for each spectrum is noted next to the signal with a focused view of the peak (5.18-5.14 ppm) in a gray box for spectral resolution comparison.
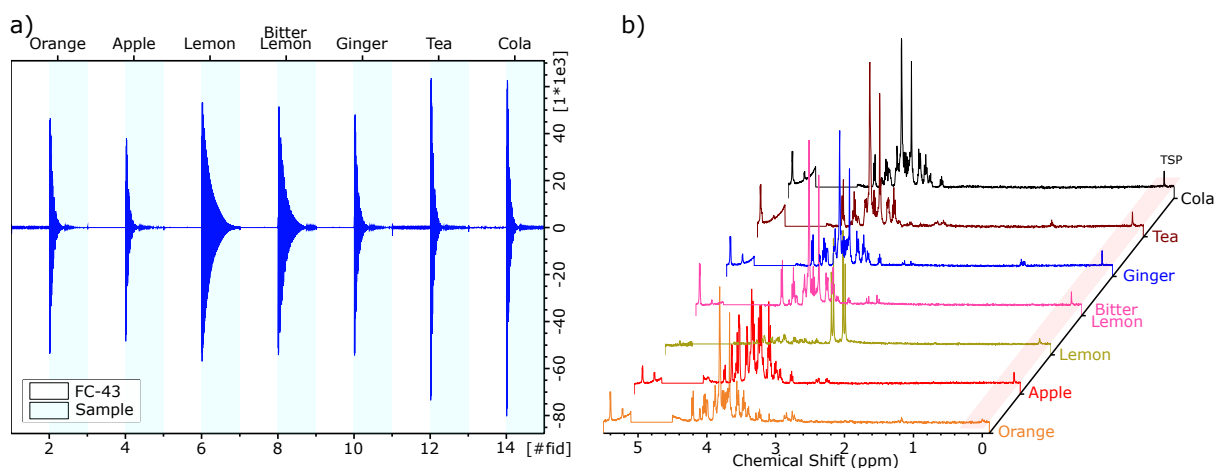
Figure 9.5: Automated NMR acquisition of beverage sample plugs. **(a)** Automatically measured FID signals of seven beverage and FC-43 oil plugs. The sample volume was 120 µL, and the FC-43 oil volume was 80 µL, the experiment ran at a flow velocity of $4\,\mathrm{mm\,s^{-1}}$. **(b)** The resulted NMR spectra of the beverage samples.

quantification (only for chemical shift referencing).

9.5   Conclusions

As the results reveal in all previous experiments: i) the developed automatic triggering system was able to separate the sample and oil signals robustly; ii) the resulted NMR signals for the different tested sample were of excellent spectral quality (both in terms of resolution and SNR); and iii) there were no additional signals recognized in the oil NMR spectra, ruling out possible diffusion into the oil plugs from the aqueous samples (at the NMR detection limit). Assuming a 1.0 mm I.D. PTFE tube, 100 µL sample plugs, and 100 µL oil plugs, then in a 100 m long PTFE tube, approximately 400 individual samples can be loaded. The number of the NMR visible plugs could be doubled by loading the immiscible phase with measurable molecules. Loading a 100 m PTFE tube is a time-limiting process, although this was also automated, as discussed in the loading Section 8.1.2. Using the developed automated measuring system with selecting a reasonable flow rate of $4\,\mathrm{mm\,s^{-1}}$ (minimum tested flow rate), considering an acquisition time of 40 s per sample (as was done in the beverage example in Section 9.4), and both plug phases contain NMR measurable content, then these 800 samples would require $\sim 9\,\mathrm{h}$ of measurement time. If the immiscible oil phase serves only to separate samples, then 400 samples would be screened in $\sim 9\,\mathrm{h}$. This could be enhanced by incorporating the flow pump into the control loop and adjusting the flow rate so that the oil plugs flow through the detection volume more quickly. In contrast, 300 samples require a measurement time of 120 h when done manually following the conventional procedure (500 µL per sample, 5 mm sample tubes, 7 min acquisition time per sample neglecting instrument adjustment time after each sample exchange, without implementing automatic sample exchanger) [236].

Conclusions and Outlook

10   Conclusion and outlook

Through the introduction chapter of this work, three main objectives were raised. The first objective was enhancing the thin-film micro-fabrication technology to address micro-MR applications. The second objective was utilizing the developed micro-fabrication technologies to solve MR-catheter issues regarding visual reliability and heating hazard. The third objective was employing the improved micro-fabrication technologies in tackling the NMR spectroscopy drawback of being a low throughput technique. This chapter concludes the key achievements in each objective and provides potential possibilities for future work.

10.1   Micro-fabrication of flexible electronics

An extensive study has been presented for the different depositing approaches for conductive seed-layers onto a flexible polymer substrate. The study covers various photolithography methods as well as fast prototyping techniques. It focuses on the seed-layer adhesion onto the flexible substrate as it is a challenging topic. Moreover, a beneficial comparison between the different approaches has been given, covering each depositing technique's advantages, disadvantages, resolution, and reproducibility.

Two novel composite insulating inks have been developed for fully inkjet-printed high quality MIM capacitors with high capacitance density. Benzocyclobutene (BCB) was used as the base polymer for the developed inks due to its low dissipation factor. In addition, $BaTiO_3$ and TiO_2 were dispersed in the BCB polymer to increase its dielectric constant, reducing the capacitor size to be compatible with microelectronic applications. Different weight ratios of the ceramic powder to BCB polymer have been analyzed. The dielectric constant, roughness and thickness of the deposited film, and quality factor have been characterized for each ink. The TiO_2/BCB inks provide surface roughness of 970-1220 nm, a loss tangent of 0.037-0.04, a dielectric constant of 7-20, and capacitance density 32-64 $pFmm^{-2}$. The $BaTiO_3$/BCB inks have surface roughnesses of 830-1000 nm, loss tangents of 0.045-0.052, dielectric constants of 10-37, and capacitance densities of 19-67 $pFmm^{-2}$. A comparison between the produced capacitors and state of art has been given. The developed printing process shows no blending between the conductive layer and the insulating layers. Moreover, the process is compatible with the fabrication of multi-layer components.

An organic Cu-PTAA-Ag Schottky diode has been developed by using inkjet-printing and the electroplating process. The low working function electrode (copper) of the diode was formed by printing silver electrode and then electroplating with copper. PTAA p-type semiconductors have been used due to their stability in the ambient atmosphere. The developed diode was successfully used to build a half-wave rectifier, which provided a DC output voltage up to 3 V at 1 MHz.

A versatile and programmable current source based on MHCS was developed for the pulsed electroplating process. The current source have precise and stable output power even when operating under relatively high current densities ($\approx 6\,Adm^{-2}$) and various frequencies (DC up to few kHz). The developed system offers extensive freedom to set the pulsed electroplating parameters, opening further

exploration of complex pulsed electroplating waveforms. The developed plating setup has been used in controlling the deposited layer's micro-structure and has been employed in several crucial applications: i) solving the delamination issue when electroplating inkjet-printed conductive traces on unstructured flexible substrates, ii) electroplating of a laser carbonized polyaramid-based film, iii) electroplating of carbon micro-lattice architecture achieved by 3D stereo-lithography printing. The current source is compatible with the parallelization concept, where the output current channel can be duplicated. A developed system with eight channels was successfully utilized for plating eight 4 inch wafer in parallel, which saved materials, time, and effort. The setup is cost-effective and straightforward to be copied and used laboratory which maintains moderate electronic skills.

10.2   Interventional MRI using MR-catheters

A novel wireless decoupling approach has been introduced to address the MR-catheter heating hazard. Moreover, an innovative double-saddle coil is developed to maintain catheter visibility in MR images through the entire range of axial orientations during interventions. The system tracks a micro-resonator placed on the catheter tip wirelessly through induction coupling. The catheter micro-resonator is connected to a variable capacitor controlled via a DC signal provided by a half-wave rectifier. The input power to the half-wave rectifier is wirelessly transmitted through induction coupling between two coils tuned at a frequency far from the Larmor frequency. The MR-resonator on the catheter tip along with the decoupling system has been fabricated using inkjet-printing on a 25 μm Kapton film. The developed system was successfully used for wirelessly controlling the resonance frequency of the catheter micro-resonator within a range of 15 MHz.

The proposed double saddle detector offers wireless tracking of MR-catheters with orientation independence during interventional MRI operations. A comparison between the performance of the proposed double saddle detector and that of a traditional single saddle detector was done using numerical simulations and verified by experiments. The generated magnetic fields B_1 by the micro detectors were numerically simulated using COMSOL multiphysics and were experimentally mapped in a low field 1 T MRI scanner. The double saddle detector generated a homogeneously distributed magnetic field surrounding the catheter tube. The induction coupling efficiency between a surface resonator and the micro detectors was numerically simulated using COMSOL multiphysics and experimentally characterized using a home-built setup. The double saddle detector maintains near-constant coupling through the entire range of axial orientations. On the other hand, the coupling between the surface coil and the conventional single detector decreases as the angle between their B_1 fields increases, and no coupling was observed at orthogonal orientation of their fields. A novel multi-layer fabrication processes for rolled MEMS were developed for fabricating the double saddle detector. One method was based on standard lithography micro-fabrication, and the other employed inkjet-printing. Both processes were successful in fabricating double saddle detectors, which were then rolled around a 5 fr catheter tube.

Within this work, the developed coupling system is fabricated with inkjet-printing except for the varicap. As a future plan, the varicap could also be fabricated via inkjet-printing of p-type and n-type semiconductors. Hence, a wireless tunable MR-resonator could be fully printed to be compatible with roll to roll

inkjet-printing fabrication technique, enabling mass production and disposable electronics. The main focus of this work was developing and characterizing the hardware. However, the introduced wireless tuning methodology offers a large room for further enhancements and applications in micro MRI and NMR applications where the MR-detector has limited access. Therefore, the developed MR-catheter with a wireless decoupling system is ready for the next step to be tested in vivo.

10.3   Automated high throughput NMR spectroscopy

A novel plug flow-based approach has been introduced to address the NMR spectroscopy drawback of low sample throughput. The proposed technology enhances NMR throughput by a factor of 40 (when operating at the minimum efficiency) and reduces the NMR sample volume at the same time to under a hundred micro-liters. The introduced system consists of a custom-built NMR probe head that takes advantage of thin-film micro-NMR detectors combined with microfluidic technologies. The key concept integrates thin-film flow capacitive sensors interfaced to a microcontroller unit. Together with the NMR sensor, they enable real-time detection of sample plugs in a flow-based sample handling system with high sensitivity to differences in relative permittivity. The NMR signal acquisition system gains a degree of automation by implementing an independent measuring mode for flow positing and velocity, further improving throughput. A detailed description of the system design, fabrication, and characterization has been given in Chapter 8. The micro-NMR detector enables high-resolution NMR spectroscopy with a sensitivity of $2.18 \, \text{nmol s}^{1/2}$ with the flow sensors in operation. The spectral resolution under stationary conditions, quantified by resonance line width, was found to be $1.25 \, \text{Hz}$ for the water signal. The flow sensors had a high sensitivity to a relative permittivity detection difference of 0.2, allowing them to distinguish between most typical solvents. The modeling, simulation, and characterization of the NMR-detector and flow sensor are included. The probe head is plug-and-play ready with market-available NMR systems. After installing the developed probe head into the NMR system, a microfluidic tube is fed through the probe head loaded with a sample series, comprising of an unlimited number of different sample plugs, separated by an immiscible fluid. The system was successfully used to automate flow-based NMR measurement in a 500 MHz NMR system. A complete characterization of the automated flow-based NMR system has been given in Chapter 9. It was demonstrated that fully automated NMR spectroscopy of nine different $120 \, \mu\text{L}$ samples could be done in 3.6 min or effectively 15.3 s per sample.

The NMR flow-sensing approach, described in this thesis, has opened up a new concept toward automated high throughput NMR spectroscopy by splitting a large sample into small droplets. The NMR spectrum is individually acquired for each droplet with high SNR. Furthermore, the developed NMR probe head is an additional step towards increasing the NMR system functionality, allowing for greater experimental flexibility and complexity or improved SNR compared to standard equipment. The platform is compatible with the parallelization concept described in Chapter 7 and, as recently reported for low-field NMR spectroscopy [237], potentially further increasing NMR sample throughput scaled by the number of parallel NMR channels. Additionally, the application space could be extended by reducing the system dimensions to enable particle sensing within a carrying medium towards, for example, NMR measurement of cells.

Bibliography

[1] A. Kalfe, A. Telfah, J. Lambert, and R. Hergenröder, "Looking into Living Cell Systems: Planar Waveguide Microfluidic NMR Detector for in Vitro Metabolomics of Tumor Spheroids," *Analytical chemistry*, vol. 87, no. 14, p. 7402–7410, 2015.

[2] A. Yilmaz and M. Utz, "Characterisation of oxygen permeation into a microfluidic device for cell culture by: In situ NMR spectroscopy," *Lab on a Chip*, vol. 16, no. 11, pp. 2079–2085, 2016.

[3] E. Montinaro, M. Grisi, M. Letizia, L. Pethö, M. Gijs, R. Guidetti, J. Michler, J. Brugger, and G. Boero, "3D printed microchannels for sub-nL NMR spectroscopy," *PLoS ONE*, vol. 13, no. 5, p. e0192780, 2018.

[4] V. V. Zhivonitko, V. Telkki, and I. V. Koptyug, "Characterization of microfluidic gas reactors using remote-detection MRI and parahydrogen-induced polarization," *Angewandte Chemie (International ed. in English)*, vol. 51, no. 32, pp. 8054–8058, 2012.

[5] A. Brächer, S. Hoch, K. Albert, H. Kost, B. Werner, E. von Harbou, and H. Hasse, "Thermostatted micro-reactor NMR probe head for monitoring fast reactions," *Journal of magnetic resonance (San Diego, Calif. : 1997)*, vol. 242, pp. 155–61, 2014.

[6] A. Brächer, R. Behrens, E. von Harbou, and H. Hasse, "Application of a new micro-reactor 1H NMR probe head for quantitative analysis of fast esterification reactions," *Chemical Engineering Journal*, vol. 306, pp. 413–421, 2016.

[7] K. C. Tijssen, B. J. van Weerdenburg, H. Zhang, J. Janssen, M. C. Feiters, P. J. M. van Bentum, and A. P. Kentgens, "Monitoring heterogeneously catalyzed hydrogenation reactions at elevated pressures using in-line flow NMR," *Analytical chemistry*, vol. 91, no. 20, pp. 12636–12643, 2019.

[8] I. Swyer, S. von der Ecken, B. Wu, A. Jenne, R. Soong, F. Vincent, D. Schmidig, T. Frei, F. Busse, H. J. Stronks, *et al.*, "Digital microfluidics and nuclear magnetic resonance spectroscopy for in situ diffusion measurements and reaction monitoring," *Lab on a Chip*, vol. 19, no. 4, pp. 641–653, 2019.

[9] M. Mompeán, R. M. Sánchez-Donoso, A. De La Hoz, V. Saggiomo, A. H. Velders, and M. V. Gomez, "Pushing nuclear magnetic resonance sensitivity limits with microfluidics and photochemically induced dynamic nuclear polarization," *Nature communications*, vol. 9, no. 1, pp. 1–8, 2018.

[10] G. Carret, T. Berthelot, and P. Berthault, "Inductive coupling and flow for increased NMR sensitivity," *Analytical chemistry*, vol. 90, no. 19, pp. 11169–11173, 2018.

[11] J. Eills, W. Hale, M. Sharma, M. Rossetto, M. H. Levitt, and M. Utz, "High-Resolution nuclear magnetic resonance spectroscopy with picomole sensitivity by hyperpolarization on a chip," *J Am Chem Soc*, vol. 141, no. 25, pp. 9955–9963, 2019.

[12] L. Bordonali, N. Nordin, E. Fuhrer, N. MacKinnon, and J. G. Korvink, "Parahydrogen based NMR hyperpolarisation goes micro: an alveolus for small molecule chemosensing," *Lab Chip*, vol. 19, pp. 503–512, 2019.

[13] H. Davoodi, N. Nordin, L. Bordonali, J. G. Korvink, M. Neil, and V. Badilita, "An NMR-compatible microfluidic platform enabling in situ electrochemistry," *Lab Chip*, vol. 20, no. 17, pp. 3202–3212, 2020.

[14] H. Ritchie and M. Roser, "Causes of death," *Our World in Data*, 2018. https://ourworldindata.org/causes-of-death. Accessed: 15 Sept 2021.

[15] M. Pellecchia, D. S. Sem, and K. Wüthrich, "NMR in drug discovery," *Nature Reviews Drug Discovery*, vol. 1, no. 3, pp. 211–219, 2002.

[16] S. Keiffer, M. G. Carneiro, J. Hollander, M. Kobayashi, D. Pogoryelev, A. Eiso, S. Theisgen, G. Müller, and G. Siegal, "NMR in target driven drug discovery: why not?," *Journal of Biomolecular NMR*, vol. 74, no. 10, pp. 521–529, 2020.

[17] P. Breakthroughs Staff, "Inside the 'molecular library' with 4m compounds used to investigate potential medicines," 2017. https://www.breakthroughs.com/impacts-innovation/inside-molecular-library-4m-compounds-used-investigate-potential-medicines. Accessed: 15 Sept 2021.

[18] I. I. Rabi, J. R. Zacharias, S. Millman, and P. Kusch, "A new method of measuring nuclear magnetic moment," *Physical review*, vol. 53, no. 4, p. 318, 1938.

[19] F. Bloch, "Nuclear induction," *Physical review*, vol. 70, no. 7-8, p. 460, 1946.

[20] E. M. Purcell, H. C. Torrey, and R. V. Pound, "Resonance absorption by nuclear magnetic moments in a solid," *Physical review*, vol. 69, no. 1-2, p. 37, 1946.

[21] P. C. Lauterbur, "Image formation by induced local interactions: examples employing nuclear magnetic resonance," *nature*, vol. 242, no. 5394, pp. 190–191, 1973.

[22] M. H. Levitt, *Spin Dynamics: Basics of Nuclear Magnetic Resonance*. Chichester, UK: John Wiley & Sons Ltd, 2nd ed., 2008.

[23] H. Günther, *NMR Spectroscopy: Basic Principles, Concepts and Applications in Chemistry*. Weinheim, Germany: Wiley-VCH, 3rd ed., 2013.

[24] D. W. McRobbie, E. A. Moore, M. J. Graves, and M. R. Prince, *MRI from Picture to Proton*. Cambridge, UK: Cambridge University Press, 2nd ed., 2006.

[25] A. Nowogrodzki, "The world's strongest MRI machines are pushing human imaging to new limits," *Nature*, vol. 563, no. 7732, pp. 24–27, 2018.

[26] Bruker, "World's first superconducting 1.1 gigahertz magnet," 2019. https://ir.bruker.com/press-releases/press-release-details/2019/Bruker-Announces-Worlds-First-Su

perconducting-11-Gigahertz-Magnet-for-High-Resolution-NMR-in-Structural-Bi
ology. Accessed: 15 Sept 2021.

[27] D. I. Hoult and R. Richards, "The signal-to-noise ratio of the nuclear magnetic resonance experiment," *Journal of Magnetic Resonance (1969)*, vol. 24, no. 1, pp. 71–85, 1976.

[28] T. L. Peck, R. L. Magin, and P. C. Lauterbur, "Design and analysis of microcoils for NMR microscopy," *Journal of Magnetic Resonance, Series B*, vol. 108, no. 2, pp. 114–124, 1995.

[29] J. B. Johnson, "Thermal agitation of electricity in conductors," *Physical review*, vol. 32, no. 1, p. 97, 1928.

[30] V. Badilita, R. C. Meier, N. Spengler, U. Wallrabe, M. Utz, and J. G. Korvink, "Microscale nuclear magnetic resonance: a tool for soft matter research," *Soft Matter*, vol. 8, no. 41, pp. 10583–10597, 2012.

[31] W. S. Wong and A. Salleo, *Flexible Electronics: Materials and Applications*, vol. 11. New York, NY, USA: Springer Science & Business Media LLC, 2009.

[32] Allied Market Research, *Flexible Electronics Market Outlook–2027*, 2020. https://www.alli
edmarketresearch.com/flexible-electronics-market. Accessed: 15 Sept 2021.

[33] K. Nomura, H. Ohta, A. Takagi, T. Kamiya, M. Hirano, and H. Hosono, "Room-temperature fabrication of transparent flexible thin-film transistors using amorphous oxide semiconductors," *nature*, vol. 432, no. 7016, pp. 488–492, 2004.

[34] G. P. Crawford, *Flexible flat panel displays*. Chichester, UK: John Wiley & Sons Ltd, 2005.

[35] M. Pagliaro, R. Ciriminna, and G. Palmisano, "Flexible solar cells," *ChemSusChem: Chemistry & Sustainability Energy & Materials*, vol. 1, no. 11, pp. 880–891, 2008.

[36] R. Singh, E. Singh, and H. S. Nalwa, "Inkjet printed nanomaterial based flexible radio frequency identification (rfid) tag sensors for the internet of nano things," *RSC advances*, vol. 7, no. 77, pp. 48597–48630, 2017.

[37] G. Schwartz, B. C. K. Tee, J. Mei, A. L. Appleton, D. H. Kim, H. Wang, and Z. Bao, "Flexible polymer transistors with high pressure sensitivity for application in electronic skin and health monitoring," *Nature communications*, vol. 4, no. 1, pp. 1–8, 2013.

[38] D. Huston, *Structural sensing, health monitoring, and performance evaluation*. Boca Raton, FL, USA: Taylor & Rrancis Group, LLC. CRC Press, 2010.

[39] M. Stoppa and A. Chiolerio, "Wearable electronics and smart textiles: a critical review," *sensors*, vol. 14, no. 7, pp. 11957–11992, 2014.

[40] C. Gabardo and L. Soleymani, "Deposition, patterning, and utility of conductive materials for the rapid prototyping of chemical and bioanalytical devices," *Analyst*, vol. 141, no. 12, pp. 3511–3525, 2016.

[41] S. M. Khan, J. M. Nassar, and M. M. Hussain, "Paper as a substrate and an active material in paper electronics," *ACS Applied Electronic Materials*, vol. 3, no. 1, pp. 30–52, 2021.

[42] M. A. Hubbe and R. A. Gill, "Fillers for papermaking: a review of their properties, usage practices, and their mechanistic role," *BioResources*, vol. 11, no. 1, pp. 2886–2963, 2016.

[43] N. L. Salmen and E. L. Back, "Moisture-dependent thermal softening of paper, evaluated by its elastic modulus," *Tappi*, vol. 63, no. 6, pp. 117–120, 1980.

[44] P. Bhandari, T. Narahari, and D. Dendukuri, "'fab-chips': a versatile, fabric-based platform for low-cost, rapid and multiplexed diagnostics," *Lab on a Chip*, vol. 11, no. 15, pp. 2493–2499, 2011.

[45] I. Yakimets, D. MacKerron, P. Giesen, K. J. Kilmartin, M. Goorhuis, E. Meinders, and W. A. MacDonald, "Polymer substrates for flexible electronics: Achievements and challenges," *Trans Tech Publications*, vol. 93, pp. 5–8, 2010.

[46] Q.-H. Lu and F. Zheng, "Chapter 5 - polyimides for electronic applications," in *Advanced Polyimide Materials* (S.-Y. Yang, ed.), pp. 195–255, Amesterdam, Netherlands: Elsevier, 2018.

[47] DuPont™, *Kapton® HN*, 2019. https://www.dupont.com/content/dam/dupont/amer/us/en/products/ei-transformation/documents/DEC-Kapton-HN-datasheet.pdf, Technical Data. Accessed: 15 Sept 2021.

[48] M. C. Wapler, J. Leupold, I. Dragonu, D. von Elverfeld, M. Zaitsev, and U. Wallrabe, "Magnetic properties of materials for MR engineering, micro-MR and beyond," *Journal of magnetic resonance*, vol. 242, pp. 233–242, 2014.

[49] M. J. Madou, *Fundamentals of Microfabrication: The Science of Miniaturization.* Boca Raton, FL, USA: CRC Press LLC, 2nd ed., 2002.

[50] M. Van Rossum, "Integrated circuits," in *Encyclopedia of Condensed Matter Physics* (F. Bassani, G. L. Liedl, and P. Wyder, eds.), pp. 394–403, Oxford, UK: Elsevier, 2005.

[51] J. G. Korvink, P. J. Smith, and D.-Y. Shin, *Inkjet-based micromanufacturing*. Weinheim, Germany: Wiley-VCH, 2012.

[52] Research and markets, *Printed Electronics Market*, 2020. https://www.researchandmarkets.com/reports/5135680/, Report. Accessed: 15 Sept 2021.

[53] J. Chang, X. Zhang, T. Ge, and J. Zhou, "Fully printed electronics on flexible substrates: High gain amplifiers and dac," *Organic Electronics*, vol. 15, no. 3, pp. 701–710, 2014.

[54] S. Inoue, H. Kawai, S. Kanbe, T. Saeki, and T. Shimoda, "High-resolution microencapsulated electrophoretic display (epd) driven by poly-si tfts with four-level grayscale," *IEEE Transactions on Electron Devices*, vol. 49, no. 9, pp. 1532–1539, 2002.

[55] Y. Wu, Y. Li, and B. S. Ong, "A simple and efficient approach to a printable silver conductor for printed electronics," *Journal of the American Chemical Society*, vol. 129, no. 7, pp. 1862–1863, 2007.

[56] T. Sekitani, H. Nakajima, H. Maeda, T. Fukushima, T. Aida, K. Hata, and T. Someya, "Stretchable active-matrix organic light-emitting diode display using printable elastic conductors," *Nature materials*, vol. 8, no. 6, pp. 494–499, 2009.

[57] C. C. Ho, K. Murata, D. A. Steingart, J. W. Evans, and P. K. Wright, "A super ink jet printed zinc–silver 3D microbattery," *Journal of Micromechanics and Microengineering*, vol. 19, no. 9, p. 094013, 2009.

[58] S. B. Fuller, E. J. Wilhelm, and J. M. Jacobson, "Ink-jet printed nanoparticle microelectromechanical systems," *Journal of Microelectromechanical systems*, vol. 11, no. 1, pp. 54–60, 2002.

[59] X. Lin, H. Subbaraman, Z. Pan, A. Hosseini, C. Longe, K. Kubena, P. Schleicher, P. Foster, S. Brickey, and R. T. Chen, "Towards realizing high-throughput, roll-to-roll manufacturing of flexible electronic systems," *Electronics*, vol. 3, no. 4, pp. 624–635, 2014.

[60] R. Abbel, P. Teunissen, E. Rubingh, T. van Lammeren, R. Cauchois, M. Everaars, J. Valeton, S. van de Geijn, and P. Groen, "Industrial-scale inkjet printed electronics manufacturing—production up-scaling from concept tools to a roll-to-roll pilot line," *Translational Materials Research*, vol. 1, no. 1, p. 015002, 2014.

[61] M. Meissner, N. Spengler, D. Mager, N. Wang, S. Kiss, J. Höfflin, P. While, and J. Korvink, "Inkjet printing technology enables self-aligned mould patterning for electroplating in a single step," *Journal of Micromechanics and Microengineering*, vol. 25, no. 6, p. 065015, 2015.

[62] E. Tekin, P. J. Smith, and U. S. Schubert, "Inkjet printing as a deposition and patterning tool for polymers and inorganic particles," *Soft Matter*, vol. 4, no. 4, pp. 703–713, 2008.

[63] H. Sirringhaus, T. Kawase, R. Friend, T. Shimoda, M. Inbasekaran, W. Wu, and E. Woo, "High-resolution inkjet printing of all-polymer transistor circuits," *Science*, vol. 290, no. 5499, pp. 2123–2126, 2000.

[64] B.-J. De Gans, P. C. Duineveld, and U. S. Schubert, "Inkjet printing of polymers: state of the art and future developments," *Advanced materials*, vol. 16, no. 3, pp. 203–213, 2004.

[65] J. Perelaer, P. J. Smith, D. Mager, D. Soltman, S. K. Volkman, V. Subramanian, J. G. Korvink, and U. S. Schubert, "Printed electronics: the challenges involved in printing devices, interconnects, and contacts based on inorganic materials," *Journal of Materials Chemistry*, vol. 20, no. 39, pp. 8446–8453, 2010.

[66] J. Perelaer, A. W. De Laat, C. E. Hendriks, and U. S. Schubert, "Inkjet-printed silver tracks: low temperature curing and thermal stability investigation," *Journal of Materials Chemistry*, vol. 18, no. 27, pp. 3209–3215, 2008.

[67] H. Meier, U. Löffelmann, D. Mager, P. J. Smith, and J. G. Korvink, "Inkjet printed, conductive, 25 µm wide silver tracks on unstructured polyimide," *physica status solidi (a)*, vol. 206, no. 7, pp. 1626–1630, 2009.

[68] S. Gamerith, A. Klug, H. Scheiber, U. Scherf, E. Moderegger, and E. J. List, "Direct Ink-Jet Printing of Ag–Cu Nanoparticle and Ag-Precursor Based Electrodes for OFET Applications," *Advanced Functional Materials*, vol. 17, no. 16, pp. 3111–3118, 2007.

[69] M. Research and E. Trends, *Global Capacitors Industry*, 2021. https://www.reportlinker.com/p05864202/Global-Capacitors-Industry.html?utm_source=GNW. Accessed: 15 Sept 2021.

[70] D.-H. Kim, Y.-S. Kim, J. Wu, Z. Liu, J. Song, H.-S. Kim, Y. Y. Huang, K.-C. Hwang, and J. A. Rogers, "Ultrathin silicon circuits with strain-isolation layers and mesh layouts for high-performance electronics on fabric, vinyl, leather, and paper," *Advanced Materials*, vol. 21, no. 36, pp. 3703–3707, 2009.

[71] S. Bauer, S. Bauer-Gogonea, I. Graz, M. Kaltenbrunner, C. Keplinger, and R. Schwödiauer, "25th anniversary article: a soft future: from robots and sensor skin to energy harvesters," *Advanced Materials*, vol. 26, no. 1, pp. 149–162, 2014.

[72] E. M. Kardoulaki, R. R. Syms, I. R. Young, M. Rea, and W. M. Gedroyc, "Thin-film micro-coil detectors: Application in mr-thermometry," *Sensors and Actuators A: Physical*, vol. 226, pp. 48–58, 2015.

[73] Y. Cheung, K. Li, and H. Choi, "Flexible free-standing III-nitride thin films for emitters and displays," *ACS applied materials & interfaces*, vol. 8, no. 33, pp. 21440–21445, 2016.

[74] F. C. Krebs, "Fabrication and processing of polymer solar cells: A review of printing and coating techniques," *Solar energy materials and solar cells*, vol. 93, no. 4, pp. 394–412, 2009.

[75] P. M. Grubb, H. Subbaraman, S. Park, D. Akinwande, and R. T. Chen, "Inkjet printing of high performance transistors with micron order chemically set gaps," *Scientific reports*, vol. 7, no. 1, pp. 1–8, 2017.

[76] S. Chen, C. Lai, A. Chin, J. Hsieh, and J. Liu, "High-density MIM capacitors using Al_2O_3 and AlTiOx dielectrics," *IEEE Electron Device Letters*, vol. 23, no. 4, pp. 185–187, 2002.

[77] A. Chin, C. Liao, C. Lu, W. Chen, and C. Tsai, "Device and reliability of high-k Al_2O_3 gate dielectric with good mobility and low d_{it}," in *1999 Symposium on VLSI Technology. Digest of Technical Papers (IEEE Cat. No. 99CH36325)*, (Berlin, Germany), pp. 135–136, IEEE, 1999.

[78] A. Kar-Roy, C. Hu, M. Racanelli, C. A. Compton, P. Kempf, G. Jolly, P. N. Sherman, J. Zheng, Z. Zhang, and A. Yin, "High density metal insulator metal capacitors using PECVD nitride for mixed signal and RF circuits," in *Proceedings of the IEEE 1999 International Interconnect Technology Conference (Cat. No. 99EX247)*, (San Francisco, CA, USA), pp. 245–247, IEEE, 1999.

[79] S. J. Kim, B. J. Cho, M.-F. Li, S.-J. Ding, M. Yu, C. Zhu, A. Chin, and D.-L. Kwong, "Engineering of voltage nonlinearity in high-k MIM capacitor for analog/mixed-signal ICs," in *Digest of Technical Papers. 2004 Symposium on VLSI Technology, 2004*, (Honolulu, HI, USA), pp. 218–219, IEEE, 2004.

[80] K. Chiang, C.-C. Huang, G. Chen, W. J. Chen, H. Kao, Y.-H. Wu, A. Chin, and S. P. McAlister, "High-performance SrTiO$_3$ MIM capacitors for analog applications," *IEEE transactions on electron devices*, vol. 53, no. 9, pp. 2312–2319, 2006.

[81] C. Zhu, H. Hu, X. Yu, S. Kim, A. Chin, M. Li, B. J. Cho, and D. Kwong, "Voltage and temperature dependence of capacitance of high-K HFO$_2$ MIM capacitors: a unified understanding and prediction," in *IEEE International Electron Devices Meeting 2003*, pp. 36–5, IEEE, 2003.

[82] Y. Liu, T. Cui, and K. Varahramyan, "All-polymer capacitor fabricated with inkjet printing technique," *Solid-State Electronics*, vol. 47, no. 9, pp. 1543–1548, 2003.

[83] B. J. Kang, C. K. Lee, and J. H. Oh, "All-inkjet-printed electrical components and circuit fabrication on a plastic substrate," *Microelectronic Engineering*, vol. 97, pp. 251–254, 2012.

[84] Y.-Y. Noh and H. Sirringhaus, "Ultra-thin polymer gate dielectrics for top-gate polymer field-effect transistors," *Organic Electronics*, vol. 10, no. 1, pp. 174–180, 2009.

[85] Y. Li, R. Torah, S. Beeby, and J. Tudor, "An all-inkjet printed flexible capacitor on a textile using a new poly (4-vinylphenol) dielectric ink for wearable applications," in *SENSORS, 2012 IEEE*, pp. 1–4, IEEE, 2012.

[86] T. Hanemann and D. V. Szabó, "Polymer-nanoparticle composites: from synthesis to modern applications," *Materials*, vol. 3, no. 6, pp. 3468–3517, 2010.

[87] J. Lim, J. Kim, Y. J. Yoon, H. Kim, H. G. Yoon, S.-N. Lee, and J. Kim, "All-inkjet-printed metal-insulator-metal (MIM) capacitor," *Current Applied Physics*, vol. 12, pp. e14–e17, 2012.

[88] G. Vescio, J. López-Vidrier, R. Leghrib, A. Cornet, and A. Cirera, "Flexible inkjet printed high-k HfO 2-based MIM capacitors," *Journal of Materials Chemistry C*, vol. 4, no. 9, pp. 1804–1812, 2016.

[89] M. Mikolajek, T. Reinheimer, N. Bohn, C. Kohler, M. J. Hoffmann, and J. R. Binder, "fabrication and characterization of fully inkjet printed capacitors based on ceramic/polymer composite dielectrics on flexible substrates," *Scientific reports*, vol. 9, no. 1, pp. 1–13, 2019.

[90] D. Burdeaux, P. Townsend, J. Carr, and P. Garrou, "Benzocyclobutene (BCB) dielectrics for the fabrication of high density, thin film multichip modules," *Journal of Electronic Materials*, vol. 19, no. 12, pp. 1357–1366, 1990.

[91] DOW, *Advanced Packaging Polymers Product Selection Guide*, 2014. `https://www.microres ist.de/?jet_download=4822`, Technical Data. Accessed: 15 Sept 2021.

[92] M.-J. Pan and C. A. Randall, "A brief introduction to ceramic capacitors," *IEEE electrical insulation magazine*, vol. 26, no. 3, pp. 44–50, 2010.

[93] M. Berggren, D. Nilsson, and N. D. Robinson, "Organic materials for printed electronics," *Nature materials*, vol. 6, no. 1, pp. 3–5, 2007.

[94] S. R. Forrest, "The path to ubiquitous and low-cost organic electronic appliances on plastic," *Nature*, vol. 428, no. 6986, pp. 911–918, 2004.

[95] T. Someya, S. Bauer, and M. Kaltenbrunner, "Imperceptible organic electronics," *MRS Bulletin*, vol. 42, no. 2, pp. 124–130, 2017.

[96] C.-m. Kang, H. Shin, and C. Lee, "High-frequency organic rectifiers through interface engineering," *MRS Communications*, vol. 7, no. 4, pp. 755–769, 2017.

[97] Y. Chu, C. Qian, P. Chahal, and C. Cao, "Printed diodes: Materials processing, fabrication, and applications," *Advanced Science*, vol. 6, no. 6, p. 1801653, 2019.

[98] H.-S. Kim, S. R. Dhage, D.-E. Shim, and H. T. Hahn, "Intense pulsed light sintering of copper nanoink for printed electronics," *Applied Physics A*, vol. 97, no. 4, p. 791, 2009.

[99] S. H. Ko, H. Pan, C. P. Grigoropoulos, C. K. Luscombe, J. M. Fréchet, and D. Poulikakos, "All-inkjet-printed flexible electronics fabrication on a polymer substrate by low-temperature high-resolution selective laser sintering of metal nanoparticles," *Nanotechnology*, vol. 18, no. 34, p. 345202, 2007.

[100] M. Schlesinger and M. Paunovic, *Modern electroplating*. Hoboken, NJ, USA: John Wiley & Sons Inc, 5th ed., 2011.

[101] U. Erb, K. T. Aust, and G. Palumbo, "Chapter 6 - electrodeposited nanocrystalline metals, alloys, and composites," in *Nanostructured Materials: processing, properties and applications* (C. C. Koch, ed.), pp. 235–292, Norwich, NY, USA: William Andrew Publishing, 2nd ed., 2007.

[102] P. C. Andricacos, "Copper on-chip interconnections," *The Electrochemical Society Interface*, vol. 8, no. 1, p. 6, 1999.

[103] I. Gurrappa and L. Binder, "Electrodeposition of nanostructured coatings and their characterization—a review," *Science and Technology of Advanced Materials*, vol. 9, no. 4, p. 043001, 2008.

[104] S. Tjong and H. Chen, "Nanocrystalline materials and coatings," *Materials Science and Engineering: R: Reports*, vol. 45, no. 1-2, pp. 1–88, 2004.

[105] M. Chandrasekar and M. Pushpavanam, "Pulse and pulse reverse plating—conceptual, advantages and applications," *Electrochimica Acta*, vol. 53, no. 8, pp. 3313–3322, 2008.

[106] J. Rasmussen, "Making pulse plating work for pcb metallization," *Circuitree*, vol. 17, no. 9, pp. 28–30, 2004.

[107] N. Mandich, "Pulse and pulse-reverse electroplating," *Metal Finishing*, vol. 97, no. 1, pp. 375–380, 1999.

[108] N. Kanani, *Electroplating: basic principles, processes and practice*. Amesterdam, Netherlands: Elsevier, 2004.

[109] G. Milazzo, S. Caroli, and R. D. Braun, "Tables of standard electrode potentials," *Journal of The Electrochemical Society*, vol. 125, no. 6, p. 261C, 1978.

[110] S. Franssila, *Introduction to microfabrication*. Chichester, UK: John Wiley & Sons Ltd, 2nd ed., 2010.

[111] V. García-Morales and K. Krischer, "Fluctuation enhanced electrochemical reaction rates at the nanoscale," *Proceedings of the National Academy of Sciences*, vol. 107, no. 10, pp. 4528–4532, 2010.

[112] P. Odetola, P. Popoola, O. Popoola, and D. Delport, "Chapter 3 - parametric variables in electrodeposition of composite coatings," in *Electrodeposition of Composite Materials* (A. M. Mohamed and T. G. Golden, eds.), pp. 39–56, Rijeka, Croatia: InTech, 2016.

[113] F. Walsh and C. Ponce de Leon, "A review of the electrodeposition of metal matrix composite coatings by inclusion of particles in a metal layer: an established and diversifying technology," *Transactions of the IMF*, vol. 92, no. 2, pp. 83–98, 2014.

[114] N. Ibl, "Some theoretical aspects of pulse electrolysis," *Surface Technology*, vol. 10, no. 2, pp. 81–104, 1980.

[115] J.-C. Puippe and F. Leaman, *Theory and practice of pulse plating*. Orlando, FL, USA: American Electroplaters and Surface Finishers Society, 1986.

[116] C. J. Raub and A. Knödler, "The electrodeposition of gold by pulse plating," *Gold Bulletin*, vol. 10, no. 2, pp. 38–44, 1977.

[117] D. E. Engelhaupt, "Method of forming electrodeposited anti-reflective surface coatings," 1994. US Patent 5,326,454.

[118] D. Landolt and A. Marlot, "Microstructure and composition of pulse-plated metals and alloys," *Surface and Coatings Technology*, vol. 169, pp. 8–13, 2003.

[119] G. Devaraj, S. Guruviah, and S. Seshadri, "Pulse plating," *Materials Chemistry and physics*, vol. 25, no. 5, pp. 439–461, 1990.

[120] P. Bradley and D. Landolt, "Pulse-plating of copper–cobalt alloys," *Electrochimica Acta*, vol. 45, no. 7, pp. 1077–1087, 1999.

[121] T. Pearson and J. Dennis, "Facts and fiction about pulse plating," *Transactions of the IMF*, vol. 69, no. 3, pp. 75–79, 1991.

[122] V. Raj, M. Rajaram, G. Balasubramanian, S. Vincent, and D. Kanagaraj, "Pulse anodizing—an overview," *Transactions of the IMF*, vol. 81, no. 4, pp. 114–121, 2003.

[123] J. L. Martin, S. Menard, and D. N. Michelen, "Programmed pulse electroplating process," June 6 2000. US Patent 6,071,398.

[124] C. Toumazou, F. Lidgey, and C. Makris, "Extending voltage-mode op amps to current-mode performance," *IEE Proceedings G-Circuits, Devices and Systems*, vol. 137, no. 2, pp. 116–130, 1990.

[125] R. Bragos, J. Rosell, and P. Riu, "A wide-band ac-coupled current source for electrical impedance tomography," *Physiological measurement*, vol. 15, no. 2A, p. A91, 1994.

[126] P. Bertemes-Filho, B. Brown, and A. Wilson, "A comparison of modified howland circuits as current generators with current mirror type circuits," *Physiological Measurement*, vol. 21, no. 1, p. 1, 2000.

[127] F. Seoane, R. Bragós, and K. Lindecrantz, "Current source for multifrequency broadband electrical bioimpedance spectroscopy systems. a novel approach," in *Engineering in Medicine and Biology Society, 2006. EMBS'06. 28th Annual International Conference of the IEEE*, (New York, NY, USA), pp. 5121–5125, IEEE, 2006.

[128] H. Hong, M. Rahal, A. Demosthenous, and R. H. Bayford, "Comparison of a new integrated current source with the modified howland circuit for eit applications," *Physiological measurement*, vol. 30, no. 10, p. 999, 2009.

[129] L. Constantinou, I. F. Triantis, R. Bayford, and A. Demosthenous, "High-power cmos current driver with accurate transconductance for electrical impedance tomography," *IEEE transactions on biomedical circuits and systems*, vol. 8, no. 4, pp. 575–583, 2014.

[130] D. Bouchaala, O. Kanoun, and N. Derbel, "High accurate and wideband current excitation for bioimpedance health monitoring systems," *Measurement*, vol. 79, pp. 339–348, 2016.

[131] P. Bertemes-Filho, A. Felipe, and V. C. Vincence, "High accurate howland current source: Output constraints analysis," *Circuits and Systems*, vol. 4, no. 07, p. 451, 2013.

[132] A. S. Ross, G. Saulnier, J. Newell, and D. Isaacson, "Current source design for electrical impedance tomography," *Physiological measurement*, vol. 24, no. 2, p. 509, 2003.

[133] E. Basham, Z. Yang, and W. Liu, "Circuit and coil design for in-vitro magnetic neural stimulation systems," *IEEE transactions on biomedical circuits and systems*, vol. 3, no. 5, pp. 321–331, 2009.

[134] K. Sooksood, T. Stieglitz, and M. Ortmanns, "An active approach for charge balancing in functional electrical stimulation," *IEEE Transactions on Biomedical Circuits and Systems*, vol. 4, no. 3, pp. 162–170, 2010.

[135] D. Sheingold, "Impedance & admittance transformations using operational amplifiers," *Lightning Empiricist*, vol. 12, no. 1, pp. 1–8, 1964.

[136] T. Instruments, *AN-1515 A Comprehensive Study of the Howland Current Pump*, 2008. `https://www.ti.com/lit/an/snoa474a/snoa474a.pdf?ts=1633268802631&ref_url=https`, Application Report. Accessed: 15 Sept 2021.

[137] A. Mahnam, H. Yazdanian, and M. M. Samani, "Comprehensive study of howland circuit with non-ideal components to design high performance current pumps," *Measurement*, vol. 82, pp. 94–104, 2016.

[138] B. Trump, *Power Amplifier Stress and Power Handling Limitations*, 1993. `https://www.ti.com/lit/an/sboa022/sboa022.pdf?ts=1633269367504&ref_url=https`, Application Bulletin. Accessed: 15 Sept 2021.

[139] G. Hammond, C. Speake, and M. Stiff, "Noise analysis of a howland current source," *International Journal of Electronics*, vol. 95, no. 4, pp. 351–359, 2008.

[140] P. Bertemes-Filho and A. Felipe, "The effect of the random distribution of electronic components in the output characteristics of the howland current source," in *Journal of Physics: Conference Series*, vol. 434, p. 012019, IOP Publishing, 2013.

[141] D. Mager, A. Peter, L. Del Tin, E. Fischer, P. J. Smith, J. Hennig, and J. G. Korvink, "An MRI receiver coil produced by inkjet printing directly on to a flexible substrate," *IEEE transactions on medical imaging*, vol. 29, no. 2, pp. 482–487, 2010.

[142] F. Molina-Lopez, D. Briand, and N. De Rooij, "All additive inkjet printed humidity sensors on plastic substrate," *Sensors and Actuators B: Chemical*, vol. 166, pp. 212–222, 2012.

[143] N. Wang, M. Meissner, N. MacKinnon, V. Luchnikov, D. Mager, and J. Korvink, "Fast prototyping of microtubes with embedded sensing elements made possible with an inkjet printing and rolling process," *Journal of Micromechanics and Microengineering*, vol. 28, no. 2, p. 025003, 2017.

[144] B. Warren, "X-ray diffraction in random layer lattices," *Physical Review*, vol. 59, no. 9, p. 693, 1941.

[145] M. Islam, A. D. Lantada, M. R. Gómez, D. Mager, and J. G. Korvink, "Microarchitectured carbon structures as innovative tissue-engineering scaffolds," *Advanced Engineering Materials*, vol. 22, no. 6, p. 2000083, 2020.

[146] M. Islam, J. Flach, and R. Martinez-Duarte, "Carbon origami: A method to fabricate lightweight carbon cellular materials," *Carbon*, vol. 133, pp. 140–149, 2018.

[147] Y. Yildizhan, N. Erdem, M. Islam, R. Martinez-Duarte, and M. Elitas, "Dielectrophoretic separation of live and dead monocytes using 3d carbon-electrodes," *Sensors*, vol. 17, no. 11, p. 2691, 2017.

[148] K. Malladi, C. Wang, and M. Madou, "Fabrication of suspended carbon microstructures by e-beam writer and pyrolysis," *Carbon*, vol. 44, no. 13, pp. 2602–2607, 2006.

[149] C. S. Sharma, A. Verma, M. M. Kulkarni, D. K. Upadhyay, and A. Sharma, "Microfabrication of carbon structures by pattern miniaturization in resorcinol-formaldehyde gel," *ACS applied materials & interfaces*, vol. 2, no. 8, pp. 2193–2197, 2010.

[150] K. Pushparajah, H. Chubb, and R. Razavi, "Mr-guided cardiac interventions," *Topics in Magnetic Resonance Imaging*, vol. 27, no. 3, pp. 115–128, 2018.

[151] M. J. Kern, A. Lerman, J.-W. Bech, B. De Bruyne, E. Eeckhout, W. F. Fearon, S. T. Higano, M. J. Lim, M. Meuwissen, J. J. Piek, *et al.*, "Physiological assessment of coronary artery disease in the cardiac catheterization laboratory: a scientific statement from the american heart association committee on diagnostic and interventional cardiac catheterization, council on clinical cardiology," *Circulation*, vol. 114, no. 12, pp. 1321–1341, 2006.

[152] A. T. Rai, A. E. Seldon, S. Boo, P. S. Link, J. R. Domico, A. R. Tarabishy, N. Lucke-Wold, and J. S. Carpenter, "A population-based incidence of acute large vessel occlusions and thrombectomy eligible patients indicates significant potential for growth of endovascular stroke therapy in the usa," *Journal of neurointerventional surgery*, vol. 9, no. 8, pp. 722–726, 2017.

[153] R. A. Kleinerman, "Cancer risks following diagnostic and therapeutic radiation exposure in children," *Pediatric radiology*, vol. 36, no. 2, pp. 121–125, 2006.

[154] F. A. Jolesz and S. M. Blumenfeld, "Interventional use of magnetic resonance imaging," *Magnetic resonance quarterly*, vol. 10, no. 2, pp. 85–96, 1994.

[155] M. Bock and F. K. Wacker, "Mr-guided intravascular interventions: Techniques and applications," *Journal of Magnetic Resonance Imaging: An Official Journal of the International Society for Magnetic Resonance in Medicine*, vol. 27, no. 2, pp. 326–338, 2008.

[156] T. Rogers and R. J. Lederman, "Interventional cmr: clinical applications and future directions," *Current cardiology reports*, vol. 17, no. 5, p. 31, 2015.

[157] A. Glowinski, J. Kursch, G. Adam, A. Bucker, T. G. Noll, and R. Gunther, "Device visualization for interventional MRI using local magnetic fields: basic theory and its application to catheter visualization," *IEEE transactions on medical imaging*, vol. 17, no. 5, pp. 786–793, 1998.

[158] M. R. Prince, E. K. Yucel, J. A. Kaufman, D. C. Harrison, and S. C. Geller, "Dynamic gadolinium-enhanced three-dimensional abdominal mr arteriography," *Journal of Magnetic Resonance Imaging*, vol. 3, no. 6, pp. 877–881, 1993.

[159] K. Ratnayaka, A. Z. Faranesh, M. A. Guttman, O. Kocaturk, C. E. Saikus, and R. J. Lederman, "Interventional cardiovascular magnetic resonance: still tantalizing," *Journal of Cardiovascular Magnetic Resonance*, vol. 10, no. 1, pp. 1–23, 2008.

[160] C. L. Dumoulin, S. Souza, and R. Darrow, "Real-time position monitoring of invasive devices using magnetic resonance," *Magnetic resonance in medicine*, vol. 29, no. 3, pp. 411–415, 1993.

[161] E. Atalar, P. A. Bottomley, O. Ocali, L. C. Correia, M. D. Kelemen, J. A. Lima, and E. A. Zerhouni, "High resolution intravascular MRI and MRS by using a catheter receiver coil," *Magnetic resonance in medicine*, vol. 36, no. 4, pp. 596–605, 1996.

[162] O. Ocali and E. Atalar, "Intravascular magnetic resonance imaging using a loopless catheter antenna," *Magnetic resonance in medicine*, vol. 37, no. 1, pp. 112–118, 1997.

[163] E. Larose, Y. Yeghiazarians, P. Libby, E. K. Yucel, M. Aikawa, D. F. Kacher, E. Aikawa, S. Kinlay, F. J. Schoen, A. P. Selwyn, *et al.*, "Characterization of human atherosclerotic plaques by intravascular magnetic resonance imaging," *circulation*, vol. 112, no. 15, pp. 2324–2331, 2005.

[164] W. R. Nitz, A. Oppelt, W. Renz, C. Manke, M. Lenhart, and J. Link, "On the heating of linear conductive structures as guide wires and catheters in interventional MRI," *Journal of Magnetic Resonance Imaging*, vol. 13, no. 1, pp. 105–114, 2001.

[165] M. K. Konings, L. W. Bartels, H. F. Smits, and C. J. Bakker, "Heating around intravascular guidewires by resonating rf waves," *Journal of Magnetic Resonance Imaging*, vol. 12, no. 1, pp. 79–85, 2000.

[166] C. W. Ellenor, P. P. Stang, M. Etezadi-Amoli, J. M. Pauly, and G. C. Scott, "Offline impedance measurements for detection and mitigation of dangerous implant interactions: An rf safety prescreen," *Magnetic resonance in medicine*, vol. 73, no. 3, pp. 1328–1339, 2015.

[167] C. J. Yeung, R. C. Susil, and E. Atalar, "RF safety of wires in interventional MRI: using a safety index," *Magnetic Resonance in Medicine: An Official Journal of the International Society for Magnetic Resonance in Medicine*, vol. 47, no. 1, pp. 187–193, 2002.

[168] S. Park, R. Kamondetdacha, A. Amjad, and J. Nyenhuis, "MRI safety: RF-induced heating near straight wires," *IEEE transactions on magnetics*, vol. 41, no. 10, pp. 4197–4199, 2005.

[169] M. E. Ladd and H. H. Quick, "Reduction of resonant rf heating in intravascular catheters using coaxial chokes," *Magnetic Resonance in Medicine: An Official Journal of the International Society for Magnetic Resonance in Medicine*, vol. 43, no. 4, pp. 615–619, 2000.

[170] S. Weiss, P. Vernickel, T. Schaeffter, V. Schulz, and B. Gleich, "Transmission line for improved rf safety of interventional devices," *Magnetic Resonance in Medicine: An Official Journal of the International Society for Magnetic Resonance in Medicine*, vol. 54, no. 1, pp. 182–189, 2005.

[171] R. Syms, L. Solymar, I. Young, and T. Floume, "Thin-film magneto-inductive cables," *Journal of Physics D: Applied Physics*, vol. 43, no. 5, p. 055102, 2010.

[172] R. R. Syms, I. R. Young, M. M. Ahmad, S. D. Taylor-Robinson, and M. Rea, "Magneto-inductive catheter receiver for magnetic resonance imaging," *IEEE Transactions on Biomedical Engineering*, vol. 60, no. 9, pp. 2421–2431, 2013.

[173] S. Fandrey, S. Weiss, and J. Müller, "A novel active MR probe using a miniaturized optical link for a 1.5-T MRI scanner," *Magnetic resonance in medicine*, vol. 67, no. 1, pp. 148–155, 2012.

[174] B. Sarioglu, O. Aktan, A. Oncu, S. Mutlu, G. Dundar, and A. D. Yalcinkaya, "An optically powered CMOS receiver system for intravascular magnetic resonance applications," *IEEE Journal on Emerging and Selected Topics in Circuits and Systems*, vol. 2, no. 4, pp. 683–691, 2012.

[175] C. D. Jordan, B. R. Thorne, A. Wadhwa, A. D. Losey, E. Ozhinsky, S. Kondapavulur, V. Fratello, T. Moore, C. Stillson, C. Yee, *et al.*, "Wireless resonant circuits printed using aerosol jet deposition for MRI catheter tracking," *IEEE Transactions on Biomedical Engineering*, vol. 67, no. 3, pp. 876–882, 2019.

[176] T. Kuehne, R. Fahrig, and K. Butts, "Pair of resonant fiducial markers for localization of endovascular catheters at all catheter orientations," *Journal of Magnetic Resonance Imaging: An Official Journal of the International Society for Magnetic Resonance in Medicine*, vol. 17, no. 5, pp. 620–624, 2003.

[177] D. Ellersiek, H. Fassbender, P. Bruners, J. G. Pfeffer, T. Penzkofer, A. H. Mahnken, T. Schmitz-Rode, W. Mokwa, and U. Schnakenberg, "A monolithically fabricated flexible resonant circuit for catheter tracking in magnetic resonance imaging," *Sensors and Actuators B: Chemical*, vol. 144, no. 2, pp. 432–436, 2010.

[178] H. H. Quick, M. O. Zenge, H. Kuehl, G. Kaiser, S. Aker, S. Massing, S. Bosk, and M. E. Ladd, "Interventional magnetic resonance angiography with no strings attached: wireless active catheter visualization," *Magnetic Resonance in Medicine: An Official Journal of the International Society for Magnetic Resonance in Medicine*, vol. 53, no. 2, pp. 446–455, 2005.

[179] M. A. Rube, A. B. Holbrook, B. F. Cox, J. G. Houston, and A. Melzer, "Wireless MR tracking of interventional devices using phase-field dithering and projection reconstruction," *Magnetic resonance imaging*, vol. 32, no. 6, pp. 693–701, 2014.

[180] M. Kaiser, M. Detert, M. A. Rube, A. El-Tahir, O. J. Elle, A. Melzer, B. Schmidt, and G. H. Rose, "Resonant marker design and fabrication techniques for device visualization during interventional magnetic resonance imaging," *Biomedical Engineering/Biomedizinische Technik*, vol. 60, no. 2, pp. 89–103, 2015.

[181] M. Detert, S. Friesecke, M. Deckert, G. Rose, B. Schmidt, and M. Kaiser, "Using the hot embossing technology for the realization of microtechnical structures in medical imaging," *Biomedical Engineering/Biomedizinische Technik*, vol. 57, no. SI-1-Track-E, pp. 599–602, 2012.

[182] D. D. Wheeler and M. S. Conradi, "Practical exercises for learning to construct nmr/mri probe circuits," *Concepts in Magnetic Resonance Part A*, vol. 40, no. 1, pp. 1–13, 2012.

[183] R. Ediss and U. Philips Semiconductors, "Probing the magnetic field probe," *EMC & Compliance Journal*, 2003.

[184] A. Ross and H. Senn, "Automation of measurements and data evaluation in biomolecular NMR screening," *Drug discovery today*, vol. 6, no. 11, pp. 583–593, 2001.

[185] K. Lilly, "Sample changer for NMR spectrometers," July 9 1996. US Patent 5,534,780.

[186] Bruker, "NMR automation sample case." `https://www.bruker.com/en/products-and-sol utions/mr/nmr/nmr-automation/SampleCase.html`. Accessed: 15 Sept 2021.

[187] JEOL, "Auto sample changers." `https://www.jeolusa.com/PRODUCTS/Nuclear-Magneti c-Resonance/Sample-Changers?fbclid=IwAR0CvTUNRi1KH7PcOO8eapjT2f8Hdt9mR3488y k3XRF4rkZt91L20qHWDVM`. Accessed: 15 Sept 2021.

[188] E. MacNamara, T. Hou, G. Fisher, S. Williams, and D. Raftery, "Multiplex sample NMR: an approach to high-throughput NMR using a parallel coil probe," *Analytica chimica acta*, vol. 397, no. 1-3, pp. 9–16, 1999.

[189] H. Wang, L. Ciobanu, A. Edison, and A. Webb, "An eight-coil high-frequency probehead design for high-throughput nuclear magnetic resonance spectroscopy," *Journal of Magnetic Resonance*, vol. 170, no. 2, pp. 206–212, 2004.

[190] A. M. Wolters, D. A. Jayawickrama, A. G. Webb, and J. V. Sweedler, "NMR detection with multiple solenoidal microcoils for continuous-flow capillary electrophoresis," *Analytical chemistry*, vol. 74, no. 21, pp. 5550–5555, 2002.

[191] Q. He and Z. Wei, "Convection compensated electrophoretic NMR," *Journal of magnetic resonance*, vol. 150, no. 2, pp. 126–131, 2001.

[192] O. Gökay and K. Albert, "From single to multiple microcoil flow probe NMR and related capillary techniques: a review," *Analytical and bioanalytical chemistry*, vol. 402, no. 2, pp. 647–669, 2012.

[193] B. J. Stockman, K. A. Farley, and D. T. Angwin, "Screening of compound libraries for protein binding using flow-injection nuclear magnetic resonance spectroscopy," *Methods in enzymology*, vol. 338, pp. 230–246, 2001.

[194] Gilson Inc, *Gilson Multiple Probe 215 Liquid Handler User's Guide*. `https://conquerscien tific.com/wp-content/product-images/2011/08/GIlson-Multiple-Probe-215-Liqu id-Handler-Users-Guide.pdf`, Technical Data. Accessed: 15 Sept 2021.

[195] J. Rehbein, B. Dietrich, M. D. Grynbaum, P. Hentschel, K. Holtin, M. Kuehnle, P. Schuler, M. Bayer, and K. Albert, "Characterization of bixin by LC-MS and LC-NMR," *Journal of separation science*, vol. 30, no. 15, pp. 2382–2390, 2007.

[196] M. A. Macnaughtan, T. Hou, J. Xu, and D. Raftery, "High-throughput nuclear magnetic resonance analysis using a multiple coil flow probe," *Analytical chemistry*, vol. 75, no. 19, pp. 5116–5123, 2003.

[197] T. Hou, J. Smith, E. MacNamara, M. Macnaughtan, and D. Raftery, "Analysis of multiple samples using multiplex sample NMR: selective excitation and chemical shift imaging approaches," *Analytical chemistry*, vol. 73, no. 11, pp. 2541–2546, 2001.

[198] J. A. Rogers, R. J. Jackman, G. M. Whitesides, D. L. Olson, and J. V. Sweedler, "Using microcontact printing to fabricate microcoils on capillaries for high resolution proton nuclear magnetic resonance on nanoliter volumes," *Applied physics letters*, vol. 70, no. 18, pp. 2464–2466, 1997.

[199] K. Kratt, V. Badilita, T. Burger, J. Mohr, M. Börner, J. G. Korvink, and U. Wallrabe, "High aspect ratio pmma posts and characterization method for micro coils manufactured with an automatic wire bonder," *Sensors and actuators A: Physical*, vol. 156, no. 2, pp. 328–333, 2009.

[200] N. Spengler, A. Moazenzadeh, R. C. Meier, V. Badilita, J. Korvink, and U. Wallrabe, "Microfabricated helmholtz coil featuring disposable microfluidic sample inserts for applications in nuclear magnetic resonance," *Journal of Micromechanics and Microengineering*, vol. 24, no. 3, p. 034004, 2014.

[201] D. L. Olson, T. L. Peck, A. G. Webb, R. L. Magin, and J. V. Sweedler, "High-resolution microcoil 1H-NMR for mass-limited, nanoliter-volume samples," *Science*, vol. 270, no. 5244, pp. 1967–1970, 1995.

[202] R. Kc, I. D. Henry, G. H. Park, A. Aghdasi, and D. Raftery, "New solenoidal microcoil NMR probe using zero-susceptibility wire," *Concepts in Magnetic Resonance Part B: Magnetic Resonance Engineering*, vol. 37, no. 1, pp. 13–19, 2010.

[203] R. C. Meier, J. Höfflin, V. Badilita, U. Wallrabe, and J. G. Korvink, "Microfluidic integration of wirebonded microcoils for on-chip applications in nuclear magnetic resonance," *Journal of Micromechanics and Microengineering*, vol. 24, no. 4, p. 045021, 2014.

[204] N. Spengler, J. Höfflin, A. Moazenzadeh, D. Mager, N. MacKinnon, V. Badilita, U. Wallrabe, and J. G. Korvink, "Heteronuclear Micro-Helmholtz Coil Facilitates μm-Range Spatial and Sub-Hz Spectral Resolution NMR of nL-Volume Samples on Customisable Microfluidic Chips," *PLOS ONE*, vol. 11, p. e0146384, jan 2016.

[205] J. Mispelter, M. Lupu, and A. Briguet, *NMR probeheads for biophysical and biomedical experiments: theoretical principles and practical guidelines*. London, UK: Imperial College Press, 2nd ed., 2015.

[206] C. Massin, G. Boero, F. Vincent, J. Abenhaim, P.-A. Besse, and R. Popovic, "High-Q factor RF planar microcoils for micro-scale NMR spectroscopy," *Sensors and Actuators A: Physical*, vol. 97, pp. 280–288, 2002.

[207] O. Gruschke, L. Clad, N. Baxan, K. Kratt, M. Mohmmadzadeh, D. von Elverfeldt, A. Peter, J. Hennig, V. Badilita, U. Wallrabe, *et al.*, "Multilayer phased microcoil array for magnetic resonance imaging," in *2011 16th International Solid-State Sensors, Actuators and Microsystems Conference*, pp. 962–965, IEEE, 2011.

[208] A. Kentgens, J. Bart, P. Van Bentum, A. Brinkmann, E. Van Eck, J. G. Gardeniers, J. Janssen, P. Knijn, S. Vasa, and M. Verkuijlen, "High-resolution liquid-and solid-state nuclear magnetic resonance of nanoliter sample volumes using microcoil detectors," *The Journal of chemical physics*, vol. 128, no. 5, p. 052202, 2008.

[209] S. Eroglu, B. Gimi, B. Roman, G. Friedman, and R. L. Magin, "NMR spiral surface microcoils: design, fabrication, and imaging," *Concepts in Magnetic Resonance Part B: Magnetic Resonance Engineering: An Educational Journal*, vol. 17, no. 1, pp. 1–10, 2003.

[210] J. Stocker, T. Peck, A. Webb, M. Feng, and R. Magin, "Nanoliter volume, high-resolution NMR microspectroscopy using a 60-μm planar microcoil," *IEEE Transactions on biomedical engineering*, vol. 44, no. 11, pp. 1122–1127, 1997.

[211] J. Dechow, A. Forchel, T. Lanz, and A. Haase, "Fabrication of NMR—microsensors for nanoliter sample volumes," *Microelectronic engineering*, vol. 53, no. 1-4, pp. 517–519, 2000.

[212] M. Grisi, G. Gualco, and G. Boero, "A broadband single-chip transceiver for multi-nuclear NMR probes," *Review of Scientific Instruments*, vol. 86, no. 4, p. 044703, 2015.

[213] E. Montinaro, M. Grisi, M. Letizia, L. Pethö, M. Gijs, R. Guidetti, J. Michler, J. Brugger, and G. Boero, "3D printed microchannels for sub-nL NMR spectroscopy," *PloS one*, vol. 13, no. 5, p. e0192780, 2018.

[214] I. Swyer, S. von der Ecken, B. Wu, A. Jenne, R. Soong, F. Vincent, D. Schmidig, T. Frei, F. Busse, H. J. Stronks, *et al.*, "Digital microfluidics and nuclear magnetic resonance spectroscopy for in situ diffusion measurements and reaction monitoring," *Lab on a Chip*, vol. 19, no. 4, pp. 641–653, 2019.

[215] R. F. Lee, R. O. Giaquinto, and C. J. Hardy, "Coupling and decoupling theory and its application to the MRI phased array," *Magnetic Resonance in Medicine: An Official Journal of the International Society for Magnetic Resonance in Medicine*, vol. 48, no. 1, pp. 203–213, 2002.

[216] O. G. Gruschke, N. Baxan, L. Clad, K. Kratt, D. von Elverfeldt, A. Peter, J. Hennig, V. Badilita, U. Wallrabe, and J. G. Korvink, "Lab on a chip phased-array MR multi-platform analysis system," *Lab on a Chip*, vol. 12, no. 3, pp. 495–502, 2012.

[217] H. Davoodi, N. Nordin, H. Munakata, J. G. Korvink, N. MacKinnon, and V. Badilita, "Untuned broadband spiral micro-coils achieve sensitive multi-nuclear NMR TX/RX from microfluidic samples," *Scientific reports*, vol. 11, no. 1, pp. 1–12, 2021.

[218] X. Zhang, K. Ugurbil, and W. Chen, "Microstrip RF surface coil design for extremely high-field MRI and spectroscopy," *Magnetic Resonance in Medicine: An Official Journal of the International Society for Magnetic Resonance in Medicine*, vol. 46, no. 3, pp. 443–450, 2001.

[219] R. F. Lee, C. J. Hardy, D. K. Sodickson, and P. A. Bottomley, "Lumped-element planar strip array (LPSA) for parallel MRI," *Magnetic Resonance in Medicine: An Official Journal of the International Society for Magnetic Resonance in Medicine*, vol. 51, no. 1, pp. 172–183, 2004.

[220] X. Zhang, K. Ugurbil, and W. Chen, "A microstrip transmission line volume coil for human head MR imaging at 4T," *Journal of Magnetic Resonance*, vol. 161, no. 2, pp. 242–251, 2003.

[221] K. Jasiński, A. Młynarczyk, P. Latta, V. Volotovskyy, W. P. Węglarz, and B. Tomanek, "A volume microstrip RF coil for MRI microscopy," *Magnetic resonance imaging*, vol. 30, no. 1, pp. 70–77, 2012.

[222] J. Bart, J. Janssen, P. Van Bentum, A. Kentgens, and J. G. Gardeniers, "Optimization of stripline-based microfluidic chips for high-resolution NMR," *Journal of magnetic resonance*, vol. 201, no. 2, pp. 175–185, 2009.

[223] I. Swyer, R. Soong, M. D. Dryden, M. Fey, W. E. Maas, A. Simpson, and A. R. Wheeler, "Interfacing digital microfluidics with high-field nuclear magnetic resonance spectroscopy," *Lab on a Chip*, vol. 16, no. 22, pp. 4424–4435, 2016.

[224] N.-T. Nguyen, S. Lassemono, and F. A. Chollet, "Optical detection for droplet size control in microfluidic droplet-based analysis systems," *Sensors and actuators B: Chemical*, vol. 117, no. 2, pp. 431–436, 2006.

[225] C. Cramer, P. Fischer, and E. J. Windhab, "Drop formation in a co-flowing ambient fluid," *Chemical Engineering Science*, vol. 59, no. 15, pp. 3045–3058, 2004.

[226] M. C. Cole and P. J. Kenis, "Multiplexed electrical sensor arrays in microfluidic networks," *Sensors and Actuators B: Chemical*, vol. 136, no. 2, pp. 350–358, 2009.

[227] C. Elbuken, T. Glawdel, D. Chan, and C. L. Ren, "Detection of microdroplet size and speed using capacitive sensors," *Sensors and Actuators A: Physical*, vol. 171, no. 2, pp. 55–62, 2011.

[228] N. Srivastava and M. A. Burns, "Electronic drop sensing in microfluidic devices: automated operation of a nanoliter viscometer," *Lab on a Chip*, vol. 6, no. 6, pp. 744–751, 2006.

[229] B. Jin, Z. Zhang, and H. Zhang, "Structure design and performance analysis of a coaxial cylindrical capacitive sensor for liquid-level measurement," *Sensors and Actuators A: Physical*, vol. 223, pp. 84–90, 2015.

[230] L. R. Soenksen, T. Kassis, M. Noh, L. G. Griffith, and D. L. Trumper, "Closed-loop feedback control for microfluidic systems through automated capacitive fluid height sensing," *Lab on a Chip*, vol. 18, no. 6, pp. 902–914, 2018.

[231] E. Ghafar-Zadeh and M. Sawan, "A hybrid microfluidic/cmos capacitive sensor dedicated to lab-on-chip applications," *IEEE transactions on biomedical circuits and systems*, vol. 1, no. 4, pp. 270–277, 2007.

[232] G. Finch, A. Yilmaz, and M. Utz, "An optimised detector for in-situ high-resolution NMR in microfluidic devices," *Journal of Magnetic Resonance*, vol. 262, p. 73, 2016.

[233] X. B. Li, S. D. Larson, A. S. Zyuzin, and A. V. Mamishev, "Design principles for multichannel fringing electric field sensors," *IEEE Sensors Journal*, vol. 6, no. 2, pp. 434–440, 2006.

[234] Z. H. Zargar and T. Islam, "A novel cross-capacitive sensor for noncontact microdroplet detection," *IEEE Transactions on Industrial Electronics*, vol. 66, no. 6, pp. 4759–4766, 2018.

[235] 3M Science. Applied to Life.™, *3M™ Fluorinert™ Electronic Liquid FC-43*, 2019. `https://multimedia.3m.com/mws/media/648890/3m-novec-fluorinert-electronic-liquid-fc43.pdf`, Technical Data. Accessed: 15 Sept 2021.

[236] N. MacKinnon, W. Ge, P. Han, , J. T. Wei, T. Raghunathan, A. M. Chinnaiyan, T. M. Rajendiran, and A. Ramamoorthy, "NMR-Based metabolomic profiling of urine: Evaluation for application in prostate cancer detection," *Natural Product Communications*, vol. 14, no. 5, pp. 1–13, 2019.

[237] K. Lei, D. Ha, Y. Song, R. M. Westervelt, R. Martins, P. Mak, and D. Ham, "Portable NMR with parallelism," *Anal Chem*, vol. 92, no. 2, pp. 2112–2120, 2020.

[238] N. Balabanian, *Electric circuits*. New York, NY, USA: McGraw-Hill, 1994.

[239] D. Hoult, "The principle of reciprocity in signal strength calculations—a mathematical guide," *Concepts in Magnetic Resonance: An Educational Journal*, vol. 12, no. 4, pp. 173–187, 2000.

A   Appendix to chapter 3

Inkjet-printed BCB insulating ink
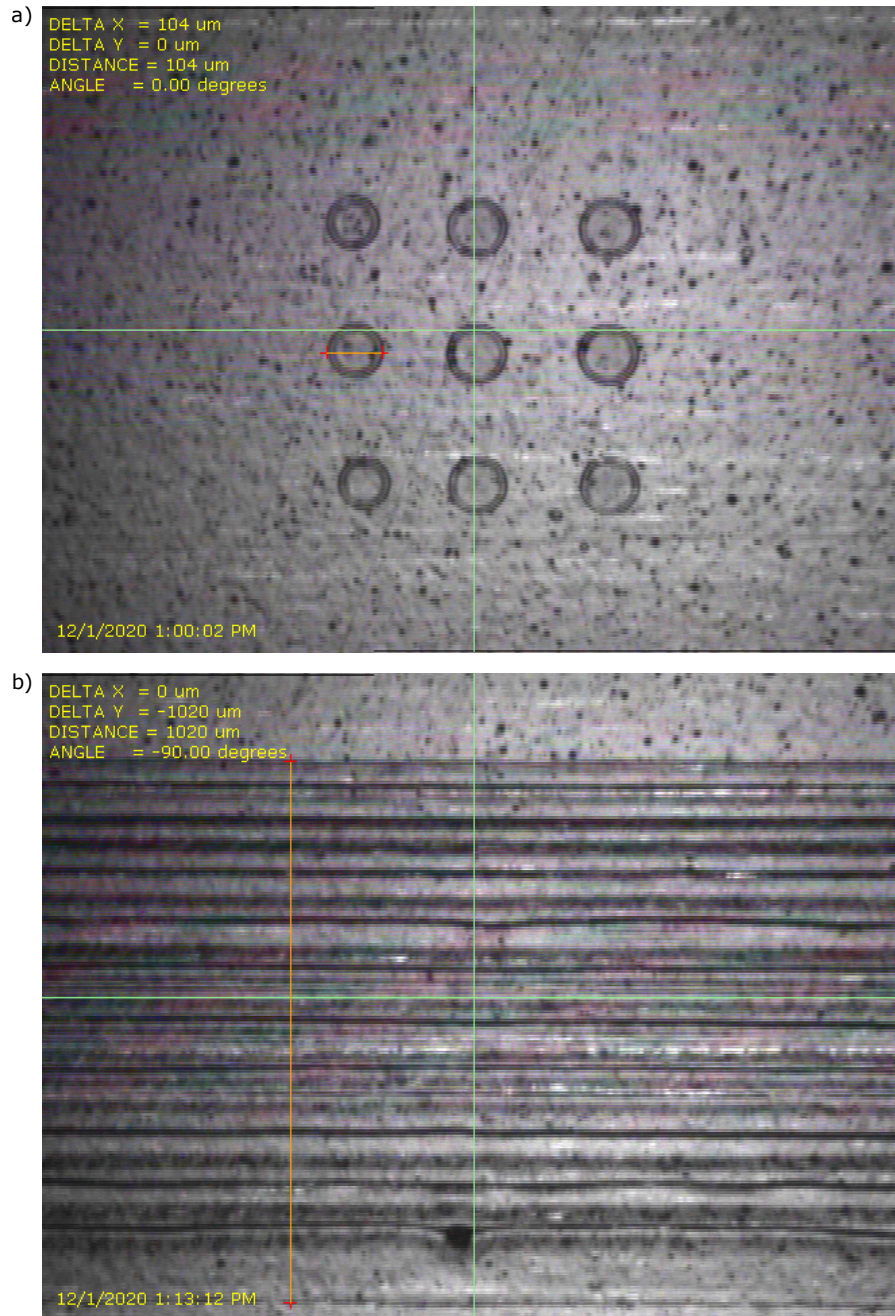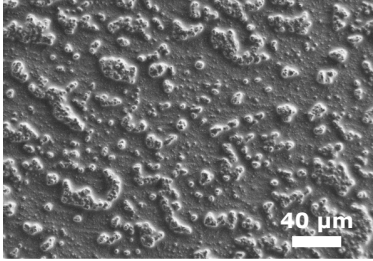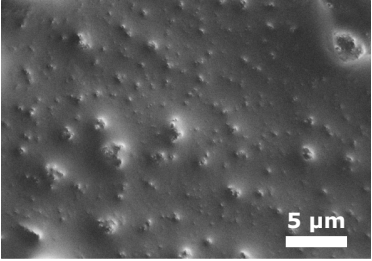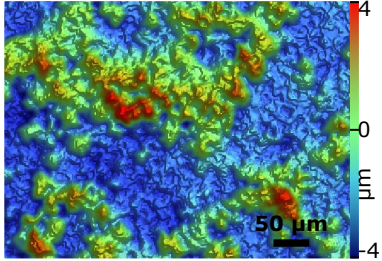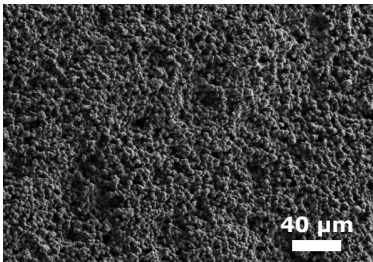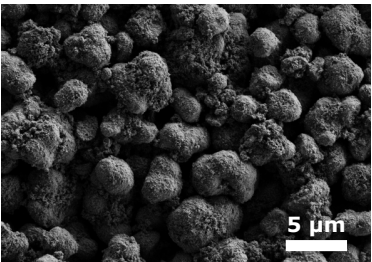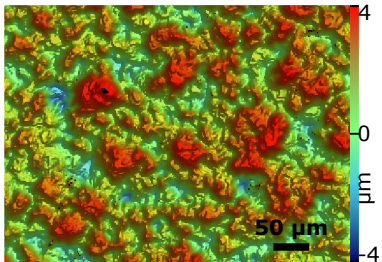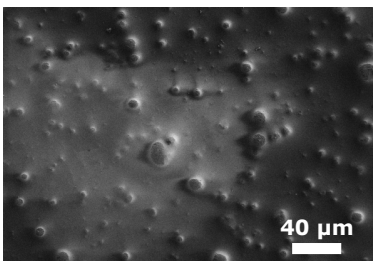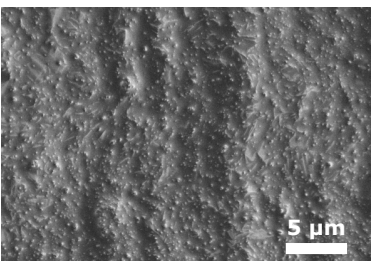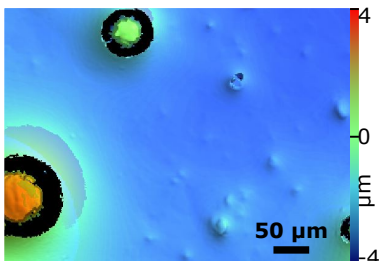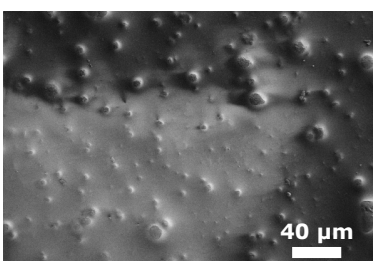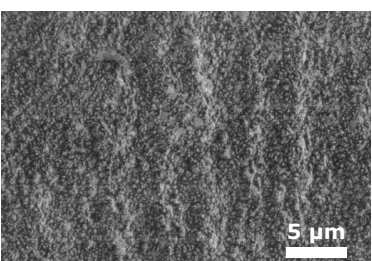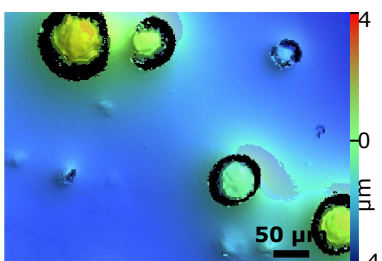
Figure A.1: Inkjet-printed droplets and straight lines of the BCB insulating ink. The measured droplets diameter was $\approx 105\,\mu$m, therefore, the drop spacing was set to $50\,\mu$m.

Inkjet-printed composite insulating ink

Table A.1: Surface morphology of the inkjet-printed insulating film using composite inks.

	SEM ×1K	SEM ×10K	WLI
20wt% TiO$_2$			
40wt% TiO$_2$			
20wt% BaTiO$_3$			
40wt% BaTiO$_3$			

Spin-coated PTAA semiconductor of MS diode
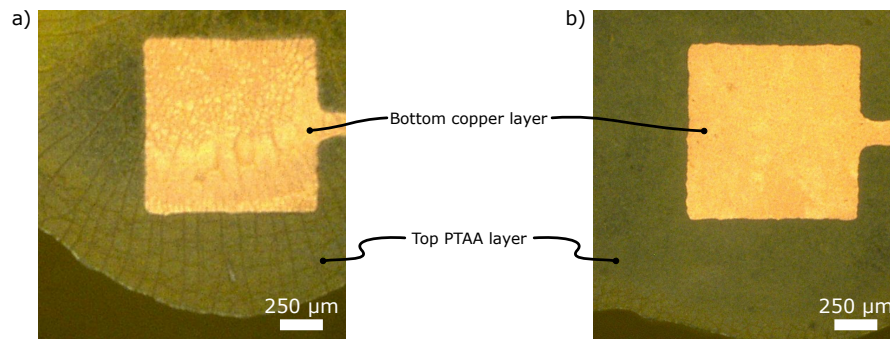
Figure A.2: Spin-coated PTAA semiconductor of MS diode with different weight concentrations. PTAA powder was dissolved in toluene solvent with concentrations of **(a)** 5wt.% and **(b)** 2wt.%. Both solutions were spin-coated at 1000 rpm for 1 min. High PTAA concentrations lead to a cracked semiconductor layer which results in a short circuit.

B Appendix to chapter 4

2.1 Modified Howland Current Source (MHCS) modeling

Transfer function
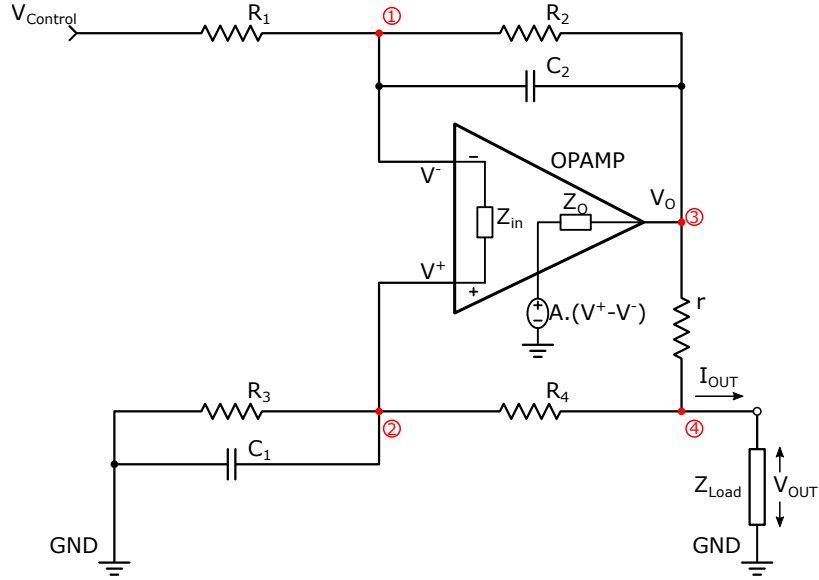
Figure B.1: Equivelant schematic circuit of the Modified Howland Current Source (MHCS).

The output current (I_{OUT}) of the *MHCS* can be expressed in terms of the input control signal ($V_{Control}$) by applying Kirchhoff's Current Law (*KCL*) (nodal analysis) at the nodes from 1-4,

$$@ \text{ node } 1: \quad \frac{V^- - V_{Control}}{R_1} + \frac{V^- - V_O}{R_2} + \frac{V^- - V^+}{Z_{in}} = 0, \tag{B.1a}$$

$$@ \text{ node } 2: \quad \frac{V^+}{R_3} + \frac{V^+ - V_{OUT}}{R_4} + \frac{V^+ - V^-}{Z_{in}} = 0, \tag{B.1b}$$

$$@ \text{ node } 3: \quad \frac{V_O - V_{OUT}}{r} + \frac{V_O - V^-}{R_2} + \frac{V_O - (V^+ - V^-) \cdot A}{Z_O} = 0, \tag{B.1c}$$

$$@ \text{ node } 4: \quad I_{OUT} = \frac{V^+ - V_{OUT}}{R_4} + \frac{V_O - V_{OUT}}{r}. \tag{B.1d}$$

An ideal operational amplifier (*OPAMP*) is assumed to have infinite open-loop gain, infinite input impedance (Z_{in}), and zero output impedance (Z_O). Hence, no electric current flow between the input terminals of the opamp leading to $V^+ = V^-$. Solving the three equations B.1a - B.1c together, V^+, V^- and V_O can be expressed in terms of $V_{Control}$ and V_{OUT},

$$V^+ = V_{OUT} \frac{R_3}{R_3 + R_4}, \tag{B.2a}$$

$$V_O = V_{OUT} \frac{R_3(R_2 + R_1)}{R_1(R_3 + R_4)} - V_{Control} \frac{R_2}{R_1}. \tag{B.2b}$$

Substituting by B.2a and B.2b in B.1d, the output current (I_{OUT}) can be driven as follow,

$$I_{\text{OUT}} = -V_{Control}\frac{R_2}{R_1 r} + V_{OUT}\frac{R_1(R_4 + r) - R_2 R_3}{R_1 r(R_3 + R_4)}. \tag{B.3}$$

Virtual capacitance

Following the technical report provided by Texas Instrument [136], the virtual output capacitance of the *MHCS* (C_{OUT}) can be derived by calculating the *OPAMP*'s output current (I_O) in the presence of a time-varying signal at the output node of the circuit (dV_T/dt) and a very small error input signal (V_{error}) across the *OPAMP*'s inputs. The applied voltage at the output node of the *MHCS* is assumed to be a ramp signal moving from a negative voltage in the positive direction. The system is solved at the moment when the signal passes zero volts, ($V_T = 0 + dV_T/dt$). The calculated current, in that case I_O, is known as the capacitive current since it's related only to dV_T/dt.

The rate of change of an *OPAMP*'s output voltage is function in the input signal across it's inputs and the Gain Bandwidth Product (*GBMP*):

$$\frac{dV_O}{dt} = V_{error}\, 2\pi GBWP, \tag{B.4a}$$

$$\therefore V_{error} = \frac{dV_O}{dt}\frac{1}{2\pi GBWP}. \tag{B.4b}$$

When applying a time-changing signal at the output node of the *MHCS* (dV_T/dt), the rate of change of the voltage at the positive terminal of the *OPAMP* can be derived using potential divider rule:

$$\frac{dV^+}{dt} = \frac{R_3}{R_3 + R_4}\frac{dV_T}{dt}, \tag{B.5a}$$

Taking into consideration the applied error signal (V_{error} and assuming an ideal *OPAMP*, the the rate of change of the voltage at the negative terminal of the *OPAMP* can be derived:

$$\frac{dV^-}{dt} = \frac{R_3}{R_3 + R_4}\frac{dV_T}{dt} + V_{error}, \tag{B.5b}$$

hence, the rate of change of the voltage at the *OPAMP*'s output is the same as the change at the negative input magnified by $R_1 + R_2/R_1$,

$$\frac{dV_O}{dt} = \frac{R_3}{R_3 + R_4}\frac{R_1 + R_2}{R_1}\frac{dV_T}{dt} - V_{error}\frac{R_1 + R_2}{R_1}. \tag{B.5c}$$

By solving Equations B.4b and B.5c together:

$$V_{error} = \frac{dV_T}{dt}\frac{1}{2\pi GBWP}\frac{R_3}{R_3 + R_4}\frac{R_1 + R_2}{R_1} - V_{error}\frac{1}{2\pi GBWP}\frac{R_1 + R_2}{R_1}. \tag{B.6}$$

The momentary when $V_T = 0 + dV_T/dt$, the value of the *OPAMP*'s output voltage at is:

$$V_O = \frac{R_1 + R_2}{R_1}V_{error}, \tag{B.7a}$$

$$\therefore V_O = \frac{dV_T}{dt}\frac{1}{2\pi GBWP}\frac{R_3}{R_3 + R_4}[\frac{R_1 + R_2}{R_1}]^2 - V_{error}\frac{1}{2\pi GBWP}[\frac{R_1 + R_2}{R_1}]^2. \tag{B.7b}$$

The momentary when $V_T = 0 + dV_T/dt$, no electric current is going through R_4 and the current going through r is,

$$I_O = I_r = V_O/r, \tag{B.8a}$$

$$\therefore I_O = \frac{dV_T}{dt} \frac{1}{2\pi r GBWP} \frac{R_3}{R_3 + R_4} \left[\frac{R_1 + R_2}{R_1}\right]^2 - V_{error} \frac{1}{2\pi r GBWP} \left[\frac{R_1 + R_2}{R_1}\right]^2. \tag{B.8b}$$

This capacitive current is equivalent to $I_O = C_O \, dV_T/dt$,

$$\boxed{C_O = \frac{R_3(R_1 + R_2)^2}{2\pi r R_1^2 (R_3 + R_4) GBWP}.} \tag{B.9}$$

2.2 Electronic schematics of the electroplating current source
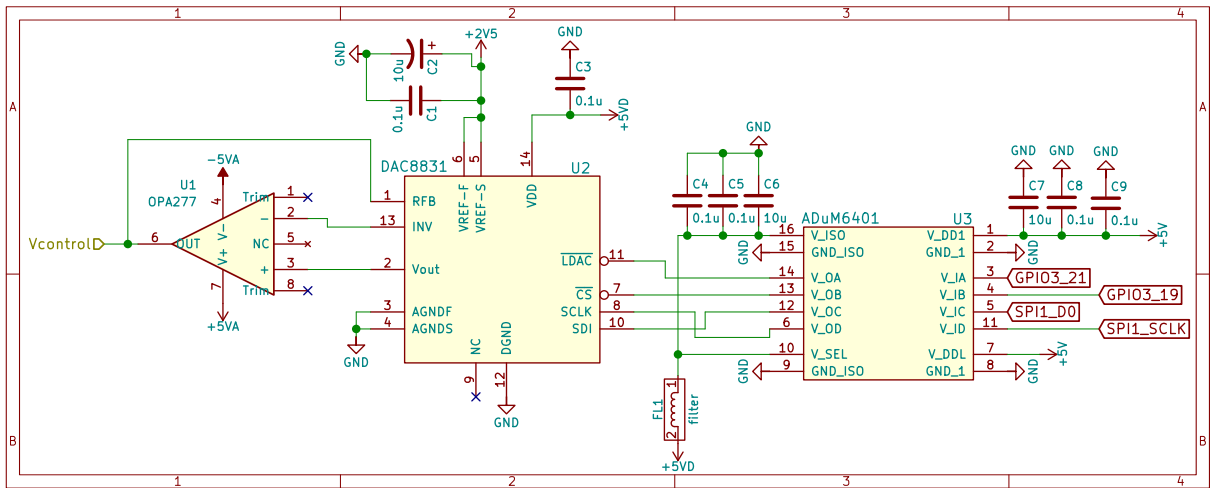
Figure B.2: Schematic of the module used for generating the voltage control signal.
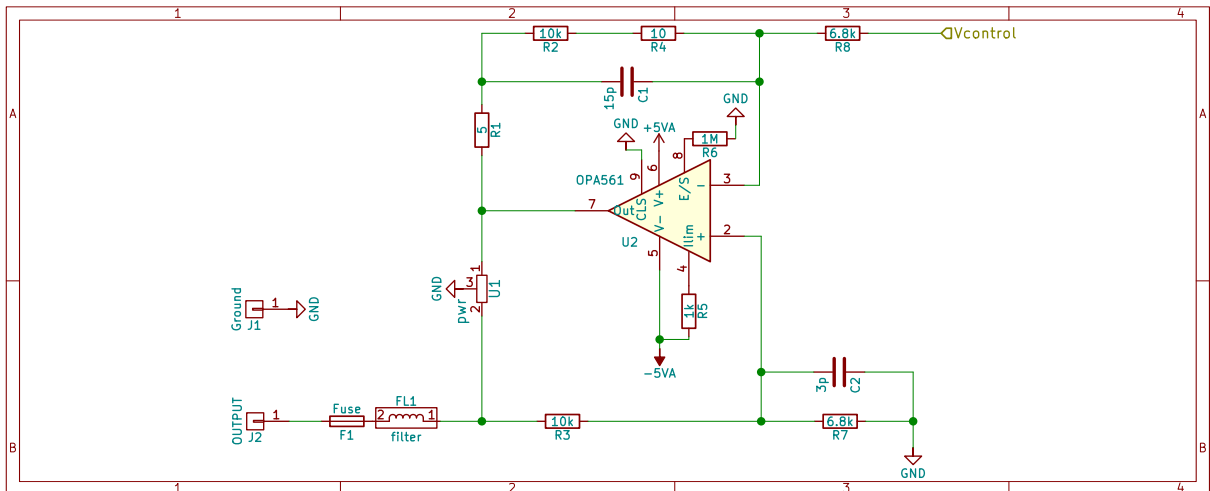
Figure B.3: Schematic of the MHCS.
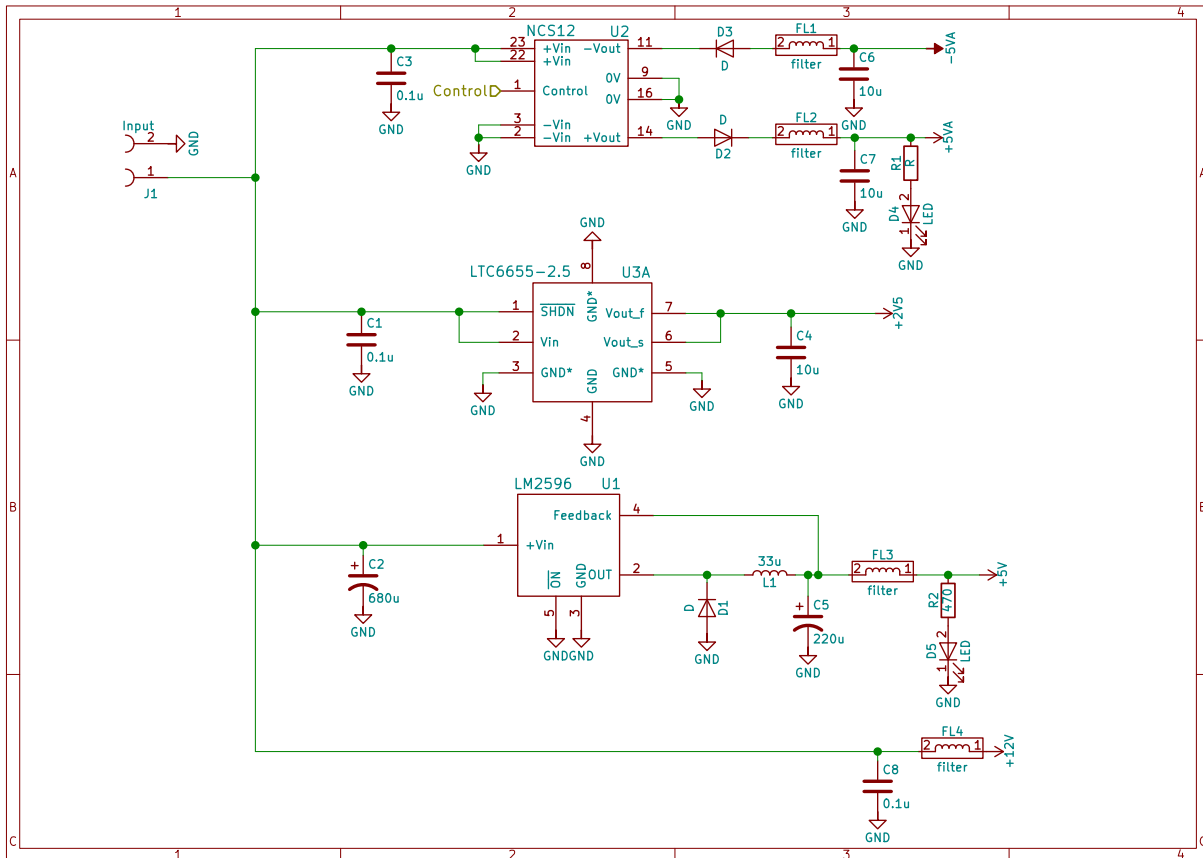
Figure B.4: Schematic of the power supply module.
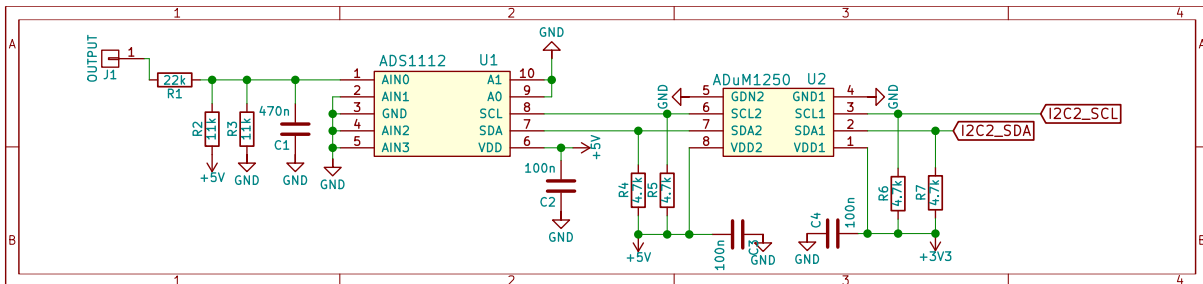
Figure B.5: Schematic of the feedback module module.
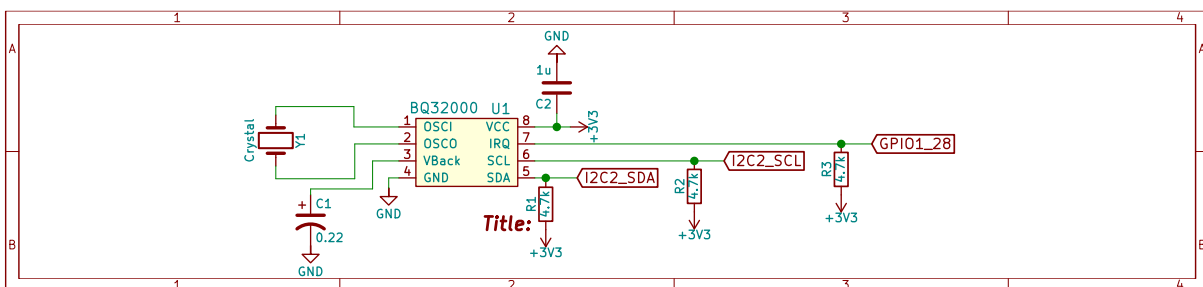
Figure B.6: Schematic of the real-time clock (RTC) module.
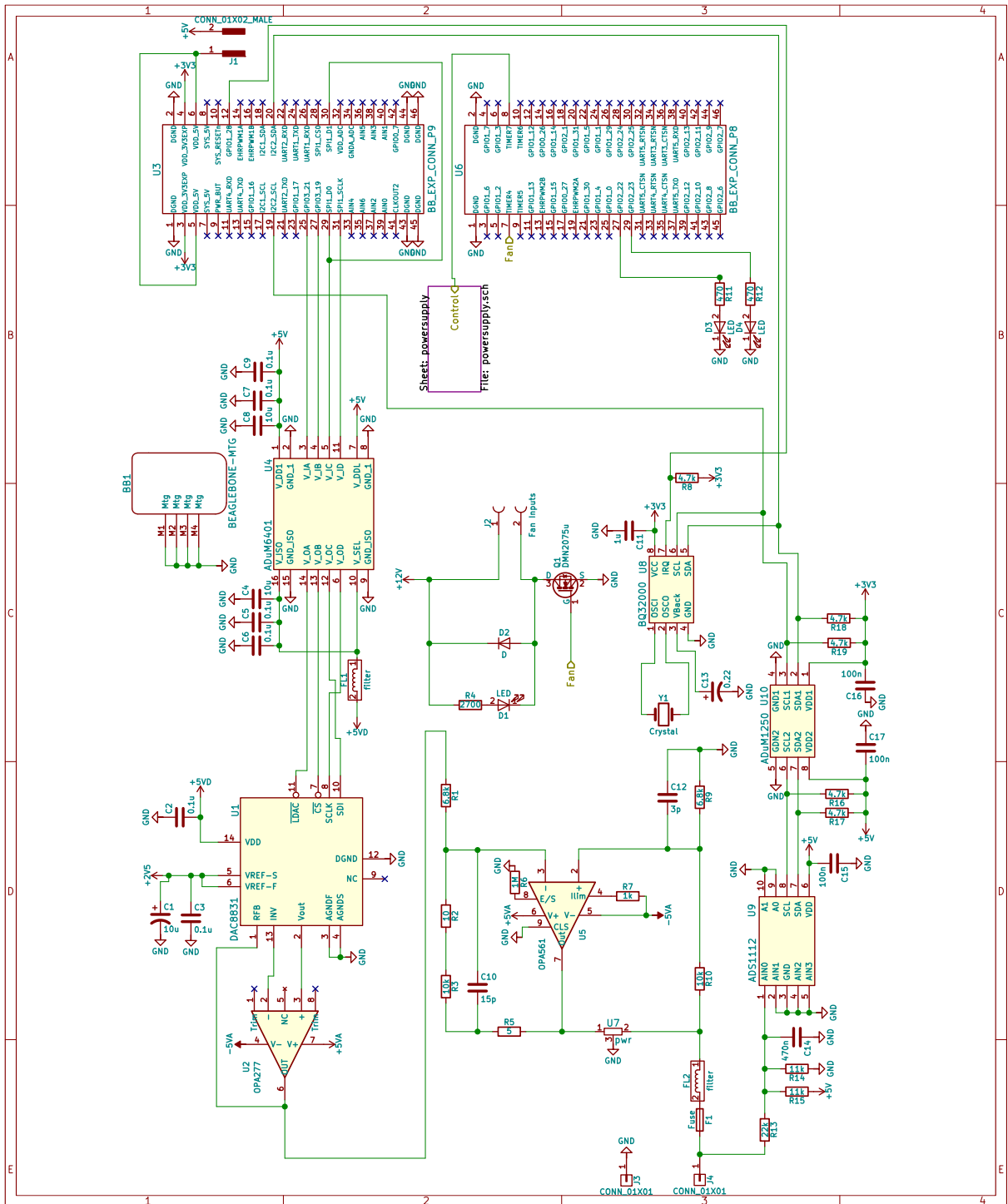
Figure B.7: Full schematic without the power supply module.
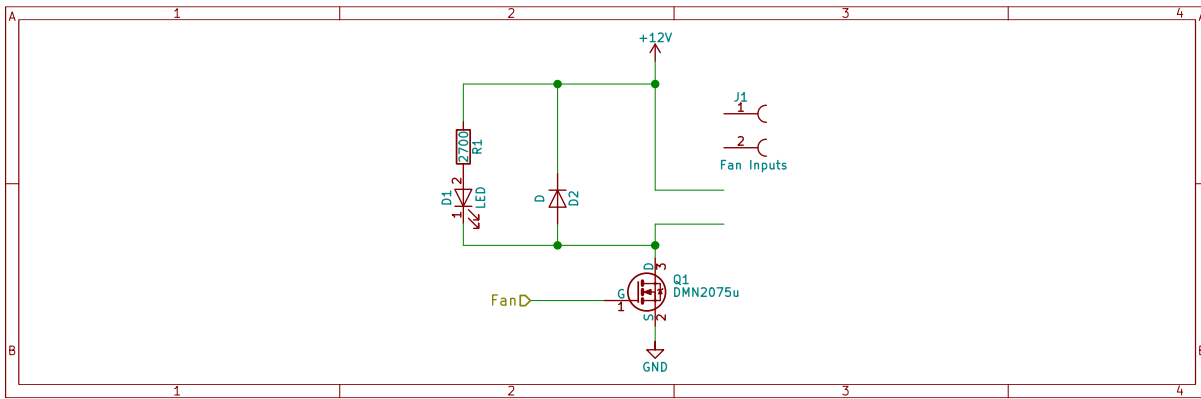
Figure B.8: Schematic of the fan control module.

2.3   Source codes

After connecting the developed current source circuit to the BeagleBone Black (BBB) wireless board, the following steps need to be followed for the BBB software setup:

1. Install the *python-sumbus* package.

2. Install the *Adafruit* library.

3. Install *PySimpleGUI* library.

4. Configure the SPI and I^{2}C pins of the BBB (the configuration shell script included below).

5. Run the current source python file (included below).

BeagleBone board configuration code

The configuration code (in Shell Script) needs to run once after booting the BeagleBone board to configure the SPI and I^{2}C pins :

```
#!/bin/bash
config-pin P9_17 spi_cs
config-pin P9-18 spi
config-pin P9-21 spi
config-pin P9-22 spi_sclk
config-pin P9-28 spi_cs
config-pin P9-29 spi
config-pin P9-30 spi
config-pin P9-31 spi_sclk
config-pin -q P9_17
config-pin -q P9_18
config-pin -q P9_21
```

```
13  config-pin -q P9_22
14  config-pin -q P9_28
15  config-pin -q P9_29
16  config-pin -q P9_30
17  config-pin -q P9_31
18  config-pin P9_19 i2c
19  config-pin P9_20 i2c
20  config-pin -q P9_19
21  config-pin -q p9_20
```

Electroplating power source code

The following python code generate uni-polar waveform:

```
1   import Adafruit_BBIO.GPIO as GPIO #library controlling GPIOs
2   from  Adafruit_BBIO.SPI import SPI #library controlling SPIs
3   import time #BBB time library
4
5   #function for calulating SPI 16bit word for a given current
6   def word(I):
7     Rone = 10000 #Resistors values of the MHCS
8     Rtwo = 6800
9     Rfive= 10
10    Vin = ((I)*Rtwo*Rfive/(Rone+Rfive))/1000 #MHCS transfer function
11    volt_b = int((abs(Vin)*32768/2.5)+32768)
12    if I > 0:
13      volt_b = volt_b ^ 0xffff
14    a = (volt_b >> 8) & 0xff
15    b = volt_b & 0xff
16    return a, b
17
18  #Setup GPIOs
19  GPIO.setup("P8_27",GPIO.OUT) #led
20  GPIO.setup("P8_29",GPIO.OUT) #led
21  GPIO.setup("P8_8",GPIO.OUT)  #power supply
22  GPIO.setup("P8_7",GPIO.OUT)  #fan
23  GPIO.setup("P9_25",GPIO.OUT) #LDAC
24  GPIO.setup("P9_27",GPIO.OUT) #CS
25
26  #Control GPIOs
27  GPIO.output("P8_27",GPIO.LOW) #led off
28  GPIO.output("P8_29",GPIO.LOW) #led off
29  GPIO.output("P8_8",GPIO.LOW)  #power supply off
```

```
30 GPIO.output("P8_7",GPIO.LOW)   #fan off
31 GPIO.output("P9_25",GPIO.LOW) #LDAC is tied low
32 GPIO.output("P9_27",GPIO.HIGH)
33
34 time.sleep(0.05)
35
36 # Send the SPI word from the BBB to the ADC
37 spi = SPI(2,1)
38 a, b = word(0+2.7)
39 GPIO.output("P9_27",GPIO.LOW)
40 print spi.xfer2([a,b])
41 GPIO.output("P9_27",GPIO.HIGH)
42 GPIO.output("P8_8",GPIO.HIGH)
43
44 #A loop for generating a uni-polar waveform with Ip=20mA, TON=200ms
      , and TOFF=100ms.
45 while 1:
46   a, b = word(20)
47   GPIO.output("P9_27",GPIO.LOW)
48   print spi.xfer2([a,b])
49   GPIO.output("P9_27",GPIO.HIGH)
50   time.sleep(0.2)
51   a, b = word(0+2.9)
52   GPIO.output("P9_27",GPIO.LOW)
53   print spi.xfer2([a,b])
54   GPIO.output("P9_27",GPIO.HIGH)
55   time.sleep(0.1)
```

The previous Python code is used for generating any other waveform by replacing the part of the code inside the while loop (from line number 46) with the required waveform. Below is a python code template for explaining how to generate any waveform:

```
1 #This following block with five lines is used to generate a single
     pulse:
2
3 #The following code line is used to take the required current's
     value (I) and convert it to a 16-bit word using the previously
     defined function.
4 #The value of I is in mA and can be positive, negative, or zero.
5     a, b = word(I)
6
7 #The following three code lines are used to transfer the 16-bit
```

```
     word from the BBB to the ADC.
8    GPIO.output("P9_27",GPIO.LOW)
9    print spi.xfer2([a,b])
10   GPIO.output("P9_27",GPIO.HIGH)
11
12 #The final line of the code is used to set the pulse-width by
     inserting T in ms.
13   time.sleep(T)
14
15 #The previous code block is repeated each time the current level
     change within a single waveform cycle.
```

Below are the python codes for the plating waveforms used through the thesis:

Bipolar waveform: $I_C = 20\,\text{mA}$, $I_A = -20\,\text{mA}$, $T_C = 200\,\text{ms}$, and $T_A = 50\,\text{ms}$.

```
1 # Positive pulse
2    a, b = word(20)
3    GPIO.output("P9_27",GPIO.LOW)
4    print spi.xfer2([a,b])
5    GPIO.output("P9_27",GPIO.HIGH)
6    time.sleep(0.2)
7 # Negative pulse
8    a, b = word(-20)
9    GPIO.output("P9_27",GPIO.LOW)
10   print spi.xfer2([a,b])
11   GPIO.output("P9_27",GPIO.HIGH)
12   time.sleep(0.05)
```

Bipolar with off time: $I_C = 20\,\text{mA}$, $I_A = -20\,\text{mA}$, $T_C = 200\,\text{ms}$, $T_A = 50\,\text{ms}$, $T_{\text{Off}} = 10\,\text{ms}$, and $T^{'}_{\text{Off}} = 20\,\text{ms}$.

```
1 #Positive pulse
2    a, b = word(20)
3    GPIO.output("P9_27",GPIO.LOW)
4    print spi.xfer2([a,b])
5    GPIO.output("P9_27",GPIO.HIGH)
6    time.sleep(0.2)
7 #Off
8    a, b = word(0)
9    GPIO.output("P9_27",GPIO.LOW)
10   print spi.xfer2([a,b])
11   GPIO.output("P9_27",GPIO.HIGH)
12   time.sleep(0.01)
```

```python
13  #Negative pulse
14      a, b = word(-20)
15      GPIO.output("P9_27",GPIO.LOW)
16      print spi.xfer2([a,b])
17      GPIO.output("P9_27",GPIO.HIGH)
18      time.sleep(0.05)
19  #Off'
20      a, b = word(0)
21      GPIO.output("P9_27",GPIO.LOW)
22      print spi.xfer2([a,b])
23      GPIO.output("P9_27",GPIO.HIGH)
24      time.sleep(0.02)
13  #Negative pulse
```

C   Appendix to chapter 6

Frequency splitting modeling
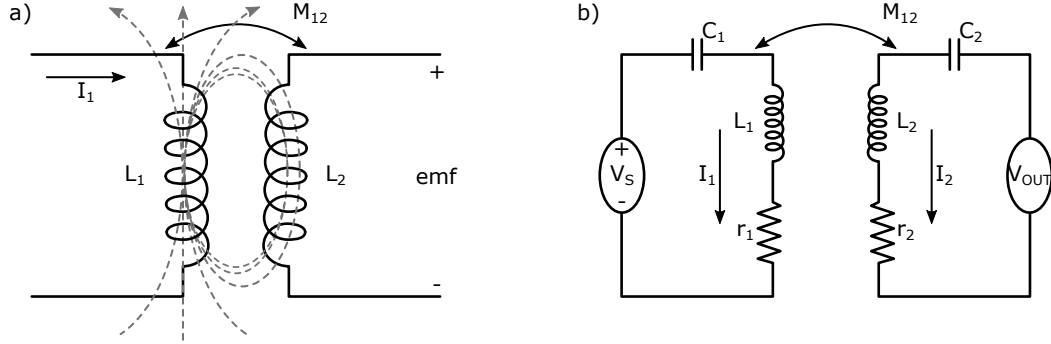
Figure C.1: Equivalent schematic of inductively coupled resonators. **(a)** Magnetic flux linkage between two indicators. **(b)** Equivalent schematic circuit of a pair of inductively coupled resonators.

As a pair of inductors approach each other, the electric current (I) variation in one of the inductors developed a magnetic field around the inductor that induces an electromotive force (emf) in the other inductor, as shown Fig. C.1a. The magnetic coupling linking inductors is described by Faraday's law of induction, where the emf is the variation of the magnetic flux with time. The magnetic flux, in turn, is defined by the magnetic flux density (B) and the enclosed area (A),

$$\text{emf} = \frac{d\phi_B}{dt}, \quad \phi_B = \int_\Sigma B.dA. \tag{C.1}$$

The electric currents flowing in both inductors (I_1 and I_2) contribute to the flux leakage of each inductor (λ_1 and λ_2),

$$\lambda_1 = L_1 I_1 + M_{12} I_2, \tag{C.2a}$$

$$\lambda_2 = L_2 I_2 + M_{12} I_1, \tag{C.2b}$$

where L_1 and L_2 are the self-inductance of each inductor, and M is the mutual induction connecting the two inductors. The magnitude of the magnetic coupling can be expressed by calculating the ratio between the flux linkage of the two inductors at two special cases: 1) in the one case, the first inductor is left open ($I_1 = 0$); and 2) in the other case, the second inductor is left open ($I_2 = 0$). The previous calculation result in a ratio between the mutual inductance and the mean of the self-inductance, which is known as coupling coefficient (K),

$$K = \frac{M_{12}}{\sqrt{L_1 L_2}}. \tag{C.3}$$

An electrical resonator is an inductor connected in parallel to a capacitor, as shown in Fig. C.1b. Practically, the conductive wire forming the inductor has a resistance, thus the total impedance (Z) of a resonator (*RLC*) is,

$$Z = j(\omega L - \frac{1}{\omega C}) + R(\omega). \tag{C.4}$$

The resonance frequency (ω_0) of a resonator is the frequency at which the electrical inductance and capacitance compensate each other. At the resonance frequency, the energy on the resonator oscillates between its two forms; electrical and magnetic. From Equation C.4, the resonator's resonance frequency can be derived:

$$\omega_0 = \frac{1}{\sqrt{LC}}. \tag{C.5}$$

Equation C.2 reveals that mutual inductance, as for self-inductance, relates magnetic flux and electric current. Hence, mutual inductance contributes to the resonator's impedance and consequently influences its resonance frequency. According to Kirchhoff's law, the loop equations of a pair of coupled resonators equivalent to zero [238]:

$$Z_1 I_1 + j\omega M_{12} I_2 = 0, \tag{C.6a}$$

$$Z_2 I_2 + j\omega M_{12} I_1 = 0. \tag{C.6b}$$

Solving these two loop equations together results in two resonance frequencies (ω_1 and ω_2). This means that magnetic coupling between a pair of resonator introduces an additional degree-of-freedom (current path), as shown:

$$\omega_{1,2}^2 = (\omega_{01}^2 + \omega_{02}^2)\frac{-1 \pm \sqrt{1 - \frac{4(1-K^2)}{(\omega_{01}/\omega_{02})^2 + (\omega_{02}/\omega_{01})^2 + 2}}}{2(1-K^2)}. \tag{C.7}$$

This Equation shows the two resulting resonance frequencies ($\omega_{1,2}$) from the magnetic coupling depends on the individual resonators' initial resonance frequencies(ω_{01} and ω_{02}). In case both of the inductively coupled resonators are tuned to the same resonance frequency ($\omega_{01} = \omega_{02} = \omega_0$), a splitting of this initial resonance frequency occurs, resulting in two resonance frequencies shifted to the right and left of the initial value:

$$\omega_{1,2} = \frac{\omega_0}{\sqrt{1 \pm K}}. \tag{C.8}$$

Applying a potential difference to one of the two coupled resonators (V_S) induces an output voltage in the other resonator (V_{OUT}), as shown in Fig. C.1b. By solving the two loop equations in (C.6), we obtain:

$$V_{\text{Out}} = V_S \frac{Z_2 j\omega M_{12}}{Z_1 Z_2 + (j\omega M_{12})^2}. \tag{C.9}$$
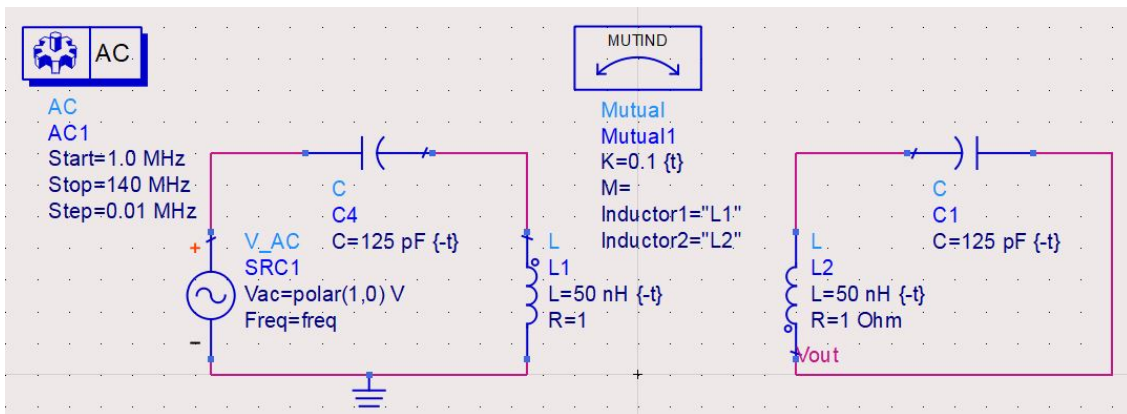
Figure C.2: ADS simulation environment of inductively coupled resonators.

Sniffer coil

A *sniffer coil* is a probe coil used for the experimental characterization of the resonators, e.g., determining the resonance frequency of the resonators [183, 239]. Sniffer coil is made of a $50\,\Omega$ semi-rigid coaxial cable with a particular configuration as a loop antenna. The main advantage of the sniffer coil is that it is sensible only to magnetic fields and suppresses the effect of electric fields on the inner conductor of the cable. The sniffer coil is constructed by stripping off the heat shrink tubing and insulation materials of one end of the coaxial cable, connecting the ground and signal wires to an SMA connector. At the other end, the ground wire, heat shrink tubing, and the insulation materials are stripped off. Consequently, the signal wire is rounded in the form of a small loop and soldered to the ground to achieve a short circuit, as shown in Fig.5a. Based on Faraday's law, if a magnetic field passes through a coil loop, a voltage is induced proportional to the magnetic flux's rate of change,

$$\varepsilon = -N\frac{\Delta\varphi}{\Delta t}, \tag{C.10}$$

where ε is the induce voltage, N is the number of turns, and $\Delta\varphi/\Delta t$ is the rate of change of the magnetic flux. A resonator's resonance frequency can be determined by placing the sniffer coil in its vicinity and measuring the reflection coefficient (S_{11}) of the sniffer coil over a wide range of frequencies. The whole signal going through the sniffer coil will be reflected except for the resonator's resonance frequency, as the magnetic field generated by the sniffer coil at this frequency will be converted into an induced voltage in the resonator. Hence, a dip in the sniffer coil S_{11} curve will be observed at the resonator's resonance frequency as it absorbed the sniffer coil magnetic field, as illustrated in Fig.5b.
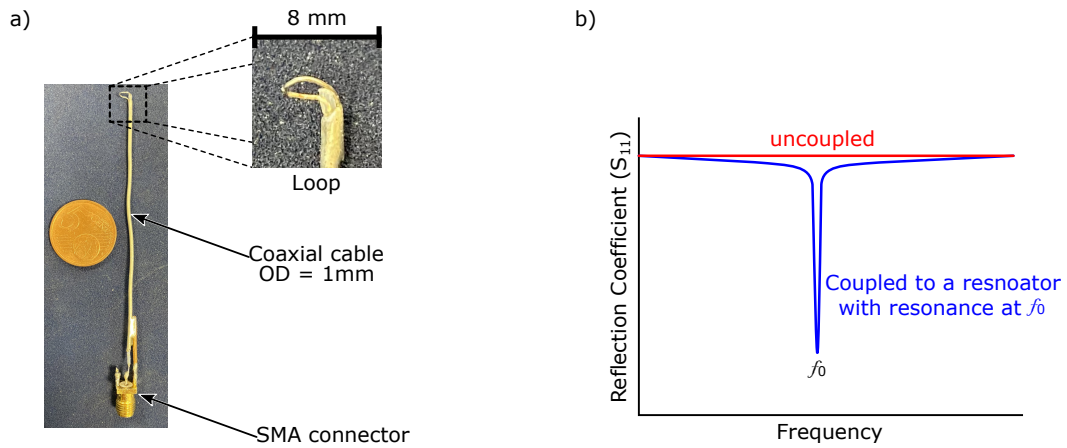
Figure C.3: **(a)** Photo of a sniffer coil. **(b)** Expected reflection coefficient (S_{11}) of a sniffer coil.

D Appendix to chapter 8

4.1 Technical working drawing
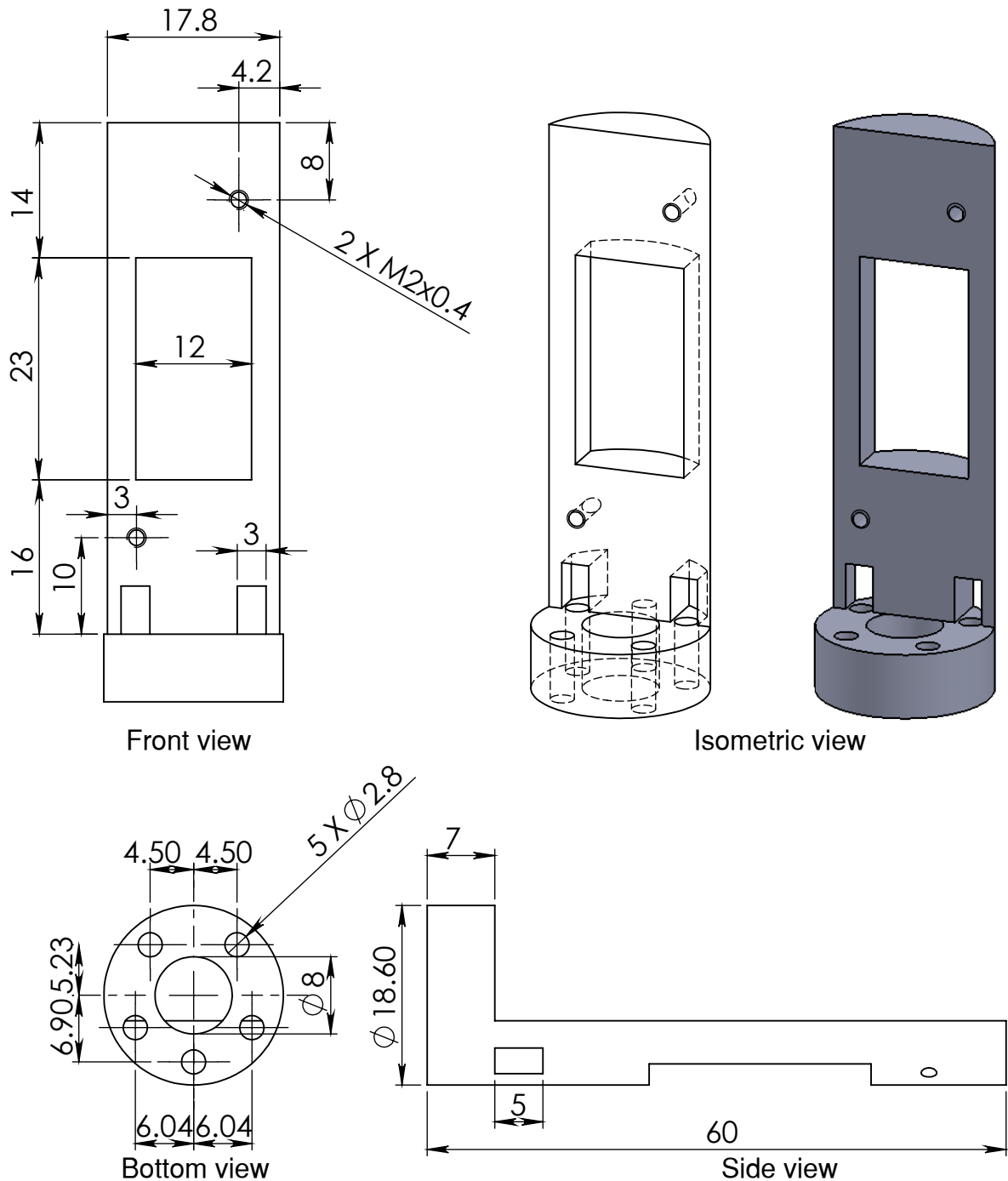
Figure D.1: Technical working drawing of the 3D printed probe head holder. The insert was printed using an Ultimaker 2$^+$ printer out of polylactic acid (PLA). All dimensions are in mm, and the figure scale is 1.5:1.
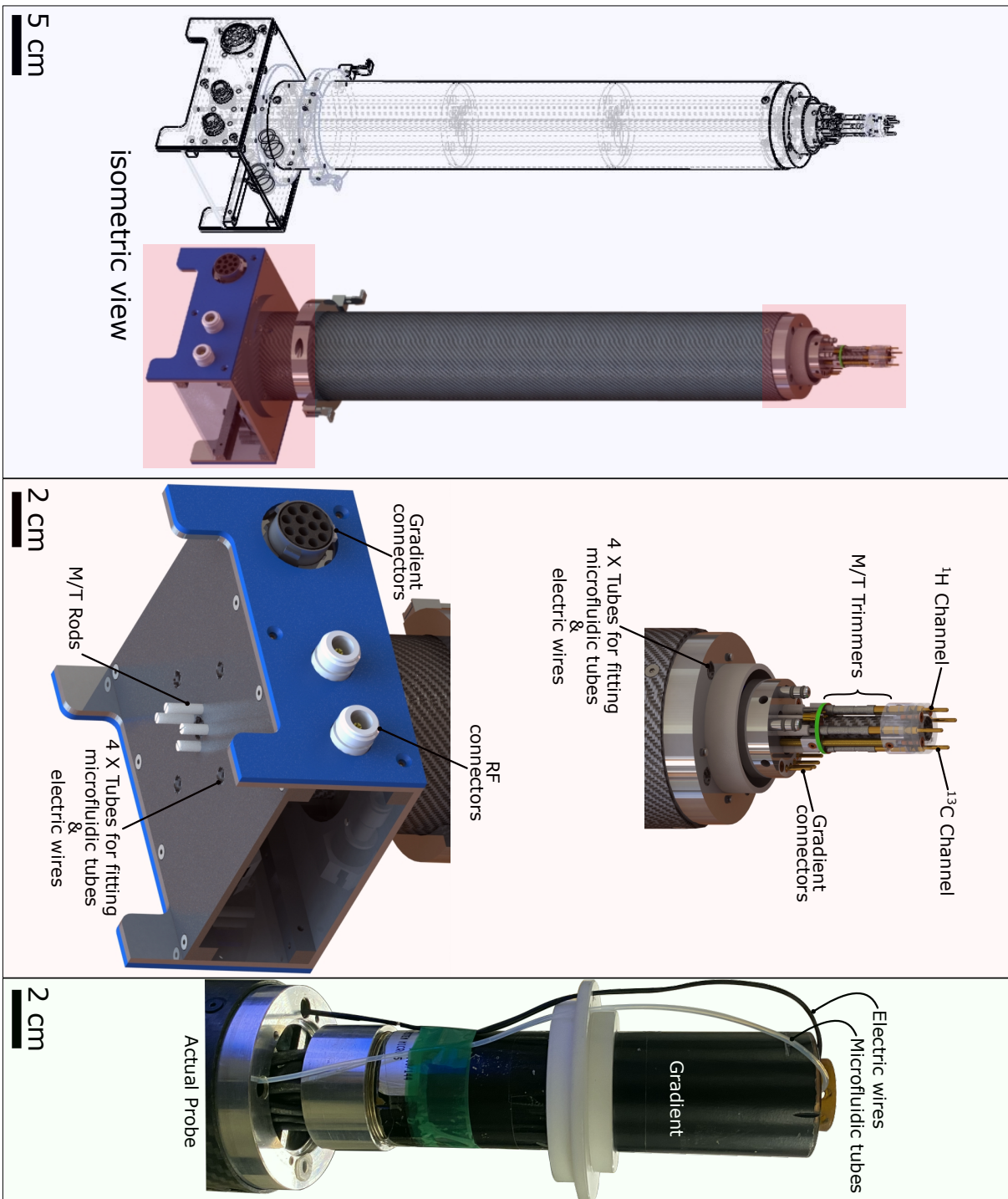
Figure D.2: NMR probe compatible with flow-based spectroscopy. The probe was designed and built by *Erwin Fuhrer*.

4.2   Source codes

NMR acquisition software pulse program

The pulse program was written for software: TopSpin 3.5pl2, Bruker BioSpin.

```
1  #include <Avance.incl>
2  "d11=1m"                  ;Delay for writing to disc
3  "l2 = 1"
4  ze                        ;Reset the scan counter
5  1 d1
6  2 p1 ph1
7    0.1m
8    if trigpl2
9    {
10     if "l2 != 1"
11     {
12       goto 3              ;l2 is greater than 1
13     }
14     else
15     {
16       0.2u iu2            ;l2 is less than 1
17       go=1 ph31
18     }
19   }
20   else
21   {
22     0.2u iu2              ;Trigger is not on
23     go=1 ph31
24   }
25 3 d11 wr #0 if #0    ;FID is written
26   0.1u ru2
27   lo to 1 times td1
28 exit
29 ph1=0 2 2 0 1 3 3 1
30 ph31=0 2 2 0 1 3 3 1
```

Micro-controller unite source code

The MCU source code was written for Arduino Uno board using Arduino IDE software.

```
1  #include <Wire.h>   //I2C library
2
3  ////Define Variables////
4  int flag_1 = 0;//flag
5  int flag_2 = 0;//flag
6  unsigned long t;//hold current time
7  unsigned long tt;//hold current time
8  unsigned long d = 0;//Delay before TTL signal
9  unsigned long sensor_1_th = 3500000;//1st IDC sensor threshold
10 unsigned long sensor_2_th = 5000000;//2nd IDC sensor threshold
11 int TTL_width = 500;//The TTL pulse width in ms
12 int button_state = 0 ;//hold the manual triggering pushbutton state
13 byte shift = 88;//Variable to shift the capacitance input range
14 int TTL = 2;//Trigger signal Digital PIN
15 int TTL_LED = 3;//Trigger signal LED state Digital PIN
16 int Sample_LED_1 = 6;//Sample LED state 1 Digital PIN
17 int Sample_LED_2 = 7;//Sample LED state 2 Digital PIN
18 float sensor_1_value;//hold 1st IDC sensor value
19 float sensor_2_value;//hold 2nd IDC sensor value
20
21 ////AD7746 registers' addresses////
22 #define RGTR_Status 0x00
23 #define RGTR_Cap_Data 0x01
24 #define RGTR_Cap_Setup 0x07
25 #define RGTR_Exc_Setup 0x09
26 #define RGTR_Configuration  0x0A
27 #define RGTR_Cap_DAC_A 0x0B
28 #define RGTR_Cap_Offset 0x0D
29 #define I2C_ID  0x48
30 #define Reset_ID 0xBF
31 #define Manual_TTL A0//Pushbutton for manual triggering
32
33 ////Set the IC (AD7746) settings////
34 void setup()
35 {
36   Wire.begin();//Start I2C connection
37   Serial.begin(9600);//Serial communication's baud rate
38   pinMode(TTL,OUTPUT);//Set TTL pin as an output
39   pinMode(TTL_LED,OUTPUT);//Set TTL LED state pin as an output
```

```
40   pinMode(Sample_LED_1,OUTPUT);//Sample LED state 1 pin as an
      output
41   pinMode(Sample_LED_2,OUTPUT);//Sample LED state 2 pin as an
      output
42   digitalWrite(TTL,LOW);//Start with TTL switched off
43   digitalWrite(TTL_LED,LOW);//Start with TTL LED switched off
44   digitalWrite(Sample_LED_1,LOW);//Start with sample LED 1 switched
      off
45   digitalWrite(Sample_LED_2,LOW);//Start with sample LED 2 switched
      off
46   Wire.beginTransmission(I2C_ID);//start I2C communication channel
47   Wire.write(Reset_ID);//Reset the IC (Ad7756) settings
48   Wire.endTransmission();//Terminate I2C communication channel
49   delay(50);//Delay 50 ms
50   updatergtr(RGTR_Exc_Setup,_BV(5)|_BV(3)|_BV(1)|_BV(0));//Enable
      EXC_A and EXC_B with a voltage level of Vdd
51   updatergtr(RGTR_Cap_Setup,_BV(7));// Enable capacitive channel
52   updatergtr(RGTR_Configuration ,_BV(7)|_BV(6)|_BV(5)|_BV(4)|_BV(3)
      |_BV(0));//Set Conversion times and mode
53   shift &=0x7f;//AND with 1111111 to make sure shift is 7bit
54   updatergtr(RGTR_Cap_DAC_A,_BV(7)|shift);//shift the capacitance
      input range
55 }
56
57 ////Main program////
58 void loop()
59 {
60 button_state = analogRead(Manual_TTL);// Read the manual triggering
      push button's state
61 if (button_state > 0)//In case the pushbutton is pressed, send a
      TTL signal
62    {digitalWrite(TTL,HIGH);
63     digitalWrite(TTL_LED,HIGH);
64     delay(TTL_width);
65     digitalWrite(TTL,LOW);
66     digitalWrite(TTL_LED,LOW);}
67
68 updatergtr(RGTR_Cap_Setup, 0b10000000);//Switch to the first
      capacitive input
69 sensor_1_value = readcap();//Get the value of the first sensor
70 while(sensor_1_value > sensor_1_th)
```

```
71      {t = millis();
72       if (flag_1==0)
73          {delay(d);
74           digitalWrite(TTL,HIGH);
75           digitalWrite(TTL_LED,HIGH);
76           delay(TTL_width);
77           digitalWrite(TTL,LOW);
78           digitalWrite(TTL_LED,LOW);
79           digitalWrite(Sample_LED_1,HIGH);
80           flag_1 = 1;}
81      updatergtr(RGTR_Cap_Setup,0b11000000);//Switch to the second
    capacitive input
82      sensor_2_value = readcap();//Get the value of the first
    sensor
83      updatergtr(RGTR_Cap_Setup, 0b10000000);//Switch to the first
    capacitive input
84      sensor_1_value = readcap();//Get the value of the first
    sensor
85      while (sensor_2_value > sensor_2_th)
86           {tt = millis();
87            d = (tt-t)/3;
88            digitalWrite(Sample_LED_2,HIGH);
89            updatergtr(RGTR_Cap_Setup, 0b10000000);//Switch to the
     first capacitive input
90            sensor_1_value = readcap();//Get the value of the
    first sensor
91            updatergtr(RGTR_Cap_Setup,0b11000000);//Switch to the
    second capacitive input
92            sensor_2_value = readcap();//Get the value of the
    first sensor
93            if (sensor_1_value < sensor_1_th && flag_2==0)
94              {delay(d);
95               digitalWrite(TTL,HIGH);
96               digitalWrite(TTL_LED,HIGH);
97               delay(TTL_width);
98               digitalWrite(TTL,LOW);
99               digitalWrite(TTL_LED,LOW);
100              digitalWrite(Sample_LED_1,LOW);
101              flag_2 = 1;}
102           }
103     digitalWrite(Sample_LED_1,LOW);
```

```
104        flag_1 = 0;
105        flag_2 = 0;}
106 updatergtr(RGTR_Cap_Setup,0b11000000);//Switch to the second
        capacitive input
107 sensor_2_value = readcap();//Get the value of the first sensor
108 while(sensor_2_value > sensor_2_th)
109      {t = millis();
110       if (flag_1==0)
111         {delay(d);
112          digitalWrite(TTL,HIGH);
113          digitalWrite(TTL_LED,HIGH);
114          delay(TTL_width);
115          digitalWrite(TTL,LOW);
116          digitalWrite(TTL_LED,LOW);
117          digitalWrite(Sample_LED_1,HIGH);
118          flag_1 = 1;}
119       updatergtr(RGTR_Cap_Setup, 0b10000000);//Switch to the first
    capacitive input
120       sensor_1_value = readcap();//Get the value of the first
    sensor
121       updatergtr(RGTR_Cap_Setup,0b11000000);//Switch to the second
    capacitive input
122       sensor_2_value = readcap();//Get the value of the first
    sensor
123       while (sensor_1_value > sensor_1_th)
124            {tt = millis();
125             d = (tt-t)/3;
126             digitalWrite(Sample_LED_2,HIGH);
127             updatergtr(RGTR_Cap_Setup,0b11000000);//Switch to the
    second capacitive input
128             sensor_2_value = readcap();//Get the value of the
    first sensor
129             updatergtr(RGTR_Cap_Setup, 0b10000000);//Switch to the
     first capacitive input
130             sensor_1_value = readcap();//Get the value of the
    first sensor
131               if (sensor_2_value < sensor_2_th && flag_2==0)
132                 {delay(d);
133                  digitalWrite(TTL,HIGH);
134                  digitalWrite(TTL_LED,HIGH);
135                  delay(TTL_width);
```

```
136                       digitalWrite(TTL,LOW);
137                       digitalWrite(TTL_LED,LOW);
138                       digitalWrite(Sample_LED_1,LOW);
139                       flag_2 = 1;}
140                }
141        digitalWrite(Sample_LED_1,LOW);
142        flag_1 = 0;
143        flag_2 = 0;}
144 }
145 ////End main program////
146
147 long readcap()//Function to read the input capacitance
148 { long capreturn = 0;
149   uint8_t data[3];
150   char status = 0;
151   while (!(status & (_BV(0) | _BV(2))))//wait for conversion
152   {status= readrgtr(RGTR_Status);}
153   unsigned long value =  readLong(RGTR_Cap_Data);
154   value >>=8;
155   capreturn = value;
156   return capreturn;}
157
158 void updatergtr(unsigned char m, unsigned char n)//Function to
       write data to a register in AD7746
159 { Wire.beginTransmission(I2C_ID);
160   Wire.write(m);
161   Wire.write(n);
162   Wire.endTransmission();}
163
164 unsigned char readrgtr(unsigned char m)//Function to read data from
       a register in AD7746
165 { unsigned char n;//Variable to hold the received data
166   Wire.beginTransmission(I2C_ID);
167   Wire.write(m);//Address of the register to read
168   Wire.endTransmission();
169   Wire.requestFrom(I2C_ID, 1);
170   while(Wire.available()==0) {}//Wait till data is received
171   n = Wire.read();
172   return n;}
173
174 unsigned long readLong(unsigned char r)
```

```
175 {  union {
176     char data[4];
177     unsigned long value;
178         }
179   byteMappedLong;
180   byteMappedLong.value = 0L;
181   Wire.beginTransmission(I2C_ID);//begin read cycle
182   Wire.write(0);//pointer to first data register
183   Wire.endTransmission();//end cycle
184   //the data pointer is reset anyway - so read from 0 on
185   Wire.requestFrom(I2C_ID,r+4);//reads 2 bytes plus all bytes
       before the register
186   while (!Wire.available()==r+4) {
187       ; //wait
188     }
189   for (int i=r+3; i>=0; i--) {
190     uint8_t c = Wire.read();
191     if (i<4) {
192       byteMappedLong.data[i]= c;
193     }
194   }
195   return byteMappedLong.value;}
```

4.3   Automatic loading system GUI

The MCU controls the robot arm and the syringe pump for loading the microfluidic tube with the sample plugs. The user fills a 96 well plate with the target samples and immiscible fluid required to be loaded into the microfluidic tube. The user sets the filling sequence of the experiment via the excel workbook file (below). Three columns are available in the "Sample Sequence" sheet of the worksheet. The first column contains well plate locations and is limited by selecting 96 possible well coordinates for the 96 well plate, the order of the entered well coordinates define the loading order. The second column corresponds to the name of the sample, the user is free to enter any descriptive name. The third column is used for specifying the sample volume in μL, positive values for loading the plug into the tube, and negative values to push the sample out of the tube. Once the experiment parameters are entered, the user presses the button "Program Experiment". The button will launch a back-end accompanying python script that transfers the values entered by the user to the MUC, which in turn controls the robot arm's motion with synchronizing the pump activity to complete the required filling sequence.
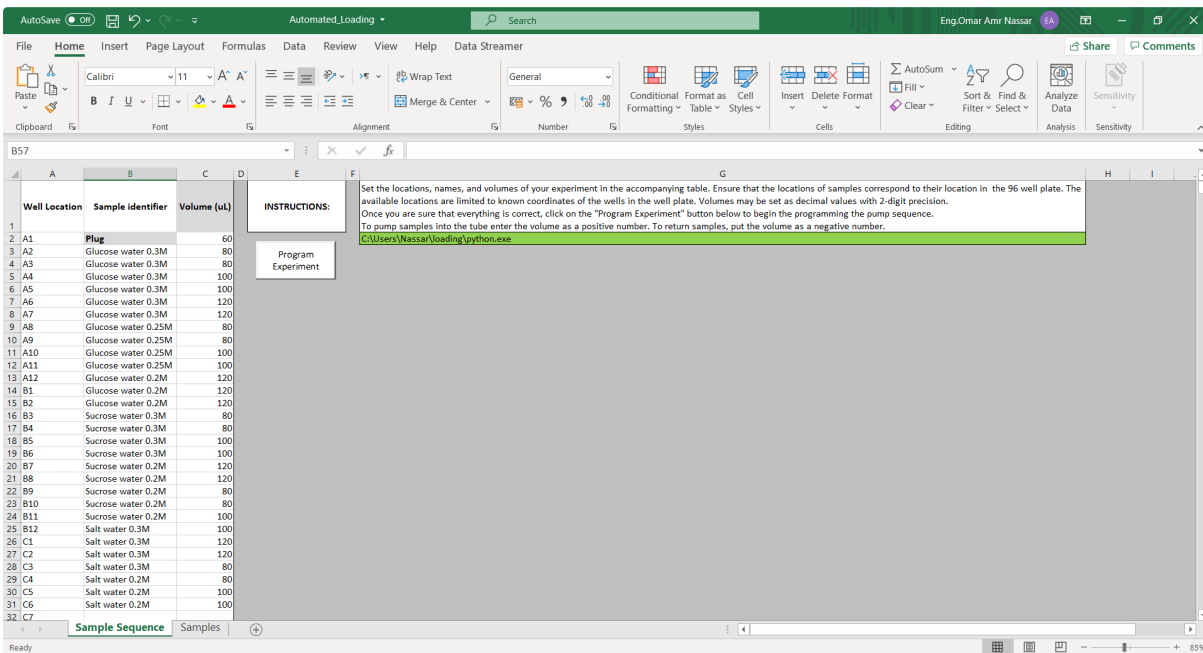
Figure D.3: GUI of the automatic sample loading system.

4.4   Electronic schematics
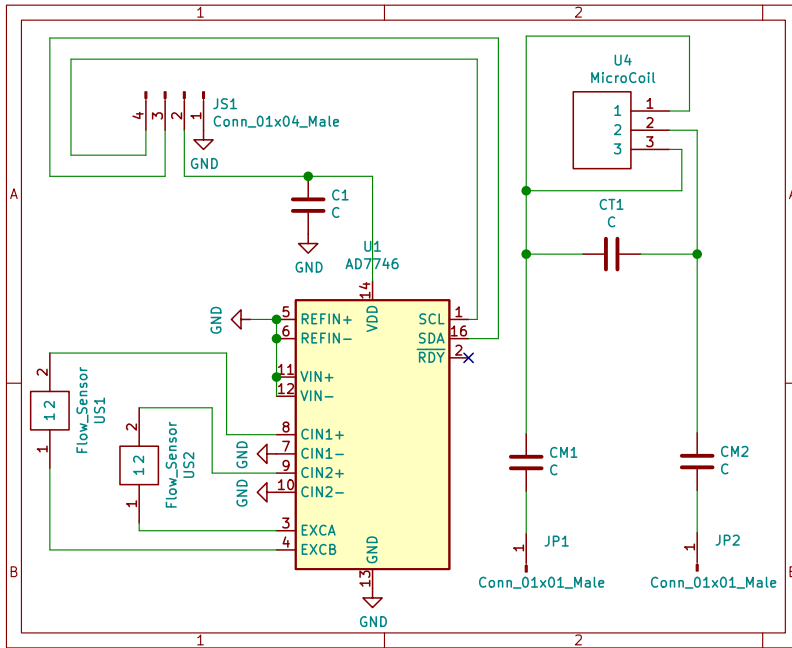
Figure D.4: Probe head PCB using CDC chip.
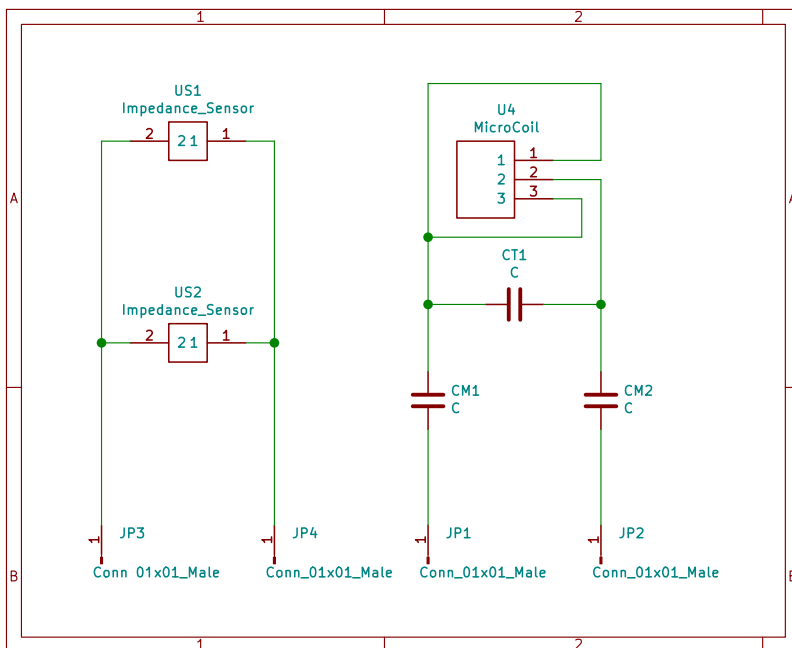
Figure D.5: Probe head PCB without CDC footprint to be used with Lock-in amplifier.
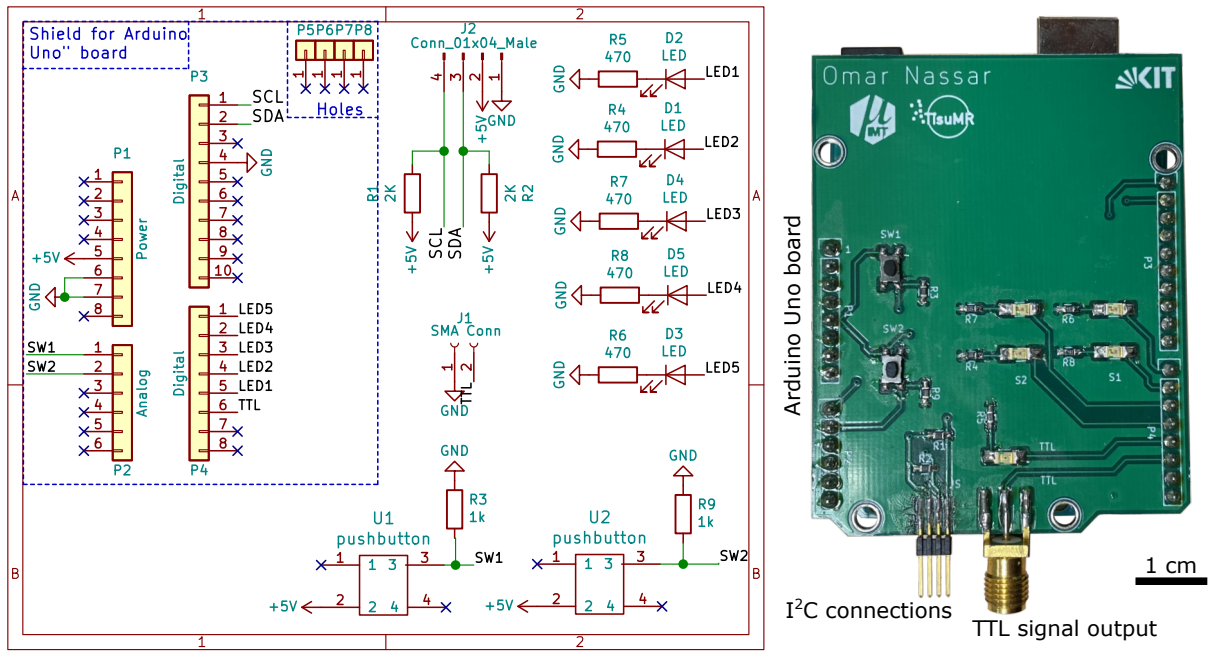
Figure D.6: Arduino Uno NMR shield.
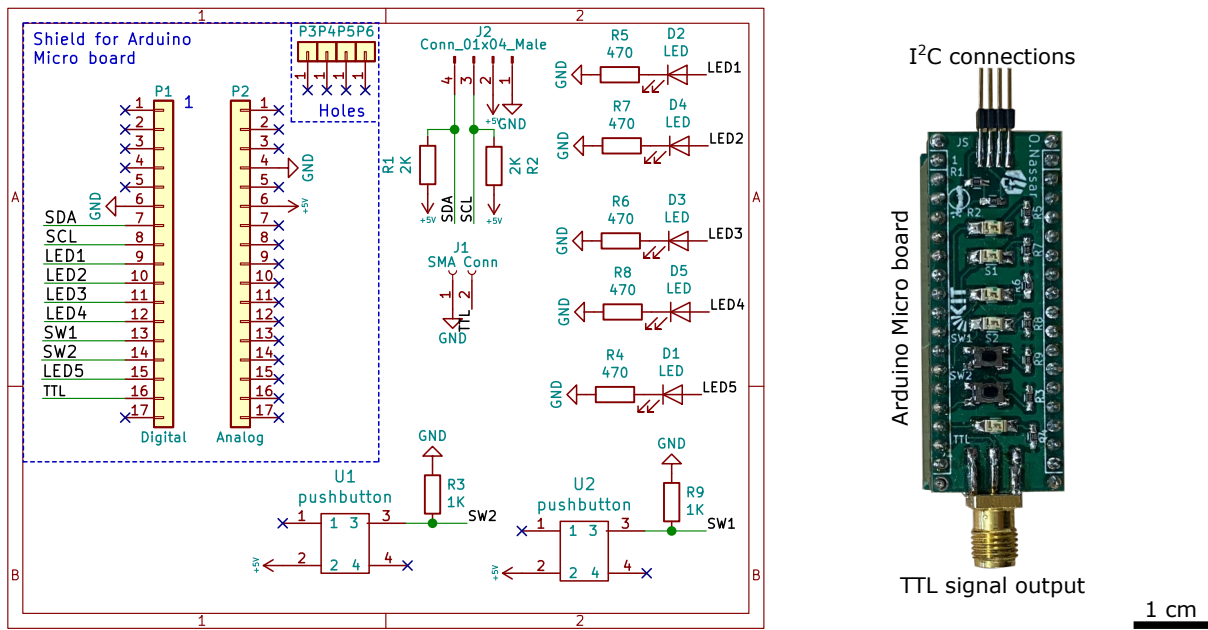
Figure D.7: Arduino Micro NMR shield

Microfabrication results (full)
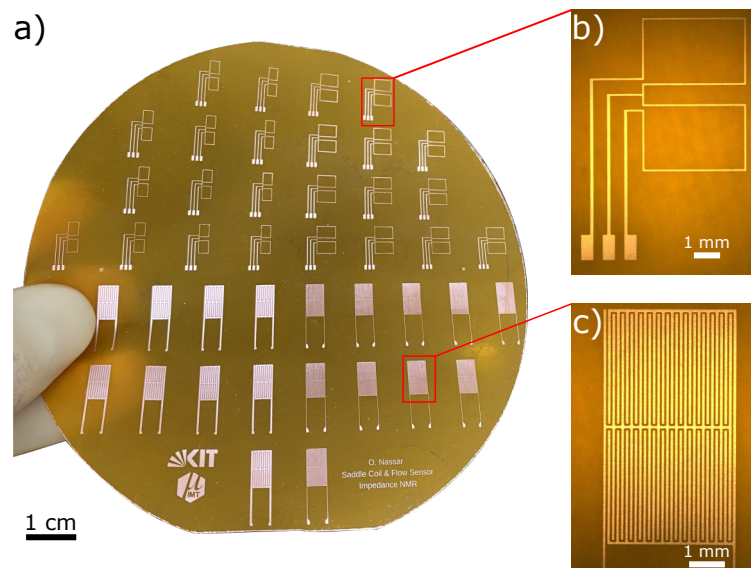
Figure D.8: Representative microfabrication results of the flow NMR detector and sensors. **(a)** A photographic image of a fully patterned Kapton foil in the shape of a 100 mm wafer. The foil contains a batch of the micro-saddle NMR coil and the IDC flow sensor, demonstrating the developed process's compatibility with mass production. The sub-figures illustrate focused microscopic images of the 2D patterned **(b)** Micro-saddle coil and **(c)** IDC sensor.

List of Figures

List of Tables

Publications

Journal articles

[ON1] O. Nassar, M. V. Meissner, S. Wadhwa, J. G. Korvink, and D. Mager, "Load sensitive stable current source for complex precision pulsed electroplating," *Review of Scientific Instruments*, vol. 90, no. 10, p. 104704, 2019. DOI: 10.1063/1.5113790

[ON2] E. R. Mamleyev, F. Falk, P. G. Weidler, S. Heissler, S. Wadhwa, O. Nassar, C. N. S. Kumar, C. Kübel, C. Wöll, M. Islam, D. Mager, and J. G. Korvink, "Polyaramid-Based Flexible Antibacterial Coatings Fabricated Using Laser-Induced Carbonization and Copper Electroplating," *ACS Applied Materials & Interfaces*, vol. 12, no. 47, pp. 53193–53205, 2020. DOI: 10.1021/acsami.0c13058

[ON3] O. Nassar, D. Mager, and J. G. Korvink, "Wireless Double Micro-Resonator for Orientation Free Tracking of MR-Catheter During Interventional MRI," *IEEE Journal of Electromagnetics, RF and Microwaves in Medicine and Biology*, vol. 5, no. 1, pp. 78–83, 2020. DOI: 10.1109/JERM.2020.3010093

[ON4] S. Wadhwa, M. Jouda, Y. Deng, O. Nassar, D. Mager, and J. G. Korvink, "Topologically optimized magnetic lens for magnetic resonance applications," *Magnetic Resonance*, vol. 1, no. 2, pp. 225–236, 2020. DOI: 10.5194/mr-1-225-2020

[ON5] O. Nassar, M. Jouda, M. Rapp, D. Mager, J. G. Korvink, and N. MacKinnon, "Integrated impedance sensing of liquid sample plug flow enables automated high throughput NMR spectroscopy," *Microsystems & Nanoengineering*, vol. 7, no. 1, pp. 1–17, 2021. DOI: 10.1038/s41378-021-00253-2

Proceedings

[ON6] O. Nassar, D. Mager, and J. G. Korvink, "A Novel Sensor Design and Fabrication for Wireless Interventional MRI Through Induction Coupling," in *2019 IEEE SENSORS*, pp. 1-4, IEEE, 2019.

[ON7] O. Nassar, M. Jouda, J. G. Korvink, D. Mager, and N. MacKinnon, "Integrated Impedance Sensors in a Microfluidic System: Toward a Fully Automated High Throughput NMR Spectroscopy," in *24th International Conference on Miniaturized Systems for Chemistry and Life Sciences (MicroTAS)*, 2020.

Conference contributions

[ON8] O. Nassar, M. Jouda, N. Wang, M. Rapp, J. G. Korvink, D. Mager, and N. MacKinnon, "Synchronizing MR measurements on fluidic plugs using integrated impedance spectroscopy," *European Magnetic Resonance Meeting (EUROMAR)*, (Nantes, France), 2018, (Poster).

[ON9] O. Nassar, D. Mager, and J. G. Korvink, "Fast Prototyping of interventional Magnetic Resonance Imaging (iMRI) Resonators using Inkjet Printing," *Kyoto Winter School 2019*, (Kyoto, Japan), 2019, (Talk and Poster).

[ON10] O. Nassar, M. Jouda, N. Wang, M. Rapp, J. G. Korvink, D. Mager, and N. MacKinnon, "Integrated Impedance Spectroscopy for Automated High Throughput MR Measurements on Fluidic Plugs," *60th Experimental Nuclear Magnetic Resonance Conference (ENC)*, (Pacific Grove, CA, USA), 2019, (Talk).

[ON11] O. Nassar, M. Jouda, N. Wang, M. Rapp, J. G. Korvink, D. Mager, and N. MacKinnon, "Synchronizing MR measurements on fluidic plugs using integrated impedance spectroscopy," *BioInterfaces International Graduate School Retreat 2019*, (Trier, Germany), 2019, (Poster).

[ON12] O. Nassar, D. Mager, and J. G. Korvink, "Double micro-resonators for orientation-free MR-catheter tracking during interventional MRI, enabled by inductive coupling," *ISMAR EUROMAR Joint Conference 2019*, (Berlin, Germany), 2019, (Poster).

[ON13] E. R. Mamleyev, O. Nassar, S. Wadhwa, D. Mager, M. Islam, and J. G. Korvink, "Laser-induced carbonization of polyaramid substrate towards fabrication of fire-resistant flexible electrical circuits," *30th International Conference on Diamond and Carbon Materials*, (sevilla, Spain), 2019, (Poster).

[ON14] O. Nassar, D. Mager, and J. G. Korvink, "A Novel Sensor Design and Fabrication for Wireless Interventional MRI Through Induction Coupling," *IEEE SENSORS 2019*, (Montreal, Canada), 2019, (Talk).

[ON15] B. Meng, S. L. Grage, M. Takamiya, V. Middel, N. MacKinnon, O. Nassar, T. Schober, I. Hutskalov, O. Babii, U. Straehle, J. G. Korvink, and A. S. Ulrich, "Correlative in vivo Fluorescence Imaging and ^{19}F-MRI of Zebrafish Embryos," *64th Annual Meeting of the Biophysical Society*, (San Diego, CA, USA) 2020, (Talk).

[ON16] O. Nassar, D. Mager, and J. G. Korvink, "Orientation free tracking of MR-Catheters during interventional MRI, wirelessly through induction coupling," *61st Experimental Nuclear Magnetic Resonance Conference (ENC)*, (Baltimore, MD, USA), 2020, (Poster).

[ON17] O. Nassar, M. Jouda, J. G. Korvink, D. Mager, and N. MacKinnon, "Integrated Impedance Sensors in a Microfluidic System: Toward a Fully Automated High Throughput NMR Spectroscopy," *24th International Conference on Miniaturized Systems for Chemistry and Life Sciences (MicroTAS)*, (virtual), 2020, (Poster).

[ON18] O. Nassar, M. Jouda, D. Mager, J. G. Korvink, and N. MacKinnon, "Automated high throughput NMR spectroscopy," *BioInterfaces International Graduate School Retreat 2021*, (Karlsruhe, Germany), 2021, (Talk).

Acknowledgement

I would like to express my sincere gratitude to my supervisor Prof. Dr. Jan Korvink for giving me the opportunity to conduct my PhD degree in his group. Working under your supervision taught me a lot, not only on the scientific side but also on the personal and thinking side. Your support, guidance, and advice are invaluable, and I am incredibly grateful for all the knowledge you passed to me. I appreciate the vibrant and exciting research atmosphere you established in your group, which made the journey full of fun and a fantastic experience. I appreciate the freedom you offer to the students for directing their research and the time you spend with the students, constantly listening and offering out-of-the-box solutions and intelligent ideas.

I am my very thankful to Prof. Dr. Michael Bock for examining my thesis. I would like to express my gratitude for hosting me in a visit to your laboratory. It is my great pleasure to have you in my examination committee.

I owe my deepest gratitude to my group leader Dr. Dario Mager for his outstanding support and guidance. You were always willing to assist and support not only on the research side but also in professional and personal life. Thank you very much, it wouldn't be possible without your help. I would also like to express my most tremendous appreciation to Dr. Neil MacKinnon for the knowledge he gave me in the field of NMR. I have learned a lot from you. I am very appreciative of the success we achieved together, it was my pleasure collaborating with you.

Many thanks to Prof. Dr. Uli Lemmer for spending time and effort attending my TAC meetings. I am grateful for your advice and motivation.

I would like to express special gratitude to Dr. Mazin Jouda and Dr. Hossein Davoodi for their kindness, friendship, and support. They are always willing to support and never hesitate to offer help and advice. I appreciate all the help and knowledge you provided. I would like to thank Emil Mamleyev for all the help and support he provided regarding the SEM images and the technical advice in the field of material science. I would like to acknowledge Dr. Nurdiana Nordin for answering all my chemistry questions. I would like to present my gratitude to Shyam Adhikari for providing help and support in the cleanroom. I would like to thank Erwin Fuhrer for the fruitful discussions we had together.

It was my pleasure to share the office with Anna Zakhurdaeva, Sagar Wadhwa, and Natheer Almtireen. Thank you for all the moments and discussions we had together for more than three years. I would like to thank the rest of the low-cost MEMS group Markus Meissner, Dr. Monsur Islam, Ahsana Sadaf. I was lucky to be part of the group.

I would like to show my most tremendous appreciation to the entire Prof. Korvink group for the professional and friendly environment they provide. I would like to thank Prof. Dr. Jürgen Brandner, Dr. Lorenzo Bordonali, Albina Julius, Mohammad Abdo, Mehrdad Alinaghian, Andrea Rivera, Julia Schulte-Hermann, Pedro Silva, Sofa Toto, Dr. Ali Moazenzadeh, and Dr. Ronald Kampmann.

I am particularly grateful for the assistance provided by the cleanroom team at IMT, Dr. Uwe Köhler, Mrs. Heike Fornasier, Mr. Marco Heiler, Mrs. Barbara Matthis, and Dr. Richard.

My heartfelt gratitude goes to my lovely parents Amr and Eman, my brother Alaa, my sister Sarah and my wife's family. Thank you very much for everything. It was only possible because of your motivation, support, and prayers.

Most important, I would like to thank my lovely wife Nourhan for all the support she provided throughout the entire process. I am indebted to you for everything and for taking care of our lovely son Malek, whom I am grateful for all the joy he added to my life. I am thankful for all the moments, happiness, and challenges we went through together. It was only you the reason for me to reach this point.